INFORMATION TO USERS

This manuscript has been reproduced from the microfilm master. UMI films the text directly from the original or copy submitted. Thus, some thesis and dissertation copies are in typewriter face, while others may be from any type of computer printer.

The quality of this reproduction is dependent upon the quality of the copy submitted. Broken or indistinct print, colored or poor quality illustrations and photographs, print bleedthrough, substandard margins, and improper alignment can adversely affect reproduction.

In the unlikely event that the author did not send UMI a complete manuscript and there are missing pages, these will be noted. Also, if unauthorized copyright material had to be removed, a note will indicate the deletion.

Oversize materials (e.g., maps, drawings, charts) are reproduced by sectioning the original, beginning at the upper left-hand corner and continuing from left to right in equal sections with small overlaps.

Photographs included in the original manuscript have been reproduced xerographically in this copy. Higher quality 6" x 9" black and white photographic prints are available for any photographs or illustrations appearing in this copy for an additional charge. Contact UMI directly to order.

Bell & Howell Information and Learning
300 North Zeeb Road, Ann Arbor, MI 48106-1346 USA
800-521-0600

FAR-RED TO NEAR INFRARED EMISSION AND SCATTERING SPECTROSCOPY FOR BIOMEDICAL APPLICATIONS

by

GANG ZHANG

A dissertation submitted to the Graduate Faculty in Engineering in partial fulfillment of the requirements for the degree of Doctor of Philosophy, The City University of New York

2001

Bell & Howell Information and Learning Company
300 North Zeeb Road
P.O. Box 1346
Ann Arbor, MI 48106-1346

This manuscript has been read and accepted for the Graduate Faculty in Engineering in satisfaction of the dissertation requirement for the degree of Doctor in Philosophy.

1/2/2001 — Date:

Chairman of the Examining Committee:
Dr. R. R. Alfano, Distinguished Professor of Science and Engineering, Department of Physics, Engineering Department of Graduate School, The City College of the City University of New York.

1/2/2001 — Date:

Co-Chairman of the Examining Committee:
Dr. P. P. Ho, Professor, Department of Electrical Engineering, The City College of The City University of New York.

1/24/2001 — Date:

Executive Officer:
Dr. M. Kassir.

Dr. A. Spielmen, Professor, Department of Psychology, The City College of The City University of New York.

Dr. K. Shum, Professor, Department of Electrical Engineering, The City College of The City University of New York.

Dr. W. Wang, Institute for Ultrafast Spectroscopy and Lasers, The City College of New York.

Dr. A. Walser, Professor, Department of Electrical Engineering, The City College of The City University of New York.

Supervisory Committee

The City University of New York

Abstract

Far Red to Near Infrared Emission and Scattering Spectroscopy for Biomedical Applications

by
Gang Zhang

Advisor: Professor R. R. Alfano

Co-Advisor: Professor P. P. Ho

The thesis investigates the far-red and near infrared (NIR) spectral region from biomedical tissue samples for monitoring the state of tissues. The NIR emission wing intensity is weak in comparison to the emission in the visible spectral region. The wing emission from biomedical samples has revealed meaningful information about the state of the tissues. A model is presented to explain the shape of the spectral wing based on a continuum of energy levels. The wing can be used to classify different kinds of tissues; especially it can be used to differentiate cancer part from normal human breast tissues. The research work of the far-red emission from thermal damaged tissue samples shows that the emission intensity in this spectral region is proportional to the extent of the thermal damage of the tissue.

Near infrared spectral absorption method is used to investigate blood hemodynamics (perfusion and oxygenation) in brain during sleep-wake transition. The

result of the research demonstrates that the continuous wave (CW) type near infrared spectroscopy (NIRS) device can be used to investigate brain blood perfusion and oxygenation with a similar precision with frequency domain (FD) type device. The human subject sleep and wake transition, has been monitored by CW type NIRS instrument with traditional electroencephalograph (EEG) method. Parallel change in oxy-Hb and deoxy-Hb is a discrete event that occurs in the transition from both sleep to wakefulness and wakefulness to sleep. These hemodynamic switches are generally about few seconds delayed from the human decided transition point between sleep and wake on the polygraph EEG recording paper. The combination of NIRS and EEG methods monitor the brain activity, gives more information about the brain activity. The sleep apnea investigation was associated with recurrent apneas, insufficient nasal continuous positive airway pressure (CPAP) and the different response of the peripheral and central compartments to breathing events. The different results with finger pulse oximetry and NIRS suggest that optical monitoring of the brain may have advantages that may help clarify the morbidity of obstructive sleep apnea (OSA) Syndrome.

Acknowledgments

I would like to acknowledge my deep appreciation for the constant guidance and counsel of Professor Alfano and Professor Ho during this thesis work. I wish to thank Dr. Alfano for giving me the opportunity to carry out and complete my thesis research. His new and exciting ideas, sharp vision and broad knowledge in optics, biophotonics and laser physics was a stimuli for this thesis work, resulting in most of the encouraging progress. I feel much gratitude towards Professor Ho for his guidance in defining my thesis topic and many discussions.

I am deeply indebted to my wife Dana, my parents, and my son Robert. I would like to take this opportunity to express my sincere thanks to my wife and my parents. They have continuously encouraged me to pursue higher education and have made many sacrifices to give me tremendous supports. Without their encourages and sacrifices, it would have been impossible for me to continuous study. I will always be frateful to them for their encouragement and support. I thank them for always being a source of deep understanding and strong support. This work is dedicated to them, for their love, patience and encouragement.

I thank Dr. Spielman instructing me to finish complicate research work in the sleep lab. In addition Dr. Stankovic helps me complete experiment with piglet animal model and solve the validation problem using CW type NIRS device monitoring blood perfusion of brain tissue. Not of all I thank Dr. S. Demos to help me starting far-red emission research work and Dr. J. Tang to help me to investigate thermal damaged tissue. Dr. J. Ying contributes his idea for setting up a model to explain the mechanism of the

far-red emission from tissue. Furthermore I thank all the research fellows at IUSL for helping me to accomplish my thesis work in the laser and sleep labs.

I thank several agencies for support of my research during the years: NYS, DOE, Mediscences Technology Corp., and CUNY.

Table of Contents

List of Tables

List of Figures

1. Introduction

1.1. Background

Most pathology methods for disease diagnosis are invasive procedures. These methods are effective in detecting disease. There are many disadvantages with the conventional methods, such as, cross-infection, pain, complicated operation procedures and cost. Modern technology offers several ways to develop noninvasive techniques for clinical applications. One of these methods is optical spectroscopy, which is established by Professor Alfano in the 1980's to diagnose tissues.

The main interactions of light with any kind of materials are displayed in Figure 1-1 involving scattering, absorption, and emission. Light can be widely used to acquire fundamental knowledge about various physical, chemical, and biological properties of biomaterials. Optical spectroscopy has been extensively studied as a potential in-vivo and in vitro diagnostic tool that can provide information about both the chemical and the morphologic structure of the tissue [1-5]. Various research groups have attempted to classify, diagnose, and monitor the states and the metabolism of living tissue using optical spectroscopy [6-12]. It has been known that molecular spectroscopic properties are highly dependent on environmental parameters, such as polarity, pH value and viscosity. Optical techniques have become important methods to develop non-invasive diagnostic method of tissue structure and chemical components.

Many of the in-vivo and in-vitro studies concentrated on absorption and fluorescence spectroscopy in the ultraviolet (UV) to visible spectral region [5-18]. Various research groups have attempted to classify and diagnose tissue states using

fluorescence and Raman spectroscopy [3, 14, 19]. The main fluorophores in the UV and visible spectral regions are tryptophan, collagen, elastin, nicotinamine adenine dinucleotide (NADH), nicotinamine adenine dinucleotide phosphate (NADPH), flavin and porphyrins [20]. Time resolved optical spectroscopy could be used to determine whether the light emitting process arises from radiation transitions between electronic states or from a scattering process [21-23]. Raman spectroscopy, an inelastic scattering process, provides spectrally narrow features that can be related to the specific molecular structure of the sample. Raman scattering measurements in tissues shows the presence of a Stokes spectral wing through a visible light source [24-31]. This makes the observation of the fine details in the Raman scattering vibrational spectrum very difficult. The origin of this background signal in the far-red and near infrared (NIR) spectral region in Raman scattering measurements of tissues has never been discussed before. Figure 1-2 shows the Raman spectral profiles from normal breast tissue under different wavelength excitation. The intensity of the Stokes spectral wing becomes weaker as the pump wavelength increases [24]. This spectral wing is considered as fluorescence noise and is usually subtracted from the Raman spectral profile. This latter uses complex fitting parameters to acquire the spectral features associated with the Raman active vibration modes [25, 26].

Elastic scattering and absorption spectroscopy has been widely used to investigate the biomedical samples in vitro and to monitor the physiological parameters of a subject independently from other kind of methods. An example is the pulse oximeter that monitors the heart beat and body oxygenation through a subject's finger [31, 32]. Spectroscopy of blood can be traced back to the 1870s [34]. Several decades later, in the 1930s, Nicholai developed a filter wheel apparatus for finger spectroscopy in normoxia

and ischemia [34]. At the same time, Kramer developed a single beam apparatus using a Siemens barrier layer detector in 1935, followed by Millikan's first dual-wavelength hemoglobinometer in 1936. In 1939, Matthes and Gross invented the ear oximeter [34]. It was in 1977 that Jobsis first described the *in vivo* application of near infrared spectroscopy to monitor changes in the oxygenation of the brain in the intact cat-head [35].

The theoretical work and experiment results demonstrate that the photons in a turbid medium follow a well-defined path [36-39]. For the semi-infinity geometric arrangement, as shown in Figure 1-3, the shape of photon path likes a banana. The absorption and scattering properties of the turbid medium could be obtained by the reflectance optical signals. This gives us a chance to "see through" some depth inside of the human body.

Recently, several research groups used NIRS techniques to investigate muscle metabolism during sports movements, and brain activity during different neuron-active situations [6, 7]. Some research groups also investigated blood perfusion in the brain tissue in different sleep states [40, 41]. They qualitatively explain their experiment results: the HbO_2 concentration increases and Hb concentration decreases in the brain tissue during the "sleep to wake" change and vice-versa. There is a lack of knowledge about what happens to the hemoglobin concentration change in brain tissue during the sleep-wake state transition of a subject. We don't even know what is the relationship between traditional electroencephalograph (EEG) method signal and NIRS signal.

1.2. The significant of NIR spectral region for biomedical materials:

There are several advantages of the far-red to near infrared (NIR) spectral region to study biomedical materials. There are: safe to use; absorption from tissue samples are much lower in the NIR region than in the visible or UV spectral range; elastic scattering effects are much weaker; far-red to NIR spectral beams can penetrate deeper into tissues; fluorescence background is much weaker for Raman scattering in the NIR spectral region; and NIR and red light are much safer for *in vivo* applications than UV light.

The NIRS techniques may be used to diagnose tissues (brain, breast, prostate, and muscles) and to measure the oxygenation of living tissues. It can yield important physiological parameters for the clinical setting. Compared to other technologies, such as computer-aided tomography (CAT), magnetic resonance imaging (MRI) and sonarography, the NIRS devices are truly non-invasive, have high sensitivity, and are low cost and easy to use [32, 33].

1.3. Thesis statement

This thesis focuses on the study of various aspects of the far-red to NIR spectral region to investigate several biomedical applications. The objectives of my research are: (1) to classify different types of tissue using NIR spectral wing emission (such as a cancerous tumor from normal human breast tissue); (2) to evaluate the thermal damage of tissue samples using NIR spectral wing emission; (3) to investigate the blood perfusion dynamics of brain tissue of subjects during a sleep to awake transition; and (4) to study sleep disordered patients by NIR spectral back scattering. The common thread in these

projects is the use of NIR light to monitor biomedical media.

My thesis research will focus on two photonic-based approaches to probe biomedical media using far-red to NIR spectroscopy. The first part uses NIR emission to establish novel non-invasive spectroscopy and imaging methods to detect cancer and thermal damage in tissues. The purpose is to investigate the properties of far-red to NIR emission from biological tissue samples could lead to a potential method to classify different tissue states. An emission spectral wing is usually observed as the background in Raman spectra from tissue samples in far-red to NIR spectra region. Other investigators commonly subtract this background signal out by data processing as noise.

The second part uses NIR absorption and diffusion reflectance scattering to investigate hemodynamics where the blood perfusion and the oxygenation status are in the front part of the brain, during the sleep-wake transition of a subject compared with the traditional EEG method. To get validate experiment result on human brain activity with CW type NIR spectroscopy, the CW and FD types NIRS devices have been compared using a newborn piglet animal model. The purpose is to investigate the cerebral blood perfusion in the front of human brain during sleep to wake transition, using NIR back-scattering spectroscopy.

The tasks performed in this thesis includes:

- Determining the far-red emission from different type of tissue sample, especially between cancer and normal breast tissues.
- Finding the relationship between the far-red emission intensity and the extent of thermal damage to tissue samples.

- Developing a simple physical model to explain the mechanism of the laser induced far-red to NIR emission from biomedical tissue samples.
- Determining the experimental conditions of the continuous wave (CW) and frequency domain (FD) methods to obtain data of blood perfusion in brain tissue.
- Finding the relationship between blood perfusion and oxygenation in a sleep-wake status of the human subject with CW type NIRS device and EEG equipment.

1.4. Thesis format

Chapter 1 is the introduction and background information of this thesis.

In Chapter 2, a theoretical review is given on the basic interactions between light and biomedical samples. A review of the light propagation in the highly scattering media with an application of blood perfusion measuring methods is presented.

In Chapter 3, the main chromophores and fluorophores in tissue samples in the UV to visible spectral region are given. The experimental setups to obtain far-red emission signals from tissue samples, and blood perfusion changes in brain tissue of a subject are presented. It also briefly discusses laser safety considerations for the human subject, during the NIRS measurement of brain tissue blood dynamics in the sleep experiment.

Chapter 4 describes the far-red emission from tissue samples under red laser excitation. The emission intensity is used to differentiate same kinds of tumor tissue from normal tissues.

Chapter 5 gives the result of far-red emission from thermal damaged tissue samples. The relationship between the intensity of the far-red emission from the tissue

sample and the extents of the thermal damage could have the potential to measure tissue damage in laser surgery and laser welding.

Chapter 6 describes a physical model that could explain the mechanism of laser induced far-red and NIR emission from tissue samples.

Chapter 7 compares the result of monitoring the blood perfusion change in piglets' brain tissue in an animal subject model between frequency domain and continuous wave methods. This work validates the blood perfusion change of the subject, which is obtained with CW type NIRS instrument during the wake and sleep transition.

Chapter 8 describes the investigation procedure and results of changes of the blood perfusion in human brain tissue during sleep and wake transition using CW type NIRS instrument.

Chapter 9 describes the preliminary results of the hemodynamics of brain tissue in a sleep apnea patient.

Chapter 10 will present the summary of current research work

Chapter 11 suggests the direction of future research work in far-red and NIR spectral region.

1.5. References

1. Delpy D., "Optical spectroscopy for diagnosis," *Phys. World*, 1994, Aug. 34-39.
2. Alfano R. R., Tata D. B., Cordero J., Tomashefsky P., Longo R. W., Alfano M. A., "Laser Induced Fluorescence Spectroscopy from Native Cancerous and Normal Tissue," *IEEE Journal of Quantum Electronics* **20**, 1507-1511 (1984).
3. Liu C.-H., Das B. B., Sha Glassman W. L., Tang G. C., Yoo K. M., Zhu H. R., Akins D. L., Lubicz S. S., Cleary J., Prudente R., Celmer E., Caron A., Alfano R. R., "Raman, Fluorescence, and Time-Resolved Light Scattering as Optical Diagnostic Techniques to Separate Diseased and Normal Biomedical Media," *J. Photochem. Photobiol.* B: Biol., **16**, 187-209 (1992).
4. Profio A. E., "Laser Excited Fluorescence of Hematoporphyrin Derivative for Diagnosis of Cancer", *IEEE Journal of Quantum Electronics* **20**, 1502-1505 (1984).
5. Liu C. H., Tang G. C., Pradhan A., Sha W. L., Alfano R. R., "Effects of Self-Absorption by Hemoglobins on the Fluorescence Spectra from Normal and Cancerous Tissues," *Lasers in Life Sciences* **3**, 167-176 (1990).
6. McCully K. K., Kakihira H., Vanderborne K., et al., "Noninvasive measurement of activity-induced changes in muscle metabolism", *J. Biomed.*, 1991, **24**: 153-156.
7. Haller R. G., "Oxygen utilization and delivery in metabolic myopathis", *Annals of Neurology*, 1994, **36**(6): 811-813.

8. Wagnieres G. A., Linuma S., Schomacker K. T., Deutsch T. F., Hasan T., "In Vivo Tissue Characterization Using Environmentally Sensitive Fluorochromes", In: Fluorescence Microscopy and Fluorescent Probes, Ed. J. Slavik, Plenum Press, New York, NY, 1996.

9. Sterenborg H. J. C. M., Thomsen S., Jacques S. L., "*In Vivo* Autofluorescence, of an Unpigmented Melanoma in Mice. Correlation of Spectroscopic Properties to Microscopic Structure", *Melanoma Research* **5**, 1-6 (1995).

10. Alfano R. R., Tang G. C., Pradham A., Lam W., Choy D. S. J., Opher E., "Fluorescence Spectra from Normal Human Breast and Lung Tissues," *IEEE Journal of Quantum Electronics* **23**, 1806-1811 (1987).

11. Yang Y., Tang G. C., Bessler M., Alfano R. R., "Fluorescence Spectroscopy as a Photonic Pathology Method for Detecting Colon Cancer," *Lasers in Life Sciences* **6**, 259-276 (1995).

12. Yang Y., Celmer E. J., Zurawska-Szczepaniak M., Alfano R. R., "Excitation Spectrum of Malignant and Benign Breast Tissues: A Potential Optical Biopsy Approach," *Lasers in the Life Science* **7**, 249-265 (1997).

13. Sha Glassman W. L., Liu C. H., Tang G. C., Lubicz S., Alfano R. R., "Ultraviolet Excited Fluorescence Spectra from Non-Malignant and Malignant Tissues of the Gynecological Tract", *Lasers in the Life Sciences 5*, 4958 (1992).

14. Baraga J. J., Taroni P., Park Y. D., An K., Maestri A., Tong L. L., Rava R. P., Kittrell C., Dasari R. R., Feld M. S., "Ultraviolet Laser-Induced Fluorescence of Human Aorta", Spectrochimica Acta 45A, 95-99 (1989).

15. Tang G. C., Pradhan A., Sha W., Chen J., Liu C. H., Wahl S. J., Alfano R. R., "Pulsed and CW Laser Fluorescence Spectra from Cancerous, Normal, and Chemically Treated Normal Human Breast and Lung Tissues", *Applied Optics* **28**, 2337-2342 (1993).

16. Kozikowski S. D., Wolfram L. J., Alfano R. R., "Fluorescence Spectroscopy of Eumelanins", *IEEE Journal of Quantum Electronics* **20**, 1379-1382 (1984).

17. Mahadevan A., Mitchel M. F., Silva E., Thomsen S., Richards-Kortum R., "Study of the Fluorescence Properties of Normal and Neoplastic Human Cervical Tissue", *Lasers in Surgery and Medicine* **13**, 647-655 (1993).

18. Cothren R. M., Richards-Kortum R., . Sivak M. V, Fitzmaurice Jr., M., Rava R. P., Boyce G. A., Doxtader M., Blackman R., Ivanc T. B., Hayes G. B., Feld M. S., Petras R. E., "Gastrointestinal Tissue Diagnosis by Laser-Induced Fluorescence Spectroscopy at Endoscopy", *Gastrointestinal Endoscopy* **36**, 105-111 (1997). (**d**)

19. Baraga J. J., M Feld. S., R Rava. P., "*In Situ* Optical Histochemistry of Human Artery Using Near Infrared Fourier Transform Raman Spectroscopy", Proc. Natl. Acad. Sci. U.S.A. 89, 3473-3477(1993).

20. Jacques S.L., "Optical techniques for tissue science and engineering", *SPIE Proceeding of Biomedical Optics 99, 3863*, 2-7.

21. Pradhan, A., Das, B. B., Yoo, K. M., Cleary, J., Prudente, R., Celmer, E. and Alfano, R. R. "Time-resolved UV photoexcited fluorescence kinetics from malignant and non-malignant human breast tissues", *Lasers in Life Sci.* 4(4), 225-234 (1992).

22. Glassman, W. S., Steinberg, M. and Alfano, R. R. "Time resolved and steady state fluorescence spectroscopy from normal and malignant cultured human breast cell lines", *Lasers in Life Sci.* **6**(2), 91-98 (1994).

23. Meech S. R., Stubbs C. D., Phillips D., "The Application of Fluorescence Decay Measurements in Studies of Biological Systems", *IEEE Journal of Quantum Electronics* **20**, 1343-1352 (1984).

24. Frank, C. J., Redd, D. C., Gansler, T. S. and McCreery, R. L. "Characterization of human breast specimens with Near-IR Raman spectroscopy," *Anal. Chem.* **66**(3), 319-326 (1994).

25. Mahadevan, A., Ramanujam, N., Mitchell, M. F., Malpica, A., Thomsen, S. and Kortum, R. R. "Optical techniques for the diagnosis of cervical precancers: Comparison of Raman and fluorescence spectroscopies," *in Advances in Fluorescence Sensing Technology II*, J. R. Lakowicz, ed., Proc. SPIE **2388**, 110-120 (1995).

26. Baraga, J. J., Feld, M. S. and Rava, R. P. "Rapid near-infrared Raman spectroscopy of human tissue with a spectrograph and CCD detector," *Appl. Spectrosc.* **46**(2), 187-190 (1992).

27. Frank C. J., McCreery R. L., Redd D. C., "Raman Spectroscopy of Normal and Diseased Human Breast Tissue," *Anal. Chem.* **67**(5), 777-783 (1995).

28. Clarke R. H., Hanlon E. B., Isner J. M., Brody H., "Laser Raman Spectroscopy of Calcified Atherosclerotic Lesions in Cardiovascular Tissue", *Appl. Opt.* **26**, 3175-3177 (1987).

29. Keller S., Schrader B., Hoffmann A., Schrader W., Metz K., Rehlaender A., Pahnke J., Ruwe M., Budach W., "Application of Near-Infrared-Fourier Transform Raman Spectroscopy in Medical Research", *J. Raman Spectrosc.* **25**, 663-671 (1994).

30. Alfano R. R., Liu C. H., Sha W. L., Zhu H. R., Akins D. L., Cleary J., Prudente R., E Ceilmer., "Human Breast Tissues Studied by IR Fourier Transform Raman Spectroscopy", *Laser Life Sci.* **4**, 23-28 (1991).

31. Liu C.-H., Sha Glassman W. L., Zhu H. R., Akins D. L., Deckelbaum L. I., Stetz M. L., O'Brien K., Scott J., Alfano R. R., "Near-IR Fourier Transform Raman Spectroscopy of Normal and Atherosclerotic Human Aorta", *Laser Life Sci.* **4**, 257-264 (1992)

32. Severinghaus J. W., Kelleher J. F., "Recent developments in pulse oximetry", Anesthesiology, 1992, **76**(6): 1018-1037

33. Shina T., Tanabe L., Nakase Y., et al. "Development of a portable tissue oximeter using near infrared spectroscopy", *med. & Biol. Eng. & Compt.*, 1995, July: 622-626

34. Chance B, et al., "Optical investigations of physiology: a study of intrinsic and extrinsic biomedical contrast". *Philos Trans R Soc Lond B Biol Sci*, 1997. **352**: p. 707-716.

35. Jobsis FF, "Noninvasive infrared monitoring of cerebral and myocardial sufficiency and circulatory parameters". *Science*, 1977. **198**: p. 1264-1267.

36. Feng S, Zeng F, and Chance B, "Monte Carlo simulation of photon mifration phat distribution in multiple scattering media", Proc. of Photon Migration and Imaging in Random Media and tissues, 1993, SPIE 1888, pp 78-89.

37. Feng S, and Zeng F, "perturgation theory of photon migration in the presence of a single defect", OSA Proc. On Advances in Optical Imaging and Photon Migration, 1994, Vol. 21, pp 217-228.

38. Perelman LT, Wu J, Itzkan I, Wang Y, Dasari R and Feld MS, "Photon paths in turbid media: theory and experimental observation", OSA Proc. On Advances in Optical Imaging and Photon Migration, 1994, Vol. 21, pp 153-155.

39. Maier JS, Gratton E, "frequency-domain methods in optical tomography: detection of localized absorbers and a backscattering reconstruction scheme", Proc. of Photon Migration and Imaging in Random Media and tissues, 1993, SPIE 1888, pp 440-449.

40. Hoshi, Y., Mizukami, S., and Tamura, M., "Dynamic features of hemodynamic and metabolic changes in the human brain during all-night sleep as revealed by near-infrared spectroscopy", *Brain Research*, **652** (1994) 257-262.

41. Madsen, P. L., Schmidt, J. F., Wildschiodtz, G., Friberg, L., Holm, S., Vorstrup, S., and Lassen, N. A., "Cerebral oxygen O_2 metabolism and cerebral blood flow in humans during deep and rapid-eye-movement sleep", *J. Appl. Physiol.*, **70** (6) (1991) 2597-2601.

1.6. Figures

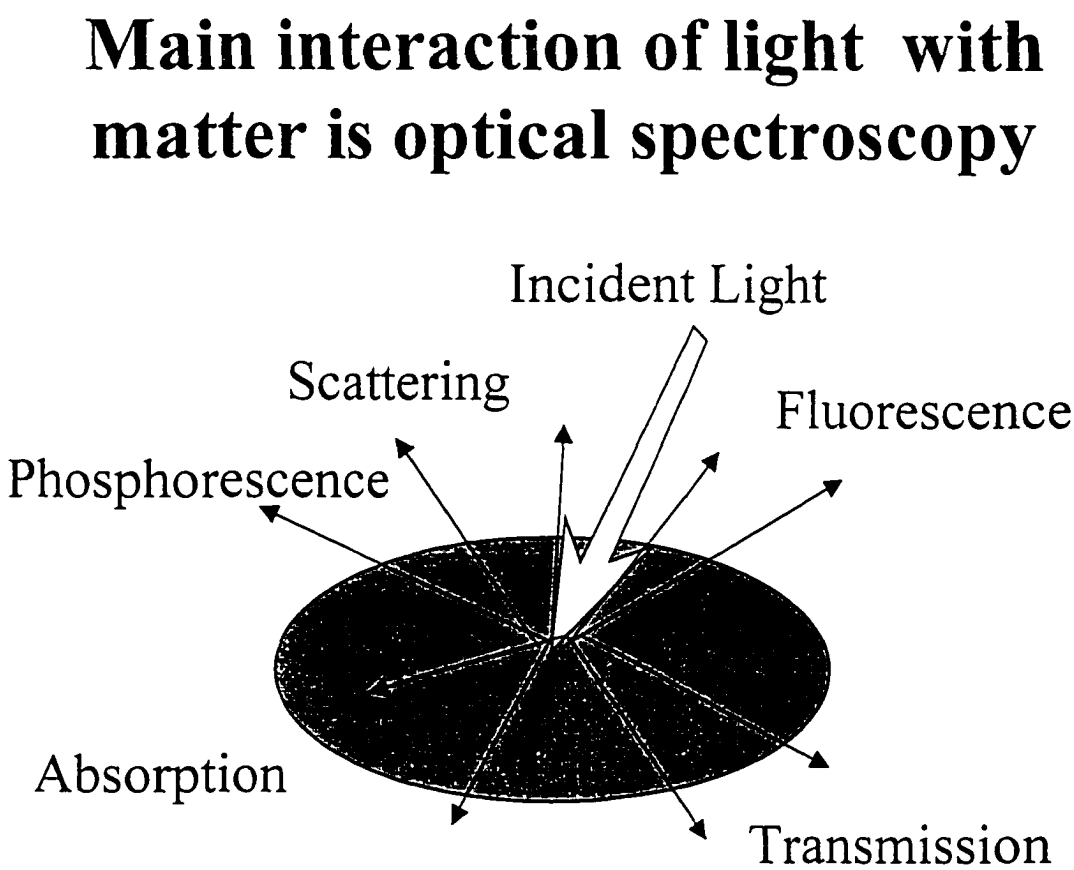

Figure 1-1 The processes are involved in spectroscopy.

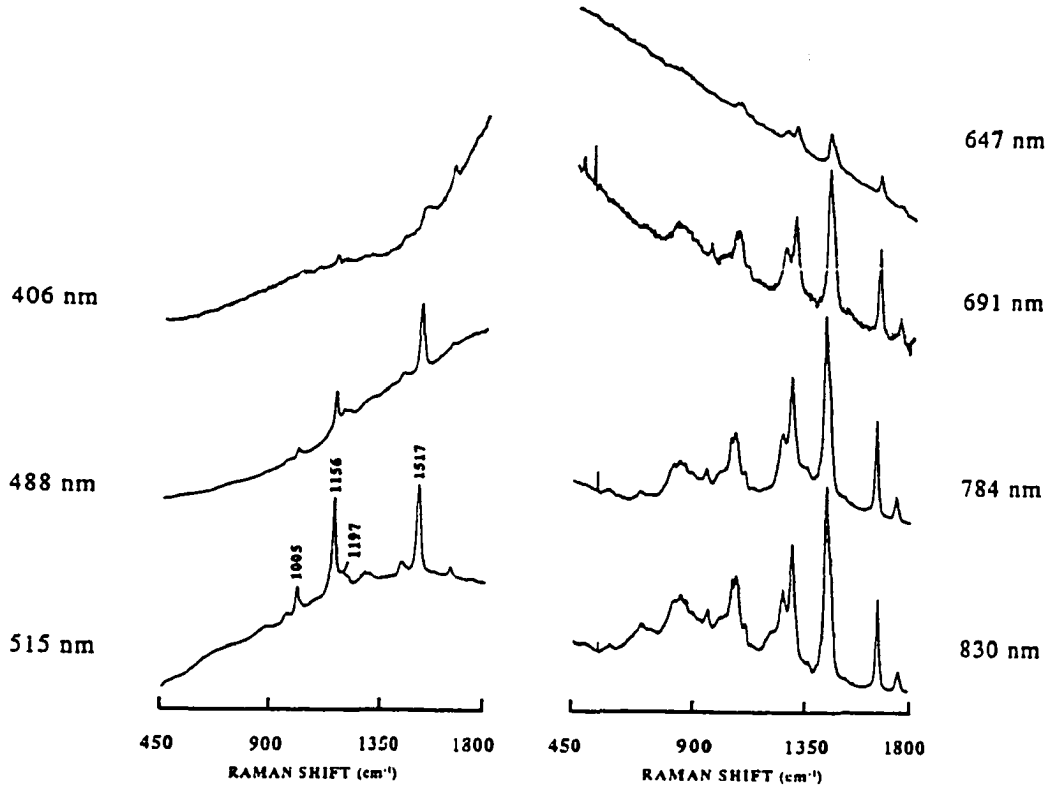

Figure 1-2 Raman spectroscopy of normal tissue form human breast with different laser wavelength excitation [24] showing the emission wing and Raman lines.

The background emission with 406 nm laser excitation could be NADH components in tissue sample. The background emission with 488 nm or 515 nm laser excitation could be contributed from flavin and its derivatives in tissue. The background emissions with the excitation longer than 600 nm are not known.

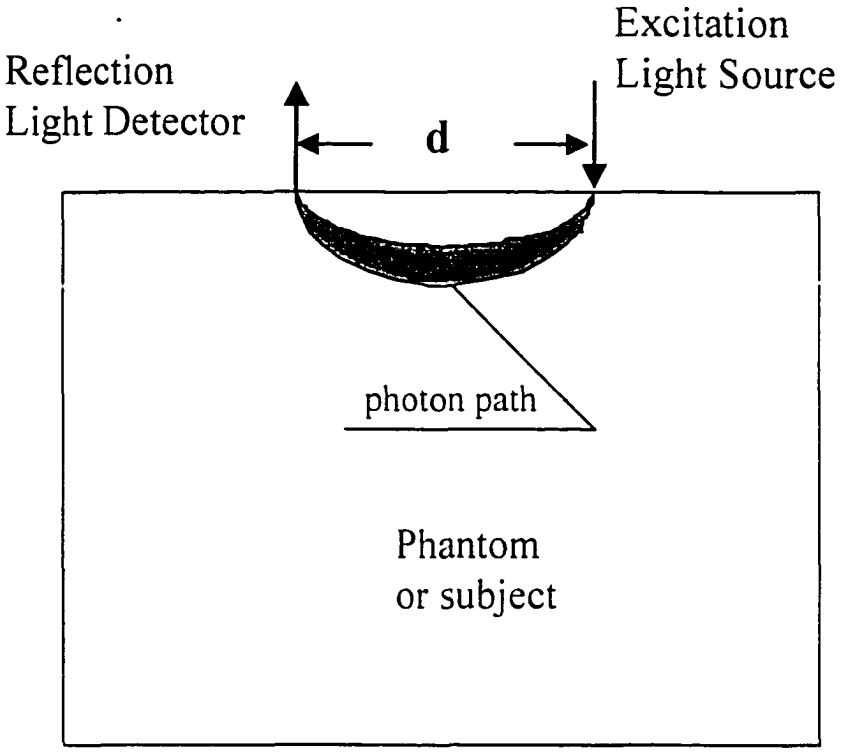

Figure 1-3 Photon path in homogeneous turbid media.

Right side is an optical source, and left side represents an optical detector. The d represents the distance between source and detector at the boundary surface of the turbid media. For typical biomedical, the depth of the mean photon path of the banana shape is $\sim d/2\sqrt{2}$ [36].

2. Underlining optical mechanisms and review of the basic interaction between light and biomedical samples

This chapter reviews the underlying physics of absorption, emission and scattering of light in a sample.

2.1. A brief review of the main absorption and emission components in tissue samples

Absorption spectra of tissues are dominated by the bands due to the water, protein, DNA, melanin, and hemoglobin content of tissues from the UV to the visible spectral regions [1]. Bilirubin and biliverdin are other strong absorbers but only exist in tissue with jaundice disease or with wounded long lime. Carotene is one of the extrinsic chromophore components and mostly exists in fat cells of the human body [2]. As shown in Figure 2-1, most of the absorption of these chromophores is in the UV and the visible light range, especially for DNA and protein [3]. In the far-red and near infrared spectral range (700 ~1100 nm), most of the biochemical components have a very low absorption factor, and consequently this is an optical window to allow the detection of information inside of the human body. Melanin is a strong absorber in the visible and NIR spectral regions and has a very flat and broadband absorption spectrum [4]. Most of the melanin component exists in black hair, and it affects optical signals originating inside of the human body, which pass through the hair. A strong hemoglobin signature indicates blood perfusion, and oxygenation of the blood can be determined from the mixture of oxy- and

deoxy- hemoglobin spectra.

The typical light induced emission spectral profile from tissue sample is shown in Figure 2-2a. It generally consists of back scattering of laser line, background emission and Raman scattering. The typical scattering intensity from laser line is about 10^{-1} of the incident light; typical fluorescence intensity is in order of 10^{-6} of incident light, and typical intensity of Raman scattering is in order of 10^{-8} of incident light or less.

Light induced auto-fluorescence is due to a variety of native fluorophores in the tissue. The main fluorophores are tryptophan, collagen, elastin, NADH, flavin, and porphyrin. Most of these fluorophores emit light in the UV and visible wavelength range [1]. Porphyrin related components can have emissions in the far-red to near infrared spectral range, such as portal-porphyrin and hemato-porphyrin whose spectra shown in Figure 2-2b. In the human body, the porphyrin ring center has a Ferrum (Fe) ion to form myoglobin and hemoglobin that will quench the fluorescence emission from the porphyrin molecules. Therefore, there are no main particular biochemical molecules in a typical tissue sample that are known to emit light in the far-red to the NIR spectral range. Tissues fluoresce differently and many investigators are using such differences to distinguish disease states [5, 6].

2.2. *The relationship between absorption and emission with the energy state transitions of molecules*

The total energy of a molecule in its ground state includes contributions from the motions of the electrons and the atomic nuclei. The nuclei have translational, vibrational, and rotational motions in space, and the electrons move in discrete orbits about one or more nuclei. Each set of electron and nuclear motions correspond to a possible energy

state of the entire molecule. The transitions between energy states induced by the absorption and emission of light may be identified by optical spectroscopy. Molecular spectra in the UV and visible regions involve transitions between different electronic energy levels. The sharp absorption lines are shown in Figure 2-3a corresponding to discrete electronic transitions. Each electronic state has a set of vibrational energy levels. For a non-linear multi-atom molecule, the number of vibrational energy levels is 3n-6, where n is the number of the atoms in the molecule. This vibronic substructure induces the broadening of the electronic transitions into bands (Figure 2-3b). In an allowed absorption process, a molecule absorbs one photon and is raised to a higher energy state. Similarly, in as allowed emission process, the molecule falls to a lower energy state and emits one photon. These transitions are efficient only when the quantum energy of the photon is close to the difference between the energy of the molecule in the initial and final states. Therefore, the character of absorption and emission spectra provides information about the structure and properties of molecules [7].

2.2.1. Absorption

At physiological temperatures, most molecules are in equilibrium with the outside environment, and they are in the lowest vibration level of the ground state ($v = 0$). After the molecule absorbs optical energy, it is in an excited electronic state or in a mixed excited electron and vibration state. If the electronic state has many vibration states, then the absorption has a wide spectral band. Most of the bio-molecule's absorption consists of this broad absorption without structure. This non-structured absorption band has the profile of many overlapping vibrational transitions [7].

Figure 2-3 displays the relationship between energy levels and the absorption

spectra. The atomic-like electronic energy levels are shown in Figure 2-3a [7]. The optical transitions are very narrow because only light of wavelength corresponding to the electronic energy differences between the sharp levels can be absorbed. The lower absorption line results by the transition from energy state S_0 to energy state S_1, while the higher absorption line results by the transition from energy state S_0 to energy state S_2. The strength of each transition is indicated by the extinction coefficient (α) of the material, and the line width is determined by the resolution of the spectrometer. Figure 2-3b shows molecular-like energy levels [7]. The higher horizontal lines are the vibrational energy states associated with the excited electronic states S_1 and S_2. The vibrational levels of the ground state S_0 are not shown and the interaction of the electronic and vibrational energy levels broadens the electronic transitions into bands. The structure in the absorption spectrum S_0 to S_1 results from the vibronic transitions 0-0', 0-1', 0-2', etc. Only the envelope of the transitions is resolved in the S_0-S_2 spectrum.

The attenuation of light through a medium will depend on the absorption strength of the material. The optical absorption at a specified wavelength is proportional to the density of absorption material c, to the extinction coefficient $\alpha(\lambda)$ of the material, and to the optical path length l through the media:

$$\frac{dI}{dl} = -I \bullet \alpha \bullet c \qquad (1)$$

The solution of this equation is: $I = I_0 e^{-\alpha c l}$,

where I_0 is the incident intensity. This is the Beer-Lambert relationship.

2.2.2. Emission

After a molecule absorbs optical energy, it is in a higher energy state called the

excited state. It is a non-equilibrium state and will return to the equilibrium state by releasing the absorbed energy. This is the relaxation process of the excited molecule. There are two kinds of relaxation processes in excited molecules: a) the radiative relaxation with molecular emission during the relaxation process; b) relaxation without radiation whereby the energy is transferred to the lattice of the molecules resulting in heating of the material.

There are two kinds of emission phenomena related to the excitation wavelength: 1) emission spectra are independent from the excitation wavelength, which is called fluorescence and phosphorescence; 2) emission spectra which are dependent on the excitation wavelength, and it is called scattering.

2.2.2.1. Fluorescence and phosphorescence spectra

When different wavelengths excite fluorescencing molecules, the emitting material could be excited into states related to the excitation wavelength. Therefore, one could think that the initially excited energy distribution and the resulting emission would be very different for different wavelengths of the excitation light. But experiments do not show in this result, many emission spectra of complex bio-molecules are independent of the excitation wavelength. Fluorescence spectra are independent of the excitation wavelength. From these observations, it can be assumed that although the initial population distributions of the excited states in the molecules are different for different wavelength excitations, the emission is always generated from the lowest excited states. After the molecule absorbs optical energy, the vibration by excited state of the original excitation transition will relax very rapidly. The times of this change are much shorter than the lifetime of the excitation state of the molecule.

The optical emission intensity for each wavelength is given by a 1st order relationship for low power excitation. which is proportional to the population of the excited states $N(\lambda)$ and the quantum efficiency $Q(\lambda)$ of the emission from this energy level to the ground state. Therefore, the emission intensity at a certain wavelength can be represented as $I(\lambda) \sim N(\lambda)Q(\lambda)$. For typical material, N and Q which are functions of the wavelength, and they depend on the particular molecule structure, the excitation method, and the excitation intensity in the experiment.

Figure 2-4 shows an energy level diagram for an organic molecule, with transitions between the singlet (S_0, S_1, S_2,...) and triplet (T_1, T_2,...) electronic levels. Inter system conversion is shown by the energy transfer between the singlet and the triplet electronic levels. The radiation decay processes depicted are fluorescence (singlet to ground state) and phosphorescence (triplet to ground state).

2.2.2.2. Raman spectra

There are two kinds of emission spectra that dependent on the excitation wavelength: the elastic scattering and the inelastic scattering spectra. Elastic scattering emits exactly the same wavelength as the excitation wavelength and is called Rayleigh scattering. There is no energy exchange between the scattering material and photons. Raman scattering is an inelastic scattering process, and features energy exchange between the photons and the scattering material. The emission wavelength of Raman scattering differs from the excitation wavelength by a fixed energy shift.

As shown in Figure 2-5, for Rayleigh and ordinary Raman scattering, the molecules absorb a photon in a virtual energy state and directly jump back to the ground state with a photon emission. When the emission is generated from the transition to the

exact original energy level, the emission is Rayleigh scattering. When the emission is generated from the transition to the higher vibration level of the ground state with an energy contribution to the molecular vibration, the emission is Stokes Raman scattering with wavelength $\nu_0 - \Delta\nu$. When the emission is generated from the transition to the lower vibration level of the ground state with an energy addition from the molecular vibration, the emission is Anti-Stokes Raman scattering with wavelength $\nu_0 + \Delta\nu$. The spectra of Raman scattering is directly generated from molecular bands. The Raman peak shift and the related intensity changes of the peaks reflect the molecules structure and their environment parameters.

Since the scattering interaction between molecules and photons is generated in virtual energy state, there is no need for a molecular energy state to be resonant with the excitation wavelength. Therefore, the scattering emission can occur at any excitation wavelength. The intensity of Raman scattering is usually a few orders of mugnitude weaker than the fluorescence emission since it is generated from a virtual energy level and the probability of emission from the virtual energy level is very low except when the excitation wavelength is close to the molecular absorption band, that is called resonant Raman scattering (see Figure 2-5).

2.2.2.3. Emission spectra of real work samples

For the biochemical spectral experiment, the emission profile could be affected by some other factors: self-absorption at certain wavelengths induced by different chromophore in the sample can reduce the practical quantum efficiency factor. The practical emission intensity can then be modified as:

$$I(\lambda) \sim N(\lambda)Q(\lambda)[1 - A(\lambda)] \quad (2)$$

where A is the absorption coefficient of the chromophore that decreases the emission quantum efficiency.

2.2.3. Lifetimes of emission

Emission lifetimes provide information about the excited state properties of molecules and their interactions with the environment. The ultra-fast laser system is the tool to measure the lifetime of the molecular emission. In general, the excitation laser pulse duration is of the order of picosecond (ps) or femtosecond (fs), and is much shorter than the lifetime of molecular fluorescence emission. In describing the process, this light pulse can be simplified as a delta function in the time domain. The emission intensity I from the excited molecules is proportional to the population of the excited molecules n. and if α is the probability of the transition from the excited state to the ground state. This process can written as:

$$dn = -\alpha \cdot n \cdot dt \quad (3)$$

That is $n = n_0 \exp(-\alpha \cdot t)$, where n_0 is the initial population in the excited state and t is the time after excitation. In the case of a transition without quenching and internal absorption, the emission intensity I depends on the reduction of the excited population. That is:

$$I = \frac{dn}{dt} = \alpha n = \alpha n_0 \exp(-\alpha t) \quad (4)$$

When t = 0, $I = \alpha n_0 = A$ is the initial emission intensity. The decay time of the emission is proportional to $1/\alpha$, that is $\tau = 1/\alpha$. The time profile of the emission can then

be written as:

$$I(t) = A\exp(-t/\tau) \tag{5}$$

It is called fluorescence when the radiation relaxation is from the singlet state to the ground state transition and the typical radiation time is 10^{-8} ~ 10^{-9}s. The phosphorescence radiation is generated from the triplet state to the ground state transition and its emission lifetime is μs to ms or longer. The lifetime of scattering emission is very short since the interaction between photons and the molecule is virtual. The typical lifetime of scattering is in the ps and sub-ps region.

In case a mixture of several kinds of emission are observed, the emission decay will be a mixture of several exponential decays:

$$I(t) = \sum A_i \exp(-t/\tau_i) \tag{6}$$

where A_i represents each individual amplitude component and τ_i represents an individual time decay constant.

2.3. Optical absorption spectroscopy with diffusion scattering to determine blood in tissue

Many diseases and physiological problems after sports activity are directly related to the body's oxygen metabolism. The energy transfer in most tissues and cells of human body depends on oxygenation. Monitoring the oxygenation of organs in the body is very important to diagnosing many diseases and to investigate the physiological status.

Oxygenated blood (HbO_2) is the medium to transfer the oxygen to the tissue area that is consuming oxygen for cell metabolism. Deoxygenated blood (Hb) is generated by living cells with the release of CO_2. The higher the metabolism rate is in a certain tissue

area, the more oxygenated blood is needed in this tissue area to support energy utilization. Therefore, to evaluate the metabolism rate in a certain tissue area, both blood perfusion, and tissue blood oxygenation are generally measured.

Optical spectroscopy of tissue blood monitoring is based on the relative optical transparency of biological tissues in the red and near infrared region as well as the distinct absorption properties of oxy-hemoglobin (HbO_2) and deoxy-hemoglobin (Hb) [8, 9]. Figure 2-6 shows absorption spectra of Hb and HbO_2 in the NIR spectral region [10]. The isobathic absorption point ($\alpha_{HbO2} = \alpha_{Hb}$) of the oxy-hemoglobin and deoxy-hemoglobin is around 800 nm. Oxidized cytochrome aa_3, existing inside of mitochondria, could be affected by tissue metabolism status as well. Figure 2-7 shows the NIR absorption spectra of cytochrome aa_3 in oxidized and reduced status. To determine the changes of all of these three chromophores, we need obtain the attenuation change ΔA with three wavelengths [11]:

$$\begin{aligned}
\Delta A(\lambda_1) &= \Delta HboE_{Hbo}(\lambda_1) + \Delta HbE_{Hb}(\lambda_1) + \Delta aa_3E_{aa3}(\lambda_1) \\
\Delta A(\lambda_2) &= \Delta HboE_{Hbo}(\lambda_2) + \Delta HbE_{Hb}(\lambda_2) + \Delta aa_3E_{aa3}(\lambda_2) \\
\Delta A(\lambda_3) &= \Delta HboE_{Hbo}(\lambda_3) + \Delta HbE_{Hb}(\lambda_3) + \Delta aa_3E_{aa3}(\lambda_3)
\end{aligned} \tag{7}$$

where $E_{HbO}(\lambda)$, $E_{Hb}(\lambda)$, and $E_{aa3}(\lambda)$ are known, and indicate the molar extinction coefficient to base e at wavelength λ for complete oxy- and deoxy- hemoglobin and oxidized cytochrome aa_3 molecules respectively. When more than three wavelengths are used, multi-linear regression can be used to provide a least squares 'fit' of the individual spectrum of each component and estimate of the size of the possible errors in the calculated concentration changes.

Due to the ratio of the absorption coefficient of hemoglobin to that of the

cytochrome aa_3 is approximately ten or even higher [12], the absorption of cytochrome aa_3 can be included in the hemoglobin concentration measurement for non-precise measurement. In this research work, two wavelengths setup was used to reduce the experiment cost.

In tissue, light is both absorbed and scattered [9, 13]. Light attenuation is due to: 1) absorption from chromospheres of a fixed concentration, 2) absorption from chromophores of variable concentration, and 3) light scattering [14]. In the absence of scattering, the total light absorption in the medium is a linear sum of that due to each chromophore [14]. In a scattering medium like tissue, this linear summation is distorted because the optical path length at each wavelength may be different [14]. This distorted spectrum is then superimposed upon further wavelength-dependent attenuation arising from light loss due to scatter, which is complex function of the μ_a (absorption) and μ_s (scattering), scattering phase function, and tissue and measurement geometry [14].

Tissue samples are highly scattering media with weak absorption in the NIR spectral region. For normal living subjects, the optical properties of tissue remain constant except for the blood perfusion rate. A blood perfusion rate change induces tissue absorption change $\Delta\mu_a$, or optical signal attenuation change ΔA at certain wavelengths. Therefore, measuring tissue absorption changes or optical attenuation changes can obtain knowledge of the blood perfusion and tissue oxygenation changes to evaluate the metabolism rate change in certain tissue locations.

The theoretical work and experiment results demonstrate that the photons in a turbid medium follow a well-defined path [15-18]. For the semi-infinity geometric arrangement, as shown in Figure 2-9, the shape of photon path likes a banana. The

absorption and scattering properties of the turbid medium could be obtained by the reflectance optical signals. For typical biomedical tissue sample, the light attenuation from illumination and collection is in order of 10^{-6} with 3 cm distance of two optical probes.

Optical instruments for tissue blood monitoring contain the following parts: (1) One or more light sources that emit light of a known wavelength and intensity; (2) One or more light detectors (usually a photodiode, photo-multiplier tube, or CCD) that measure the intensity of scattered light exiting the tissues; (3) A computer that integrates the input and output signals into clinically useful information [13, 19, 20]; and (4) algorithm.

There are three experiment methods to be used to evaluate the absorption changes inside of the living tissues by NIR spectroscopy as shown in Figure 2-8: (1) time-resolved [23, 24], (2) frequency-domain [6], and (3) continuous wave (CW) [13, 21, 22].

(1) Time-resolved instruments (time-of-flight-and-absorbance, TOFA., streak camera, TD) uses an ultra-fast laser pulse to excite the tissue sample and to measure the time profile of the scattered light at a location away from the excitation source point (see Figure 2-8a). The samples' absorption factor μ_a and scattering factor μ_s can be obtained by using a complex mathematical method to fit the data curve. This method provides scattering information from the mean transit time of pico-second light pulses and tissue absorption from the long time decay of the broadened scattered laser pulse profile [9, 23, 24, 26-29].

(2) Frequency-domain instruments are based on the photon density wave principle. It uses radio frequency-modulated light sources to excite the sample and uses a phase sensitive device to detect the modulation and phase shift of the light through the

sample (see Figure 2-8b). This method enables quantification of tissue absorption and scattering [13, 27, 30].

(3) Continuous wave spectrometers are based on the continuous wave attenuation method. It assumes that the scattering parameters of the tissue samples are not changed during the measurement time, and the attenuation will reflect the absorption change of the living tissue sample (see Figure 2-8c). This method is unable to determine the tissue scattering and optical path-length [13, 14, 23]. It is unable to provide absolute concentration measurements but they only measure the changes from a baseline with no information about whether the baseline value is normal, high, or low [20, 25]. This method gives relative changes.

Both time- and frequency-domain methods enable quantification of tissue absorption and scattering. Thus they provide absolute determination of hemoglobin concentration in situ. The detailed principle of these three kinds of methods to get the blood concentration change in tissue will be described in following sections.

2.3.1. Time resolved method

We take a consideration into a single point source of light pulses in a volume of random scatters that without any boundaries. The source of light produces a narrow pulse of photons that diffuse in all directions. We assume that the time dependent photon density $\Psi(r, t)$ generated in the volume can be described by the diffusion equation [23, 31]:

$$\frac{1}{v}\frac{\partial}{\partial t}\Psi(r,t) - D\nabla^2\Psi(r,t) + \mu_a\Psi(r,t) = S(r',t) \tag{8}$$

where v is the speed of photons in the transporting medium, D is the diffusion

coefficient, defined as:

$$D = \{3[\mu_a + \mu_s(1-g)]\}^{-1} = \{3(\mu_a + \mu_s')\}^{-1} \tag{9}$$

μ_a is the linear absorption coefficient, μs is the linear scattering coefficient, and g is the average of the cosine of the scattering angle, μ_s' is called the induced scattering coefficient, and S(r', t) is the photon source intensity.

For a short pulse from an isotropic point source with normalized intensity, S(r', t) = d(0, 0), equation (8) will become:

$$\frac{1}{v}\frac{\partial}{\partial t}\Psi(r,t) - D\nabla^2\Psi(r,t) + \mu_a\Psi(r,t) = \delta(0,0) \tag{10}$$

When $\mu_a << \mu_s'$, the solution of the above equation in an infinite medium could be written as: [31]:

$$\Psi(r,t) = v(4\pi Dvt)^{-\frac{3}{2}}\exp(-\frac{r^2}{4Dvt} - \mu_a vt) \tag{11}$$

For the semi-infinite geometrical condition, see Figure 2-9, the photon flux rate can be expressed in cylindrical coordinates by the following [31]:

$$\Psi(\rho,z,t) = \frac{\exp(-\mu_a vt)}{v(4\pi Dvt)^{3/2}}\{\exp[-\frac{(z-z_0)^2+\rho^2}{4Dvt}] - \exp[-\frac{(z+z_0)^2+\rho^2}{4Dvt}]\} \tag{12}$$

where z_0 is the treated depth of the incident photons from the boundary surface, which is equal to one transport-corrected scattering length [31]:

$$z_0 = [(1-g)\mu_s]^{-1} = 1/\mu_s' \tag{13}$$

The number of photons reaching the surface per unit time per unit area |J(r,0,t)| can be calculated from Fick's Law:

$$J(\rho,0t) = -D\nabla\phi(\rho,z,t)|_{z=0}, \tag{14}$$

Which leads to the final expression for the reflectance R(r, t) [20]:

$$R(\rho,t) = \frac{z_0 \exp(-\mu_a vt)}{t(4\pi Dvt)^{3/2}} \exp(-\frac{\rho^2 + z_0^2}{4Dvt}) \tag{15}$$

After obtaining the data profile of the time resolved signal, $\Psi(r, t)$, has been obtained from the structure shown in Figure 2-9, the parameters μ_a and μ_s' can be calculated from the above equation (15) by the mathematical fitting procedure in the time resolved method.

2.3.2. Frequency domain method

The Fourier transform of equation (10) with respect to time is [32]:

$$-D\nabla^2\Psi(r,\omega) + [\mu_a + (i\omega/v)]\Psi(r,\omega) = \delta(0,0) \tag{16}$$

It has the same form as the steady-state ($\partial/\partial t = 0$) diffusion equation with μ_a replaced by $\mu_a + i\omega/v$. The solution of the above equation is [32]:

$$\Psi(r,\omega) = \frac{1}{4\pi Dr} \exp[-r(\frac{\mu_a}{4D} + \frac{i\omega}{Dv})^{1/2}] \tag{17}$$

After applying De Moivre's theorem, the phase and the magnitude of the diffusing wave at a single frequency ω can be obtained:

$$\Psi(r,\omega) = \frac{1}{4\pi Dr} \exp\{-\alpha r[\cos(\frac{\theta}{2}) + i \cdot \sin(\frac{\theta}{2v})]\} \tag{18}$$

where

$$\alpha = [(\frac{\mu_a}{D})^2 + (\frac{\omega}{Dv})^2]^{1/4} \tag{19}$$

$$\theta = \tan^{-1}[\omega/(\mu_a v)] \tag{20}$$

At a single frequency ω, the photon density wave described by the above equation

is composed of a sinusoid-varying (ac) component superimposed upon a nonzero average (dc) component. The magnitude $M_{ac}(r)$ and the phase $\Phi(r)$ of the ac component and the magnitude $M_{dc}(r)$ of the dc component are [6, 21]:

$$M_{ac}(r) = \frac{1}{4\pi Dr}\exp\{[-r(\frac{\mu_a}{D})^2 + (\frac{i\omega}{Dv})^2]^{1/4}\cos[\frac{1}{2}\tan^{-1}(\frac{\omega}{\mu_a v})]\} \tag{21}$$

$$\phi(r) = r[(\frac{\mu_a}{D})^2 + (\frac{i\omega}{Dv})^2]^{1/4}\sin[\frac{1}{2}\tan^{-1}(\frac{\omega}{\mu_a v})]\} \tag{22}$$

$$M_{dc}(r) = \frac{1}{4\pi Dr}\exp\{[-r(\frac{\mu_a}{D})^{1/2}]\} \tag{23}$$

For a practical measurement, a high frequency (hundreds of mega Hertz) modulated light source will be used to generate a photon density wave, and a lock-in amplifier detection system will be used to get both the modulation amplitude A and the phase change ϕ from the detection point simultaneously. These two measurement parameters can be used to obtain the important optical parameters μ_a and μ_s' of the scattering medium by some calculations. for infinite geometric media with the condition that the scattering effect is much larger than the absorption in the media, $\mu_s' >> \mu_a$, and that the source-detector separation r is much greater than the photon mean-free path, the solution will be [13, 14]:

$$\Phi = r(\frac{v^2\mu_a^2+\omega^2}{v^2D^2})^{1/4}\sin[\frac{1}{2}\tan^{-1}(\frac{\omega}{v\mu_a})] \tag{24}$$

$$\ln(rM_{ac}) = -r(\frac{v^2\mu_a^2+\omega^2}{v^2D^2})^{1/4}\cos[\frac{1}{2}\tan^{-1}(\frac{\omega}{v\mu_a})] + \ln(\frac{A}{4\pi vD}) \tag{25}$$

$$\ln(rM_{dc}) = -r\sqrt{\frac{\mu_a}{D}} + \ln(\frac{1}{4\pi vD}) \tag{26}$$

where ω is the angular frequency of the modulation and A is the modulation of

the source. From the collected data at two different separation distances, r_1 and r_2, ($r_1 < r_2$), one can get the following expressions:

$$\varphi = \rho\left(\frac{v^2\mu_a^2 + \omega^2}{v^2 D^2}\right)^{1/4} \sin\left[\frac{1}{2}\arctan\left(\frac{\omega}{v\mu_a}\right)\right] \tag{27}$$

$$\delta = -\rho\sqrt{\frac{\mu_a}{D}} \tag{28}$$

$$\alpha = -\rho\left(\frac{v^2\mu_a^2 + \omega^2}{v^2 D^2}\right)^{1/4} \cos\left[\frac{1}{2}\arctan\left(\frac{\omega}{v\mu_a}\right)\right] \tag{29}$$

where $\rho = r_2 - r_1$, $\varphi = \Phi(r_2) - \Phi(r_1)$, $\delta = \ln[r_2 M_{dc}(r_2)] - \ln[r_1 M_{dc}(r_1)]$, and $\alpha = \ln[r_2 M_{ac}(r_2)] - \ln[r_1 M_{ac}(r_1)]$. The parameters μ_a and μ_s can be determined in different ways. Using the ac and the phase data, the absorption and scattering parameters will be:

$$\mu_a = -\frac{\omega}{2v}\frac{\delta}{\varphi}\left(\frac{\varphi^2}{\delta^2} + 1\right)^{-1/2} \tag{30}$$

$$\mu_s' = \frac{\delta^2}{3\mu_a\rho^2} - \mu_a \tag{31}$$

and using the dc and the phase data the μ_a and μ_s' will be:

$$\mu_a = \frac{\omega}{2v}\left(\frac{\varphi}{\alpha} - \frac{\alpha}{\varphi}\right) \tag{32}$$

$$\mu_s' = \frac{\alpha^2 - \varphi^2}{3\mu_a\rho^2} - \mu_a \tag{33}$$

In general, the ac signal will have less error from external stray light interference during the measurement procedure.

The light sources used by frequency domain method device are modulated at RF frequency. The intensity as a function of time can be shown is as follows:

$$I_0 = I(DC_0) + I(AC_0)Sin(\omega t - \phi_0) \tag{34}$$

where I_0 is the light source intensity, $I(DC_0)$ is the average component of the light source intensity, $I(AC_0)$ is the alternating component of the light source intensity, ω is the angular modulation frequency, and Φ_0 is the phase of the light source. The frequency domain method device determines the μ_a and μ_s' of the tissue by measuring the AC, DC and phase change as a function of distance d through the tissue [13, 30, 33, 34].

The multiple source-detector pairs configuration for the FD method device are generally considered to eliminate the error due to light source and geometric difference of the probes on the sample surface. Assuming that $\mu_s' >> \mu_a$, the light transport through tissue can be described by the following equations [13, 30, 33, 34]:

$$Ln(d^2 DC) = d \cdot S(DC) + K(DC) \tag{35}$$

$$Ln(d^2 AC) = d \cdot S(AC) + K(AC) \tag{36}$$

$$\Phi = d \cdot S(\Phi) + K(\Phi) \tag{37}$$

where K is the constants and S(AC), S(DC) and S(Φ) are slopes of the AC, DC, and of the phase respectively, and d is the distance between source and detector. The slopes are the functions of μ_a and μ_s' and other known parameters such as frequency and the speed of light in tissue. After obtaining the slopes, the μ_a and μ_s can be calculated using any two of the slopes, AC and the phase, or AC and DC, or DC and the phase.

For the AC and the phase pair, the μ_a and μ_s' of a semi-infinite medium in the diffusion approximation are given by [13, 30, 33, 34]

$$\mu_a = (\omega / 2v)[S(\Phi)/S(AC) - S(AC)/S(\Phi)] \tag{38}$$

$$\mu_s' = [S(AC)^2 - S(\Phi)^2]/3\mu_a - \mu_a \tag{39}$$

where ω is the angular modulation frequency of the source intensity, and v is the speed of light in the tissue. In this method, μ_s' and μ_a can be measured separately.

2.3.3. Continuous wave method

When the modulation frequency becomes very low (below mega Hertz), the frequency part contribution in formula (21, 22) goes to zero, and this formula becomes applicable for the CW type method measurement. In practice, the phase change data will become non-detectable since the wavelength of the photon density wave is too long. The phase changes related to the distance change or media scattering change is smaller than the phase noise generated from the measurement device, and the ac amplitude change becomes the dc amplitude change. For the condition $\mu_s' >> \mu_a$, the μ_a part can be omitted and the dc signal in the equation (23) will become:

$$M_{dc}(r) = \frac{3(\mu_a + \mu_s')}{4\pi r}\exp(-r\sqrt{3\mu_a\mu_s'}) \tag{40}$$

And the dc signal in equation (28) will become:

$$\delta = -\rho\sqrt{3\mu_a\mu_s'} \tag{41}$$

It is easy found from the above formulas that μ_a and μ_s' are coupled together in diffusion factor D (formula 9) in the exponential part of the formula. This indicates that the optical parameters μ_a and μ_s' for the scattering medium cannot be separated by the CW method measurement.

In practice, in a highly scattering medium such as tissue, photons travel a mean distance, which is far greater than the geometrical path-length d. In continuous wave

spectroscopy, changes of tissue chromophore concentrations from the baseline can be obtained from the modified Beer-Lambert relationship, if the mean optical path length is known or can be estimated. The Beer-Lambert relationship could be modified to include the differential path-length factor (DPF) B and the additive term G due to scattering loss and a multiplier to account for the increased optical path-length from the scattering, namely:

$$A = \lg(I_0 / I) = \alpha \cdot c \cdot d \cdot B + G \tag{42}$$

where A is the attenuation measured in OD; I_0 is the light intensity incident on the medium; I is the light intensity transmitted through the medium; α is the specific extinction coefficient of the absorbing compound measured in $\mu molar^{-1}\ cm^{-1}$; c is the concentration of the absorbing compound in the media measured in μmolar; and d is the distance between the points where the light enters and leaves the media measured in cm. The differential path-length factor (DPF) B can be evaluated by the time resolved method [35] or by the frequency domain method [13].

The modified Beer-Lambert Law will not yield an absolute measurement of concentration since G is unknown and dependent upon the measurement geometry and the scattering coefficient of the tissue is interrogated. Without knowledge of G, the equation cannot be solved to provide a measure of the absolute concentration of a chromophore in the medium from a measure of absolute attenuation. If G does not change during the measurement period, it is possible to determine the changes (Δc) in the concentration of the chromophore from the measured changes in attenuation (ΔA). This can be represented as follows:

$$\Delta A = \Delta c \cdot a \cdot d \cdot B \tag{43}$$

The quantification of the change in concentration still depends on the measurement of the geometric distance d and on the differential path-length factor B, which is the true optical pathlength traveled by the scattered light. For a non-scattering medium the total optical path-length is equivalent to the straight-line distance d, since DPF is seem as unity. The differential path-length factor B is different for different types of tissues. For example, the B value of human brain and piglet head is approximately 6 [13, 35]. This means for the probe distance of 3 cm, the mean distance that the light travels in the head is approximately 18 cm. Since the absolute concentration of chromophore is unknown, all measurements are expected to give absolute concentration changes from an arbitrary zero at the start of the measurement period.

2.3.4. Conversion into Hemoglobin Parameters

The absorption spectra of oxy-hemoglobin (HbO_2) and deoxy-hemoglobin (Hb) in the NIR region are displayed in Figure 2-6. The isobathic ($\alpha_{HbO2} = \alpha_{Hb}$) absorption point of oxy-hemoglobin and deoxy-hemoglobin is around 800 nm. We have decided to provide wavelengths above and below 800 nm. Table 2-1 lists the absorption extinction coefficients of oxy-hemoglobin and deoxy- hemoglobin [10].

From Table 2-1, we could evaluate the Hb, and HbO_2 changes by monitoring the two optical signal changes at different wavelengths (at least 2). Our measurement setup condition uses 780 nm and 830 nm light sources for the CW method, and 758 and 830 nm for the FD method.

The optical attenuation change for two wavelengths measurement have following relationships:

$$\Delta A(\lambda_1) = \Delta Hbo_2 E_{Hbo2}(\lambda_1) + \Delta HbE_{Hb}(\lambda_1) \quad (41)$$

$$\Delta A(\lambda_2) = \Delta Hbo_2 E_{Hbo2}(\lambda_2) + \Delta HbE_{Hb}(\lambda_2) \quad (42)$$

where the λ is the light wavelength, $E_{Hb}(\lambda)$ and $E_{HbO2}(\lambda)$ are the absorption coefficients of oxy- and deoxy-hemoglobin at wavelength λ respectively, and indicates the molar extinction coefficient to base e at wavelength λ for the complete oxy- and deoxy- hemoglobin molecules.

After obtaining the absorption changes (ΔA) from the measurement instrument for at least two wavelengths, the hemoglobin concentrations change can be calculated by the following formula [36]:

$$\Delta Hbo_2 = \frac{\Delta A(\lambda_1)E_{Hb}(\lambda_2) - \Delta A(\lambda_2)E_{Hbo2}(\lambda_1)}{E_{Hbo2}(\lambda_1)E_{Hb}(\lambda_2) - E_{Hbo2}(\lambda_2)E_{Hb}(\lambda_1)} \quad (43)$$

$$\Delta Hb = \frac{\Delta A(\lambda_2)E_{Hbo2}(\lambda_1) - \Delta A(\lambda_1)E_{Hb}(\lambda_2)}{E_{Hbo2}(\lambda_1)E_{Hb}(\lambda_2) - E_{Hbo2}(\lambda_2)E_{Hb}(\lambda_1)} \quad (44)$$

2.4. References

1. Jacques S.L., "Optical techniques for tissue science and engineering", SPIE Proceeding of Biomedical Optics 99, 3863, 2-7

2 Yang Y.L., Celmer E. J., Koutcher J.A., and Alfano R.R., "DNA and protein changes in tissue probed by Kubelka Munk spectral function", Optical Biopsy III, (2000), pp 150-153. SPIE Proc. 3917

3 Yang Y.L., Celmer E. J., Koutcher J.A., Ho P.P., and Alfano R.R., "DNA and protein change in human breast tissues by diffuse reflectance spectrum", in Optical sensing, imaging, and manipulation for biological and biomedical applications, SPIE Proc. 4082, pp 71-74, (2000).

4 Wolbarsht M.L., Walsh A.W., and George G., "Melanin, a unique biological absorber", Appl. Opt., 20(13), (1981) 2184-2186.

5. D. R. Ingrams, J. K. Dhingra, K. Roy, D. F. Perrault, I. D. Bottrill, S. Kabani, E. E. Rebeiz, M. M. Pankratov, S. M. Shapshay, R. Manoharan, I. Itzkan, M. S. Feld, Autofluorescence Characterization of Oral Mucosa, Head & Neck 19, 27-32 (1997).

6. C.-H. Liu, B. B. Das, W. L. Sha Glassman, G. C. Tang, K. M. Yoo, H. R. Zhu, D. L. Akins, S. S. Lubicz, J. Cleary, R. Prudente, E. Celmer, A. Caron, R. R. Alfano, "Raman, Fluorescence, and Time-Resolved Light Scattering as Optical Diagnostic Techniques to Separate Diseased and Normal Biomedical Media," J. Photochem. Photobiol. B: Biol., 16, 187-209 (1992).

7. "The science of photobiology" by Kendric C. Smith, 2nd edition, Plenum press, 1989.

8. Kurth CD, Steven JM, Benaron D, Chance B. "Near-infrared monitoring of cerebral circulation." J Clin Monit, 1993. 9: p. 163-170.

9. Benaron DA, Cheong WF, and S. DK., "Tissue Optics". Science, 1997. **276**: p. 2002-2003.

10. van Assendelft, O.W., "Spectrophotometry of haemoglobin derivatives", Cherls C. Thomas, Assen, The Netherlands, 1970, pp.53-57.

11. Wray S, Cope M, Delpy DT, Wyatt JS and Reynolds E O, "Characterization of the near infrared absorption spectra of cytochrome aa3 and hemoglobin for the non-invasive monitoring of cerebral oxygenation" Bioch. Biophy Acta, 933 (1988) 184-192.

12. Cope M, VanDerZee P, Essenpreis M, Arridge SR, and Delpy DT, "Data analysis methods for near infrared spectroscopy of tissue: problems in determining the relative cytochrome aa_3 concentration", in Time-resolved spectroscopy and imaging of tissues, Ed. By Chance B., Proc. SPIE Vol. 1431, p 251-262 (1991).

13. Fantini S, Hueber D, Franceschini MA, Gratton E, Rosenfeld W, Stubblefield PG, Maulik D, Stankovic MR, 1999 "Non-invasive optical monitoring of the newborn piglet brain using continuous wave and frequency domain spectroscopy." *Phys Med Biol*,. **44**: p. 1543-1563.

14. Delpy DT, C.M., "Quantification in tissue near-infrared spectroscopy". Philos Trans R Soc Lond B Biol Sci, 1997. **352**: p. 649-659.

15. Feng S, Zeng F, and Chance B, "Monte Carlo simulation of photon mifration phat distribution in multiple scattering media", Proc. of Photon Migration and Imaging in Random Media and tissues, 1993, SPIE 1888, pp 78-89.

16. Feng S, and Zeng F, "perturgation theory of photon migration in the presence of a single defect", OSA Proc. On Advances in Optical Imaging and Photon Migration, 1994, Vol. 21, pp 217-228.

17. Perelman LT, Wu J, Itzkan I, Wang Y, Dasari R and Feld MS, "Photon paths in turbid media: theory and experimental observation", OSA Proc. On Advances in Optical Imaging and Photon Migration, 1994, Vol. 21, pp 153-155.

18. Maier JS, Gratton E, "frequency-domain methods in optical tomography: detection of localized absorbers and a backscattering reconstruction scheme", Proc. of Photon Migration and Imaging in Random Media and tissues, 1993, SPIE 1888, pp 440-449.

19. Stankovic MR, Maulik D, Boas DA, Stubblefield PG, "Emerging Technologies: Fetal Optical Monitoring", in *Asphyxia and Fetal Brain Damage*, M. D, Editor. 1998, John Wiley & Sons, Inc.: New York. p. 345-364.

20. Wahr JA, Tremper KK, Samra S, Delpy DT, "Near-infrared spectroscopy: Theory and applications". J Cardiothoracic and Vascular Anesthesia, 1996. **3**: p. 406-418.

21. Stankovic MR, Fujii A, Maulik D, Boas D, Kirby D, "Optical monitoring of cerebral hemodynamics and oxygenation in the neonatal piglet." J Maternal Fetal Invest, 1998. **8**(2): p. 71-78.

22. Tsuji M, duPlessis A, Taylor G, Crocker R, Volpe JJ, "Near infrared spectroscopy detects cerebral ischemia during hypotension." Pediatr Res, 1998. **44**(4): p. 591-595.

23. Delpy DT, Cope M, van der Zee P, Arridge S, Wray S, Wyatt J, "Estimation of optical pathlength through tissue from direct time of flight measurement" Phys Med Biol, 1988. **33**: p. 1433-1442.

24. Benaron DA, Cheong WF, and Stevenson DK, "Tomographic time-of-flight optical imaging device" Adv Exp Med Biol, 1994. **361**: p. 609-617.

25. Brazy JE, "Cerebral oxygen monitoring with near infrared spectroscopy: Clinical application to neonates". J Clin Monit, 1991. **7**: p. 325-334.

26. Benaron DA, Benitz WE, Ariagno RL, "Noninvasive methods for estimating in vivo oxygenation". Clinical Pediatrics, 1992. **31**: p. 258-273.

27. Chance B, "Near-infrared images using continuous, phase-modulated, and pulsed light with quantitation of blood and blood oxygenation". Ann N Y Acad Sci, 1998. **838**: p. 29-45.

28. Alfano RR, Demos SG, and G. SK, "Advances in optical imaging of biomedical media". Ann N Y Acad Sci, 1997. **820**: p. 248-70.

29. Alfano RR, Demos SG, Galland P, Gayen SK, Guo Y, Ho PP, Liang X, Liu F, Wang L, Wang QZ, Wang WB, "Time-resolved and nonlinear optical imaging for medical applications". Ann N Y Acad Sci, 1998. **838**: p. 14-28.

30. Fantini S, Franceschini MA, and G. E, Semi-Infinite-Geometry Boundary Problem for Light Migration in Highly Scattering Media: a Frequency-Domain Study in the Diffusion Approximation. J Opt Soc Am, 1994. **B 11**: p. 2128-2138.

31. Patterson M. S., Chance B., and Wilson B. C., "Time resolved reflectance and transmittance for the noninvasive measurement of tissue optical properties", Appl. Opt. 28, 2331-2336. (1989)

32. Schmitt J.M., Knuttel A., and Knutson J.R., "Interference of diffusive light waves," J. Opt. Soc. Am. A Vol. 9(10), 1832-1843.

33. Franceschini MA, Fantini S, Paunescu LA, Maier JS, Gratton E, "Influence of a Superficial Layer in the Quantitative Spectroscopic Study of Strongly Scattering Media". Appl. Opt., **37**(31) p. 7447-7458 (1998)

34. Gratton E, Fantini S, Franceschini MA, Gratton G, Fabiani M, "Measurements of scattering and absorption changes in muscle and brain". Philos Trans R Soc Lond B Biol Sci, 1997. **352**: p. 727-735.

35. Essenpreis, M., C. E. Elwell, M. Cope, P. van der Zee, S. R. Arridge, and D. T. Delpy, (1993) "Spectral dependence of temporal point spread function in human tissues," Appl. Opt. Vol. 32, No. 4, p 418-25.

36. Fantini S, Franceschini-Fantini M A, Maier J S, Walker S A, Barbieri B, and Gratton E, "Frequency-domain multichannel optical detector for noninvasive tissue spectroscopy and oximetry", Opt. Engr. 34(1), 32-42 (1995)

37. Fishkin J. B., and Gratton E., "Propagation of photon-density waves in strongly scattering media containing an absorbing semi-infinite plane bounded by a straight edge", J. Opt. Soc. Am. A, vol.10, No. 1, 1993, 127-140.

38. Fantini S, Franceschini M. A., Fishkin J. B., Barbieri B., and Gratton E., "Quantitative determination of the absorption of chromophores in strongly

scattered media: a light-emitting-diode based technique", Appl. Opt. 33, 5204-5213.

2.5. Tables

Table 2-1 Hemoglobin absorption coefficient in interested wavelength (780 nm and 830 nm), OD ~ mM/ cm. [10]

Wavelength	Hb	HbO_2	ΔOD (Hb - HbO_2)
780 nm	0.28	0.18	+0.1
830 nm	0.21	0.245	-0.035

2.6. *Figures*

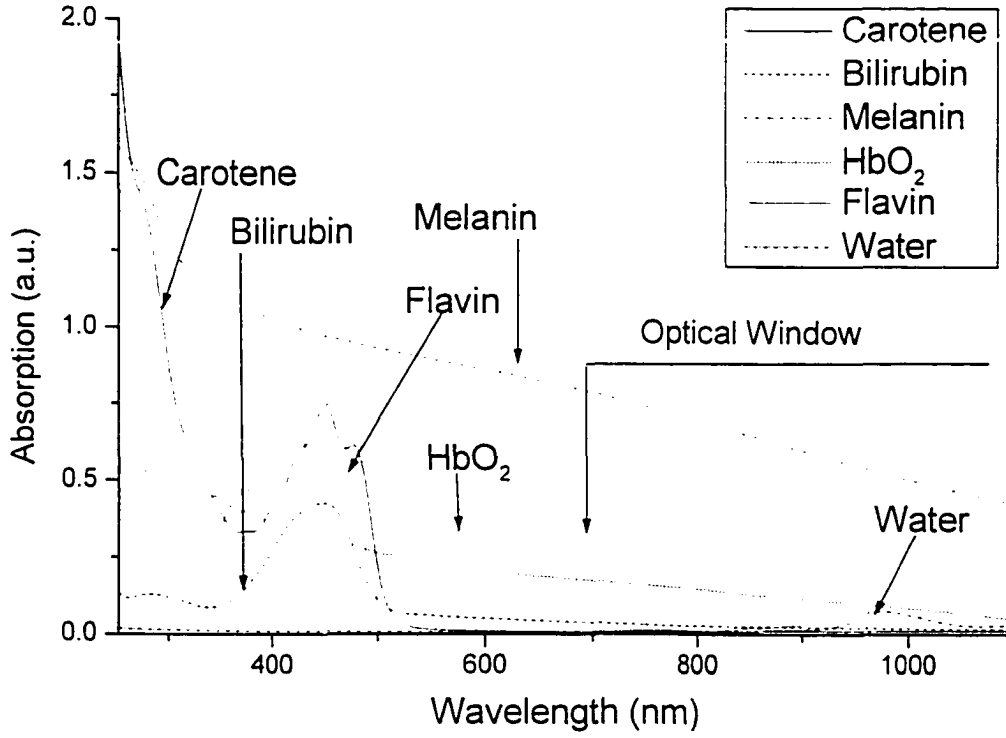

Figure 2-1 Absorption spectra of typical known chromophores that exist in tissue from near UV to near IR spectral range.

The near infrared region (700 ~ 1100 nm) is an optical window to see through the body.

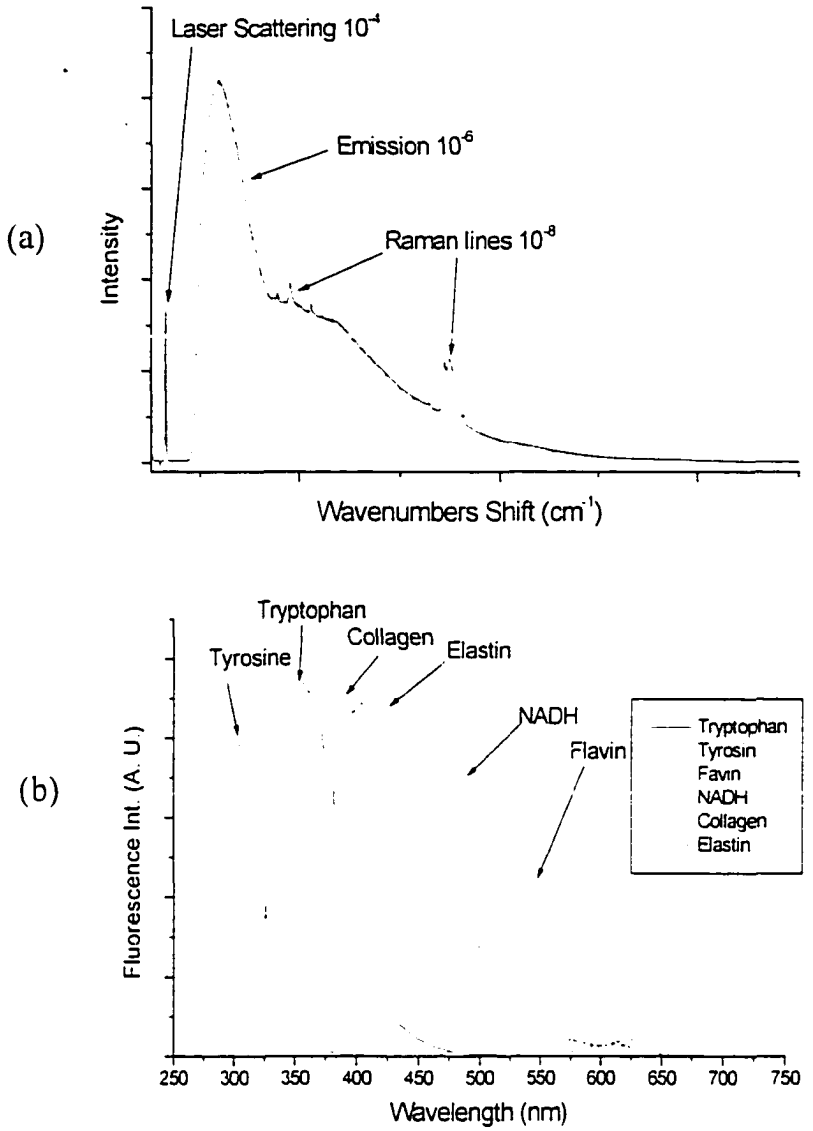

Figure 2-2 Emission spectra.

(a) Typical emission spectral profile from tissue sample. (b) Fluorescence spectra of typical known fluorophores that exist in human tissue from near UV to near IR spectral range.

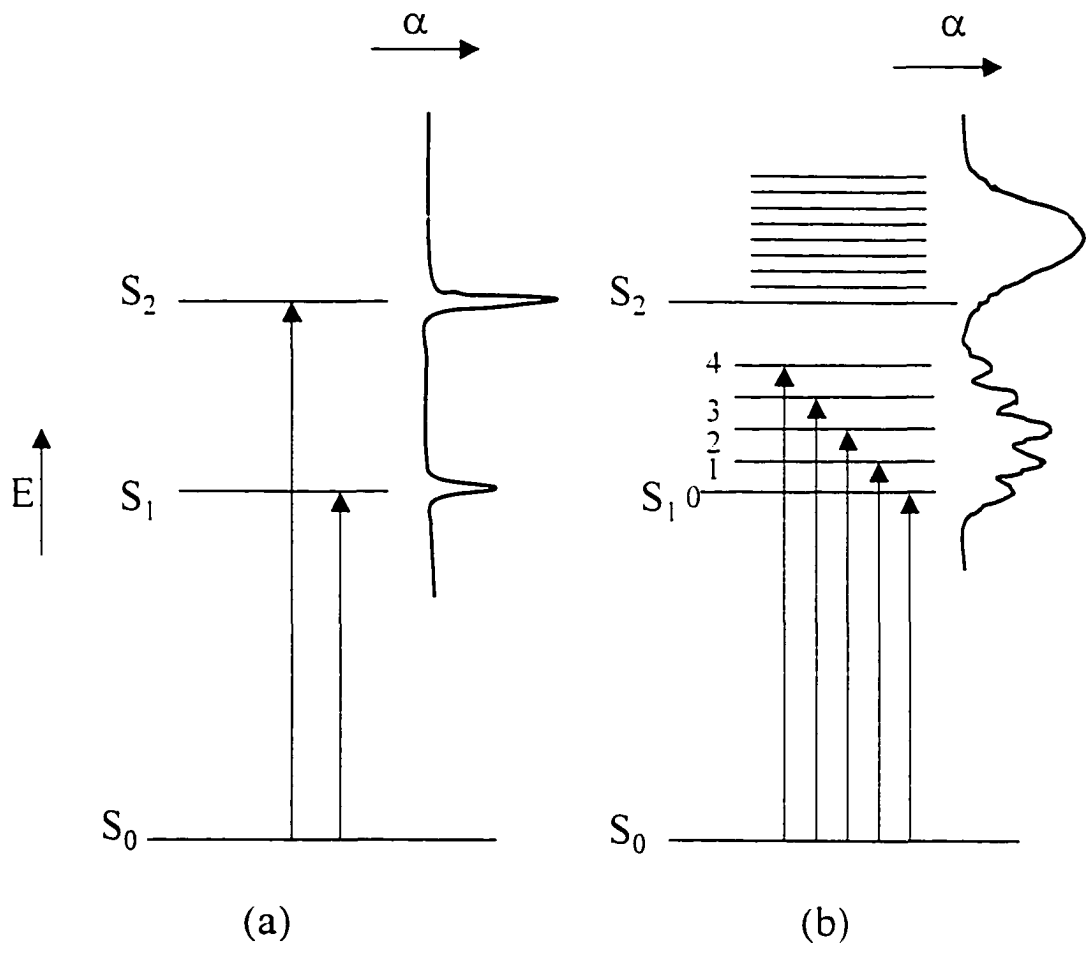

Figure 2-3 Energy level and absorption spectra.

(a) The narrow band spectra generated from atomic-like electronic energy levels. (b) The broadband spectra are generated from molecular-like energy levels.

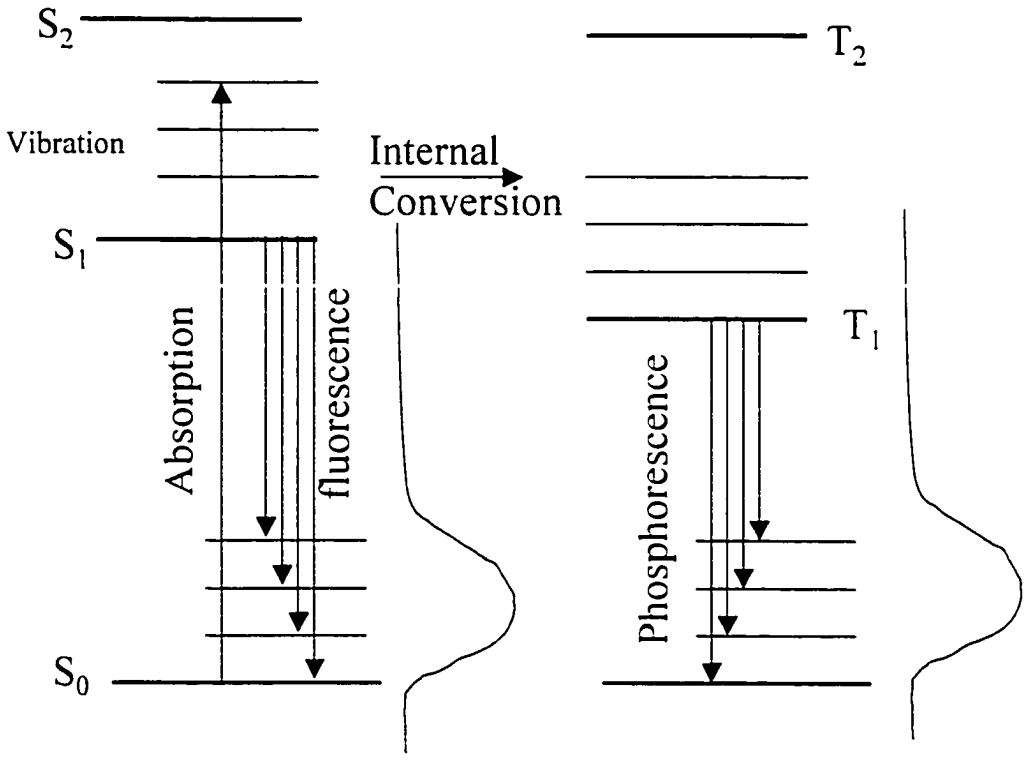

Figure 2-4 The energy level diagram for emission spectra independent from excitation wavelength.

These emissions include fluorescence (singlet to ground state) and phosphorescence (triplet to ground state).

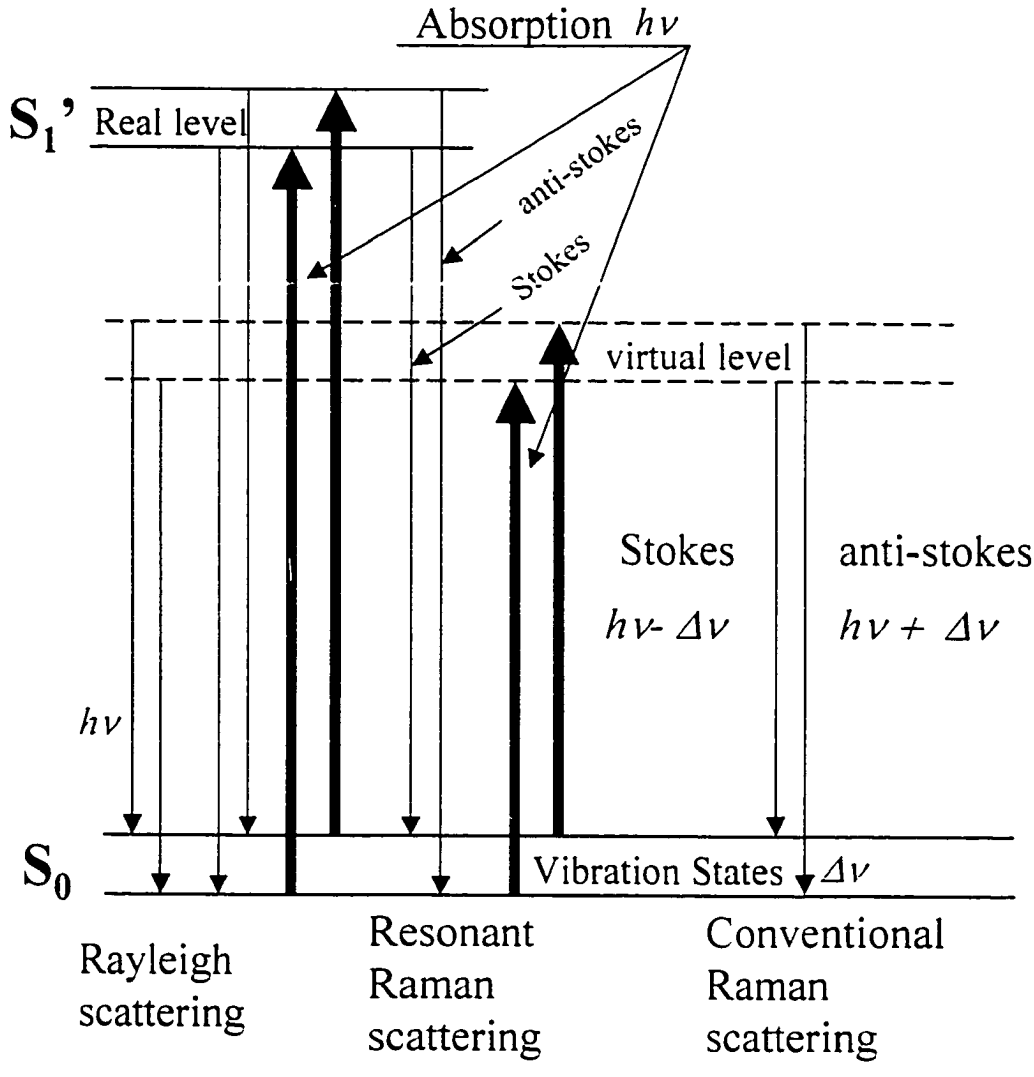

Figure 2-5 The energy level diagram for emission spectra dependent from excitation wavelength.

These emissions include elastic scattering (Rayleigh scattering) and inelastic scattering (Raman scattering).

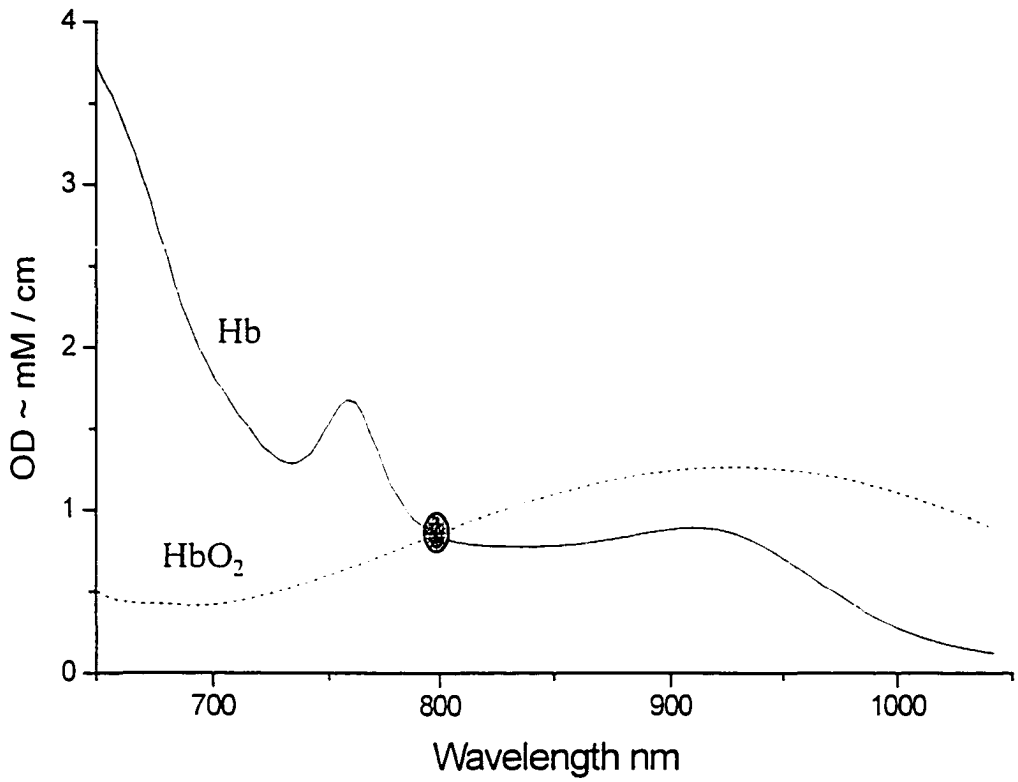

Figure 2-6 The absorption spectra of Hb and HbO_2 in NIR spectral region [10].

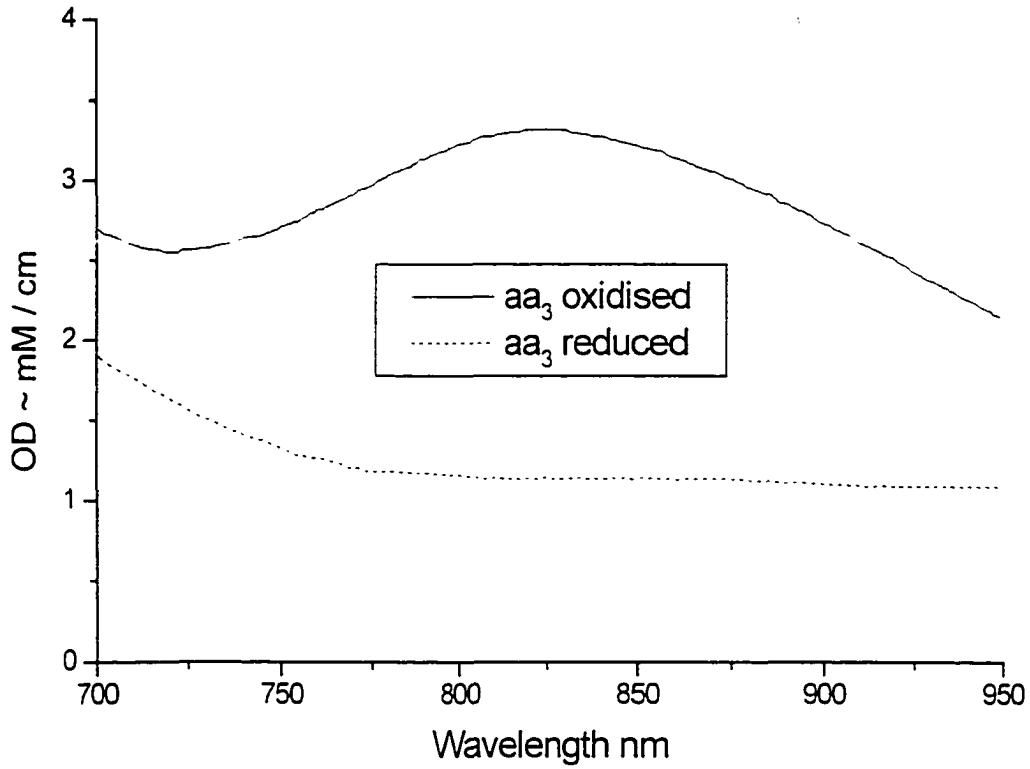

Figure 2-7 The absorption spectra of cytochrome aa_3 in NIR spectral region oxidized and reduces form [12].

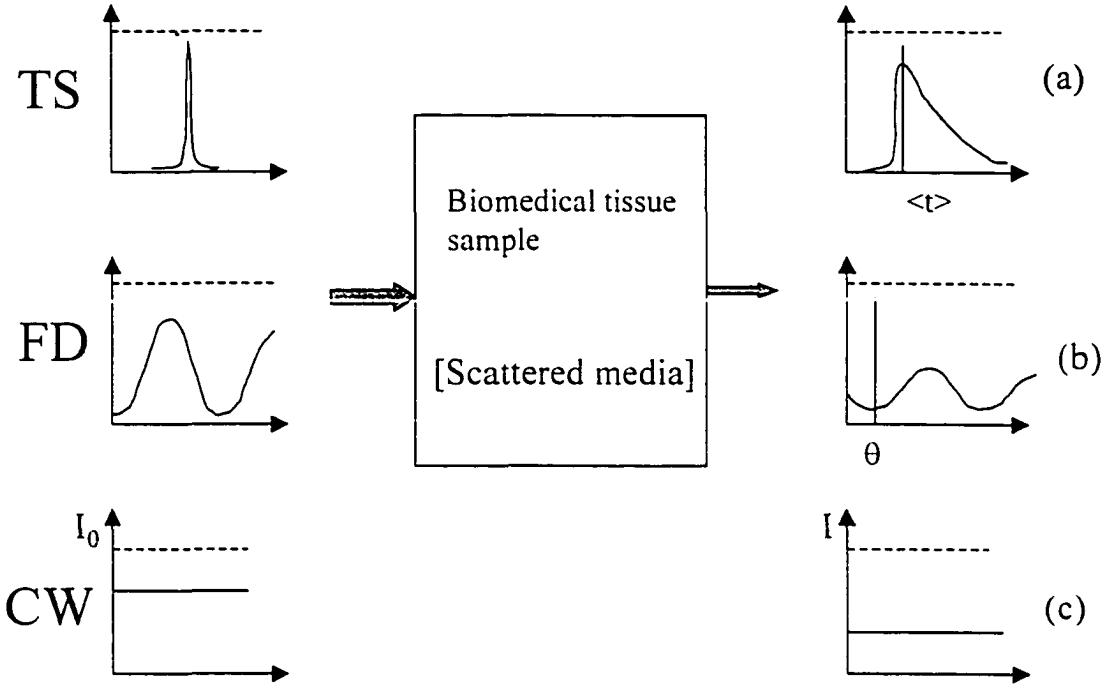

Figure 2-8 The principle methods to be used to evaluate the absorption changes inside of the living tissues by NIR spectroscopy.

(a) Time-resolved (TS) method, (b) frequency-domain (FD) method, and (c) continuous wave (CW) method.

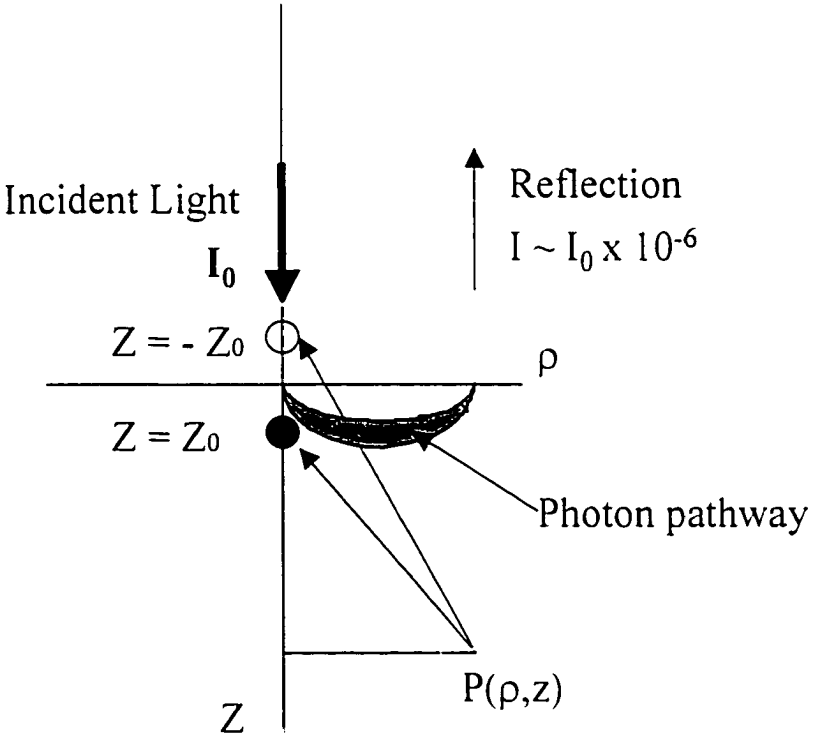

Figure 2-9 Geometry of the calculation of R(ρ, t) for semi-infinity homogeneous medium.

The incident beam is assumed to create an isotropic photon source at depth Z_0, indicated by the filled circle. The boundary condition $\Psi(\rho, 0, t)$ can be met by adding a negative source by the open circle. The reflecting light can be detected from the media surface away from the light source in distance ρ to get the scattering and absorption parameter of the media.

3. NIR spectroscopy Methods

This chapter describes the methods that used to obtain far-red emission signals from tissue samples, and to determine the blood perfusion change in brain tissue from light scattering and absorption. For far-red to NIR emission wing investigation, the detection setup includes: 1) steady state spectra of far-red to NIR emission from tissue samples, 2) the time resolved signal detection of far-red to NIR emission from tissue samples, and 3) the image map of far-red to NIR emission from tissue samples. For blood perfusion change measurements, two detection setups are used: 1) a CW NIRS device setup assembled at CCNY, and 2) an FD method NIRS device, the commercial ISS Oximeter (Model 96208, ISS, Inc., Champaign, IL).

3.1. Laser Excitation of the emission spectral wing measurements

In the far-red to the NIR spectral region, there is no obvious emission spectral structure from tissue samples. In the experiment, we are only interested in the emission spectra region beyond 650 nm. Due to existing equipment conditions, 532 nm and 632 nm are selected as the excitation light sources for the time resolved spectra. For steady state spectroscopy measurements, the 532 nm, 632 nm and 800 nm laser lines are used.

There are several different light sources used for the tissue emission spectral wing measurement setup. For the time resolved emission measurements, the laser system consists of a mode-locked Nd:YAG laser, a pulse compressor, and a synchronously pumped dye laser. The laser line at 532 nm, with a 4 ps pulse width and a few milliwatts output originates from the YAG laser followed by a frequency double crystal. The laser

line at 632nm, with a 500 fs pulse width and few milliwatts power output arises from a dye laser pumped by a 532 nm light source.

For steady state spectra measurements, several different laser devices are used. For 532 nm wavelength excitation, the same laser source is used as in the time resolved spectra measurements. For 632 nm wavelength excitation, the light source comes from a He-Ne laser with about 5 mw output. For 800 nm wavelength excitation, a solid-state semiconductor single mode laser which generates about 50 mw output is used.

3.2. Steady state spectroscopy measurement

Figure 3-1 shows the steady state emission spectroscopy setup. The measurements were performed using a quarter meter spectrograph (ARC SpectroPro 275) and a cooled CCD camera (Princeton Instrument model TE/CCD-512SF). The laser beam was transmitted through a narrow band filter (laser line) and focused by a 20 cm focal length lens (L_1) on the sample. The emitted light from the tissue sample was collected in the back-scattering geometry by an 85 mm focal length camera lens (L_2) and after passing through a laser-line notch filter (NF), it was coupled into the 0.1 mm slit of the spectrograph.

3.3. Time resolved spectroscopy setup

The time resolved experimental setup is shown in Figure 3-2. The laser system is composed of a mode-locked Nd:YAG laser, a pulse compressor, and a synchronously pumped dye laser. The 532 nm, 4 ps frequency doubled output of the YAG laser and the 632 nm, 500 fs output of the dye laser were used to illuminate the samples with an average powers of a few milliwatts. The detection system is a streak camera (Hamamatsu

Model C1587) having a spectral response range from the visible to 1.1 μm. The polarized excitation beam was transmitted through a laser-line narrow band filter to ensure monochromatic illumination and focused by a 25-cm focal length lens (L_1) on the tissue sample. The emitted light from the tissue sample was collected in the back-scattering geometry using a 3 cm focal length lens (L_2). A laser line notch filter (NF) rejects the scattered laser light, and after a 665 nm long-pass filter (LP), the emitted light was coupled into the input of a streak camera using an optical fiber bundle. The temporal resolution of the system was ~14 ps.

3.4. Imaging setup for far-red emission detection

In the imaging experimental setup shown in Figure 3-3, the 632 nm laser beam passes through a narrow band filter (NB) and is then expanded by a 2 cm focal length lens (L_1). The central portion of the expanded beam was used to illuminate the sample. The emitted light from the sample was collected by an 85 mm focal length camera lens (L_2) in the back-scattering geometry and it was imaged into a cooled CCD camera after passing through a laser line notch filter (NF). This was done in order to block out the laser-line scattered light in the sample with a 665 nm long-pass filter (LP) in order to cut off the short-wavelength emission. This allows for an imaging based on the far-red emission of the sample.

3.5. Imaging setup for scattering intensity measurement

The schematic diagram of the scattering intensity measurement setup is shown in Figure 3-4. The 632 nm laser beam passes through a narrow band filter (NB) and then is expanded by a holographic light shape diffuser (LSD) to make the illumination on the

sample area homogeneous. The scattered light from the sample was collected by an 85 mm focal length camera lens (L) in the back-scattering geometry and it was imaged into a cooled CCD camera.

3.6. Setup for tissue blood perfusion using a CW NIRS

The CW spectrometer setup is shown by the block diagrams in Figure 3-5. Two diode lasers were used at 830 nm and 780 nm. These wavelengths were selected on each side of the isochromatic point of the oxy-hemoglobin and deoxy-hemoglobin absorption spectra around 800 nm. The beam was modulated at different low frequencies, 367 Hz and 600 Hz, respectively. The light propagates through a 1.0 mm optical fiber to the sample surface of the subject delivering about 0.25 mw (0.1 mw for the 780 nm and 0.15 mw for the 830 nm) at the output point. The output power of the fiber is set below 0.32 mw for each wavelength, which is the safety level for human subjects (IRB approved at CCNY). The output power at the illumination optical fiber terminal will be measured before each run.

A 5 mm diameter liquid optical waveguide were used to collect the optical signal at a distance of 3 cm from the pump fiber. The collected optical signal is passed through a wide band filter with a center wavelength of 800 nm to remove the environmental light noise, and it is transformed to an electrical signal by a single photo multiplier tube (PMT, model R943, Hamamatsu Inc., Bridgewarter, NJ).

Two PC-board lock-in amplifiers (Ithaca model 3981, Ithaca Inc., Ithaca NY) are used for detection. The two wavelengths optical signals were detected at these chopped frequencies, read out from the two lock-in amplifiers output and recorded in a computer data file for post data processing. The attenuated optical signals, I(780) and I(830), are

recorded and the attenuation changes will be calculated by the formula, $\Delta A = -\log (I/I0)$, for each wavelength.

The optical fiber probes are located perpendicular to the surface of the subject. For human subjects, the probes are located on the surface of the skin.

3.6.1. Effect of linearity and S/N between two wavelength channels

The experiment conditions for testing the affect of the linearity and S/N between two wavelengths are as follows:

Excitation:

780 nm, 0.22 mw at 512 Hz (relative 100% intensity);

830 nm, 0.28 mw at 306 Hz (relative 100% intensity).

The pre-calibrated ND filters were used to reduce the input signal intensity for each channel respectively. The input intensities are varied from 100% to about 10% for the variable channel and the other one is fixed.

Collection: 2.5 mm optical fiber bundle,

wide band optical filter (800 nm),

PMT (R943).

Lock-in amplifier:

time constant is 33 ms,

sampling interval is 0.5 s.

Phantom media: 2% intralipid (volume), l_t = 0.5 mm (brain).

The probe distance was fixed at 3 cm.

The testing results are displayed in Figure 3-6. From these simulation experiment

result, the further experiment condition on human skin submitted to IRB of CCNY are:

Source to detector distance:	3 cm,	
Excitation power:	780 nm,	0.10 mw;
	830 nm,	0.15 mw.
PMT type:		R943.
Optical fiber diameter:	Excitation,	1.0 mm,
	collection,	5.0 mm liquid guide.

3.6.2. Skin test signal to noise ratio (S/N) with optical probe

There were four subjects who signed the consent forms for the preliminary testing and these forms were kept in file. Few testing points were recorded from each person (arm, hand, cheek or neck, see the result listed in the Table 3-1). The result showed that the signal intensity of 780 nm was from 0.11 mv to 7.9 mv with S/N from 55 to 180. The signal intensity of 830 nm was from 0.31 mv to 11.4 mv with S/N from 150 to 190. The S/N was much higher 10, which was minimum requirement of the testing. Therefore, this setup could be used for further measurement of brain activity under the low laser power safety condition.

3.7. The apparatus for the ISS Oximeter using the NIRS FD method

In order to make accurate determinations of the absorption coefficient, scattering must be accounted for. The FD NIRS device (ISS Oximeter) measures the scattering coefficient directly and is able to determine hemoglobin concentration in high by

scattering tissue media.

A dual-channel frequency-domain tissue spectrometer (Model 96208, ISS, Inc., Champaign, IL) allows for the determination of the average value (dc), amplitude (ac), and phase (Φ) of the modulated optical signal intensity at four different source-detector distances at each wavelength. The light sources used by this ISS Oximeter are modulated at an RF frequency of 110 MHz. The intensity as a function of time is as follows:

$$I_0 = I(DC_0) + I(AC_0)Sin(\varpi t - \Phi_0) \qquad (1)$$

where I_0 is the light source intensity, $I(DC_0)$ is an average component of the light source intensity, $I(AC_0)$ is an alternating component of the light source intensity, ω is the angular modulation frequency, and Φ_0 is the phase of the light source.

This multi-distance method affords the quantitative assessment of the absorption (μ_a) and the reduced scattering (μ_s') coefficients of tissues by use of either the (dc, Φ) or (ac, Φ) pairs of data. In this study, the (ac, Φ) pair method was used to minimize the effect from possible leakage of room light into the optical probe, and from the optical cross-talk with the other CW spectrometer. It has eight 400 μm diameter source optical fibers (four guiding light at 758 nm, four at 830 nm), and one 3 mm diameter detector fiber bundle as shown in Figure 3-7. The eight laser diodes were multiplexed at a rate of 50 Hz, so that only one light source was on for 20 ms at a time. The average power of the illuminations at the optical fiber probe terminal is about 0.25 mw at 758 nm and about 0.5 mw at 830 nm. The acquisition time per cycle over the eight light sources was 160 ms. The average of 16 cycles to get an overall acquisition time of 2.56 s was considered to be sufficient to monitor the relatively slow dynamic processes resulting from changes in cerebral hemodynamics and oxygenation.

Measurements were made as follows: one light source is then turned on and light passes from one emitter fiber, through the tissue and into the collector. After the termination of the measurement, the next light source is turned on, and the process continues as explained above. A measurement cycle is complete when all 8 light sources have been sequentially turned on and measured.

3.8. Safety considerations of laser power limitation on the human subject

In this section, the safety considerations will be briefly discussed for laser illumination of human subjects for brain blood perfusion, monitoring of human subjects for studying the sleep and wake transition.

3.8.1. Consideration

The increasingly widespread use of lasers requires more people to become familiar with the potential hazards associated with the misuse of this valuable new product of modern science. Applications exist in many technologies, including material processing, construction, medicine, communications, energy production, and national defense. Of recent importance from a safety consideration is the introduction of laser devices into more consumer-oriented retail products, such as laser scanning devices, which read special package labels in retail stores. Lasers are also becoming integral components of office copy machines and television recording sets. Most of the devices in this market emit relatively low energies and, consequently, are easily engineered for safety use.

Laser beams applied to the human body in the biomedical field have different

power levels. 1) Measurement by lasers should use as low a power as possible to excite the sample area so as to get enough signal to noise ratio. 2) Treatment lasers should use medium power incident on the sample region of patients so as to get sufficient photon-biochemical reactions and be under the safety level. 3) Laser surgery uses strong laser beams to cut off or to ablate the lesion part of the body.

3.8.2. Definition

Maximum permission exposure (**MPE**) values are below known hazardous levels. Exposure to levels at the given MPE values may be uncomfortable to sight or feel upon the skin. Thus, it is good practice to maintain exposure levels as far below the MPE value as is practicable [1].

The large skin surface makes this body tissue readily available to accidental and repeated exposures to laser radiation. The biological significance of irradiation of the skin by lasers operating in the visible and infrared regions is considerably less than exposure of the eye, as skin damage is usually reparable or reversible. Effects may vary from mild reddening (erythema) to blisters and charring. Depigmentation, ulceration, and scarring of the skin and damage to underlying organs may occur from extremely high power laser radiation.

Under the regulation of the American National Standard (ANS) for the safe use of lasers (1993), the maximum power of laser beams incident on the skin of a subject must be below the limitation for safety consideration [1]. Table 3-2 and Table 3-3 shows the safety calculation parameters to determine MPE values at different wavelengths.

3.8.3. Calculation

From Table 3-2 [1], Parameters and Correction Factors for Exposure time up to 3 x 10^{4} s: $C_A = 10^{2(\lambda-0.700)}$ for λ: 0.700 ~ 1.050 μm. The C_A values are C_A (0.758) = 1.31 for 758 nm, C_A (0.780) = 1.44 for 780 nm, and C_A (0.830) = 1.82 for 830 nm.

From Table 3-3 [1], the Maximum Permissible Exposure (MPE) for Skin Exposure to a laser Beam up to 3 x 10^{4} s: MPE = 0.2 C_A for λ: 0.700 ~ 1.050 μm. The values of MPE are MPE (0.780) = 289 mw / cm^2 for λ = 780 nm, and MPE (0.830) = 364 mw / cm^2 for λ = 830 nm for skin exposure for a duration up to 3 x 10^{4} s (> 8 hours) of use [1].

3.8.4. Result

For the experimental setup using the CW method on human subjects, the total practical experimental excitation power on the human skin will be less than 0.3 mw with a 1.125 mm diameter fiber (< 30 mw / cm^2). This value is below the limitation (289 mw / cm^2 for 780 nm, and 364 mw / cm^2 for 830 nm) for skin exposures up to 3 x 10^{4} s (> 8 hours) of use.

A typical experiment takes less than 4 hours at most. **The used power density level in this research is 10 times less than MPE value for CW method device setup.** The power intensity on skin surface of human subjects is under the limitation of safety control class I, which is no warning requirement for the laser source during the experiment.

3.9. References

1 Laser Institute of America, American National Standards for Use of Lasers, ANSI. Z136.1, 1993, Table 6, p 42, Table 7, p 43, Table 8, p44.

3.10. Tables

Table 3-1 Testing results from different sample points in four subjects

Point	780 nm			830 nm		
	Signal (mv)	Noise (mv)	S/N	Signal (mv)	Noise (mv)	S/N
Subject 1-cheek	0.25	0.004	63	0.97	0.005	194
Subject 1-arm	0.59	0.006	98	1.25	0.007	178
Subject 2-cheek	0.35	0.0025	140	0.45	0.0025	180
Subject 2-arm	0.4	0.003	133	1.06	0.006	177
Subject 3-arm	0.17	0.0025	68	0.72	0.0045	160
Subject 3-neck	0.11	0.002	55	0.31	0.002	155
Subject 4-arm	5.4	0.03	180	7.6	0.04	190
Subject 4-neck	7.9	0.04	198	11.4	0.06	190
Subject 4-cheek	4.0	0.024	167	5.1	0.03	170
Subject 4-hand	3.6	0.02	180	4.9	0.03	163

Table 3-2 Parameters and Correction Factors for laser safety calculation [1].

	Correction Factor	Wavelength (μm)
1	$T_1=10x10^{20(\lambda-0.550)}$	0.550 to 0.700
2	$C_B=1.0$	0.400 to 0.550
3	$C_B=10^{15(\lambda-0.550)}$	0.550 to 0.700
4	$C_A=1.0$	0.400 to 0.700
5	$C_A=10^{2(\lambda-0.700)}$	0.700 ro1.050
6	$C_A=5.0$	1.050 to 1.400
7	$C_P=n^{-1/4}$ *	0.400 to 1.400
8	$C_E=1.0 \quad \alpha < \alpha_{min}$	0.400 to 1.400
9	$C_E=\alpha / \alpha_{min} \quad \alpha_{min} < \alpha < 100$	0.400 to 1.400
10	$C_E=\alpha^2 / (100\ \alpha_{min}) \quad \alpha > 100$	0.400 to 1.400
11	$C_C=1.0$	1.050 to 1.150
12	$C_C=10^{18(\lambda-1.150)}$	1.150 to 1.200
13	$C_C=8$	1.200 to 1.400

* For pulse repetition frequencies below 55 KHz (0.4 to 1.05 μm) and below 20 kHz (1.05 to 1.4 μm).

Notes: 1. For wavelengths between 0.400 and 1.400 μm:

α_{min} = 1.5 mrad for $t \leq 0.7$ s

$\alpha_{min} = 2\ t^{3/4}$ mrad for $0.7 \text{ s} < t < 10$ s

α_{min} = 11 mrad for $t \geq 10$ s

2. The wavelength region λ_1 to λ_2 means $\lambda_1 \leq \lambda < \lambda_2$.

Table 3-3 Maximum Permissible Exposure (MPE) for skin exposure to a laser beam [1].

Wavelength	Exposure Duration	MPE		Notes
(μm)	(s)	($J * cm^{-2}$)	($W * cm^{-2}$)	
Ultraviolet				
0.180 to 0.302	10^{-9} to $3x10^{4}$	3×10^{-3}		3.5 limiting aperture, see Table 3-4.
0.303	10^{-9} to $3x10^{4}$	4×10^{-3}		
0.304	10^{-9} to $3x10^{4}$	6×10^{-3}		
0.305	10^{-9} to $3x10^{4}$	1.0×10^{-2}		
0.306	10^{-9} to $3x10^{4}$	1.6×10^{-2}		
0.307	10^{-9} to $3x10^{4}$	2.5×10^{-2}		
0.308	10^{-9} to $3x10^{4}$	4.0×10^{-2}		
0.309	10^{-9} to $3x10^{4}$	6.3×10^{-2}		
0.310	10^{-9} to $3x10^{4}$	1.0×10^{-1}		
0.311	10^{-9} to $3x10^{4}$	1.6×10^{-1}		
0.312	10^{-9} to $3x10^{4}$	2.5×10^{-1}		
0.313	10^{-9} to $3x10^{4}$	4.0×10^{-1}		
0.314	10^{-9} to $3x10^{4}$	6.3×10^{-1}		
0.315 to 0.400	10^{-9} to 10	$0.56\ t^{1/4}$		
0.315 to 0.400	10 to 10^{3}	1		
0.315 to 0.400	10^{3} to 3×10^{4}		1×10^{-3}	
Visible and near infrared				
0.400 to 1.400	10^{-9} to 10^{-7}	$2C_A \times 10^{-2}$		3.5 limiting aperture, see Table 3-4.
	10^{-7} to 10	$1.1C_A\ t^{1/4}$		
	10 to $3 x10^{4}$		$0.2C_A$	
Far Infrared				
1.400 to 10^{3}	10^{-9} to 10^{-7}	10^{-2}		See Table 3-4.
	10^{-7} to 10	$0.56\ t^{1/4}$		
	> 10		0.1	

Note: the wavelength region λ_1 to λ_2 means $\lambda_1 \leq \lambda < \lambda_2$.

$C_A(780)=1.44$, $C_A(830)=1.82$.

Table 3-4 Limiting apertures for hazard evaluation [1].

Spectral region	Duration	Aperture diameters (mm)	
(μm)	(s)	Eye	Skin
0.180 to 0.400	10^{-9} to 0.25	1.0	3.5
	0.25 to 3 x 10^{4}	3.5	3.5
0.400 to 1.400	10^{-9} to 3 x 10^{4}	7.0	3.5
1.400 to 10^{2}	10^{-9} to 0.3	1.0	3.5
	0.3 to 10 *	1.5 $t^{3/8}$	3.5
	10 to 3 x 10^{4}	3.5	3.5
10^{2} to 10^{3}	10-9 to 3 x 10^{4}	11.0	11.0

* Under normal conditions these exposure durations would not be used for hazard evaluation.

Note: the wavelength region λ_1 to λ_2 means $\lambda_1 \leq \lambda < \lambda_2$.

3.11. Figures

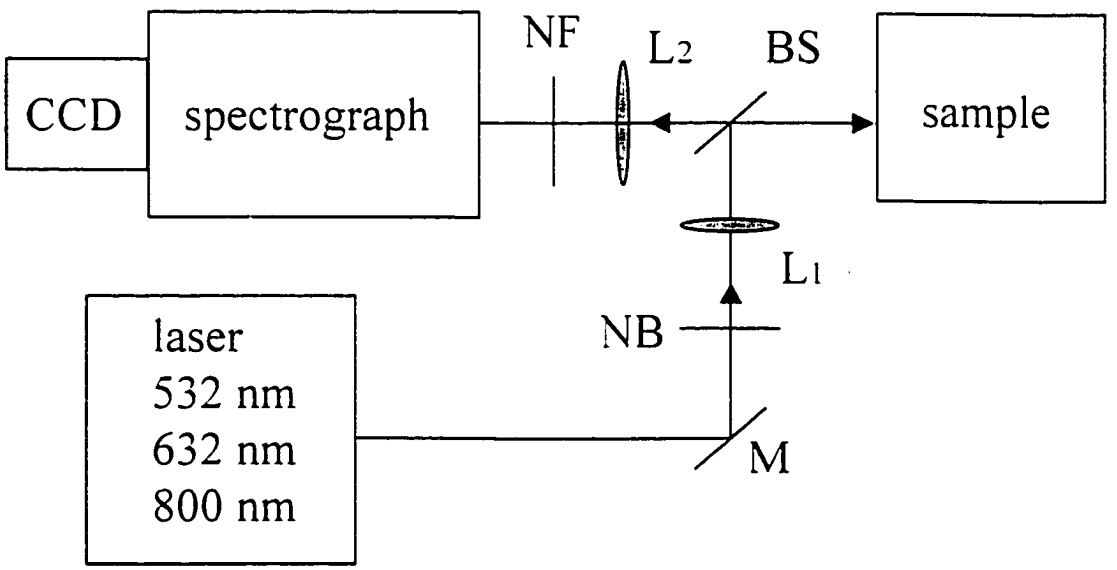

Figure 3-1 Schematic diagram of the experimental setup for the steady state spectroscopy measurements.

BS: beam splitter; NB: narrow band filter (laser line), L1: excitation lens, L2: signal collection lens, NF: notch filter (laser line).

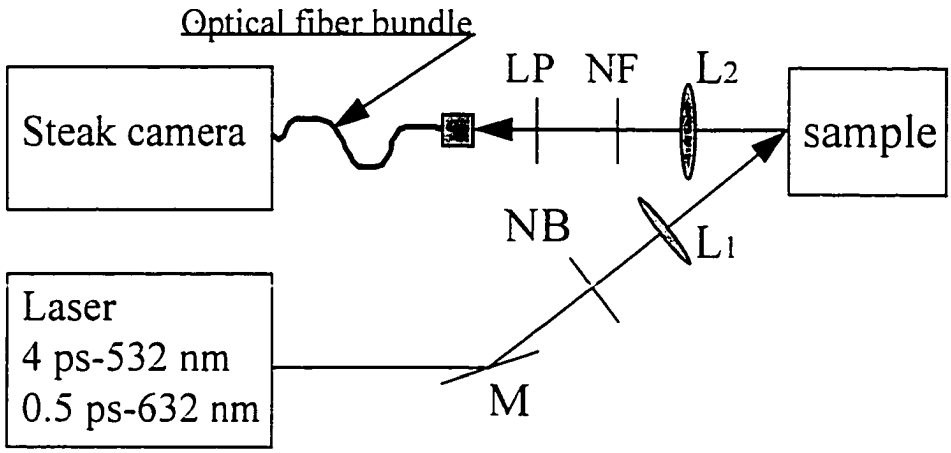

Figure 3-2 Schematic diagram of the experimental setup for the time resolved measurements.

NB: narrow band filter (laser line), L1: excitation lens, L2: signal collection lens, LP: long pass filter (665 nm), NF: notch filter (laser line).

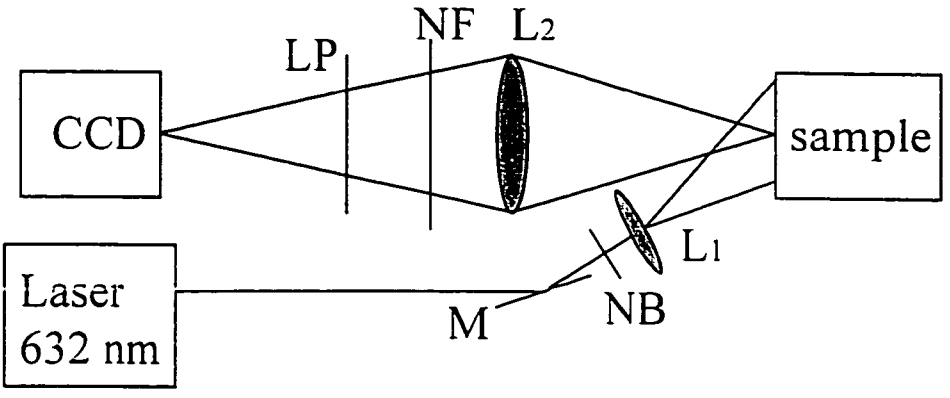

Figure 3-3 Schematic diagram of the experimental setup for spectral imaging measurements.

NB: narrow band filter (laser line), L1: excitation lens, L2: signal collection lens, LP: long pass filter (665 nm), NF: notch filter (laser line).

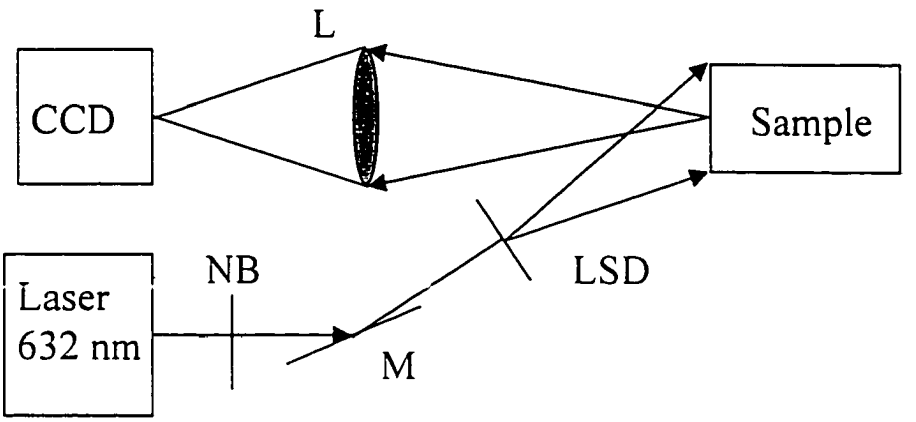

Figure 3-4: Schematic diagram of the experimental setup for the back scattering spectral imaging measurement.

NB: narrow band filter (laser line), M: mirror, LSD: holographic light shape diffuser, L: signal collection lens.

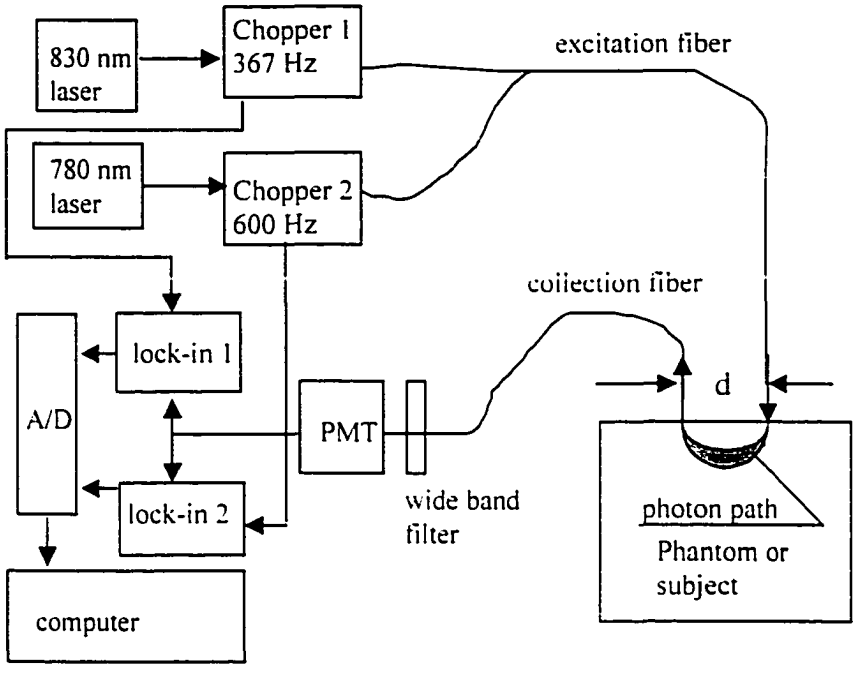

Figure 3-5 Block diagram of system setup for NIR brain monitoring.

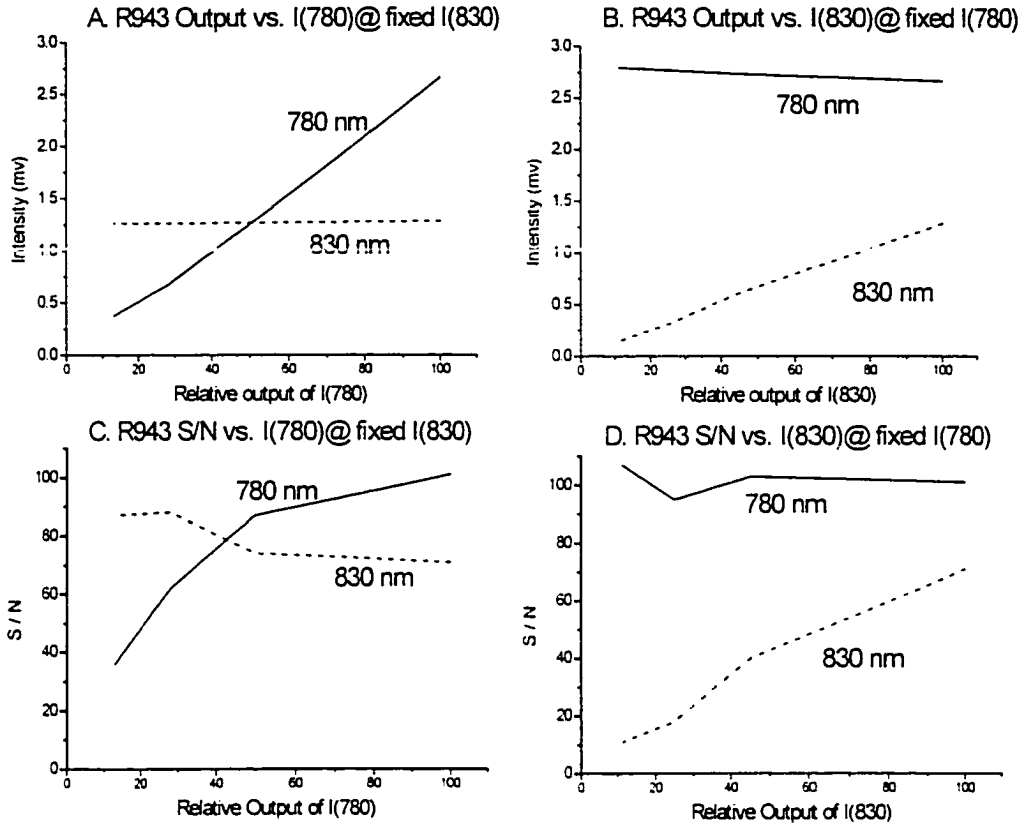

Figure 3-6 Output linearity and S/N ratio for R943.

(A) I(780) output linearity at I(830) fixed input condition, (B) I(830) output linearity at I(780) fixed input condition, (C) S/N ratio of I(780) output at I(830) at fixed input condition, (D) S/N ratio of I(830) output at I(780) at fixed input condition.

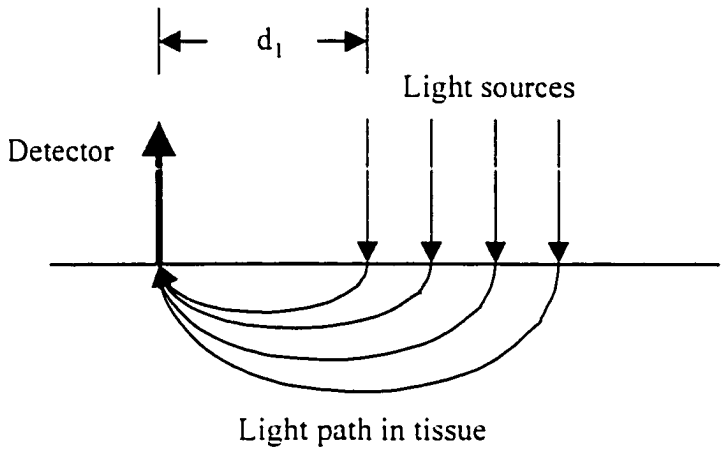

Figure 3-7 Diagram of source-detector arrangement of the FD method measurement setup.

4. Far-red and NIR emission wing from untreated tissue

4.1. Introduction

Raman scattering measurements in tissues using visible laser sources show the presence of a large Stokes spectral wing [4-7] spanning 1000's cm^{-1}, which makes the observation of the fine details in the Raman scattering vibrational spectrum very difficult. Sophisticated Raman techniques have been developed in the NIR, visible, and UV wavelength ranges, yielding important information about structure, dynamics, and composition of biomedical systems. Research works were preformed on breast biopsy samples [1], arterial walls [2], and gynecology tract tissues [3].

The intensities of this background luminescence wing from biomedical samples depend on the excitation laser wavelength [4]. The amplitude ratios between Raman peak and background luminescence, R/B, of normal human breast tissue samples range in two orders using the laser excitation from 406 to 830 nm [4]. The longer excitation wavelength used, the higher was the R/B ratio. Many of current research work with Raman spectroscopy using near infrared laser (~800 nm) to excite the tissue samples. The origin of this background signal in the far-red and near infrared (NIR) spectral region in Raman scattering measurements of tissues is not well discussed. The intensity of the Stokes spectral wing becomes weaker as the pump wavelength increases. This spectral wing has been considered as background noise [4] and is usually subtracted from the Raman spectral profile using complex fitting parameters to acquire the spectral features associated with the Raman active vibrational modes [5, 7].

The object of this part of this thesis is to **demonstrate the usefulness of wing** to

investigate the intensity, the spectral, and temporal behavior of the far-red and NIR spectral wing (SW) from human breast and chicken tissue samples. The difference in the intensity of the far-red SW emission under 632 nm excitation is used to image and distinguish different tissue components, such as normal from cancer tissues.

The experimental objectives of this part of the work are twofold: 1) to investigate the spectral characteristics of the far red and NIR SW emission in tissues under low power green, red, and NIR light photo-excitation; and 2) to utilize the "interesting" aspects of this SW emission for biomedical diagnostic applications. The first part of this objective was carried out using chicken tissue components as model tissue media. The second part of the objective was explored using different types of human breast tissue samples.

4.2. Tissue samples

The samples used in this work are normal and cancer human breast tissues obtained from the NDRI (National Disease Research Interchange) and chicken tissues obtained from the local food market. Pairs of cancer and normal tissue samples taken from the same patient were used from different patients. Specimens were not chemically treated and they were not frozen prior to our experimental measurements. The specimens were kept in the refrigerator at temperatures 2-4° C. The different tissues components were separated and homogeneous parts were selected and positioned inside a 1x1x4 cm^3 quartz cell. All measurements were performed at room temperature.

4.3. Methods

Chapter 3 (Page 55) describes the optical measurement setups used to obtain the

spectral (Figure 3-1, Figure 3-2) and temporal profiles and 2D images (Figure 3-3).

4.4. Results

The steady state far-red and NIR SW emission spectra (650 nm to 950 nm) arising from adipose and breast chicken tissue under 632 nm and 532 nm laser excitation are displayed in Figure 4-1. These spectra show that the adipose tissue exhibits stronger emission than the chicken breast tissue under identical illumination. The ratio of the integrated intensities of the emission from adipose to that of the breast tissue has an approximate value of 4 under 632 nm illumination while the same intensity ratio under 532 nm excitation is approximately 3. The emission spectra under 632 nm illumination, shown in Figure 4-1a, indicate the presence of several weak peaks around 720 nm and 780 nm arising from Raman scattering. The peak observed at 660 nm is an artifact due to the notch filter. The spectral profiles from the two types of tissues under 532 nm excitation shown in Figure 4-1b are very similar with their intensity decreasing rapidly at longer wavelengths. A small peak is observed centered at ≈870 nm for both types of tissue under 532 nm illuminations.

The temporal profiles of the NIR (beyond 670 nm) SW emission from adipose and breast chicken tissues under 532 nm and 632 nm excitation wavelengths are displayed in Figure 4-2. These temporal profiles show that the overall decay times of the NIR emission for both adipose and chicken breast tissues are smaller under 632 nm laser excitation than under 532 nm excitation. The NIR emission decay time from chicken breast tissue is shorter than from adipose tissue under 632 nm and 532 nm ps laser pulse excitations.

The temporal dynamics of the NIR emission is fitted by a combination of a

rapidly decaying component and a slow component using the following relation [8, 9]:

$$I(t) = Af*\mathrm{Exp}(-t/tf) + A_S*\mathrm{Exp}(-t/t_S) \qquad (1)$$

where $Af(A_S)$ is the amplitude and $tf(t_S)$is the decay time of the fast (slow) component.

The fitting parameters of the experimental data shown in Figure 4-2 were obtained using a linear square fit to eq. (1) and are summarized and shown in Table 4-1.

The relationship between the integrated emission intensity and the excitation laser power has been obtained in the following experiment. The full laser power on the sample side is about 2 mW. A set of different neutral density (ND) filters is used in the excitation optical pass to reduce the excitation power on the sample to be tested. These ND filters are calibrated on an optical photometer to obtain their attenuation values at the laser wavelength.

Figure 4-3 shows the experimental result of the relationship between the integrated emission intensity and the excitation power intensity on a tissue sample. The X-axis is the relative excitation power on the sample side using different ND filters until the 100% point, which is obtained without using any ND filter in the excitation beam. The Y-axis is the integrated intensity of the far-red emission corresponding to each excitation power level in arbitrary units. After the linear regression, the result shows that the emission has a linear relationship with the excitation power under He-Ne laser excitation. The dependence indicates single photon excitation not multiple photon excitation operation. This indicates that the far-red emission is a linear process under low power He-Ne laser excitation.

Figure 4-4 shows the far-red and NIR emission spectra from human breast tissue sample under 632 nm Figure 4-4a) and 532 nm (Figure 4-4b) laser excitation. The two

emission profiles were obtained under identical illuminating conditions from cancer (upper profile) and normal (lower profile) breast tissue. The ratio of the integrated intensities of the emission from cancer over the intensity from normal tissue is approximately 4 under 632 nm excitation and approximately 2 under 532 nm excitation. The Raman scattering spectral components are superimposed onto the much stronger emission background and they contribute very little to the measured ratio of the integrated intensities.

The typical spectral profile of the far-red to NIR emission from a human breast tissue sample under 800 nm excitation is shown in Figure 4-5. The two emission curves were obtained under identical illumination conditions from cancer (upper profile) and normal (lower profile) breast tissue. The ratio of the integrated intensities of the emission from cancer to the intensity from normal tissue is approximately 2. The Raman scattering spectral components are superimposed on the strong emission background. The normal tissue has much stronger Raman peaks than the cancer tissue. The cancer tissue has a stronger background emission than the normal tissue. This result was also obtained by other groups [10].

The bar graph of the normalized to peak integrated intensities for far red emission from normal and cancer tissue samples from different patients under 632 and 800 nm laser excitation is shown in Figure 4-6. Under 632 nm excitation, the integrated emission intensities (obtained in the range of 650 ~ 950 nm) from cancer samples in 10 patients are larger than from normal samples obtained from 12 patients as shown in Figure 4-6a. Under 800 nm excitation, the integrated emission intensities (obtained in the range of 825 ~ 965 nm) from cancer samples in 14 patients are stronger than from normal samples

obtained from 15 patients as shown in Figure 4-6b. These data suggest that the integrated far-red emission intensity could be used to separate normal and cancer tissue components of the human breast. Under 632 nm excitation, it is characteristic that in 9 of the 12 patients, the integrated intensities of the far-red emission of the cancer samples were about 2 fold or more times stronger than from the corresponding normal tissue samples from the same patient. Under 800 nm excitation, it is characteristic that in 12 of the 15 patients, the integrated intensities of the far-red emission of the cancer samples were about 50% or more times stronger than from the corresponding normal tissue samples from the same patient.

The difference in intensity of the far-red emission under 632 nm excitation from the two different types of chicken tissue samples (adipose and breast shown in Figure 4-1) and human breast tissues (cancer and normal shown in Figure 4-4, Figure 4-5, and Figure 4-6) provides the basis for imaging of the two types of tissue using their integrated far-red emission intensity.

The image of a sample shown in Figure 4-7a is under room light illumination. This sample consists of adipose (upper part) and breast (lower part) chicken tissue. Figure 4-7b shows th image of the same sample when using the integrated intensity of the far-red emission under 632 nm illumination. The adipose section of the tissue appears to be much brighter than the chicken breast tissue allowing for clear separation of the two regions and types of tissues. Similar results were obtained using human breast tissue.

Two human breast tissue samples positioned side by side composed of normal (left) and cancerous (right) tissue were imaged (Figure 4-8a) under room light illumination. The photographs in Figure 4-8b show the human tissue far-red emission

images under 632 nm illumination. The cancer tissue sample appears as a brighter "object" than the normal tissue sample. This result occured for 10 out of 12 sample pairs.

4.5. Discussion

The intensity, spectral and temporal profiles of the far-red and NIR SW emission from chicken tissue under 532 nm and 632 nm excitation are shown in Figure 4-1 and Figure 4-2 repactively, and reveal a number of interesting features.

The SW spectra in Figure 4-1 reveal that the ratio of the integrated spectral intensities (650 - 950 nm) from adipose and breast tissue is ≈ 3x under 532 nm excitation and ≈ 4x under 632 nm excitation. The spectral profiles are also different under 532 nm and 632 nm excitation. The temporal profiles of the emission displayed are also different for the two types of tissue and for both excitation wavelengths. These spectral and temporal differences of the emission indicate that the molecular states or molecular species involved in the far-red and NIR emission are different for 632 nm and 532 nm illuminating wavelengths. These experimental results also demonstrate that the origin of the background signal in Raman scattering measurements in tissues arises from emission from photo-excited species.

Figure 4-2(a) that shows that the time profiles of the emission from breast chicken tissue are similar under 532 and 632 nm laser excitation. In Figure 4-2(b), the emission from adipose tissue has a longer lifetime under 532 nm laser excitation than under 632 nm laser excitation. The fitted parameters of the time profiles indicate that the lifetimes of the wing emission from the tissue samples are the order of nanoseconds with a picosecond component. These observations indicate that the major energy of this emission does not arise from inelastic or elastic scattering.

The experimental result of the far-red emission intensity from a tissue sample as function of the excitation power is displayed in Figure 4-3. It shows that the emission intensity is proportional to the low power excitation light. This relationship indicates that the emission arises from a linear single photon process.

Considering that different molecular species are responsible for the differences in the emission characteristics under green (532 nm) and red (632 nm) light excitation, some contribution to the far-red and NIR emission under 532 nm laser excitation may be provided by flavins, porphyrins, and bilirubins. Porphyrins, biliverdins and/or some unknown fluorophors may be contributing to the wing under 632 nm laser excitation. There seems to be a chemical component that contributes to the background emission under 800 nm laser excitation. The far-red emission recorded under NIR laser excitation is comparable in intensity to the Raman scattering spectral components, which indicates that the quantum efficiency from this emission is very low. The exact reason is not known. Spectrum is quadra-pole emission from the ground state manifold (see model in chapter 6).

The experimental measurements of the integrated intensity of the far-red emission from cancer and normal tissue samples from different patients indicate the presence of a systematic enhanced intensity in the cancer tissue samples. This result comes out when the cancer tissue sample is compared to normal tissue under either 632 nm excitation or 800 nm excitation. From 12 patients studied under 632 nm excitation, in 10 cases the far red emission from the cancer sample was greater than from the normal sample. In one case the intensity was approximately the same, while only in one case the result was inconsistent. In more than 75% of the cases, the intensity from the tumor tissue was 2

fold or higher than the normal tissue (See Figure 4-6a). From 15 patients studied under 800 nm excitation, there are 14 cases the far-red emission from the cancer sample was greater than from the normal sample. In one case the intensity was approximately the same, while only in one case the result was inconsistent. In more than 75% of the cases, the intensity from the tumor tissue was 50% or higher than the normal tissue (See Figure 4-6b). A statistical analysis of the experimental integrated intensity from both cases shows a significant difference between normal and cancer tissue samples with $p < 0.01$ in the pair t-test [11].

This work demonstrates that the far-red and NIR SW emission, obtained using smaller than 2-eV radiation for excitation, may have the potential to differentiate tissue components in a far red and NIR fluorescence imaging arrangement (Figure 4-7 and Figure 4-8). The sample, shown in Figure 4-7a under room light illumination, containing adipose (upper part) and chicken breast (lower part) tissue, was imaged using the integrated intensity of the far-red emission under 632 nm illumination. Due to the over four-fold difference in intensity, the adipose tissue appears much more intense than the breast tissue (see Figure 4-7b), allowing for clear separation of these two tissue types. Similarly, cancer and normal tissues may be separated and imaged using the far-red and NIR emission integrated intensity, as shown by images in Figure 4-8.

In general, the quantum efficiency of the wing emission from the tumor tissue is higher than the normal tissue samples. The comparison result varies from the tumor tissue to paired normal tissue from patient to patient. The possible reason for this difference could be that the microenvironment of the tissue samples is different for normal and breast tumor tissues. This could affect the structure of the protein molecules and change

the non-radiative energy transfer channels. The different quantum efficiency from tumor samples with the paired normal samples may indicate the degree of the malignancy of the tumor. The reason of the different quantum efficiency could be the microenvironment of a higher degree malignant tumor tissue that can be more different than the normal tissue. The differences in the biochemical components in the different kinds of tissues are another possible important reason for the far-red emission difference, such as fat and chicken breast are different biomedical materials. A model is presented to describe the wing vs. λ.

This work shows that the NIR emission spectral wing has the potential to give information about the state of tissues.

4.6. References

1. Alfano R R, Liu C H, Sha W L, Zhu H R, Akins D L, Cleary J, Pridente R and Cellmer E, "Human breast tissues studies by IR Fourier transform Raman spectroscopy", *Lasers in life Sci.*, 4(1) pp. 22-28 (1991)

2. Baraga J J, Feld M S, and Rava R P, "In situ histochemistry of human artery using near infrared Fourier transform Raman spectroscopy", *Proc. Natl. Acad. Sci.* USA **89**, 3473-3477 (1992).

3. Liu, C. H., Das, B. B., Glassman, W. L., Tang, G. C., Yoo, K. M., Zhu, H. R., Akins, D. L., Lubicz, S. S., Claery, J., Prudente, R., Celmer, E., Caron A., and Alfano, R. R. "Raman fluorescence and time-resolved light scattering as optical diagnostic techniques to separate diseased and normal biomedical media," *J. Photochem Photobiol B: Biol.* **16**, 187(1992).

4. Frank C J, Redd D C B, Gansler T S, and McGreery R L, "Characterization of human breast biopsy specimens with near-IR Raman spectroscopy", *Anal. Chem.*, **66**(3), 319-326 (1994).

5. Baraga, J. J., Feld, M. S. and Rava, R. P. "Rapid near-infrared Raman spectroscopy of human tissue with a spectrograph and CCD detector," *Appl. Spectrosc.* **46**(2), 187-190 (1992)

6. Feld, M.S., Manoharan, R., Salenius, J., Orenstein-Carndona, J., Romer, T.J., Brennan, J.F., Dasari, R.R., and Wang, Y., "Detection and characterization of human tissue lesion with near infrared Raman spectroscopy," in: Advances in

fluorescence Sensing technology, Vol. II, J.R. Lokowicz, ed. Proc. SPIE 2388, 99-104 (1995).

7. Mahadevan, A., Ramanujam, N., Mitchell, M. F., Malpica, A., Thomsen, S. and Kortum, R. R. "Optical techniques for the diagnosis of cervical precancers: Comparison of Raman and fluorescence spectroscopies," *in Advances in Fluorescence Sensing Technology II*, J. R. Lakowicz, ed., Proc. SPIE **2388**, 110-120 (1995).

8. Pradhan, A., Das, B. B., Yoo, K. M., Cleary, J., Prudente, R., Celmer, E. and Alfano, R. R. "Time-resolved UV photoexcited fluorescence kinetics from malignant and non-malignant human breast tissues", *Lasers in Life Sci.* **4**(4), 225-234 (1992)

9. Glassman, W. S., Steinberg, M. and Alfano, R. R. "Time resolved and steady state fluorescence spectroscopy from normal and malignant cultured human breast cell lines", *Lasers in Life Sci.* **6**(2), 91-98 (1994)

10. Frank C J, McCreery R L, and Redd D C B, "Raman spectroscopy of nomal and diseased human breast tissues", Anal. Chem. 67(5), 777-783, (1995).

11. Glantz, S. A. *Primer of Biostatistics*, 3rd ed., McGraw-Hill, Inc. (1992)

4.7. Tables

Table 4-1: Fitting parameters of the far-red emission temporal profiles from adipose and chicken breast tissues under 532 nm and 632 nm excitations using eq. 1.

Excitation	Tissue type	t_f (ps)	t_S (ns)	A_f/A_S
532 nm	Adipose	234 ±25	1.51 ±0.15	1.16 ±0.2
632 nm	Adipose	86 ±10	1.39 ±0.15	1.41 ±0.2
532 nm	Breast	163 ±15	1.15 ±0.15	1.40 ±0.2
632 nm	Breast	136 ±15	1.37 ±0.15	2.48 ±0.3

4.8. Figures

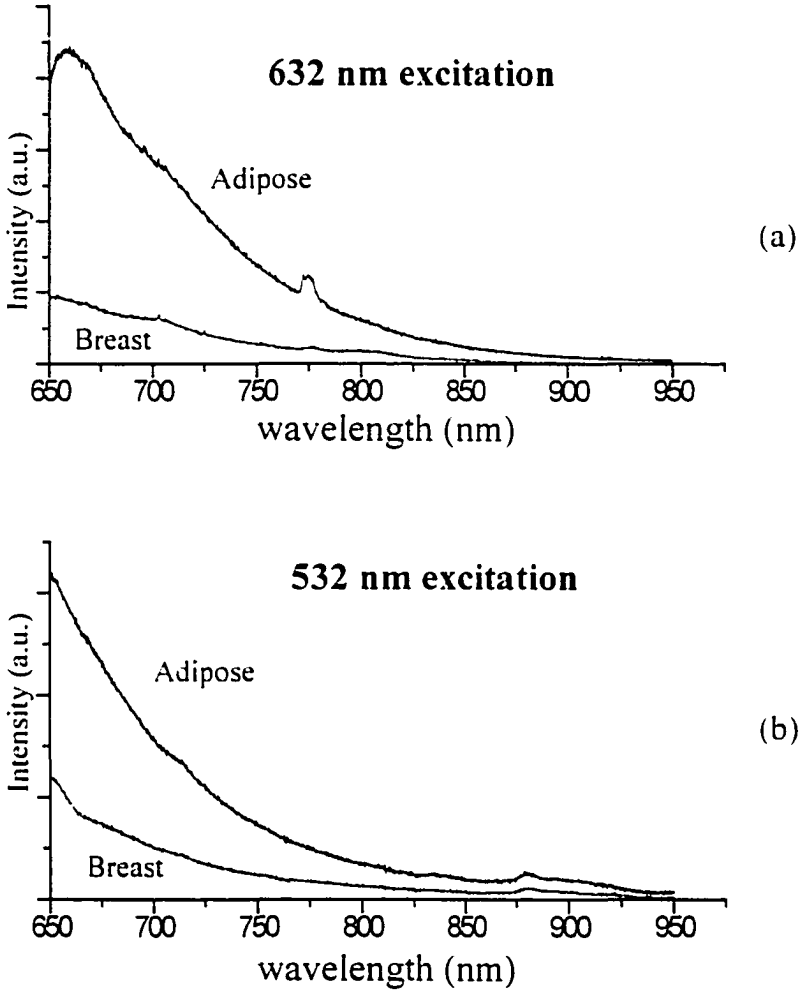

Figure 4-1: Far-red and NIR emission SW profile from adipose (upper profile) and breast (lower profile) chicken tissues under (a) 632 nm laser excitation, and (b) 532 nm laser excitation.

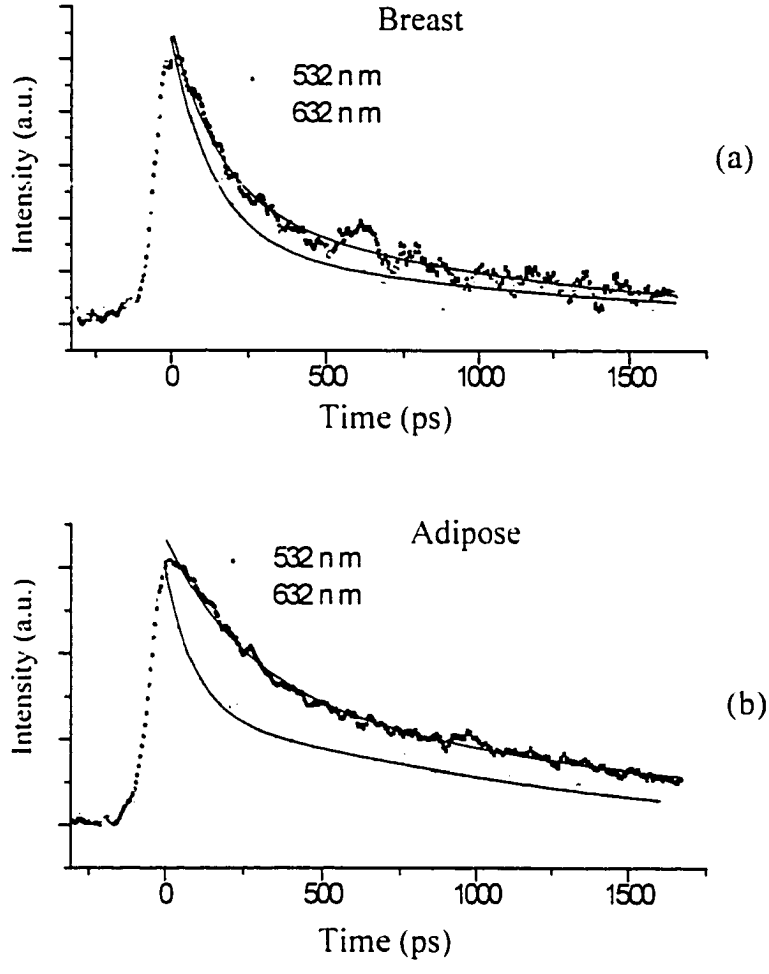

Figure 4-2: Time resolved emission SW profiles normalized at the peak intensity of adipose and chicken breast tissue under 532 nm and 632 nm laser excitation; (a) chicken breast tissue under 532 nm and 632 nm laser excitation, and (b) adipose tissue under 532 nm and 632 nm excitation.

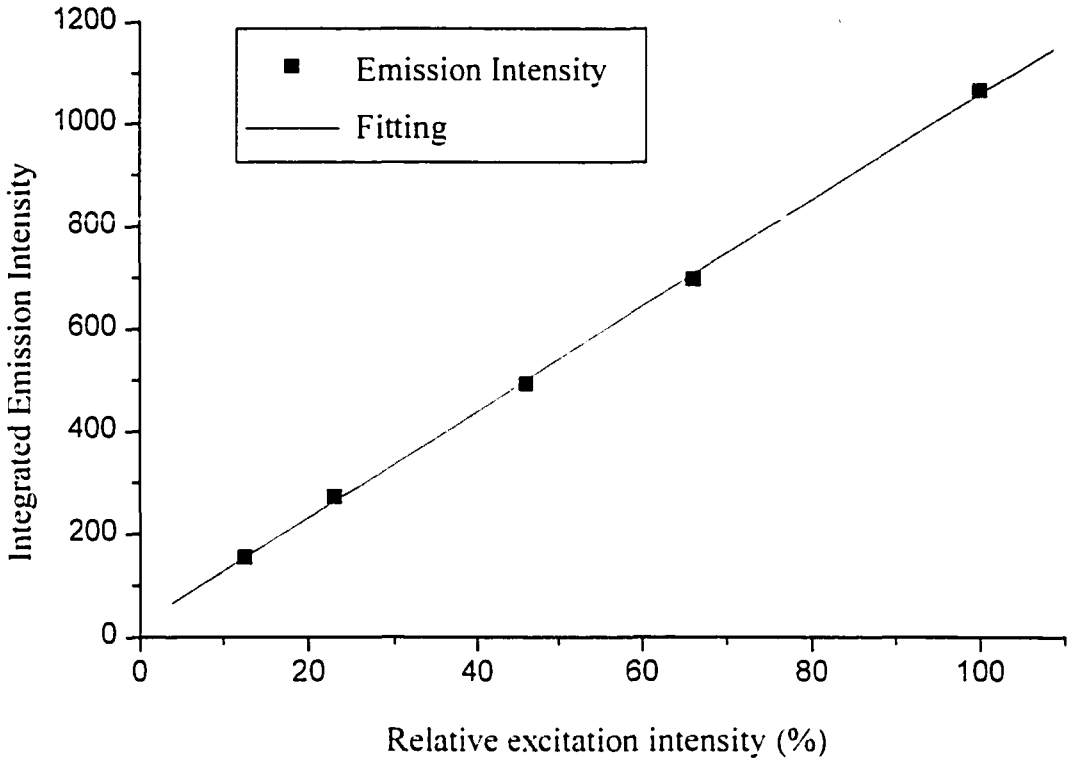

Figure 4-3. The relationship between the integrated far-red emission intensity and the excitation laser power on a tissue sample with a linear fitting curve. The X-axis is the relative excitation power from 13% to 100%. The Y-axis is the related emission intensity using arbitrary units.

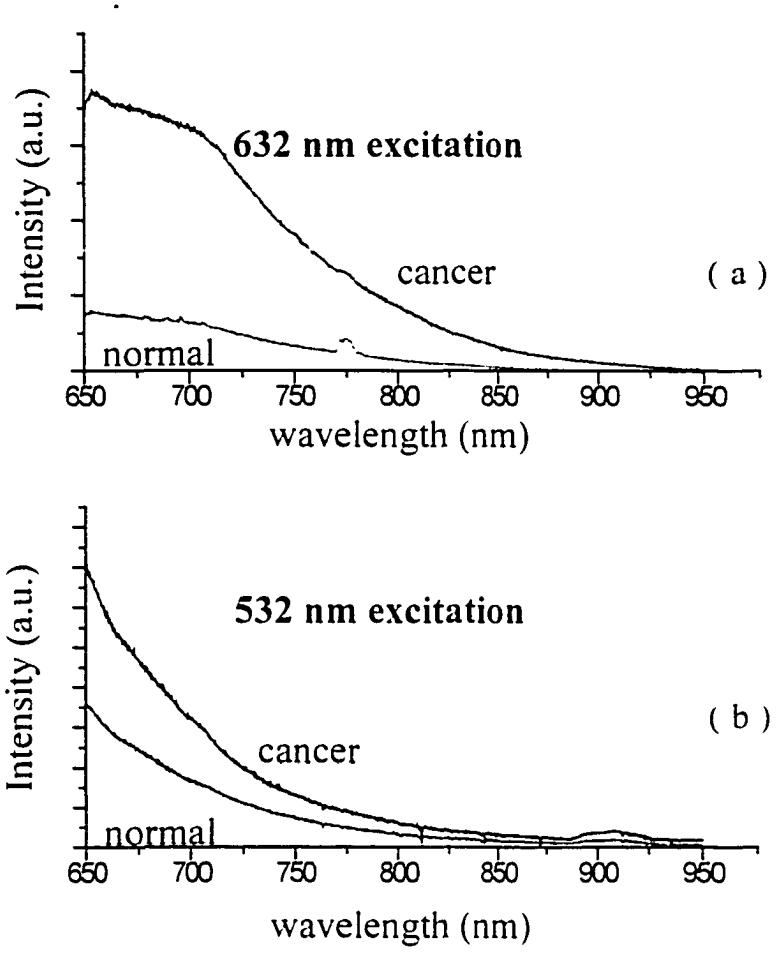

Figure 4-4: Far-red and NIR emission SW profile from cancer (upper profile) and normal (lower profile) human breast tissues under (a) 632 nm laser excitation and (b) 532 nm laser excitation.

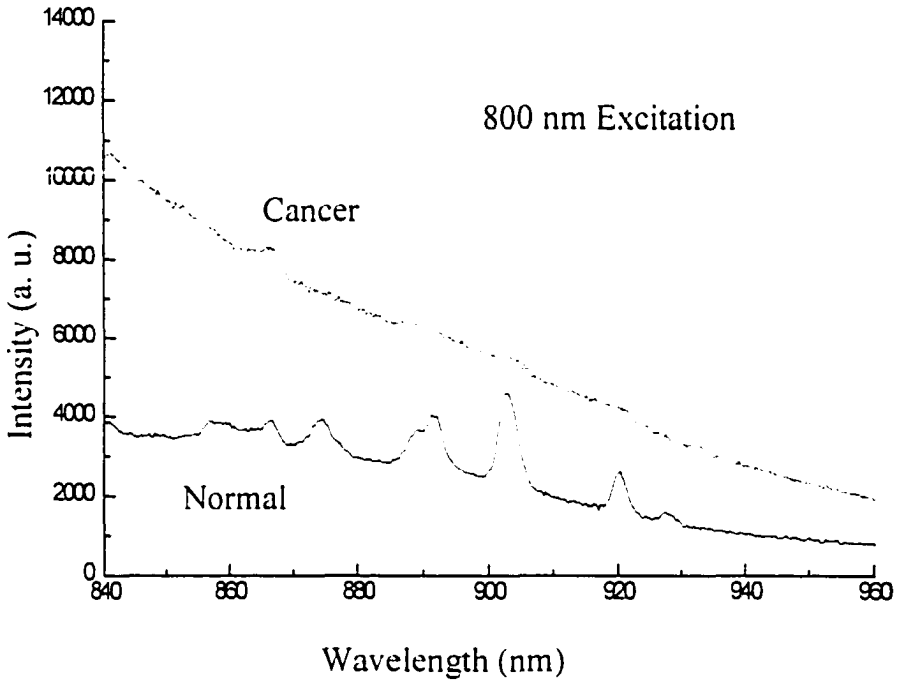

Figure 4-5: Far-red and NIR emission SW profile from cancer (upper profile) and normal (lower profile) human breast tissues under 800 nm laser excitation.

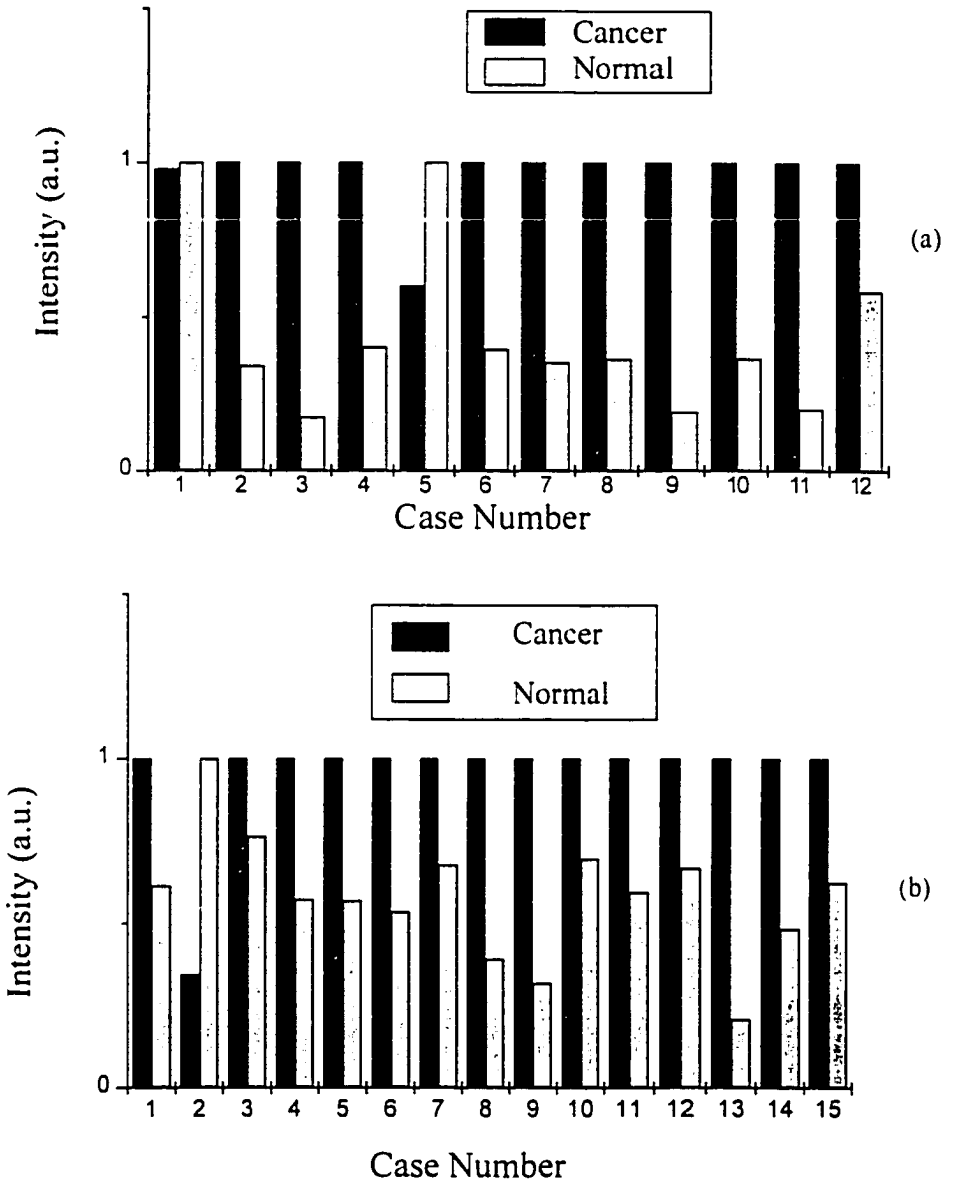

Figure 4-6: Bar chart of the normalized integrated intensities of the far-red emission from tumor and normal human breast tissues.

(a) Under 632 nm excitation for 12 different patients, (b) Under 800 nm excitation for 15 different patients.

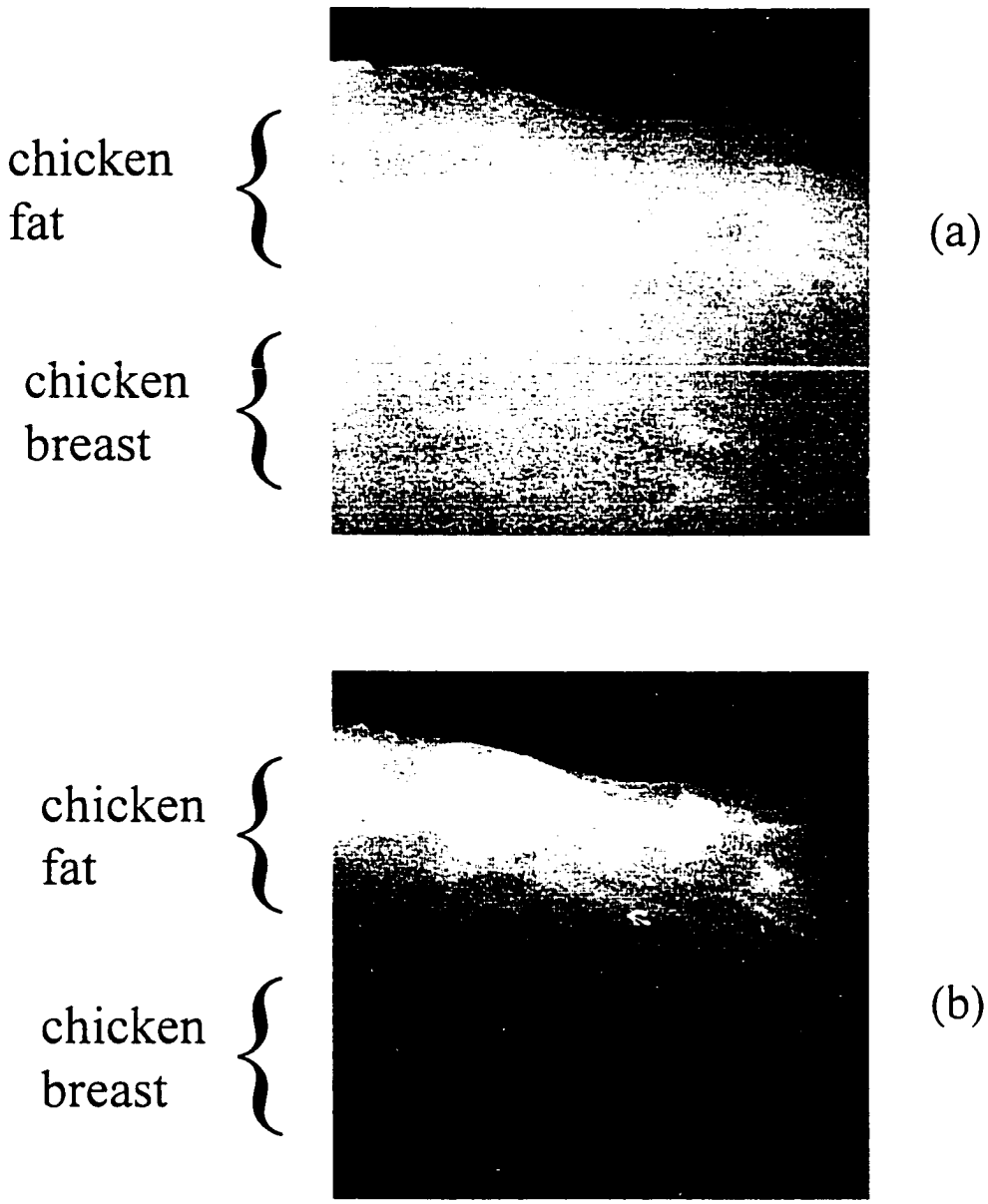

Figure 4-7: Images in the back-reflection geometry of a sample containing adipose (upper part) and breast (lower part) chicken tissues based on (a) room light illumination, and (b) the integrated intensity of the NIR emission under 632 nm laser illumination.

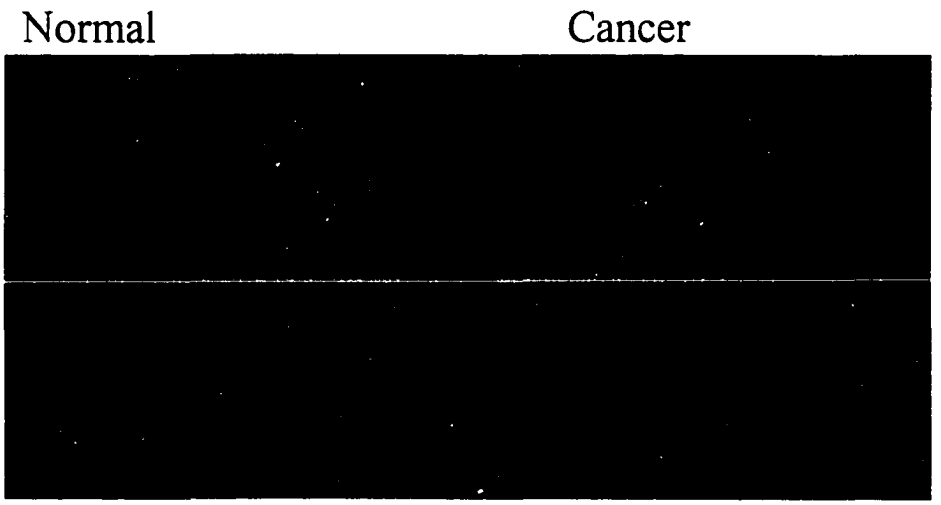

(a)

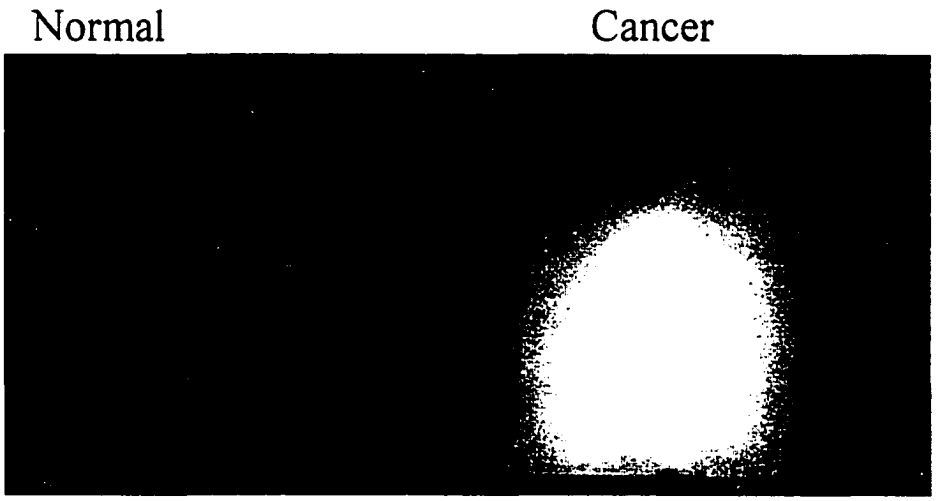

(b)

Figure 4-8: Images in the back-reflection geometry of a normal (left) and cancerous (right) human breast tissue sample using (a) room light illumination, and (b) the integrated intensity of the NIR emission (> 665 nm) under 632 nm laser illumination.

5. Far-red and NIR emission from thermal treated tissues

5.1. INTRODUCTION

Heat treatment for biological bodies has been investigated for a variety of medical applications, such as laser tissue welding for tissue reconstruction [1, 2] laser interstitial hyperthermia for cancer treatments [3], photocoagulation for homeostasis and photovaporization for tissue ablation [4-7] as well as radiofrequency ablation for treatment of cardiac arrhythmias [8-10]. Accurate temperature monitoring to control the heat source in order to improve the outcome for patients is needed. An *in situ* temperature monitoring system for laser tissue welding is important in order to obtain better bursting pressure and increased bonding strength of a weld. At present, there are few methods to detect the extent of the thermal damage after heat treatment. Histology modification is usually used as a technique to determine this extent. There are several practical factors, which limit the use of histology. First, many thermally induced morphological changes are subtle. Detectable morphological markers of thermal changes produced *in vitro* at tissue temperatures below 60°C have not been described for routinely prepared tissue for light microscopy. Second, some thermally produced tissue changes are similar to and cannot be distinguished from artifacts produced by the histological preparation for light microscopy. Third, transmission electron microscopy (TEM) reveals the tissue damage produced by heating, but the small tissue samples required for TEM do not allow for the evaluation of the total lesion [11]. The histology method could barely reveal gradual intensity changes in tissue from the damage caused by heating.

To monitor temperature, currently thermocouples offer the best, most precise and fastest response to temperature change. The temperature measured by a thermocouple is often used as the real temperature monitor [12]. A thermocouple must be in contact with the measured tissue and it is difficult to measure the surface temperature due to the presence of a laser beam or other heating source. To measure surface temperature during laser treatment, infrared thermography is used. The main problem with this method is that the target area is sometimes too small to give an accurate measurement of temperature [12].

The surge of spectroscopy to medical diagnostic applications may offer a novel remote temperature sensing method. Recently, the intensity difference of near infrared (NIR) wing emission from tissue under laser irradiation was observed with different type of tissues and can be used to identify different types of tissues [13].

The focus of this part of thesis is to investigate the relationship between the NIR emission intensity from human and chicken tissues under low power 632 nm laser excitation and the extent of tissue thermal treatment after application of heat below 100°C environment condition.

5.2. MATERIALS

Chicken leg and breast samples were purchased from a local market. After the fat and tendon tissues were completely taken out, the samples were mounted in a specially designed 4 mm diameter and 1 mm deep aluminum sample-holder used for the heating bath and spectral analysis.

The normal human thyroid gland tissue and goiter tissues were obtained from dissected specimens from Memorial Sloan-Kettering Cancer Center. The samples were cut 5 mm x 5 mm in area and 1 mm in height, which were mounted on a quartz slide.

The heating bath was produced by the circulation of pre-warmed 0.9 % saline solution in a water bath (Fisher Scientific, Model 9101, Pittsburgh, PA) for 5 min. The temperature stability was $\pm$ 0.01°C. The temperature was increased from 40°C to 100°C in 10°C steps for heating human tissue. The temperature was increased from 37°C to 49°C and from 61°C to 97°C in 6°C steps and from 49°C to 61°C in 3°C steps for heating chicken tissue. Six groups of samples from different chickens were investigated. At each temperature, six target sites were measured in each group. After cooling down to room temperature in saline solution (10 min. after heat treatment), the samples moistened with saline solution were mounted in the sample-holder and placed between quartz and aluminum slides for spectral emission intensity and scattering intensity studies. Samples hold at 40°C, 61°C and 97°C temperatures for 5 min were respectively measured with the steady state emission spectroscopy setup for NIR emission spectral wing profiles. The measurement process was finished within 30 min. after heating. The temperature of the measuring environment was 25°C.

In another set of six groups of chicken samples, three samples in each group were heated at 40°C, 61°C, and 97°C, respectively. The emission intensity was measured every hour for 3 hours after heat treatment. These groups were used for the detection of changes in the extent of emission intensity with time.

The recordings were calibrated and analyzed with the aid of the software, which came with the CCD camera system. For simplicity and due to the fact that the intensity was

virtually homogeneous, the emission intensity and the scattering intensity were measured by the maximum square drawn inside the circular sample surface (see Figure 5-1and Figure 5-2). Data is expressed as the mean $\pm$ standard deviation (SD) throughout the text and figures.

For changes in the extent of emission intensity and scattering intensity in each group, one-way ANOVA was performed. A p-value of < 0.05 was assumed to represent a significant difference.

5.3. RESULTS

The NIR emission images of the chicken sample after different temperature treatments are shown in Figure 5-1. The emission intensity distributions over the sample are found to be homogeneous. In Figure 5-1a, the right sample image is heated at 61°C for 5 min. and is brighter than the left sample image that is not treated with heat. In Figure 5-1b, the right sample image is heated to 97°C for 5 min. and is brighter than the left sample image, which is heated to 61°C. The emission intensities from the samples are proportional to the heat treatment temperature.

The laser (632 nm) elastic scattering images from the chicken samples treated at different temperature are shown in Figure 5-2. The scattering light intensity from the tissue samples increases when the treatment temperature rises from room temperature (the left sample image in Figure 5-2a) to 58°C (the right sample image in Figure 5-2a) and then it remains at the same level from 58°C (the left sample image in Figure 5-2b) to 97°C (the right sample image in Figure 5-2b).

The NIR emission spectral wing profiles from the chicken samples with different temperature treatments are shown in Figure 5-3. The emission spectral profiles are similar for the tissue samples treated at three different temperature levels. The difference between tissue samples with higher temperature treatment relative to those at lower temperature is stronger emission intensity. Similar results are obtained with human tissues.

The relationship between relative emission intensity changes of chicken tissue and time after heat application is plotted in Figure 5-4. The fluctuation of emission intensity within 3 hours after heating is not different for different thermal treatment temperatures. This shows emission intensity measurement error due to different measurement times within 3 hours after heat treatment.

Before the heat treatment, the emission intensity measured from different chicken muscle samples from different chickens (n = 36) was not statistically different (F = 0.13955, p = 0.98165). When tissue is heated from 37°C to 55°C, the emission intensity in 5 groups was not different (F = 2.41499 to 0.27576, p = 0.09661 to 0.84218). Only one group had a difference (F = 3.5974, p = 0.03158). When the tissue is heated from 55°C to 97°C, the emission intensity in each individual group obviously increases with the rise in temperature. After normalizing the emission intensity to the non-treated sample level in each individual subject sample group, the curve describing the relative emission intensity of the heat-treated samples versus temperature is plotted in Figure 5-5.

The relationship between relative emission intensity changes of human tissues and treatment temperature is plotted in Figure 5-6. The emission intensities increase with the rise in temperature above 60°C. Different slopes for human thyroid and goiter

(retromorphosis) tissues were measured. The energy transfer is different for different tissue types.

Using a linear fitting approach, the intensity of emission for chicken tissue is found to be linearly proportional to the temperature treatment on the samples from 55°C to 97°C. The data can be fitted by a linear equation as:

$$I_N(T) = Io + b(T - To) \qquad \text{for } 55°C < T < 97°C \qquad (1)$$

Where $I_N(T)$ is the normalized emission intensity which is defined *as* $I_E(T)/I_E(room\ temperature = 25°C)$, $I_E(T)$ is defined as the measured emission intensity of the sample at temperature T; Io is the normalized emission intensity of the sample at the initial onset temperature To = 55°C; and b is the slope of the temperature dependent emission intensity with the unit of per 1°C. From the linear least square fit of data displayed in Figure 5-5, the slope b for chicken is found to be 0.1000 $\pm$ 0.0032 per 1°C based upon the non-treatment sample emission level within this temperature range. This excellent linear fit from the slope indicates an accuracy of ~ 0.03 intensity change per 1°C accuracy in obtaining the temperature of tissue treatment from the NIR emission intensity technique.

The changes in scattering intensity (I_S) at 632 nm from chicken tissue with treatment temperature rise are shown in Figure 5-7. After normalizing with the non-treated samples, the relative scattering intensity increases with temperature to about 58°C. After 58°C, the intensity remains at the same level and there is no statistical difference.

In order to avoid the effect of geometric changes in the sample after heat treatment and the influence on the emission intensity by the intensity of the exciting

source, $I_N(T)$ is transformed to a ratio parameter $R(T)$ by taking the ratio of the normalized emission intensity $I_N(T)$ to the normalized scattering intensity $I_S(T)$ from the same sample. The ratio is given by:

$$R(T) = I_N(T) / I_S(T) \quad (2)$$

For 58°C < T < 97°C, the ratio has a linear relationship with treatment temperature (Fig 10). The data are fitted to the relationship:

$$R(T) = Ro + br(T - Tro) \quad (3)$$

For 58°C < T < 97°C, Ro is the normalized ratio from the sample treated at the initial onset temperature Tro = 58°C; br is the slope; and T is the treatment temperature. From data in Figure 5-8, the intensity slope for chicken from the temperature increment is found to be 0.0650 $\pm$ 0.0027 / °C over the temperature range of 58°C to 97°C.

5.4. DISCUSSION

From the data in Figure 5-5 and Eq. 1, it appears that a relationship exists between the emission intensity of the NIR emission and the extent of thermal tissue change for chicken tissue. The results show that the emission intensity on heated tissue is not statistically different at temperatures from 37°C to 55°C. When the temperature rises from 55°C to 97°C, the emission intensity increases in response to the temperature. This relationship has also been observed in the normal and pathologic human tissues with different temperature slopes. The relative emission intensity is linearly proportional to the temperature treatment of the tissue samples. The value of the emission intensity is maintained for 3 hours after heat treatment.

The relative ratio of emission intensity to back scattering light intensity is also linearly proportional to the treatment temperature in the temperature range from 58°C to 97°C (see Figure 5-8 and Eq. 3). With this measurement, the influence of the sample's geometric changes after heat treatment and the effect of the exciting source intensity can be eliminated.

The relatively increasing rate of emission intensity from the tissue after heat treatment begins at 55°C. This temperature point may be correlated to some protein structure changes, such as the unfolding of collagen [15]. It is known that when the temperature rises to 60°C, collagen denatures [11]. These changes are not reversible after the tissue temperature returns to room temperature.

The explanation for the NIR emission under 632 nm laser excitation on tissue and its intensity increase with temperature for different tissue types are still under investigation. The lack of significant modification of the spectral profiles after thermal treatment (see Figure 5-3) demonstrates that there is a small change in the fluorophores in this spectral range. The intensity changes indicate that the quantum efficiency of the fluorophors in the tissue samples is increasing proportionally to the heat treatment temperature. The most likely reason for the increase in emission efficiency is the change in the tertiary and/or secondary protein structures under thermal treatment due to hydrogen bond breakage and cross-link changes between collagen fibers and other proteins [14]. This change may indicate that higher temperatures could affect the structure of the protein molecules resulting in changes in the nonradiative energy transfer channels.

The emission intensity increase after heating tissue may be a useful measurement method to detect the extent of tissue heat damage. Walsh et al. [16] state that no significant optical microscopic alterations are observed at temperatures below 90°C. Heating tissue below 100°C is commonly used in the medical field. These applications need temperature monitoring and temperature measurement in order to improve the treatment results and limit excessive thermal injury of normal tissue.

These results show that the extent of thermal damage and welding of a tissue may be monitored non-invasively using NIR emission intensity changes. However, a calibration method is needed to determine the slope values for different type of tissues. Measurement of emission intensity on heated tissue could not only detect the extent of tissue damage after thermal injury, but could also, as a on-contact method, monitor the temperature change of the treatment.

5.5. References

1. Badeau, A. F., C. E. Lee, J. R. Morris, S. Thompson, E. G. Malk and A. J. Welch. (1986) Temperature response during microvascular anastomosis using milliwatt CO_2 laser. *Lasers Surg. Med.* **6**,179.

2. Maitinot, V. J., S. R. Mordon, V. A. Mitchell, P. N. Pellerin, and J.M. Brunetaud. (1994) Determination of efficient parameters for argon laser-assisted anastomoses in rats: macroscopic, thermal, and histological evaluation. *Lasers Surg. Med.* **15**, 168-175.

3. Bown, S.G. (1983) Phototherapy of tumors. *World J. Surg.* **7**, 700-709.

4. Prudhomme, M., J. Tang, S. Rouy, G. Delacretaz, R. P. Salathe and G. Godlewski. (1996) Interstitial diode laser hyperthermia in the treatment of subcutaneous tumor. *Lasers Surg. Med.* **19**, 445-450.

5. Robertson, G. S., M. Thomas, J. Jamieson, P. S. Veitch and A. R. Dennison. (1996) Palliation of oesophageal carcinoma using the argon beam coagulator. *Br. J. Surg.* **83**, 1769-1771.

6. Caspani B., P. R. Cecconi, R. Bottelli, P. Della Vigna, G. Ideo and G. Gozzi. (1997) The interstitial photocoagulation with laser light of liver tumors. *Radiol. Med. (Torino)* **94**, 346-354.

7. Schober, R., M. Bettage, M. Sabel, F. Ulrich and S. Hessel. (1993) Fine structure of zonal change in experimental Nd:YGY laser-induced interstitial hyperthermia. *Lasers Surg. Med.* **13**, 234-241.

8. Haines, D. E. and D. D. Watson. (1989) Tissue heating during radiofrequency catheter ablation: a thermodynamic model and observations in isolated perfused and super-perfused canine right ventricular free wall. *PACE* **12**, 962-976.

9. Haines, D. E., D. D. Watson and A. F. Verow. (1990) Electrode radius predicts lesion radius during radiofrequency energy heating. *Circ. Pes.* **67**, 124-129.

10. Dinerman, J. L., R. D. Berger, and H. Calkins. (1996) Temperature monitoring during radiofrequency ablation. *J. Cardiovasc. Electrophysiol.* 7,163-173.

11. Thomsen, S., J. A. Pearce, and W. Cheong. (1989) Changes in birefringence as markers of thermal damage in tissues. *IEEE Trans. Biomed. Engin.* **36**, 1174-1179.

12. Torres, J. H., T. A. Springer, A. J. Welch and J.A. Pearce. (1990) Limitations of a thermal camera in measuring surface temperature of laser-irradiated tissue. *Lasers Surg. Med.* **10**, 510-523.

13. Zhang, G., S. G. Demos, and R. R. Alfano. (1998) Far-red and NIR emission from tissues. *SPIE Proceeding of Optical Biopsy II* **3250**, 72-77.

14. Bailey, A. J., T. J. Sims, N. C. Avery and C. A. Miles. (1993) Chemistry of collagen cross-links: glucose-mediated covalent cross-linking of type-IV collagen in lens capsules. *Biochem. J.* **296**, 489-496.

15. Post, M. J., A. N. de Graaf-Bos, G. Posthuma, P. G. de Groot, J. J. Sixma, and C. Borst. (1996) Interventional thermal injury of the arterial wall: unfolding of von Willebrand factor and its increased binding to collagen after 55°C heating. *Thrombosis and Haemostasis* **75**, 515-519.

16. Walsh, J. T. Jr., T. J. Flotte, R. R. Anderson and T. F. Deutsch. (1988) Pulsed CO_2 laser tissue ablation: effect of tissue type and pulse duration on thermal damage. *Laser Surg. Med.* **8**, 108-118.

5.6. Figures

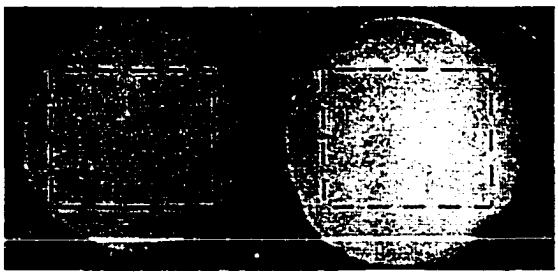

(a)

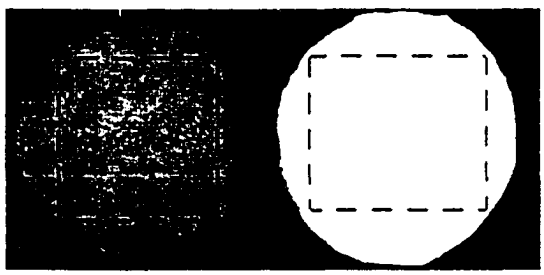

(b)

Figure 5-1 NIR emission spectral images from chicken samples with different thermal treatment temperatures.

The dashed line shows that the emission intensities were obtained inside the square. (a) The non-treated sample is on the left side and the sample treated for 5 min. at 61°C is on the right side. (b) The sample treated 5 min. at 61°C is on the left side and at 97°C is on the right side.

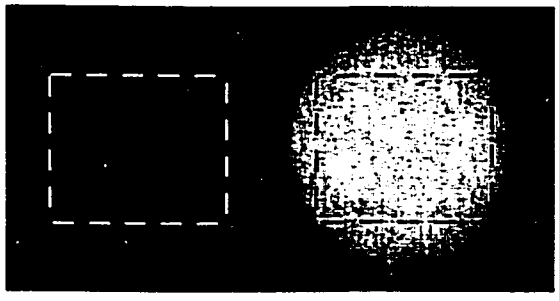

(a)

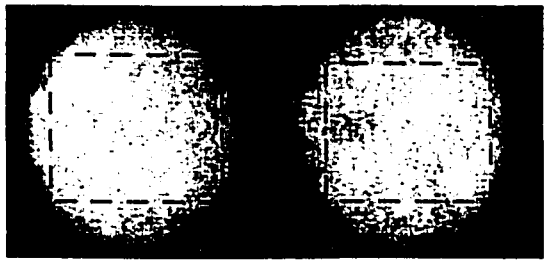

(b)

Figure 5-2 Laser elastic back scattering (632 nm) images from chicken samples with different thermal treatment temperatures.

The dashed lines show that the scattering intensities were obtained inside the square. (a) The non-treated sample is on the left side and the sample treated for 5 min. at 58°C is on the right side. (b) The sample treated 5 min. at 58°C is on the left side and at 97°C is on the right side.

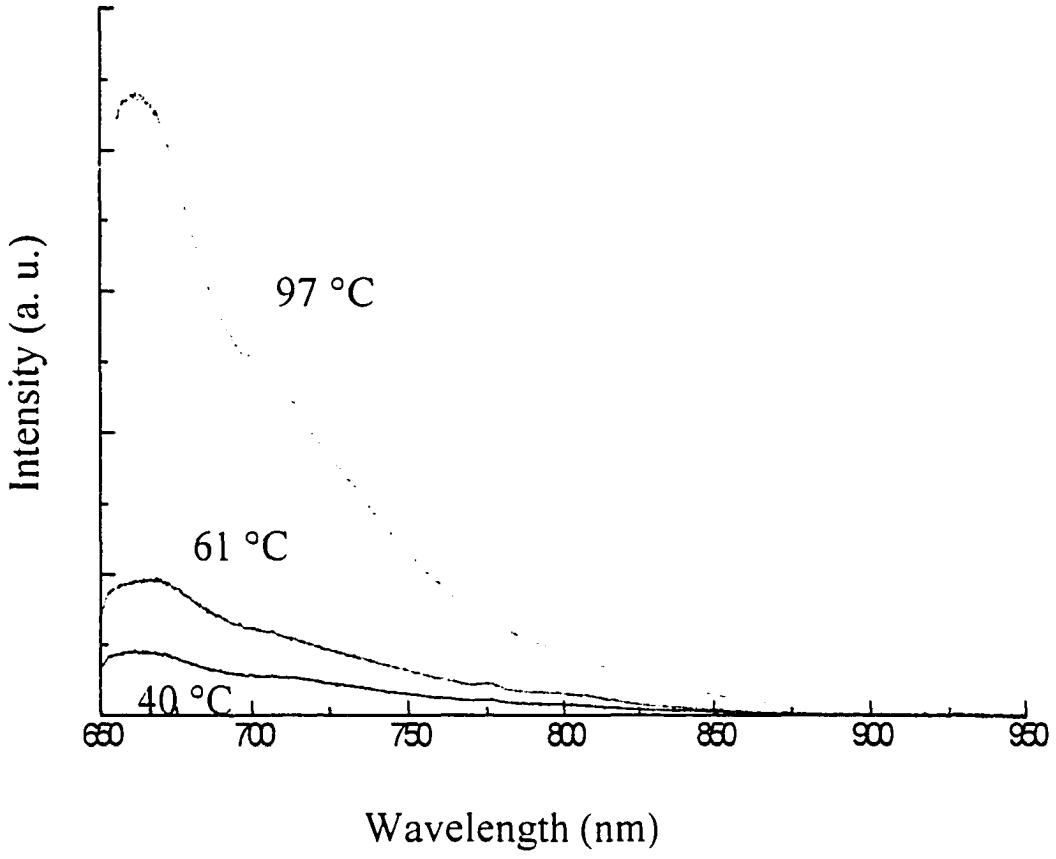

Figure 5-3 Spectral profiles of the NIR emission from chicken tissue samples with different thermal treatment temperatures (40°C, 61°C, and 97°C).

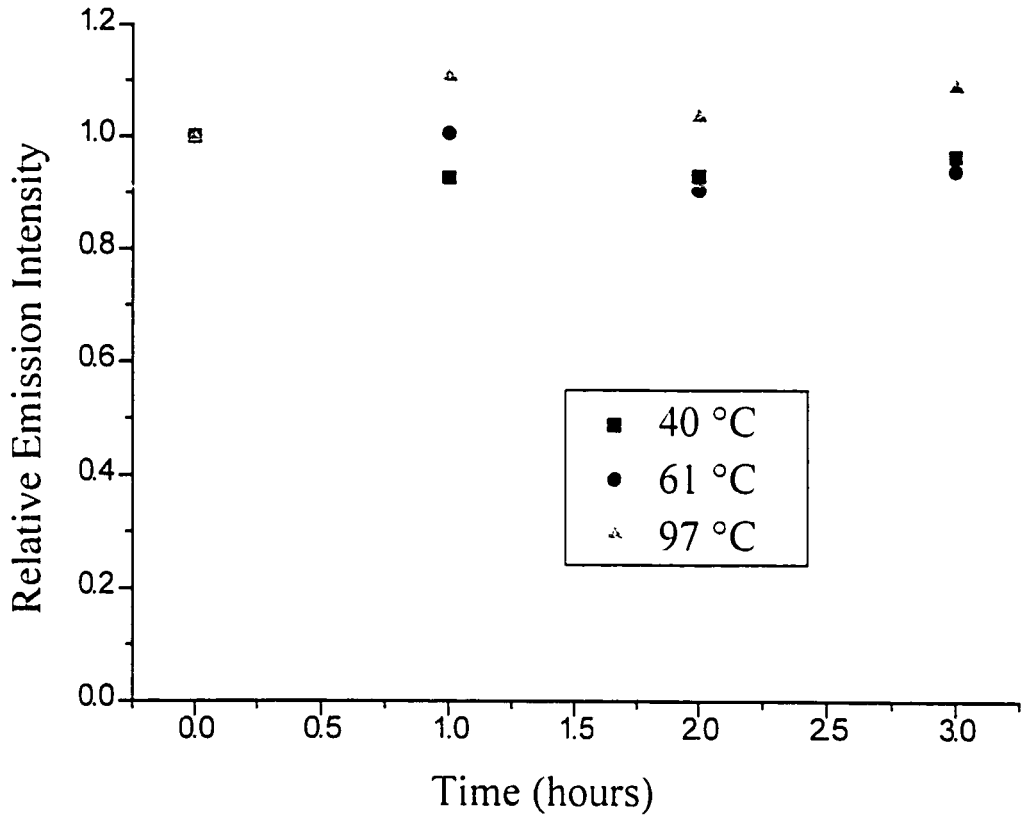

Figure 5-4 Relative intensity changes of the NIR emission from chicken tissue samples heated to different temperatures and measured at times varying from one to three hours after treatment.

There are no statistical differences between the data in each group. The treatment temperatures were 40°C, 61°C and 97°C.

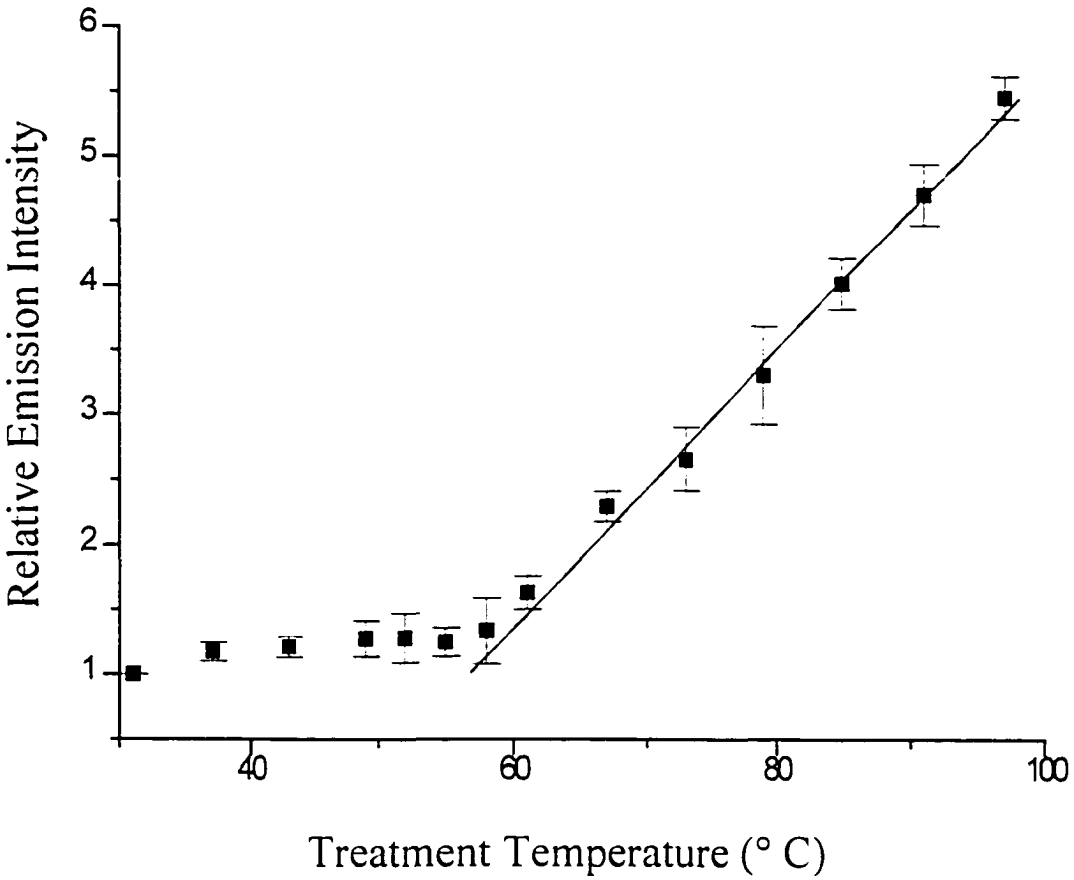

Figure 5-5 Relative intensity of NIR emission from thermally treated chicken tissue samples vs. the treatment temperature.

The data is from the six different muscle samples. The straight line shows the linear fitting result from 55°C to 97°C, To = 55°C.

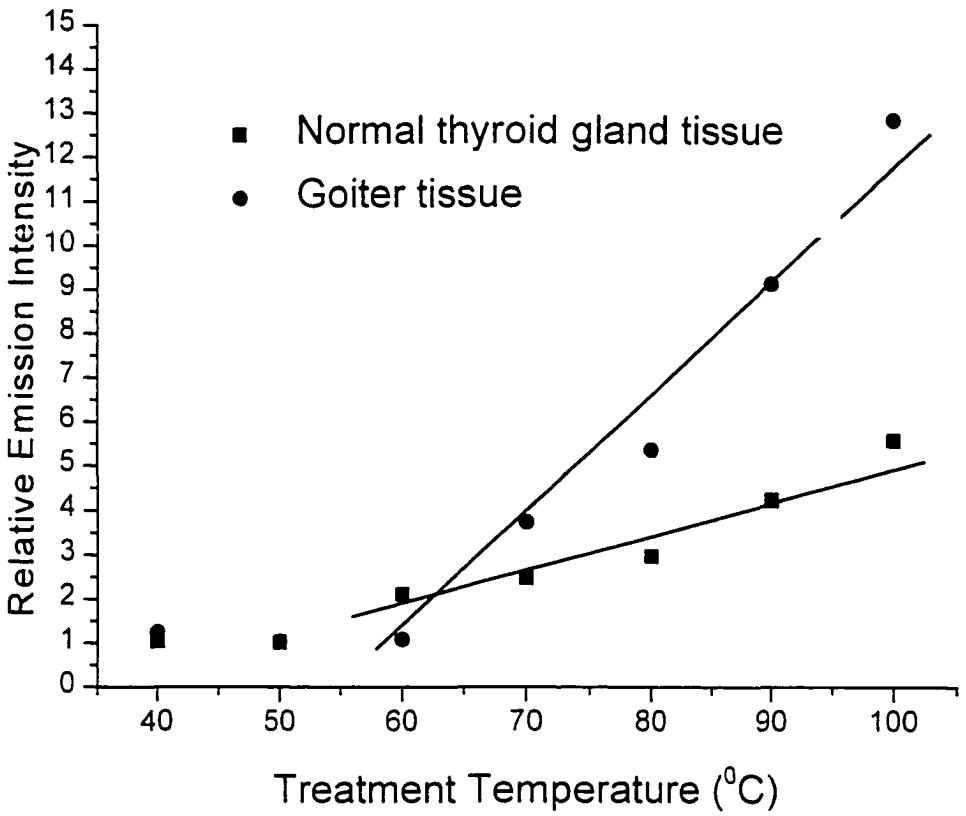

Figure 5-6. The intensity of NIR emission from different temperature treated human normal thyroid and goiter tissue.

The emission intensities obviously increase with the rise in temperatures more than 60°C, but with different increase rates.

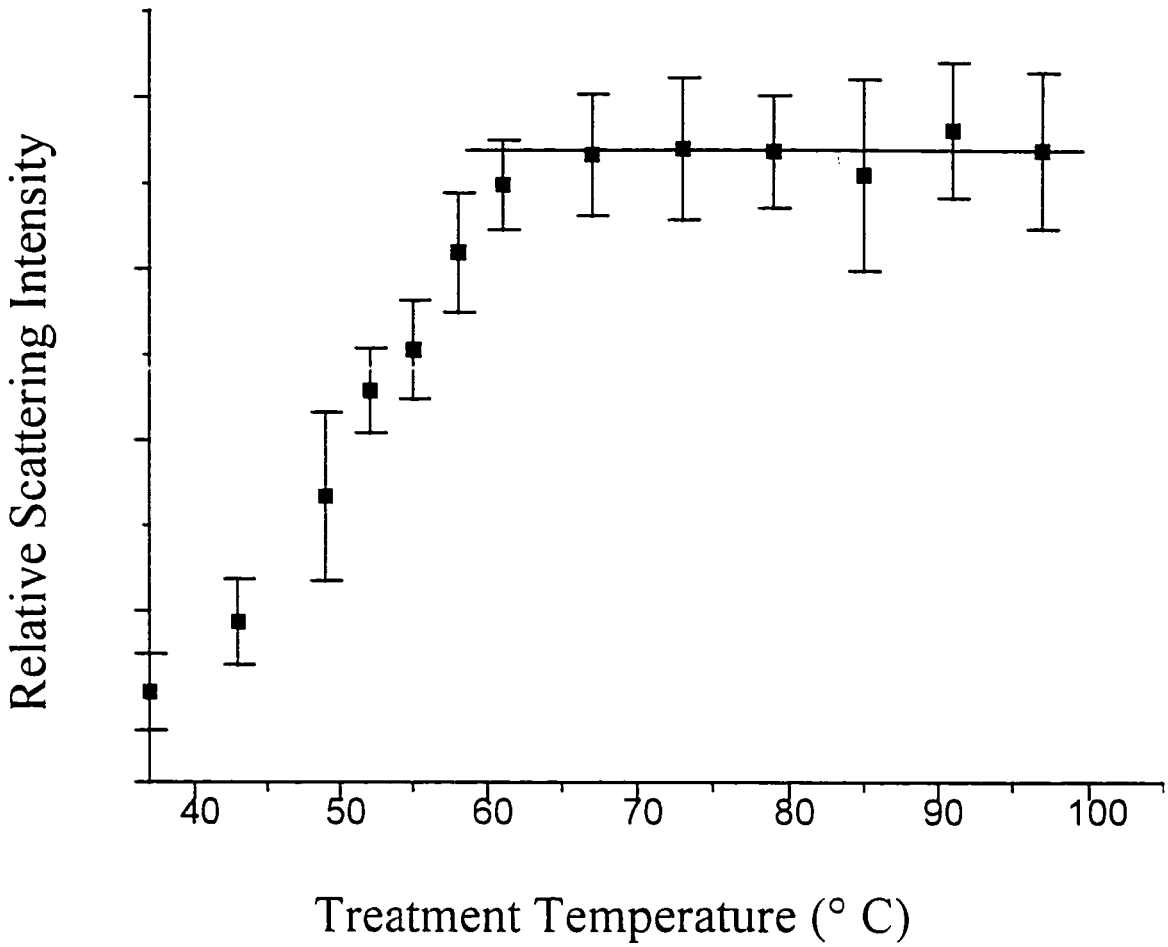

Figure 5-7 Relative intensity of scattering vs. the treatment temperature from thermal treated chicken tissues.

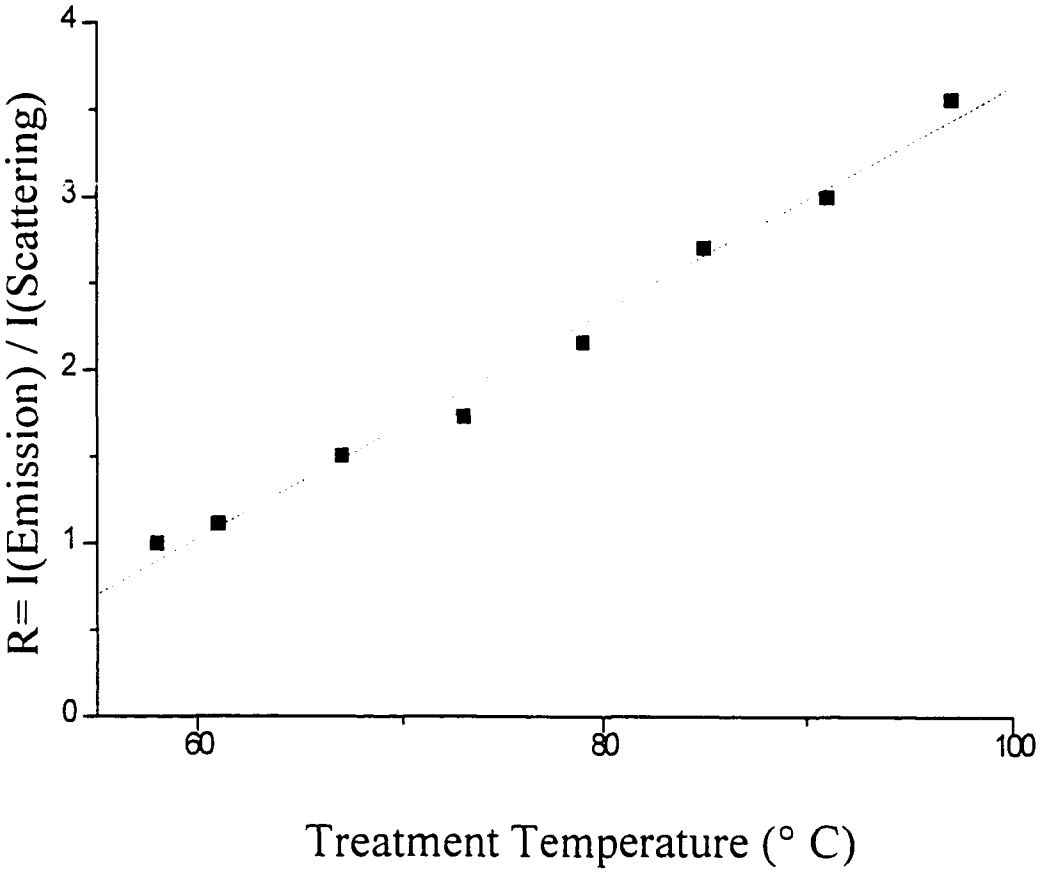

Figure 5-8 The ratio of emission and scattering intensities, R(T), versus temperature for chicken tissues.

The straight line is a theoretical linear fitting from 58°C to 97°C as $R(T) = Ro + br(T - Tro)$, where $T_{r0} = 58°C$ and $br = 0.065 / °C$.

6. Empirical model for far-red to near infrared emission wing from biomedical samples

6.1. Introduction

The spectral wing emission has been shown to yield useful information about the state of biomedical samples [1-5]. The origin of the spectral wing is unknown and still under investigation. This section describes a possible explanation for generation of the far-red emission spectral wing using a simplified model.

To determine the possible origin of the far-red emission spectral wing, different experiments were performed. The first uses a time resolved measurements, which shows that the emission profile consists of nano-second and pico-second components. The far-red emission intensity from the tissue sample was proportional to the excited laser intensity as shown in chapter 4 and the intensity was on the order of Raman signals. As the excitation wavelength was changed and increased from visible into the NIR spectral region, the intensity of NIR emission wing reduced.

In biochemical tissues, there are a lot of molecular components. These biochemical molecules exist in liquid or solid state environments in a tissue. This may induce strong intra-molecular or inter-molecular interactions. At room temperature, many of the energy levels can be coupled together into a broadband continuous energy bands. This continuous energy band consists of coupling electronic, vibrational and rotational modes through the intra-chemical bonds and inter-molecular interactions.

In this section, I will present a speculate model to provide an empirical equation to fit the wing wavelength emission and add some knowledge of the mechanism behind

the emission spectral wing.

6.2. Empirical model

Figure 6-1 shows the continuous energy levels representing the states of organic molecules within the ground state manifold. The molecules will transfer their ground energy state to higher energy level ground state or impurity state after they absorb some photon energy at E_0 (λ_0). The excited molecules will return back to the ground state through optical emission and non-radiative relaxation from upper levels of the manifold. For each excited energy level, such as E_1 shown in Figure 6-1, the energy will be reduced to zero through optical emission transition to the ground state at wavelength λ_1. Energy is transferred to lower energy level at rate **b** by non-radiative relaxation energy transfer. The optical emission intensity for each wavelength is proportional to the population of the excited states $N(\lambda)$ and to the rate of emission defined by the quantum efficiency $Q(\lambda)$ or **k** rate of the emission, from this energy level to the ground state. The emission intensity at certain wavelength can be represented as $I(\lambda) \sim N(\lambda)Q(\lambda) \sim \mathbf{k}(\lambda)N(\lambda)$. Where N and Q are the function of the wavelength. These depend on the particular molecular structure.

In this model, I assume there is a distribution density of the excited energy state and a change in number of excited molecules N in the transition between the energy level that is proportional to the energy interval ΔE. This assumption can be written by a differential equation as follows:

$$dN / N = -b \cdot dE \qquad (1)$$

where N is the population of the excited state at certain energy level, E is the energy state at this level, and b is the transition rate per unit energy per unit state numbers among the

energy levels. This equation is the basis to produce an empirical model equation to fit emission spectral profile.

Solving this differential equation [6], yields:

$$N / N_0 = \exp[-b(E_0 - E)] \tag{2}$$

where N_0 is the initial population of excitation molecules, and E_0 is energy level of the laser line excitation. The excited population N_0 is proportional to the intensity of the laser pump I_0 and to the absorption coefficient of the material. Using Plank the relationship for $E \sim hc/\lambda$, the above result can be rewritten as:

$$N / N_0 = \exp[-bhc(\frac{1}{\lambda_0} - \frac{1}{\lambda})] = \exp(-\frac{bhc}{\lambda_0} \cdot \frac{\lambda - \lambda_0}{\lambda}) \tag{3}$$

We define $B \equiv \exp(-bhc / \lambda_0) < 1$, which represents the population distribution of different energy levels, and λ_0 is the excitation laser wavelength. With the relationship $\exp(a \cdot b) = (e^a)^b$, the eq. 2 can be written as:

$$N(\lambda) = N_0 B^{[(\lambda - \lambda_0)/\lambda]} \tag{4}$$

The observed optical emission intensity $I(\lambda) = kN(\lambda)$ taking the form:

$$I(\lambda) = A(\lambda) B^{[(\lambda - \lambda_0)/\lambda]} + C, \tag{5}$$

where $A = Q(\lambda) * I_0$ is the product of emission efficiency and intensity of the excitation laser power, C is the base line change during the practical measurement. For a simple assumption, the emission quantum efficiency could be constant, that is $Q(\lambda) = Q$.

The above result can be written to quasi-empirical "master" NIR spectral wing equation:

$$I(\lambda) = AB^{[(\lambda - \lambda_0)/\lambda]} + C \tag{6}$$

In the above equation (6), the parameter A is proportional to the emission intensity from the sample point. If the experiment condition is same, the parameter A could be used to compare the relative emission efficiency in the samples. The parameter B will determine the shape of the curve; larger B value could induce more flat curve shape. The parameter C is a constant residue of fitting curve from experiment data. The shape of wing follows "master" equation (6) $I_{wing}(\lambda) \sim B^{(\lambda-\lambda_0)/\lambda}$.

6.3. Simulation of wing using master equation

Figure 6-2 shows the dependence of simulation emission spectral profiles using the above master wing equation (6) for different parameter A and B. Figure 6-2a shows the curves with a different parameters A by a factor of 2, but keeping the parameter B in constant. Figure 6-2b shows the curves with different parameter B by factor of 10, but keeping parameter A in constant. The emission profile could be affected by some other kind of factors: the Raman peak information that could be superposed on the background of the spectral wing profile; the self-absorption factor in the sample at certain wavelength could decrease the practical emission efficiency. These will induce the decrease of emission intensity and change the spectral profile during the practical data collection.

6.4. Curve fitting result from experiment data

We will use the "master" equation (6) to fit wing from tissues and molecules. Tissue basically consists of various components, such as water, proteins and fat. The protein molecules are main part in the soft tissue and have many molecules bonds and large molecular weight. The main contribution of the smooth spectra background of the soft tissue could come from the protein molecules, membranes, and other impurities.

6.4.1. Fitting emission wing spectra from pure protein samples

The wing spectral curves from pure protein samples are obtained under 632 nm laser excitation (elastin, high density lipid-protein (HDP), low density lipid-protein (LDP), and collagen, which is obtained from Sigma Co.). The far-red emission spectrum of typical protein, such as collagen IV and LDP, under 632 nm laser excitation is shown in Figure 6-3 respectively compared to the model curve fitting. The fitting parameters A and B from different type of proteins are listed in Table 6-1. It is clear to see good fittings of spectral wing for the protein from Table 6-1 and Figure 6-3. The correlation R^2 values are higher than 0.85.

6.4.2. Fitting emission spectra from thermal damaged tissue samples

The wing spectral profile from thermal damaged chicken muscle tissue under 632 nm laser excitation can be fitted by the model equation (6). The fitting parameters A and B are listed in Table 6-2. The related data with fitting curves are shown in Figure 6-4. The higher spectral wing intensity is generated from the stronger thermal damage by higher temperature treatment. The cross correlation value R^2 between data and fitting curve is higher than 0.83 for all of these thermal treated tissues. The curve-bending factor B is slightly going down followed by the thermal damage decrease on tissue samples in the low temperature damaged region.

6.4.3. Fitting emission wing spectra from human breast tissue samples

The model was used to fit the emission wing spectra profile of human breast

tissue samples with 632 nm and 800 nm laser excitation. Figure 6-5 shows the typical emission spectral wing profile from human breast tissue sample with curve fitting under 632 and 800 nm laser excitation. Figure 6-5a shows emission curves of normal and cancer breast tissues under 632 nm laser excitation. The higher spectral intensity appears from cancer tissue than from normal tissue. Figure 6-5b shows the emission curves from same tissue under 800 nm laser excitation. The emission efficiency of cancer tissue is stronger than the normal tissue as well. This difference induces the fitting parameter A from cancer tissue is higher than from the normal tissue. The fitting parameters A and B are listed in Table 6-3. The model curves that are generated closely fit the data curves in the spectral wing region under both 632 and 800 nm laser excitation.

6.5. Discussion

From simulations, the parameter A is proportional to the integrated intensity of the emission curve. Under an identical experiment condition, the parameter A can be used to compare the quantum efficiency among the samples. The parameter B determines the curvature of the fitting curve. It has much lower contribution to affect the total intensity of the emission. The parameter B represents the probability of the energy transfer from higher energy level to lower energy level through the excited molecules. The higher transfer rate between the energy levels leads the smaller difference of excitation population between the energy levels, which is the flatter shape curve with higher B value. The lower transfer rate between the energy levels induces the higher difference of excitation population between the energy levels, which is the bending shape curve with lower B value.

Most of the correlation value, (R^2), between the fitting and data curves are higher

than 0.83. These indicate the theoretical fitting curve pretty close to the wing emission curve. The only exception happens on the emission curve of normal breast human tissue with clear Raman peaks under 800 nm laser excitation. The R^2 value is still more than 0.5. The fitting curve could be used as a base line to subtract out the background from the raw data to get clear Raman spectrum.

The fitting result of wing emission from thermal damaged tissue sample indicates the higher temperature thermal damage leads higher parameter A from the fitting curve. This represents the quantum efficiency of the emission proportional to the thermal damage. The parameter B of the curve fitting is lower followed by the sample with higher treatment temperature on the sample. The lower value of parameter B indicates the decrease of the energy transfer efficiency of non-radiative relaxation of the excited molecules. The reduced B value may be correlated with the decrease number of non-radiation energy transfer channels. From above result, it could assume that the numbers of non-radiation relaxation channels are decrease by the tissue sample microstructure change in molecular level (e.g. protein folding and unfolding, and so on). Under identical excitation condition, the molecules force more energy through the radiation channels to reach their equilibrium status since the reduced number of the non-radiative relaxation channels. This could lead the radiation efficiency increase and induce higher value of parameter A from curve fitting.

The similar results are obtained from the wing emission of human breast tissue samples. The parameter A has higher value from cancer sample than from the compared normal sample. The parameter B has lower value from cancer sample than from normal sample. This may indicates that the non-radiative channels are more in normal sample

than in cancer sample.

In summary, the empirical model was used to fit emission spectra wing in order to match the spectral wing emission curves from tissue samples. Using the fitting parameters A and B, the experiment result could be quantitatively used to analyze the optical properties of the biomedical samples. This method could also be used to generate a spectral base line by fitting the emission spectral curve to extract the Raman lines. The possible reason of the spectral wing could be quadrapole induced energy levels in the ground state from impurities of biomedical sample. The higher emission efficiency with more curvature shape spectra could induce higher value for the parameter A with lower value parameter B. This could be induced from the lack of numbers of non-radiative relaxation channels in molecules.

6.6. References

1 Frank C J, McCreery R L, and Redd D C B, "Raman spectroscopy of normal and diseased human breast tissues", Anal. Chem. 67(5), 777-783, (1995).

2. Hanion EB, Itzkan I, Dasari RR, Feld MS, Ferrante RJ, McKee AC, Lathi D, Kowall NW, "Near-infrared fluorescence spectroscopy detects Alzheimer's disease in vitro", Photochem. Photobiol. 1999 Aug;70(2):236-42

3 Zhang, G., S. G. Demos, and R. R. Alfano. (1998), "Far-red and NIR emission from tissues," *SPIE Proceeding of Optical Biopsy II* **3250**, 72-77.

4 Zhang, G., S. G. Demos, and R. R. Alfano. (1999) "Far-red and NIR spectral emission from tissues under 532 and 632 nm photo-excitation", *Lasers in Life Sci.* 9(1) 1-16.

5 Zhang, G., Tang, J., Ho, P. P., and Alfano, R. R. (2000) "Probing thermal damage and monitoring the treatment temperature of tissues using the near-infrared emission wing", *Lasers in Life Sci.* 10(1), 95-109.

6 "Advanced Calculus for Applications", by Francis B. Hildebrand, 2nd Edition, pp 6-31, Prentice-Hall, Inc., 1976.

6.7. Tables

Table 6-1 Fitting parameters for far-red emission spectra profiles from some protein samples under 632 nm laser excitation.

Proteins	A ($x10^{3}$)	B ($x10^{-6}$)	R^2
Elastin	113.4	1.1	0.867
HDP	87.6	0.67	0.867
LDP	42.0	0.26	0.887
Collagen I	2.3	330	0.884
Collagen II	25.5	60	0.873
Collagen III	2.1	230	0.884
Collagen IV	3.7	4.05	0.886
Collagen V	23.4	0.18	0.851

Table 6-2 Fitting parameters for far-red emission spectral profiles from thermal damaged tissue samples with different treatment temperature.

Temperature	A ($x10^3$)	B ($x10^{-6}$)	R^2
40° C	1.6	60	0.858
61° C	3.7	50	0.849
97° C	17.4	4.5	0.832

Table 6-3 Fitting parameters of far-red emission spectral profiles from a pair of human breast tissue samples with 632 and 800 nm laser excitation.

	632 nm			800 nm		
Tissue Sample	A ($x10^3$)	B ($x10^{-6}$)	R^2	A ($x10^3$)	B ($x10^{-5}$)	R^2
Cancer	5.6	5.7	0.903	6.4	37	0.894
Normal	1.1	140	0.89	5.0	8	0.551

6.8. Figures

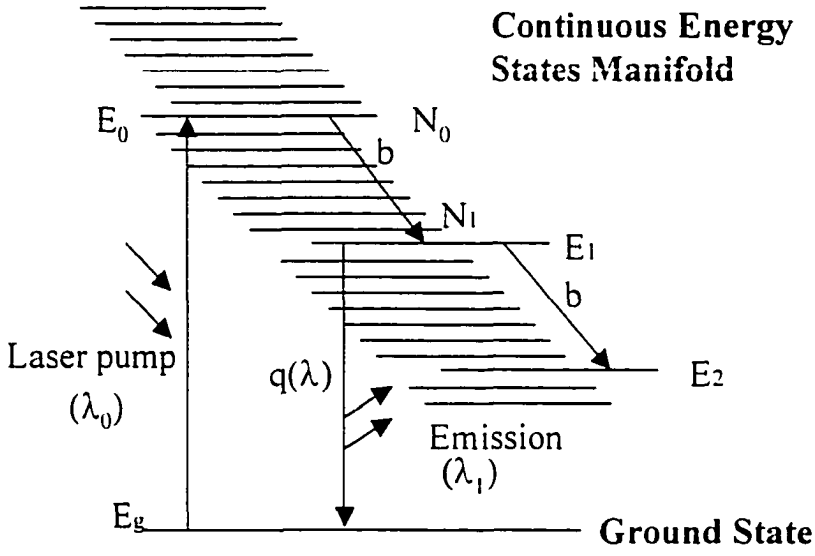

Figure 6-1 Continuous state diagram of energy levels and the diagram to explain the wing spectra wavelength dependence where E_g ground energy level, E_0 an excited energy level, E_1 middle energylevel, $q(\lambda)$ wing emission light quantum efficiency, λ_0 pumping wavelength, N population at certain energy level, λ emission wavelength, and b non-radiative energy transfer rate between energy levels.

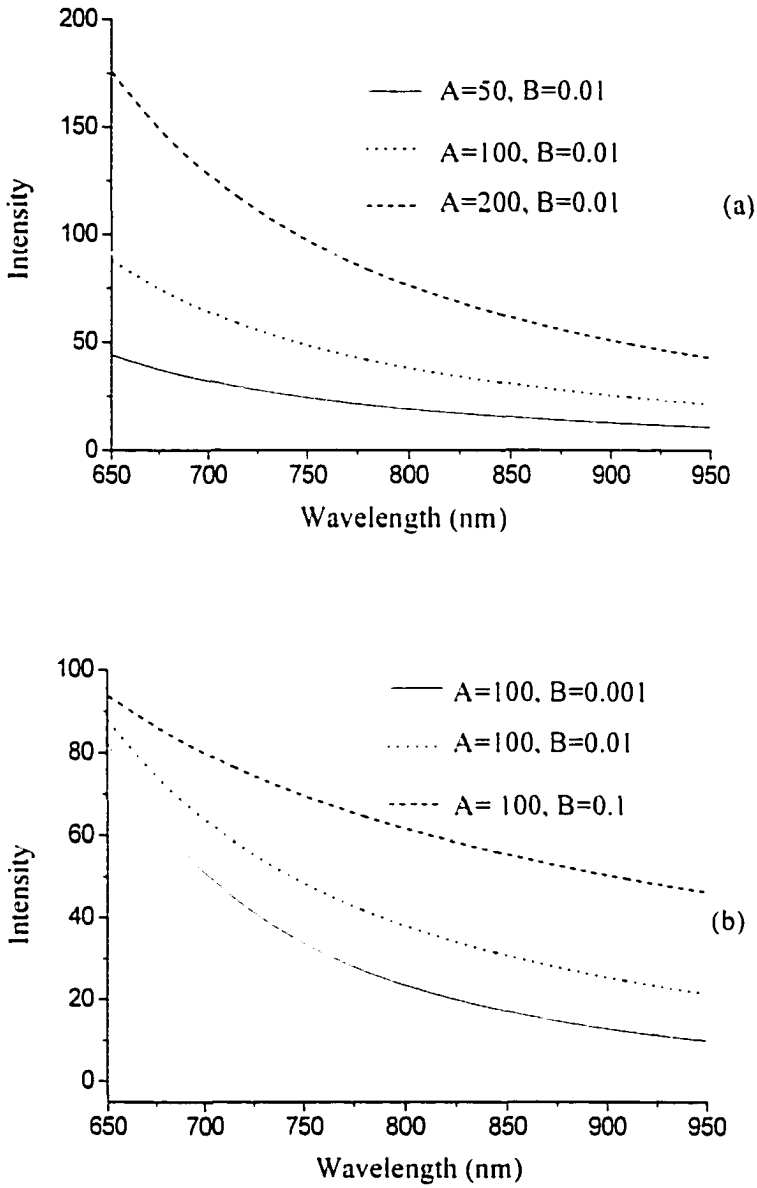

Figure 6-2 Master equation spectral profile for the NIR emission with different parameters (A and B).

a) shows different A values in factor of 2 with same B value parameters, and b) shows same A values with different B values.

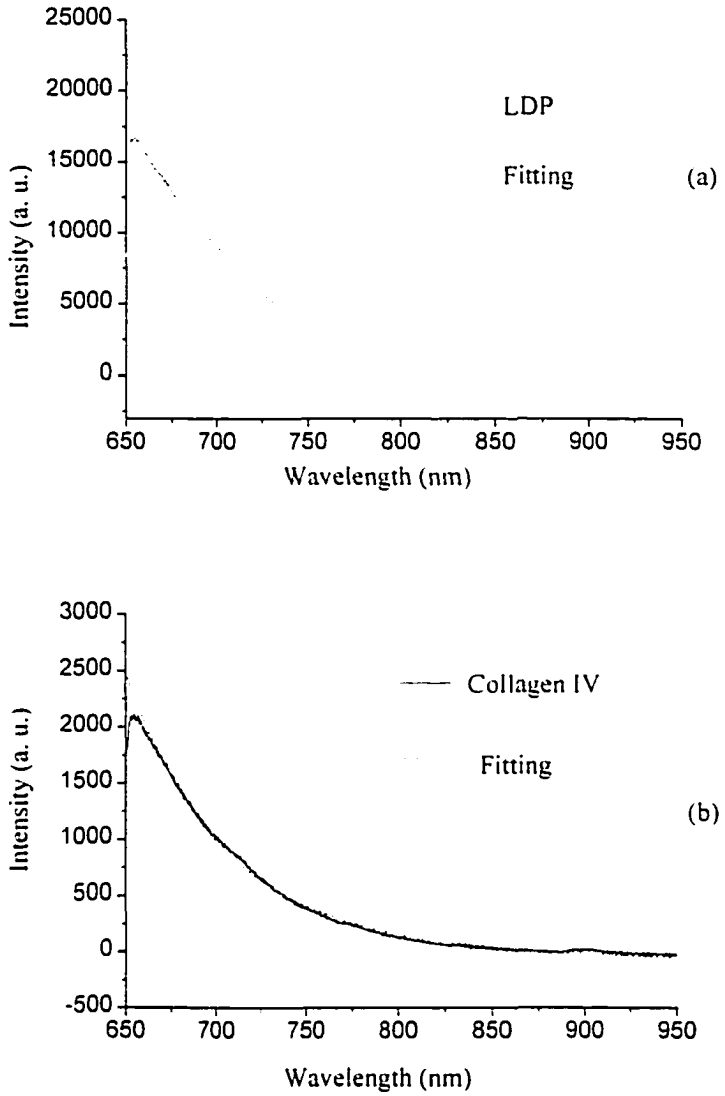

Figure 6-3 Emission profiles from protein samples with curve fitting using master equation.

The solid line represents experiment data and the dashed line represents the fitted curve. a) LDP spectrum, b) collagen IV spectrum. The fitting values for A and B are listed in Table 6-1.

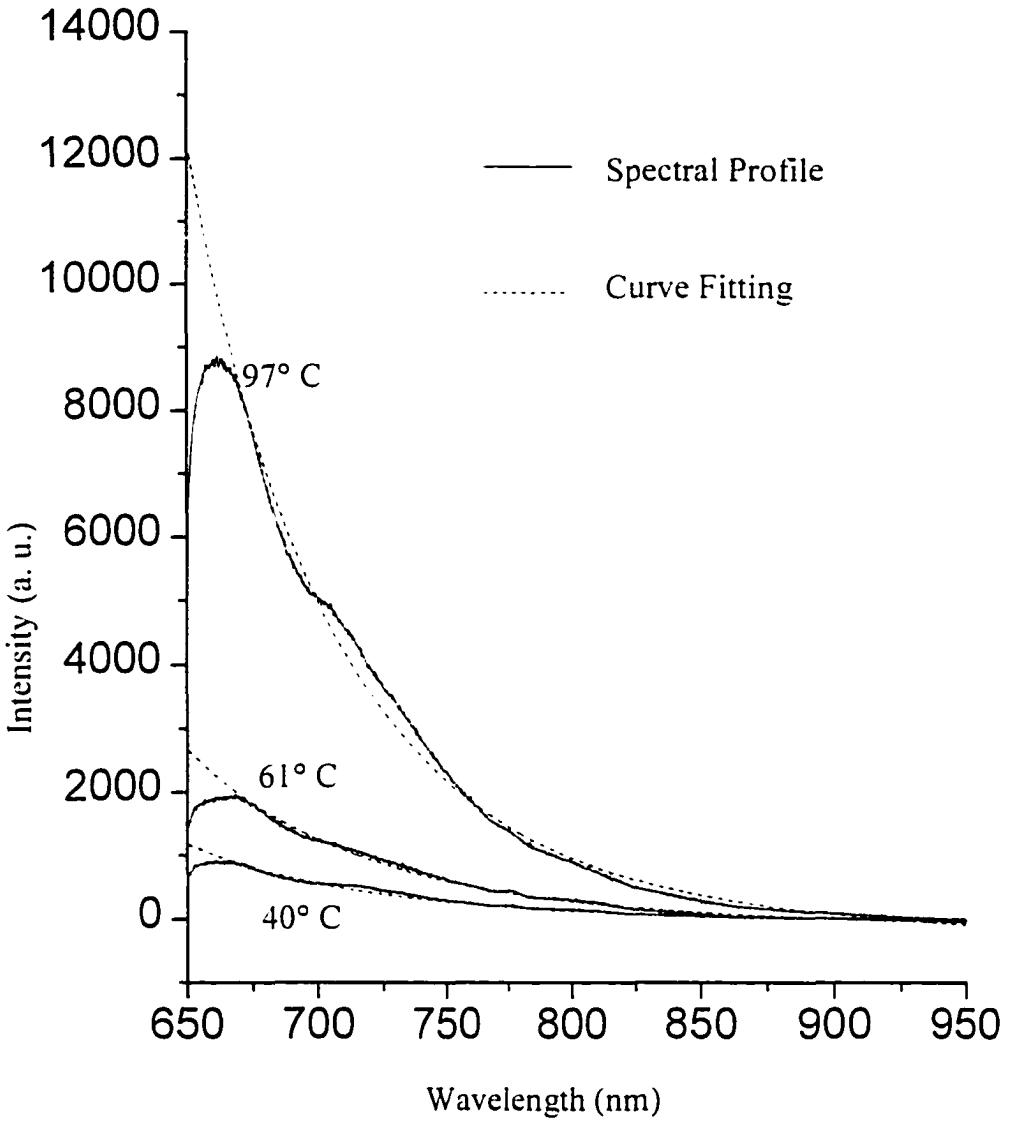

Figure 6-4 Emission profiles fitting using master equation (Eq. 5) from thermal damaged chicken tissue under different temperature treatment (40° C, 61° C, and 97° C). The solid line represents experiment data and the dashed line represents the fitted curve. The fitting value A and B are listed in Table 6-2.

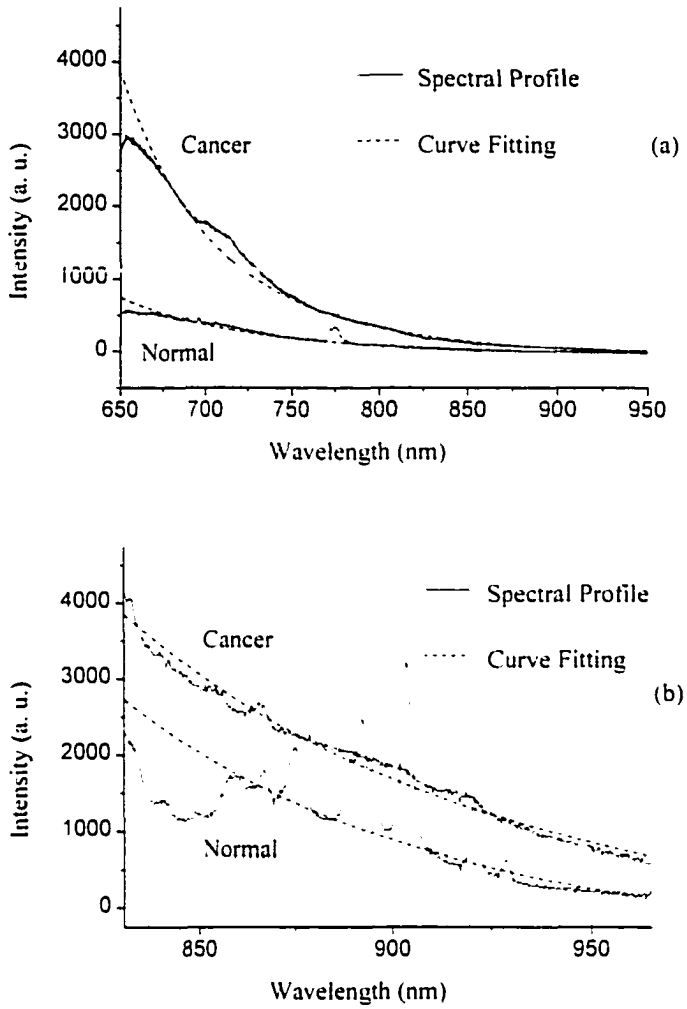

Figure 6-5 Emission profiles fitting from human breast tissue under 632 nm and 800 nm laser excitation using master equation.

The solid line represents experiment data and the dashed line represents the fitted curve to equation 5. a) Normal and tumor breast tissue spectral profile under 632 nm excitation with curve fitting. b) Normal and tumor breast tissue spectral profile under 800 nm laser excitation with curve fitting. The fitting values for A and B are listed in Table 6-3

7. Correlation in piglet brain hemodynamic study with frequency modulation and continuous wave NIRS methods

7.1. Introduction

Cerebral hemodynamics and oxygenation studies in humans and animals have demonstrated the importance of the pathogenesis of perinatal "hypoxic-hemodynamic" brain injury leading to cerebral palsy, mental retardation, and seizures [1-4]. Monitoring of these disturbances at the bedside would be the first step in the prevention and treatment of brain injury [5]. Optical spectroscopy has shown the potential to provide continuous monitoring of brain perfusion and oxygenation in real-time at the bedside [5-13].

Optical spectroscopy uses near infrared light to non-invasively monitor brain concentrations of oxy-hemoglobin and deoxy-hemoglobin [11, 14, 15]. For optical spectroscopy, hemoglobin is a contrast agent. Any change in its concentration, optical spectroscopy detects the change in tissue perfusion and oxygenation.

Although the majority of the available optical instruments has been tested in phantoms, animals, and humans, and validated with the available diagnostic techniques [5, 11, 15, 16], the question still exists whether or not, and under what conditions, data obtained by different optical instruments would be comparable.

The purpose of this part of thesis is to find the validation of our method to investigate the hemodynamics of human brain during sleep and wake transition in normal

healthy subject and on sleep disordered patients (see chapter 8 and 9) with CW NIRS device. 6 newborn piglets were used to investigate whether or not cerebrovascular changes recorded in vivo by continuous wave (CW) type instrument would be comparable to those recorded by frequency domain (FD) type instrument. The hypothesis is that the CW type instrument (City College of New York) would be sufficiently sensitive to detect both small and large changes in brain hemodynamics and oxygenation, and that its sensitivity would be comparable to that of the FD type instrument (University of Illinois - ISS, Urbana-Champaign).

7.2. Material and methods

7.2.1. Optical probes set up on the head of newborn piglet

The optical fiber probes of the CW type device were positioned perpendicular to the scalp surface. The source-detector line was centered on the left side of the piglet head, 1.5 cm from the midline (see Figure 7-1a). The collection fiber for the CW probe was fixed by a metal plate 0.6 cm from the head. This distance provided visualization of the optical coupling between the fibers and the head. Guide holes in the plate held the excitation fiber in contact with the scalp. In this fashion, good optical contact on the skin was achieved, while the fibers were prevented from retracting away from the piglet head. This maintained the flexibility necessary to adapt the optical probe to the curved surface of the piglet head.

The optical probe of the FD type device consisted of 8 emitter fibers and 1 detector fiber-optic bundle arranged at four different source-detector distances ranging from 1.48 to 2.98 cm (Figure 7-1a). The estimated sampling volume of this probe falls

between the minimum of 1.5 cc (1.5 cm length, 1 cm depth, 1 cm width) and the maximum of 12 cc (3 cm length, 2 cm depth, 2 cm width). A medium value of 5 cc (2.5 cm in length, 1 cm in depth, 2 cm in width) would be the most realistic sampling volume of the probe [17] (Stankovic *et al* 2000). One light source is then turned on and light passes from one emitter fiber, through the tissue and into the collector. After the termination of the measurement, the next light source is turned on, and the process goes on as above. A measurement cycle is complete when all 8 light sources have been sequentially turned on and measured.

There was no cross talk detected between these signals from two instruments taking data simultaneously, since the ISS instruments worked with very different modulation frequencies and decoded the signal with lock-in amplifiers at modulation reference frequency. The detailed information about the NIR optical devices is described in chapter 3.

7.2.2. Statistical Analysis

The goal of comparison studies is to determine whether the two methods agree sufficiently to be used interchangeably. In our study, the correlation analysis was used to assess the strength between the CW and FD measurements. The correlation coefficient (r) defines both the strength and the direction of the linear relationship between the measurements obtained by the two methods.

For a quantified comparison of the related data from the two different instruments, the cross correlation factor, r, has been used to find how close the data pairs are from the same subject in the experiment. r can be defined as follows [18]:

$$r = \frac{\Sigma(x - \bar{x})\Sigma(x - \bar{y})}{\sqrt{\Sigma(x - \bar{x})^2 \Sigma(y - \bar{y})^2}} \quad (1)$$

where x and y are the data obtained from different sources. The value of r will be from –1 to 1. $r > 0$ is positive correlation, $r < 0$ is negative correlation, and $r = 0$ means no correlation for the two data sets.

7.2.3. Animal Model

This animal study was approved by the Institutional Review Board (IRB) at the Winthrop University Hospital, State University of New York at Stony Brook, Mineola, NY. The animals were treated in accordance with the Guide for the Care and Use of Laboratory Animals by the Institute of Laboratory Animal Resources, National Research Council (NIH Guide, Vol. 25, n. 28, Aug. 16, 1996). The animal model used for this study has been previously described in the literature [10, 19]. Briefly, a total of six 9.3± 1.9 day old newborn piglets of either sex, weighing 2.45 ± 1.09 kg were sedated with ketamine 20 mg/kg mixed with xylazine 4 mg/kg, IM, intubated, and ventilated with an infant ventilator (Bear Medical Systems Inc., Riverside, CA). General anesthesia was maintained by a continuous intravenous infusion of propofol at a concentration of 0.8 mg/ml at 4 - 8 mg/kg/hr. Both abdominal aorta and inferior vena cava were catheterized to provide direct monitoring of the arterial blood pressure (Hewlett Packard 78353B, USA) and gases (Ciba - Corning 238 pH - Blood Gas Analyzer, Medfield, MA) and IV D5W / propofol infusion, respectively. Heart rate and arterial oxygen saturation were monitored by pulse oximetry (Nellcor, Hayward, CA) with the probe attached to the pig's tail. The core temperature was maintained at 37°C with the use of a heating blanket and continuously monitored by a rectal thermometer. To achieve a motion-artifact-free

environment, the pre-shaved animal's head was secured within a stereotaxic instrument (Lab Standard 51600, Stoelting, Wood Dale, IL) with two 18° ear bars and a nose clamp. The manipulator arm of the stereotaxic instrument allowed for three-dimensional positioning of the CW and FD optical probes and an optimal probe-to-scalp contact. The CW and FD optical fibers were positioned perpendicularly to the right and left scalp surface, respectively. No resuscitation was required at any time. At the end of the study, all piglets were sacrificed by an overdose of sodium pentobarbital (500 mg intravenous injection).

7.2.4. Experimental Protocol

After a period of stabilization for the piglet, the ventilation was adjusted to assure the normal values of the arterial blood gasses (Figure 3, Field 1). Then the baseline optical (DC, AC, ϕ, μa, $\mu s'$, HbO_2, Hb, and Hbt) and conventional variables, meaning mean arterial blood pressure (mm Hg), heart rate (beats per minute), arterial blood gases (PaO_2 and $PaCO_2$, in mm Hg), pH, and arterial oxygen saturation (SaO_2) were recorded. CO_2 is a potent vasodilator. In contrary, every decrease in $PaCO_2$ (hypocarbia) causes vasoconstriction, while a decrease in O_2 (hypoxia), along with an increase in CO_2 (hypercarbia) causes vasodilatation. In our study the arterial pH, O_2, and CO_2 were manipulated by increasing or decreasing the number of respirations per minute, hyper or hypoventilation, respectively. Changes in brain perfusion and oxygenation, associated with hyper- and hypoventilation, as detected by the two oximeters, were classified as subtle (Figure 3, Part A, Fields 1-6), as opposed to the large changes accompanying lethal injection of sodium pentobarbital (Figure 3, Part B, Field 7). Lethal sodium pentobarbital injection causes cardiac arrest, cessation of cerebral blood flow, and terminal brain

asphyxia, followed by cell death as a consequence of hypoxia. As we have previously reported, terminal brain asphyxia is a valuable source of optical information [10].

7.3. Results

Table 7-1 summarizes the systemic physiological data obtained from 6 animals. All the systemic changes were accompanied by the changes in brain hemodynamics and oxygenation, as detected by both CW and FD optical instruments. As for the optically detected brain perfusion – oxygenation changes, all animals responded to the ventilation changes and the cardiac arrest with a great deal of reproducibility (Table 7-2, Figure 7-2). Optical tracings were divided into two segments, phase A and phase B, according to the magnitude of changes (subtle changes – phase A, large changes - phase B). Figure 7-2 illustrates typical systemic and optical changes (FD instrument) recorded in one animal.

In Figure 7-3, we compare the raw (Dc) data recorded by the CW instrument at 780 and 830 nm with the source detector separation of 3 cm, with the result from the FD instrument at 758 and 830 nm with the source-detector separation of 2.98 cm. In Figure 7-4 we compare the processed data (Hb, HbO_2, and Hbt) recorded by the CW instrument (at 780 and 830 nm, (source detector separation 3 cm) and the FD instrument (at 758 and 830 nm, the multi-distance approach).

Hyperventilation (an increase in the respiratory rate) caused a decrease in $PaCO_2$, MAP, and HR, as well as an increase in pH, without affecting PaO_2 and SaO_2 (Table 7-1, Figure 7-2). In the brain, hyperventilation caused positive changes in Dc at 758/780 nm, negative changes at 830 nm (Figure 7-3 fields 1, 2, and 3), and consecutively an increase in Hb, and a decrease in HbO_2 , Hbt, and tissue saturation (Figure 7-2, Figure 7-4 - fields 1, 2, and 3).

Hypoventilation (a decrease in the respiratory rate), on the other hand, caused an increase in $PaCO_2$, and a decrease in HR, MAP, PaO_2, pH, and SaO_2 (Table 7-1, Figure 7-2). In the brain, hypoventilation caused negative changes in Dc at 758/780 nm, positive changes at 830 nm (Figure 7-3 - fields 4 and 5), and consecutively an increase in Hb and Hbt, and a decrease in HbO_2 and tissue saturation (Figure 7-2, Figure 7-4 - fields 4 and 5).

Cardiac arrest and apnea caused a further increase in $PaCO_2$, as well as a decrease in HR, MAP, pH, O_2 and SaO_2 (Figure 7-2). In the brain, cardiac arrest and apnea caused further negative changes in Dc at 758/780 nm, positive changes at 830 nm (Figure 7-3 - fields 6 and 7), and consecutively, an increase in Hb and Hbt, and a decrease in HbO_2, Hbt, and tissue saturation (Figure 7-2, Figure 7-4 - fields 6 and 7).

Table 7-2 shows the correlations between the raw (Dc) CW and FD data (Table 7-2 - columns 2 and 3) and the processed CW and FD data (Table 7-2 – columns 4, 5, 6). As for the raw data, an excellent correlation between the CW and FD instruments was noted at all wavelengths. As for the processed data, an excellent correlation was noted only during the phase A (in all 6 animals).

Scattering changes (ISS FD Oximeter) were associated only with asphyxia and death (Figure 7-5 – fields 6 and 7).

7.4. Discussion

The brain is critically dependent on oxygenation for function and viability. The critical point in the prevention of neonatal brain injury would be the maintenance of cerebral perfusion through prevention of severe hypotension and avoidance of marked cerebral vasoconstriction that can be induced by hypocarbia [20]. This and several other

studies have shown that optical spectroscopy can play a critical role in the recognition and detection of disturbances in cerebral hemodynamics and oxygenation associated with changes in blood oxygenation and CO_2 [10, 16, 21-23].

Continuous wave spectroscopy is based on several assumptions: 1) that HbO and Hb are the dominant tissue chromophores 2) that the background attenuation does not change during the course of experiment, 3) that tissue is optically homogenous with no regional variations in absorption or scattering, 4) that the spatial distribution of HbO_2 and Hb will remain constant during the experiment, 5) that there is a negligible contribution from the extracerebral hemoglobin (scalp and skull) to the NIRS signal, 6) that the physical geometry of the optical probe will remain constant, and 7) that tissue scattering characteristics are known and will remain constant throughout the experiment [11]. It is clear that deviations from these assumptions are likely to lead to significant error [11].

Over the past several years significant validation efforts have been made. Optical spectroscopy has been validated with sagittal sinus [33] and jugular vein blood sampling [22, 34], ^{133}Xenon clearance [21, 35, 36], vascular Doppler techniques [16, 37, 38], radioactive-labeled microspheres [5, 36], computer tomography [38], magnetic resonance spectroscopy [39] and imaging [38]. Still, the single high priority goal defined by the 1992 NIH-NINDS Workshop on Near Infrared Spectroscopy, that said: "... data should be comparable between different NIRS instruments and methods ...", [13] has not been sufficiently addressed so far. Whatever, this study is, to our knowledge, one of the very few studies to correlate CW and FD methods. Ferrari has demonstrated the agreement between the measurements in the muscle (ischemia) and in the brain (postural changes) obtained with the FD (first generation ISS spectrometer, i.e., OMNIA, ISS, Champaign,

IL) and the CW instrument (NIRO 500, Hamamatsu Photonics, Japan) (Ferrari *et al.* (1995) and Grubhofer *et al.* [40, 41] compared two continuous wave oximeters, namely INVOS 3100 and NIRO 500, during and after hypocapnia in 15 awake, healthy volunteers, who were hyperventilated to obtain end-tidal CO_2 values of approximately 20 mm Hg. The authors correlated their optical results with end-tidal CO_2 values. They found that cerebral hemoglobin oxygenation states were reflected more accurately by INVOS 3100 than NIRO 500. They speculated that the cause may be the different technology of the monitors, since INVOS 3100 eliminates the contribution of extracranial oxygenation [41].

Our results have shown an excellent correlation between the two DC signals at 758 (FD), 780 (CW) and 830 (FD and CW) (Table 2 – Columns 2 and 3, Figure 4). The correlation between the processed data (hemoglobin changes) was high only during the events associated with no change in μ_s (Figure 6) and subtle changes in μ_a (Table 2, Columns 4,5, & 6). The differences could be attributed to the differences in sampling volumes of the CW and GD probes as well as the structural differences between the left and the right hemisphere of the brain [29, 42]. Poor correlation between the processed CW and FD measurements (hemoglobin data) associated with the large changes in absorption and scattering (at death), are probably related to the inability of the CW system to determine the μ_a and μ_s. Therefore, absolute determination of tissue optical properties is critical. One should not forget that all the approaches are limited by the accuracy of the light transport models in the inhomogenous media [42].

7.5. Conclusion

This study describes the correlation between the signals obtained simultaneously

with two different optical instruments, continuous wave and frequency domain, in a newborn piglet brain perfusion - oxygenation model. The results have shown that continuous wave spectroscopy, although incapable of absolute determination of tissue optical properties, was able to detect and monitor both small and large changes in brain hemodynamics and oxygenation.

The result of this part of research work demonstrates that the CW type NIRS device can be used to investigate brain blood perfusion and oxygenation with a similar precision with FD type device, which will be described in the following chapters.

7.6. References

1. Meek JH, Tyszczuk L, Elwell CE, Wyatt JS 1998 Cerebral blood flow increases over the first three days of life in extremely preterm neonates. *Arch Dis Child Fetal Neonatal Ed.*. **78**(1): p. F33-F37.
2. Nelson KB and Ellenberg JH, 1986 Antecedents of cerebral palsy: Multivariate analysis of risk. *N Engl J Med.*. **315**: p. 81.
3. Volpe JJ, 1989 Intraventricular hemorrhage and brain injury in the premature infant. Neuropathology and pathogenesis. *Clin Perinatol.*. **16**: p. 361-386.
4. Perlman JM, K.K., Volpe JJ., 1984 The effect of eliminating fluctuating cerebral blood flow velocity in preterm infants with respiratory distress syndrome on the incidence and severity of intraventricular hemorrhage. *Ann Neurol.*. **16**: p. 380.
5. Tsuji M, duPlessis A, Taylor G, Crocker R, Volpe JJ 1998 Near infrared spectroscopy detects cerebral ischemia during hypotension. *Pediatr Res.*. **44**(4): p. 591-595.
6. Van Houten JP, Benaron DA, Spilman S, Stevenson DK 1996 Imaging brain injury using time resolved near infrared light scanning. *Pediatr Res.*. **39**(3): p. 470-476.
7. Brun NC, Moen A, Borch K, Saugstad OD, Greisen G 1997 Near-infrared monitoring of cerebral tissue oxygen saturation and blood volume in newborn piglets. *Am J Physiol.*. **273**(2 Pt 2): p. H682-6.

8. Stankovic MR, Fujii A, Maulik D, Boas D, Kirby D, Stubblefield PG 1998c Optical monitoring of cerebral hemodynamics and oxygenation in the neonatal piglet. *J Maternal Fetal Invest*,. **8**(2): p. 71-78.

9. Kurth CD, Steven JM, Benaron D, Chance B 1993 Near-infrared monitoring of cerebral circulation. *J Clin Monit*,. **9**: p. 163-170.

10. Fantini S, Hueber D, Franceschini MA, Gratton E, Rosenfeld W, Stubblefield PG, Maulik D, Stankovic MR 1999a Non-invasive optical monitoring of the newborn piglet brain using continuous wave and frequency domain spectroscopy. *Phys Med Biol*,. **44**: p. 1543-1563.

11. Wyatt JS, 1997 Cerebral oxygenation and haemodynamics in the foetus and newborn infant. *Philos Trans R Soc Lond B Biol Sci*,. **352**: p. 697-700.

12. Chance B, Luo Q, Nioka S, Alsop DC, Detre JA 1997 Optical investigations of physiology: a study of intrinsic and extrinsic biomedical contrast. *Philos Trans R Soc Lond B Biol Sci*,. **352**: p. 707-716.

13. Hirtz DG, 1993 Report of the National Institute of Neurological Disorders and Stroke workshop on near infrared spectroscopy. *Pediatrics*,. **91**: p. 414-417.

14. Alfano RR, Demos SG, and Gayen SK 1997 Advances in optical imaging of biomedical media. *Ann N Y Acad Sci*,. **820**: p. 248-70.

15. Wahr JA, Tremper KK, Samra S, Delpy DT 1996 Near-infrared spectroscopy: Theory and applications. *J Cardiothoracic and Vascular Anesthesia*,. **3**: p. 406-418.

16. Stankovic MR, Fujii A, Maulik D, Kirby D, Stubblefield PG 1998b Optical brain monitoring of the cerebrovascular effects induced by the acute cocaine exposure in neonatal pigs. *J Maternal Fetal Invest,*. **8**(3): p. 108-112.

17. Stankovic MR, Maulik D, Rosenfeld W, Stubblefield PG, Kofinas AD, Gratton E, Franceschini MA, Fantini S, Hueber D, (2000) "The role of frequency domain optical spectroscopy in the detection of neonatal brain hemorrhage – a newborn piglet study". J Maternal Fetal Medicine (In Press).

18. Glantz, S. A. *Primer of Biostatistics*, 3rd ed., McGraw-Hill, Inc. (1992)

19. Stankovic MR, Maulik D, Rosenfeld W, Stubblefield PG, Kofinas AD, Drexler S, Nair R, Franceschini MA, Hueber D, Gratton E, Fantini S, 1999 Real-time optical imaging of experimental brain ischemia and hemorrhage in neonatal piglets. *J Perinatol,*. **27**(4): p. 1-8.

20. Volpe JJ, 1997 Brain injury in the premature infant - from pathogenesis to prevention. *Brain & Development,*. **19**: p. 519-534.

21. Pryds O, Greisen G, Skov LL, Friis-Hansen B 1990 Carbon dioxide-related changes in cerebral volume and cerebral blood flow in mechanically ventilated preterm neonates: comparison of near infrared spectrophotometry and ^{133}Xenon clearance. *Pediatr Res,*. **27**: p. 445-9.

22. Pollard V, Prough DS, DeMelo AE, Deyo DJ, Uchida T, Widman R 1996b The influence of carbon dioxide and body position on nearinfrared spectroscopic assessment of cerebral hemoglobin oxygen saturation. *Anesth Analg,*. **82**: p. 278-287.

23. Wyatt JS, Edwards AD, Cope M, Delpy DT, McCormick DC, Potter A, Reynolds EO 1991 Response of cerebral blood volume to changes in arterial carbon dioxide tension in preterm and term infants. *Pediatr Res*,. **29**: p. 553-557.

24. Jobsis FF, 1977 Noninvasive infrared monitoring of cerebral and myocardial sufficiency and circulatory parameters. *Science*,. **198**: p. 1264-1267.

25. Alfano RR, Demos SG, Galland P, Gayen SK, Guo Y, Ho PP, Liang X, Liu F, Wang L, Wang QZ, Wang WB et al.. 1998 Time-resolved and nonlinear optical imaging for medical applications. *Ann N Y Acad Sci*,. 838: p. 14-28.

26. Chance B, 1998a Near-infrared images using continuous, phase-modulated, and pulsed light with quantitation of blood and blood oxygenation. *Ann N Y Acad Sci*,. **838**: p. 29-45.

27. Cope M and Delpy DT, 1988 System for long-term measurement of cerebral blood flow and tissue oxygenation on newborn infants by infra-red transillumination. *Med Biol Eng Comput*,. **26**: p. 289-294.

28. Pollard V, Prough DS, DeMelo AE, Deyo DJ, Uchida T, Stoddart HF 1996a Validation in volunteers of a near-infrared spectroscope for monitoring brain oxygenation in vivo. *Anesth Analg*,. **82**: p. 269-77.

29. Delpy DT, Cope M, van der Zee P, Arridge S, Wray S, Wyatt J 1988 Estimation of optical pathlength through tissue from direct time of flight measurement. *Phys Med Biol*,. **33**: p. 1433-1442.

30. Benaron DA, Benitz WE, Ariagno RL, Stevenson DK 1992 Noninvasive methods for estimating in vivo oxygenation. *Clinical Pediatrics*, **31**: p. 258-273.

31. Gratton E, Fantini S, Franceschini MA, Gratton G, Fabiani M 1997 Measurements of scattering and absorption changes in muscle and brain. *Philos Trans R Soc Lond B Biol Sci*,. **352**: p. 727-735.

32. Chance B, Cope M, Gratton E, Ramanujam N, Tromberg B 1998b Phase measurement of light absorption and scatter in human tissue. *Rev Sci Instrum*,. **69**(10): p. 3457-3481.

33. Ferrari M, Wilson DA, Hanley DF, et al., 1989 Determination of cerebral venous hemoglobin saturation by derivative near infrared spectroscopy. *Adv Exp Med Biol*,. **248**: p. 47-53.

34. Cruz J and Miner ME, 1986 Modulating cerebral oxygen delivery and extraction in acute traumatic coma, in Neurotrauma, W. KA, Editor., Butterworth: Boston. p. 55-72.

35. Skov L, Pryds O, Greisen G 1991 Estimating cerebral blood flow in newborn infants: Comparison of near infrared spectroscopy and ^{133}Xenon clearance. *Pediatr Res*,. **30**: p. 570-573.

36. Goddard-Finegold J, Louis PT, Rodriguez DL, David Y, Contant CF, Rolfe P 1998 Correlation of near infrared spectroscopy cerebral blood flow estimations and microsphere quantitations in newborn piglets. *Biol Neonate*,. **74**(5): p. 376-84.

37. Stankovic MR, Maulik D, Boas DA, Stubblefield PG, 1998a Emerging Technologies: Fetal Optical Monitoring, in Asphyxia and Fetal Brain Damage, M. D, Editor., John Wiley & Sons, Inc.: New York. p. 345-364.

38. Hintz SR, Cheong WF, van Houten JP, Stevenson DK, Benaron DA 1999 Bedside imaging of intracranial hemorrhage in the neonate using light: comparison with ultrasound, computed tomography, and magnetic resonance imaging. *Pediatr Res*,. **45**(1): p. 54-59.

39. Tsuji M, Naruse H, Volpe J, Holtzman D 1995 Reduction in cytochrome aa3 measured by near-infrared spectroscopy predicts cerebral energy loss in hypoxic piglets. *Pediatr Res*,. **37**: p. 253-259.

40. Ferrari M,.De Blasi RA, Fantini S, Franceschini MA, Barbieri B, Quaresima V, Gratton E 1995 Cerebral and muscle oxygen saturation measurement by a frequency-domain near-infrared spectroscopic technique. Proc. SPIE 2389, 868-874.

41. Grubhofer G, Tonninger W, Keznickl P, Skyllouriotis P, Ehrlich M, Hiesmayr M, Lassnigg A 1999 A comparison of the monitors INVOS 3100 and NIRO 500 in detecting changes in cerebral oxygenation. *Acta Anaesthesiol Scand*,. **43**(4): p. 470-5.

42. Delpy DT, Cope M,. 1997 Quantification in tissue near-infrared spectroscopy. *Philos Trans R Soc Lond B Biol Sci*,. **352**: p. 649-659.

7.7. Tables

Table 7-1 Physiological data obtained from 6 newborn piglets (mean ± SD).

HR – heart rate (beats per minute); MAP – mean arterial pressure (mm Hg); $PaCO_2$ – arterial carbon dioxide tension (mm Hg); PaO_2 – arterial oxygen tension (mm Hg); SaO_2 - arterial oxygen saturation (%)

Physiological Data	Baseline	Max Hyperventilation	Max Hypoventilation
HR	123.8 ± 15.4	127.7 ± 20.9	111.3 ± 14.9
MAP	72 ± 10.4	55 ± 9.8	54.3 ± 11.5
$PaCO_2$	42.2 ± 2.6	13.3 ±3.3	56.7 ± 5.8
PaO_2	119.8 ± 23.9	126.7 ± 27.9	98.7 ± 20.5
pH	7.4 ± 0.07	7.65 ± 0.09	7.16 ± 0.02
SaO_2	98.02 ± 0.75	99.05 ± 0.28	94.8 ± 2.8

Table 7-2 Correlation between the frequency domain (FD) and continuous wave (CW) oximeters.

The phase A is the subject still alive with different ventilation conditions, and phase B is the subject during the death procedure after being sacrificed by an injection of the over-dosed pentobarbital.

1	2	3	4		5		6	
Piglet #	FD @ 758 nm vs. CW @ 780 nm	FD @ 830 nm vs. CW @ 830 nm	Hb		HbO_2		Hbt	
			Phase A	Phase B	Phase A	Phase B	Phase A	Phase B
1	0.96	0.99	0.89	0.57	0.91	0.49	0.95	0.48
2	0.95	0.98	0.97	0.28	0.87	0.01	0.85	0.31
3	0.92	0.96	0.95	0.86	0.92	0.85	0.93	0.87
4	0.93	0.98	0.85	0.65	0.96	0.41	0.98	0.16
5	0.98	0.91	0.98	0.58	0.9	0.46	0.87	0.67
6	0.91	0.97	0.95	0.51	0.95	0.45	0.94	0.42

7.8. Figures

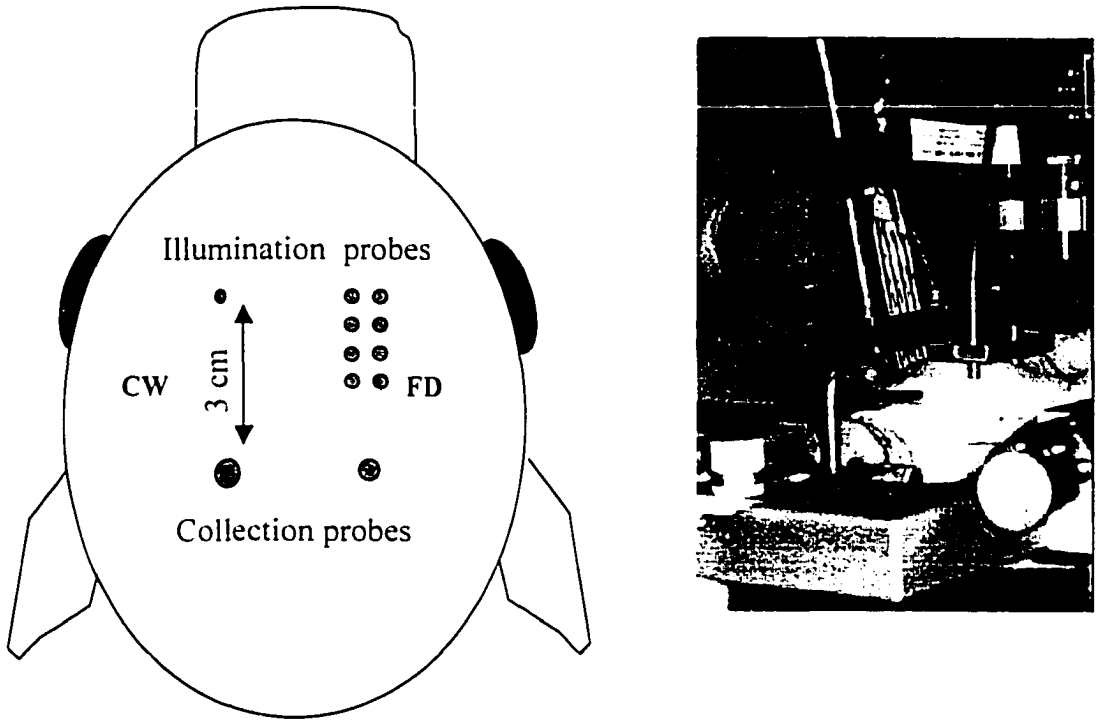

(a) (b)

Figure 7-1. Experimental setup.

(a) Shows the arrangement of optical probes of CW (left) and FD (right) type devices on the head of newborn piglet. (b) Shows the setup photograph on a newborn piglet that was in placed in the U-shaped frame. The two optical probes (CW at left and FD at right) were applied to the scalp with the help of the manipulator arm of the instrument.

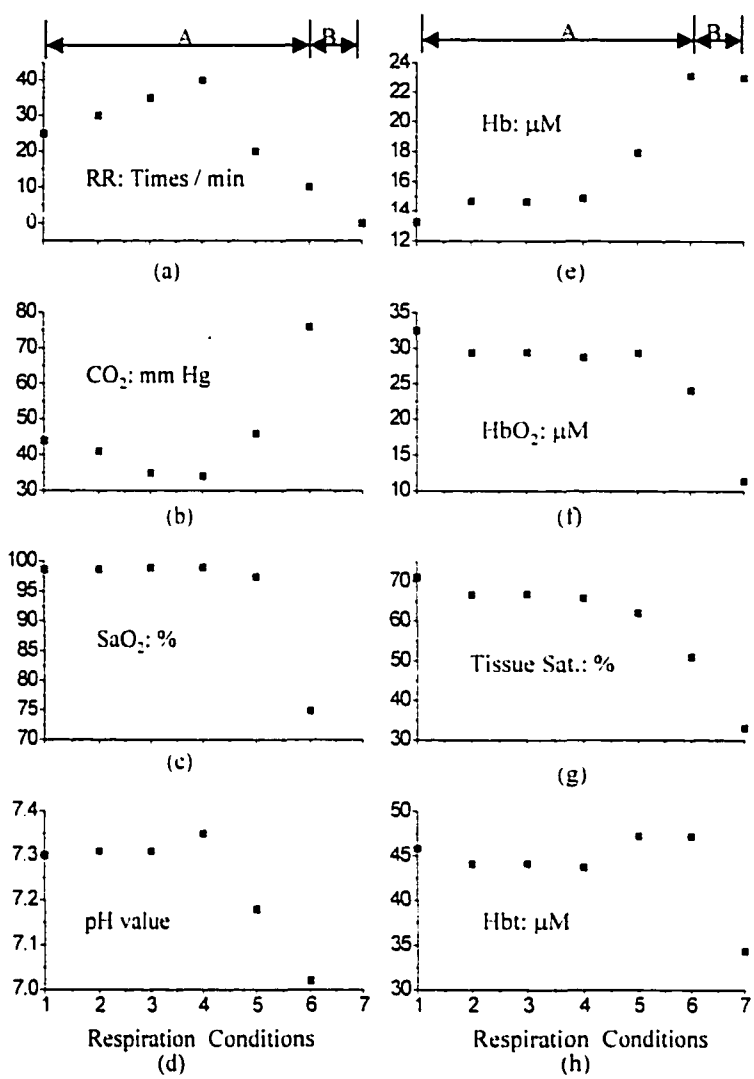

Figure 7-2 Typical hyper- and hypoventilation-induced changes in conventional variables.

(a) respiration rate (RR), (b) arterial, CO_2 (c) arterial oxygen saturation (SaO_2), and (d) pH, and cerebral optical variables, (e) deoxyhemoglobin (Hb), (f) oxyhemoglobin (HbO_2), (g) total hemoglobin (Hbt), and (h) tissue saturation.

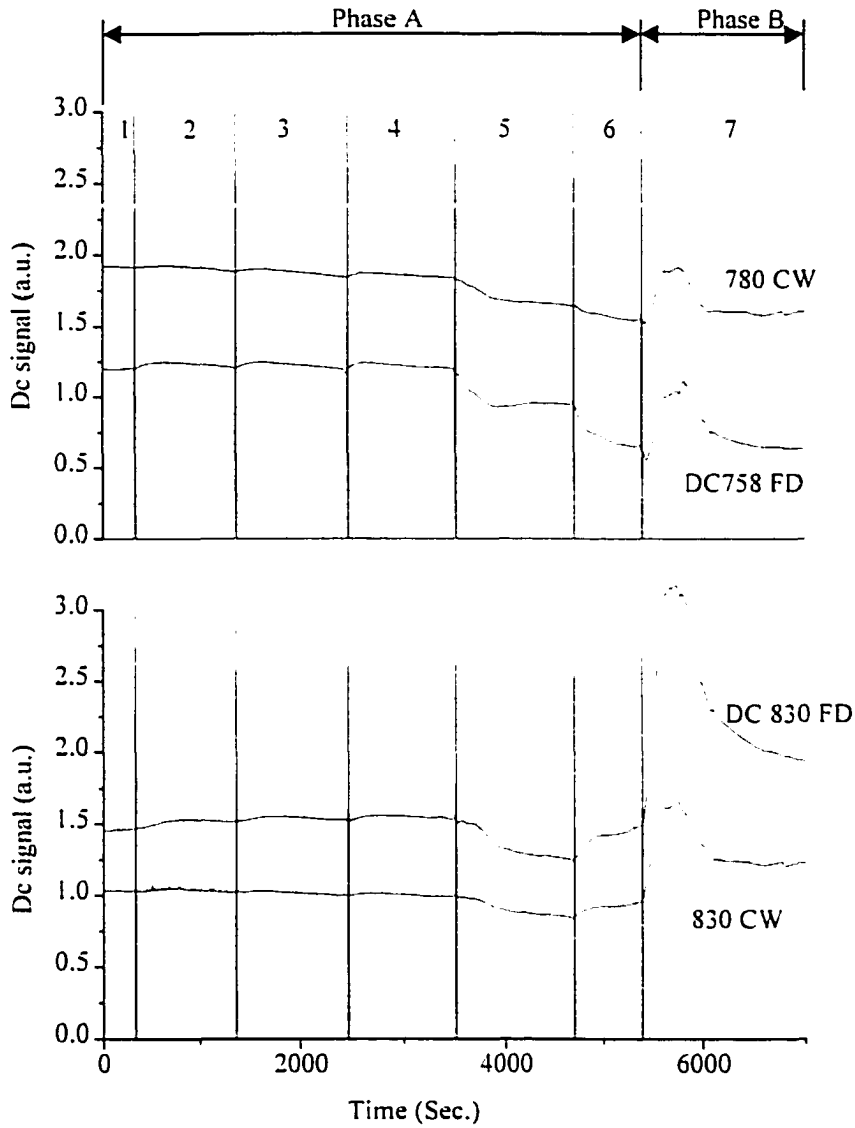

Figure 7-3 Raw data (DC outputs), as recorded by the CW oximeter at 780 and 830 nm with a source detector separation of 3 cm, and the FD oximeter at 758 and 830 nm with a source-detector separation of 2.98 cm.

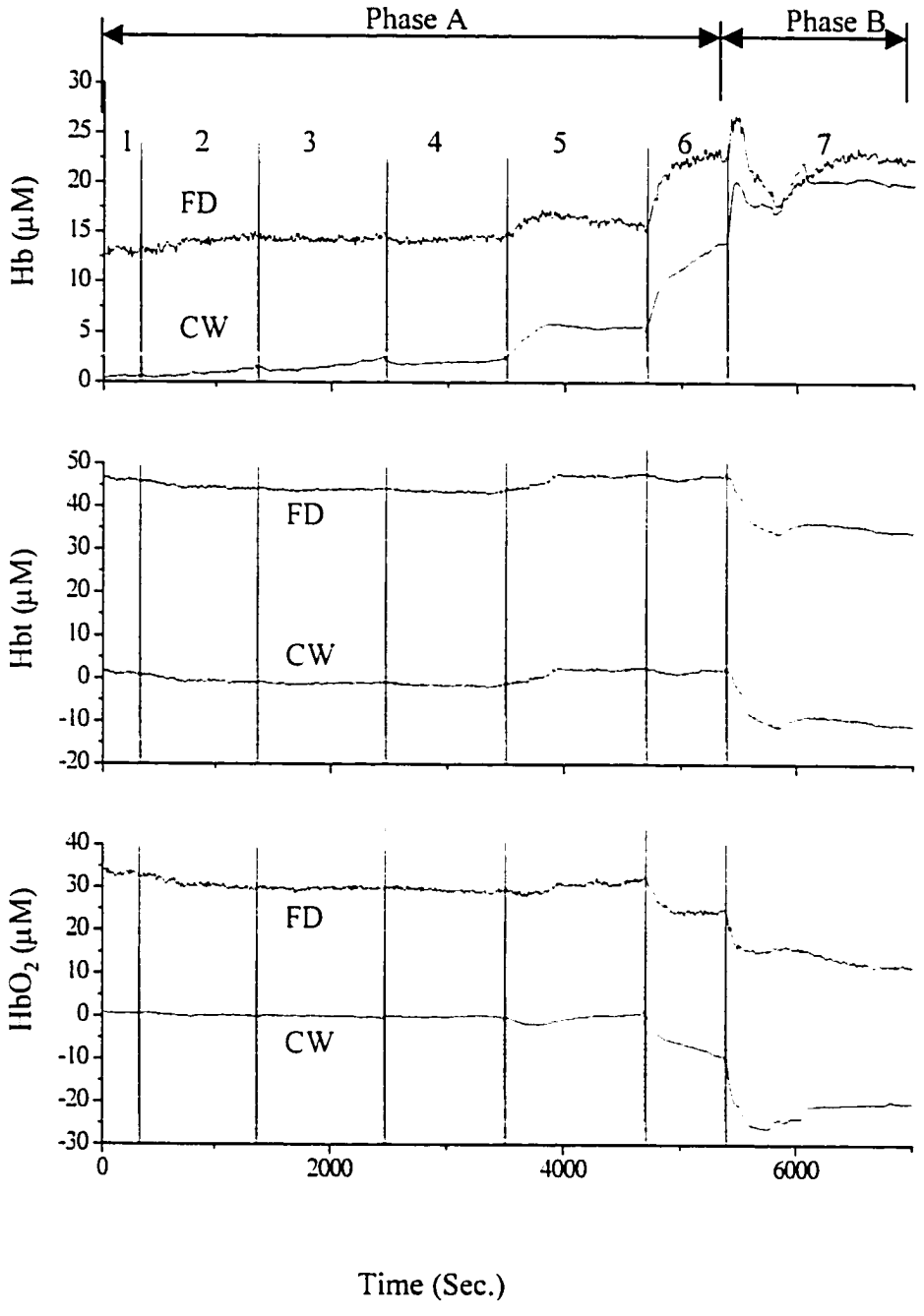

Figure 7-4 Hemoglobin parameters (i.e. Hb, HbO_2, and Hbt) recorded by the CW oximeter at 780 and 830 nm, and the FD oximeter at 758 and 830.

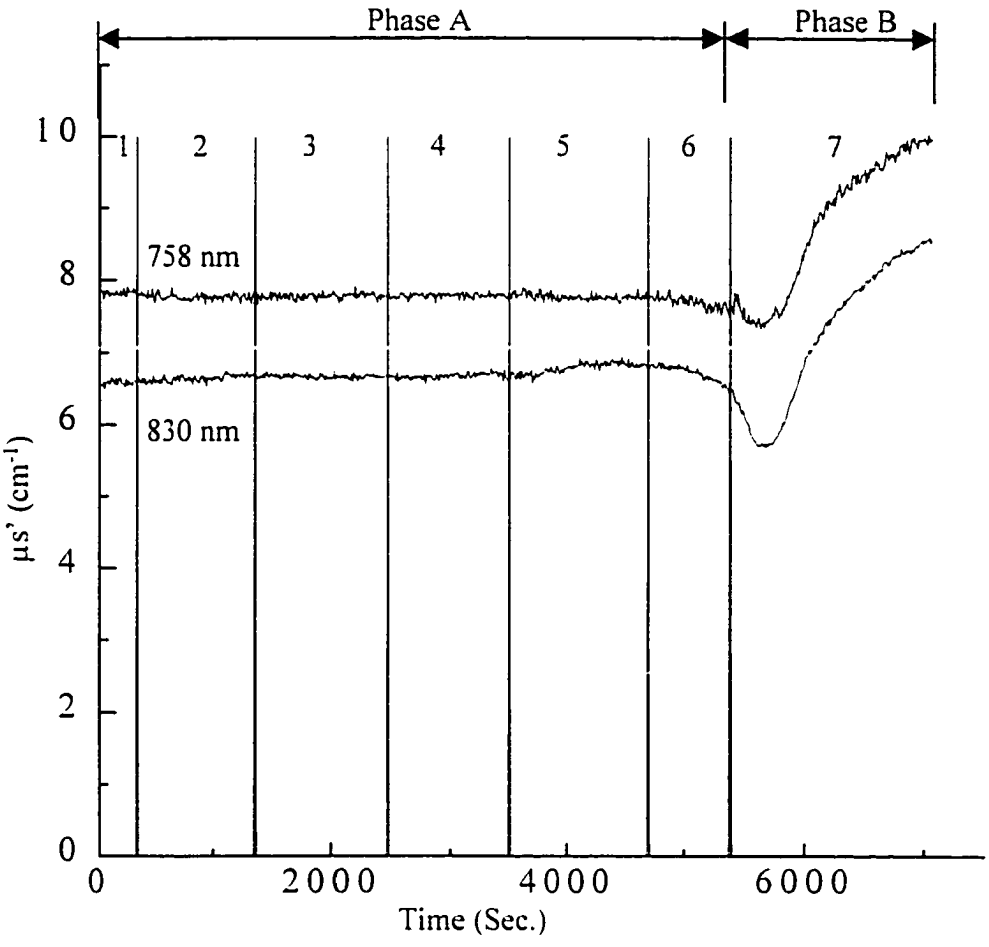

Figure 7-5 Brain tissue scattering changes detected by the FD oximeter.

8. Intracerebral hemodynamics in the transition between wakefulness and sleep probed by near infrared spectroscopy

8.1. Introduction

Many sleep disorders are life threatening, either directly (as in fatal familial insomnia and obstructive sleep apnea) or indirectly (as a result of sleep-related motor vehicle accidents). The importance of sleep is poorly recognized by the general public. The National Commission on Sleep Disorders Research (1993) reported to Congress that more than 100 Americans die on the nation's highway each day from sleep-related motor vehicle accidents. The direct yearly cost of sleep disorders to the taxpayer is estimated at $15.8 billion[1].

Researchers study sleep by recording brain activity mainly using electroencephalograph (EEG). The EEG involves inspecting wavelike tracings produced by ink pens on moving chart paper or computer screens. Generally, the EEG electrodes are fixed at certain locations on the subject head with "Standard International (10-20) Electrode Placement." The arrangement is shown in Figure 8-1. The EEG activity is characterized by both the frequency and the amplitude of the waves. The EEG is generally divided into four categories of waves according to frequency ranging from slowest to fastest: delta (δ) 0.5 ~ 4 Hz, theta (θ) 4 ~ 8 Hz, alpha (α) 8 ~ 13 Hz and beta (β) 13 ~ 30 Hz. Sometimes, other kinds of electrophysiological signals are also recorded

during sleep monitoring. One is electrooculography (EOG) to monitor the eye movement signal, the electrode placed at the left outer canthus (LOC) for left eye and located at right outer canthus (ROC) for right eye monitoring. Another is the electromyography (EMG) for muscle tone monitoring from electrodes placed under the chin to record submental electromyography activity (EMG-SM).

Initial data reduction entails summarizing waveform activity over a specified time frame, which is called an "epoch." Each polygraphic epoch is classified in stages such as wake (or W0), 1, 2, 3, 4, rapid eye movement (REM) sleep or movement time (when tracing is obscured by muscle artifact) according to electrophysiological criteria. Table 8-1 shows EEG characteristics for the different sleep stages [2].

Figure 8-2 shows the typical EEG waves of a subject occurring during the wake to sleep transition [2]. The first half of the tracing indicates the subject is still awake, and the second part shows the subject is in stage one sleep. Figure 8-3 is the typical EEG data in stage 2 sleep [2]. The K complex and sleep spindle waveforms appeared in the EEG record (see the definition in Figure 8-3). Sleep spindles are EEG waveform bursts with a mean frequency of 11.5 to 16 Hz and duration of 0.5 second or more. The K complex is high-voltage waveform that can be either slow or sharply contoured but is typically less than one-half of a second in duration.

It has been widely accepted that changes in cerebral blood flow and cerebral metabolic rate can be used as indices for changes in neuronal activity [3, 4]. Based on this blood flow concept, other sophisticated techniques have been developed such as positron emission tomography (PET) and functional magnetic resonance imaging (fMRI). These techniques possess sharp spatial resolution. However, the links between PET, fMRI and

neuronal activity are limited by the poor temporal resolution of these brain imaging techniques.

New techniques for functional imaging of the brain have great promise for elucidating basic neurobiological mechanisms [5]. While the processes of waking activation [6] and sleep-related changes [7-22] have received much attention, relatively unexplored by neuroimaging techniques are the boundary between wakefulness and sleep. Quantitative EEG brain mapping has shown that around the time of sleep onset, alpha frequency disappears and theta frequency increases, especially along the midline and in posterior regions [21]. Increased delta and decreased beta activity, as well as increased EEG power, have also been observed [23-25]. Given these distinct EEG changes and the profound and global changes in consciousness and functional capacity in the transition to sleep, it is somewhat surprising that the reduction in cerebral metabolic rate and cerebral blood flow are small and gradual [17, 19, 26, 27]. The characterization of the sleep onset process as incremental may be a function of the limitations of the techniques employed [28].

To better understand the sleep state transition process, the present study employed near-infrared spectroscopy (NIRS) to characterize regional cerebral hemodynamics during the transitions between wakefulness and sleep and sleep and wakefulness.

In this research, near infrared light passes through extracranial tissue into the brain and a portion of the light delivered scatters back to a sensor with valuable information concerning intracerebral attenuation of light [29]. The light attenuation can be attributed mainly to the fluctuating levels of several key light absorbing molecules: oxygenated hemoglobin (oxy-Hb), deoxygenated hemoglobin (deoxy-Hb), and

cytochrome oxidase [23,30]. The NIRS technique yields changes in levels of these chromophores by illuminating a small volume of the intracerebral tissue and vasculature. The use of NIRS in combination with fMRI, trascranial doppler, direct blood assays and other techniques have yielded convergent validity of the optical method [6, 31-41]. Advantages of NIRS of the brain over other imaging techniques include measurement of specific biochemical markers, localization to a fairly superficial layer of gray matter and a rapid response of approximately one second or less. The technique is non-invasive and may be used for extended periods of time, while the equipment is small, portable and inexpensive. The NIRS method is the only currently available means to measure changes in the concentration and oxygenation of hemoglobin in the brain. The apparatus can fit on a small cart, be used at the bedside of patients and provides continuous online information for hours. This technique can be used to study the brain's response to hypoxia in a wide range of conditions. The monitoring of hemodynamics may be critical in the brain, which is vulnerable to prolonged hypoxia. While the high standard necessary to impact clinical decision making has not yet been achieved by NIRS, advances in technology are likely to enhance the already valuable information that can be obtained [42-45].

Past studies of NIRS during the transition to sleep have described a number of patterns. As subjects fell asleep, an oxy-Hb decrease and deoxy-Hb increase from a frontal location were accompanied by either a decrease or no change in total hemoglobin (t-Hb) [46]. Similar findings were obtained with NIRS placed at frontal and central derivations but inverse changes; Oxy-Hb increase and deoxy-Hb decrease, were recorded from the occipital region [47]. These past studies did not specify the time period

examined, conducted no statistical analysis of the data and did not evaluate the complimentary transitional state from sleep to wakefulness.

The focus of this part of thesis is to address all of these limitations and describe the pattern of NIRS changes in the boundary between sleep and wakefulness.

8.2. Materials and methods.

8.2.1. Subjects

Nine healthy individuals with an average age of 30.3 years (range 22 to 52), 7 males, 2 females, served as subjects. The subjects restricted their sleep to about 4 hours on the night before the day of the experiment in order to facilitate sleep during the day. This study was approved by the City College of New York's Institutional Review Board (IRB) and written documentation of informed consent was obtained from the subjects.

8.2.2. Instrumentation

Figure 8-4 shows a schematic of the approach. The optical fiber probes of the CW type NIRS device (see chapter 3) were placed 3 cm apart, embedded in an elastic headband with a perpendicular orientation to the surface of the forehead. Symmetrically positioned across the midline, the input probe was to the left (near Fp2) and the detector probe to the right (near Fp1). Both probes were approximately equidistant from the eyebrows and hairline (refer Figure 8-1). We chose to apply optodes to the forehead rather than the scalp because the hair in the scalp attenuates light significantly and reduces the signal to noise ratio. In addition, there is evidence that the frontal lobes and midline structures show early changes in the transition to sleep [21, 48] and we were interested in the boundary state between wakefulness and sleep.

Bipolar EEG signals and the NIRS signals were simultaneously recorded by connecting to a polygraph recorder and a PC computer based digital recorder. Analog data from the EEG amplifier's J6 output was digitized at 12 bit at 256 Hz by a Microstar Laboratories DAP 1200 signal processing card with a dynamic range of ± 5 volts. A Pentium 166 MHz PC was used for data collection by the data acquisition software (Dapf©, von Gizycki, 1996). A Grass 7D polygraph with 7P511 amplifiers was used to acquire electrophysiological data. Amplifier settings were as follows: Sensitivity = 5 uv/mm, high filter = 1K, low filter = .30. The following seven-channel montage was used according to the international 10-20 system [49]: C_3 -A_1A_2, C_4-A_2, O_1-F_Z, O_2-F_Z, Left outer canthus-A_1, Right outer canthus-A_2, and bipolar mentalis muscle for chin electromyogram.

8.2.3. Procedure

The napping protocol began between noon and 2 pm. Following preliminary calibrations and 3 minutes of waking recording with eyes alternatively opened and closed, the room lights were turned off, the door of the sound attenuated room closed and the subject was told to go to sleep. When the polygraphic record indicated that the subject was in stage 2 sleep for over 30 s, the investigator woke the subject by calling his or her name on the intercom. The subject was kept awake for at least 30 s and then told to return to sleep. Subjects were encouraged to fall asleep more than once so that multiple sleep onsets and sleep offsets could be collected.

8.2.4. Data Analytic Strategy

The data analytic strategy was analogous for the wakefulness to sleep and the

sleep to wakefulness transition. To avoid repetition we will describe the complete procedure for only the wakefulness to sleep period.

The analysis proceeded in steps (Table 8-2). The first step was visual identification of regions of the EEG data stream that were fairly clear and unidirectional in the transition from waking to sleep. An expert scorer (AJS) examined the polygraphic record and selected segments of 20 to 120 s in duration in which the transitions between waking and sleep were relatively unambiguous and there was no gross artifact present in the NIRS signal. Polygraphic segments in which alpha activity in the EEG waxed and waned were excluded from the analysis. Within that region the point of human Scored Sleep Onset (Table 8-2, step 1) was defined, based on polysomnographic criteria, that mainly relied on the complete disappearance of alpha frequency on the EEG. In some cases, in which alpha was not abundant, this decision was based on the change to an EEG in the theta frequency range or mixed frequencies with amplitude greater than during unambiguous waking. Only a small number of wakefulness to sleep trials were included in the analysis. Our aim was to select portions of the record that demonstrated a continuous and uniform state change. Operationally, we selected segments that began with a relatively unbroken string of alpha in the EEG or an unambiguous waking EEG. In order to be selected for analysis, this portion of wakefulness needed to be followed by continuous sleep for at least 20 s. In this sleep portion either alpha disappeared completely or there was a slowing to the theta range and a slight increase in EEG amplitude. These strict criteria for selection resulted in 26 sleep onsets selected for analysis in nine subjects.

The complementary transition, from sleep to wakefulness, was provoked by

experimenters calling the subject's name over the intercom. Following the awakenings, the typical pattern was a burst of high amplitude alpha in the EEG followed by a reduction in amplitude as wakefulness continued. The first appearance of alpha was defined as the point of human Scored Sleep Offset (Table 8-2, step 1). The point demarcating the change from sleep to wakefulness was clear and abrupt. In contrast to the small number of trials in which the wakefulness to sleep transition qualified, we were able to include a more representative sample of awakenings. We analyzed 37 transitions from sleep to wakefulness in nine subjects. The scorer was blind to the NIRS data when determining the points of Scored Sleep Onset and Offset. Each subject had at least one sleep onset and offset period that qualified for analysis.

The next step was to submit the regions of EEG data around the point of Scored Sleep Onset to a Fast Fourier Transform (FFT) analysis with a moving set of two 5 s windows (see the Computer Analysis section below for algorithm). The changes in alpha power was examined for the region starting 5 seconds before and ending 20 seconds after the point of Scored Sleep Onset. Computer derived FFT Sleep Onset was defined by the program as the point of maximal decrease in relative alpha power from the first to the second 5 s window (Table 8-2, step 2). The corresponding point of increased alpha power was called computer FFT Sleep Offset (Table 8-2, step 2). The third step was to compare the Scored Sleep Onset and computer FFT Sleep Onset and see how far apart they were in the time domain (Table 8-2, step 3). This comparison served as convergent validity of the two methods.

Standard sleep stage scoring requires analysis by an epoch of either 20 or 30 seconds [50]. In order to improve the temporal resolution in the evaluation of the timing

of the hemoglobin changes we used two points; the point at which visual inspection detected the disappearance of alpha and the FFT analysis of maximum decrease in relative alpha power. While these criteria differ from standard sleep stage scoring, these EEG analyses resulted in the Switch Point from waking to sleep, taking place out of conventionally scored Stage 1 sleep.

The decision to use two 5 s data windows to evaluate the EEG during the transition period between sleep and waking was based on the well known association between EEG alpha activity and wakefulness [50]. No such well-established temporal association has been demonstrated between NIRS parameters and sleep or wakefulness. Therefore, we systematically explored window sizes between 2 and 10 seconds. We found that all window sizes yielded consistent and significant findings for oxy-Hb changes at sleep onset and offset and deoxy-Hb changes at sleep offset. For deoxy-Hb at sleep onset, data window values below 5 seconds were unstable and values between 5 and 8 s were stable hovering near $p < 0.06$ ranging between $p < 0.05$ and $p < 0.08$. We chose to use the 5 s data window because this was the shortest interval at which deoxy-Hb changes were stable.

It is well established that activation is associated with an increase in oxy-Hb [51, 52]. A preliminary examination was conducted to confirm that oxy-Hb increases at sleep offset and decreases at sleep onset. This was accomplished by the program identifying the point where there was a maximal change (either increase or decrease) in the level of oxy-Hb from the first to the second 5 s window and statistically testing the change (Table 8-2, step 4). Once the expected increase in oxy-Hb at sleep offset was confirmed we re-examined the few trials in which the largest oxy-Hb change was not an increase at sleep

offset. In these trials we visually selected that portion of the record that contained the largest oxy-Hb increase in the region of sleep offset (Table 8-2, step 5). Our aim was to examine the pattern of all NIRS changes that occur at the time of activation as indexed by the oxy-Hb rise as the subject woke up. The analogous procedure was conducted at sleep onset for the few trials in which the largest change in oxy-Hb was an increase. We then compared the magnitude and direction of the changes in oxy-Hb, deoxy-Hb and t-Hb that occurred at the same time (Table 8-2, step 6). For example, the point of maximal decrease in oxy-Hb in the region of falling asleep was used as the point around which deoxy-Hb and t-Hb values were calculated.

We visually selected that portion of the data stream at the decline in oxy-Hb at sleep onset, in which there was also a decline in deoxy-Hb. We called this data segment in which both chromophores decreased simultaneously the Switch Point (Table 8-2, Step 7). The end of this synchronized decline was defined as the first bin (one second) in which either of the chromophores was not lower than in the previous bin. This Switch Point was analyzed for the duration of the synchronized and parallel decreases in oxy-Hb and deoxy-Hb. The duration of the corresponding synchronized increases in the chromophores at sleep offset was also determined. We excluded from the analysis the 8 sleep onset trials in which there was no simultaneous decrease in the two chromophores. In these trials only reciprocal changes in oxy-Hb and deoxy-Hb were present. Similarly, we excluded 5 sleep offset trials in which there was no synchronized increase in the chromophores. In addition, we calculated the time delay from Scored Sleep Onset (and Offset) to the synchronized hemoglobin changes (Table 8-2, Step 8).

To describe the relative changes in oxy-Hb and deoxy-Hb in the region around

sleep onset, we calculated three correlation coefficients between oxy-Hb and deoxy-Hb, as follows (Table 8-2, step 9). In each of the three analyses we first standardized the data in the traditional manner [53] before performing the correlation. For a 4 second series of data at the Switch Point, for example, we took the mean of the four oxy-Hb one second bins and subtracted the mean from each of the bin values. We did the same for the four deoxy-Hb bins and then calculated the correlation between the transformed oxy-Hb and deoxy-Hb values. This preliminary transformation allowed us to perform an overall correlation across all trials. Three correlations were performed on different segments of the time series (Table 8-2, step 9). (1) A correlation was calculated between the two chromophores at the Switch Point, for the duration of the parallel and synchronized change in each sleep onset trial. (2) We then selected the data for the 5 seconds prior to the onset of the Switch Point and calculated the correlation. (3) Similarly, we selected the segment for the 5 seconds immediately following the Switch Point, and calculated the correlation. The three corresponding correlations at sleep offset were also calculated.

Previous studies have shown that CBF levels during wakefulness are different before and after a long bout of sleep [10, 26]. This study examined changes before and after a short nap and did not directly compare waking before and after the sleep period. The analyses were limited to wakefulness to sleep and sleep to wakefulness changes.

8.2.5. Computer analysis

A discrete FFT function was used to assess EEG power. The data was first detrended and then the power spectral density was computed using a 256 point FFT with 128 point hanning window. Frequency decomposition was performed using the MATLAB FFT function, and for EEG analysis, the squared absolute value of the output

of this function was used as EEG power.

As summarized in equation (1) below, alpha power of the EEG by FFT algorithm was analyzed to obtain the computer FFT Sleep Onset and Offset points. The EEG data stream was truncated to 1 s event data points. The sleep onset and offset points were determined by sampling segments of the data with a moving window as follows: Data was collected and averaged within each of two contiguous windows of 5 s. The entire data region of interest was sampled successively by moving the windows in 1 s increments and re-calculating the means of the two windows. When the difference between the averages of the first and second windows was the greatest, the transition value separating the windows was defined as the point of computer FFT Sleep Onset or Sleep Offset.

$$V = \max(\text{mean data [second 5 s]} - \text{mean data [first 5 s]}) \quad (1)$$

Expressed by formula (1) V is the transition value (point of computer FFT Sleep Onset and Offset), mean data [second 5 s] and mean data [first 5 s] are the mean values of the data after and before the transition points respectively, within 5 s windows.

In the same manner, the maximal oxy-Hb response, maximal decrease in oxy-Hb at sleep onset, maximal increase in oxy-Hb at sleep offset and the corresponding changes in deoxy-Hb and t-Hb were obtained. The NIRS signals were averaged to 1 s event data points to eliminate high frequency noise.

8.3. Results.

Figure 8-5 displays the long-term changes in the EEG and NIRS recordings for one subject. The top curve shows the EEG alpha power from electrode locations O_1-F_Z wakefulness labeled W and sleep labeled S. The lower curves present the hemoglobin

concentration changes calculated from the NIRS signal at the forehead. The vertical lines mark the points of sleep state transitions at Scored Sleep Onset and Offset. As the subject fell asleep there were reductions in EEG alpha, oxy-Hb and t-Hb. The deoxy-Hb level appears a little changed. In contrast, as the subject woke-up there were increases in EEG alpha, oxy-Hb and t-Hb. Again, the deoxy-Hb level appears a little changed.

8.3.1. Spontaneous transition from wakefulness to sleep

Figure 8-6 displays the short-term changes in EEG alpha and hemoglobin concentration for one subject. In addition to the parameters presented in Figure 8-5, this graph includes the cross correlation between oxy-Hb and deoxy-Hb for a 5 s window. The value at each point represents the correlation between oxy-Hb and deoxy-Hb for the following 5 second period. As seen in the upper panel of Figure 8-6, during wakefulness the alpha power of the EEG is high and as the subject falls asleep the signal becomes abruptly weaker. Four seconds after the point of Scored Sleep Onset (827 s) the levels of both oxy-Hb and deoxy-Hb begin to decrease at the same time. This fall in the two chromophores continues for 8 s (through 835 s). This synchronized fall, which we designate as the Switch Point, is clearly seen in the cross correlations with rs approaching 1.0 for values between 827 s and 830 s. Prior to and after the Switch Point there are small changes in oxy-Hb and deoxy-Hb. The relationship between the two chromophores in the region bordering the Switch Point is either distinctly reciprocal or mildly parallel as can be seen in the middle panel and as represented in the lower panel by r values approaching –1.0 and low positive values respectively.

As expected, grouped data show highly significant reductions in EEG alpha power at both electrode locations during the transition to sleep (Table 8-3; ps < 0.0005).

The mean point of Scored Sleep Onset was 4.7 s (SD = 3.9, t = 3.29, n = 9, $p < 0.01$) after the mean point of computer FFT Sleep Onset at the C_3-A_1A_2 placement.

The concentration of oxy-Hb was reduced in the transition to sleep (mean difference [second 5 s] minus [first 5 s] = -0.01571 arbitrary units, SD = 0.04209, t = 3.11, n = 9, $p < 0.01$). In contrast to this overall decrease in oxy-Hb, there were 6 of 26 nap trials in which the largest change was an increase. In order to examine the changes in deoxy-Hb and t-Hb that occurred at the time of the fall in oxy-Hb, we located the portion of the sleep onset record, in these 6 nap trials, in which there was the largest decrease in oxy-Hb. As subjects fell asleep and oxy-Hb decreased (Table 8-3) there was a near significant reduction in deoxy-Hb (n = 9, $p < .063$). Employing the nap trial as the unit of analysis, there was a significant reduction in deoxy-Hb (mean difference [second 5 s] minus [first 5 s] = -0.00609 arbitrary units, SD = 0.01315, t = 3.47, n = 26, $p < 0.005$). In contrast to the general reduction in deoxy-Hb at sleep onset, there were 6 of 26 nap trials in which the largest change in deoxy-Hb was an increase. At the time of the fall in oxy-Hb at sleep onset, there was also a reduction in t-Hb ($p < 0.002$).

In 18 of the 26 sleep onset trials there was a Switch Point characterized by a distinct synchronized decrease in both oxy-Hb and deoxy-Hb. In the remaining 8 trials the relationship between the chromophores was either reciprocal or indeterminate. The mean duration of the Switch Point was 3.6 s (SD = 1.6 s, n = 18). The mean delay from the Scored Sleep Onset to the start of the Switch Point was 3.8 s (SD = 8.2, n = 18). The correlation between oxy-Hb and deoxy-Hb at the Switch Point was r = 0.94 (n = 18, Figure 8-7). This simultaneous decrease in both chromophores results in a drop in t-Hb and probably reflects a brief down regulation of cerebral blood flow or volume at sleep

onset.

Before and after the Switch Point, a different NIRS pattern was seen with levels of both oxy-Hb and deoxy-Hb showing increases and decreases of small magnitude. The two chromophores showed both reciprocal changes (as one increased the other decreased) as well as parallel changes (Figure 8-7). The mean correlation of the two chromophores in the 5 seconds before ($r = 0.04$) and the 5 seconds after ($r = 0.03$) the Switch Point in the region of sleep onset approached zero ($n = 18$). Therefore, the Switch Point is a distinct and fairly uniform phase of hemodynamic regulation that is bounded by a mixture of changes.

8.3.2. The sleep to wakefulness transition produced by forced arousal

Figure 8-8 displays the data from one subject before and after being awakened. While asleep the alpha power of the EEG signals is low and abruptly increases one second after the point of Scored Sleep Offset at the 719th second. The synchronized increase of both oxy-Hb and deoxy-Hb (Switch Point) starts at the 723rd second and ends at the 729th second. This is also reflected in the cross correlation values approaching $r = 1.0$ between the 720th and 725th s in the lower panel. Prior to and after the Switch Point the relationship between oxy-Hb and deoxy-Hb is a mixture of reciprocal and parallel changes, as reflected in the wide range of positive and negative correlations in the lower panel.

Grouped data show that as subjects wake up, EEG alpha power signals increase (Table 8-4, $n = 9$, both ps < 0.0005). The mean point of Scored Sleep Offset occurred 4.1 s before the increase in FFT alpha power at the C_3-A_1A_2 placement (SD = 3.3 s, $t = 3.37$,

$n = 9, p < 0.01$).

There was a rapid and robust increase in oxy-Hb level as subjects were awakened (mean difference [second 5 s] minus [first 5 s] = 0.08056, SD = 0.04680, $t = 3.94$, $n = 9$, $p < 0.005$). In contrast to the general increase in oxy-Hb, there were 7 of 37 trials in which the largest change was a reduction. We located the segment of the sleep offset period in which oxy-Hb level was increased in these 7 trials in order to analyze the accompanying NIRS changes. As subjects woke up and oxy-Hb increased (Table 8-4), deoxy-Hb also increased ($p < .05$). At the time of the rise in oxy-Hb, t-Hb also increased ($p < 0.001$).

In 32 of 37 trials there was a synchronized and parallel increase in both oxy-Hb and deoxy-Hb upon awakening. In the remaining 5 trials the relationship between the chromophores was reciprocal or indeterminate. The mean duration of the Switch Point was 3.4 s (SD = 1.5, n = 32). The correlation between oxy-Hb and deoxy-Hb at the Switch Point was $r = 0.94$ ($n = 32$; Figure 8-9). The mean delay from the Scored Sleep Offset to the start of the Switch Point was 1.5 s (SD = 3.8, n = 32). There was no difference in the speed of the hemodynamic response at sleep offset and sleep onset. The time from the Scored Sleep Offset to the Switch Point (mean = 1.5 s, SD = 3.8, n = 32) compared to the time from the Scored Sleep Onset to the Switch Point (mean = 3.8 s, SD = 8.2) was not different ($n = 18$, $t = -1.28$, n.s.).

Before and after the Switch Point at sleep offset, oxy-Hb and deoxy-Hb showed small increases and decreases. The relationship between the two chromophores in the region outside the Switch Point was reciprocal as well as parallel (Figure 8-9). The mean correlation between the two chromophores was small in the 5 seconds before ($r = 0.13$)

and the 5 seconds after (r = 0.27) the Switch Point (n = 32; Figure 8-9).

8.4. Discussion

The current work has demonstrated that the global changes that occur between the states of wakefulness and sleep are accompanied by consistent changes in hemodynamics. The process of falling asleep, characterized by simultaneous reductions in the concentration of oxy-Hb and deoxy-Hb, suggests decreased neuronal activity, reduced oxygen consumption and reduced cerebral blood flow and volume [51,54]. It is not unexpected that this superficial layer of the frontal lobe, assessed by the NIR light, which is associated with emotionality and executive functioning such as planning and sequencing, reduces its metabolic rate upon falling asleep. The current findings are consistent with other imaging techniques, which have shown that the type of sleep seen at the beginning of the night is associated with reduced cerebral metabolic rate as measured by PET scan [8] and reduced cerebral blood flow [17, 19, 26, 27].

Previous studies using NIRS in frontal areas during the wakefulness to sleep transition in humans have also shown decreased oxy-Hb as in the current study [46, 47]. In contrast to the current work's finding of deoxy-Hb reductions, past studies have described an increase in deoxy-Hb in the transition to sleep. This discrepancy may be due to the current work's focus on the changes in the immediate region around the transition to sleep. Our analysis was limited to the 5 s preceding and 20 s following the state changes. One past study examined longer-term changes over many minutes and therefore did not concentrate on the transient change at the boundary [46]. The other study used a sampling rate of 5 sec for NIRS, which is a temporal resolution that would not be capable of detecting brief changes [47]. Alternatively, the differences between the

current and past studies with regard to deoxy-Hb may be due to methodological differences. The current study examined naps during the day, in partially sleep deprived individuals as compared with nocturnal sleep in past work. In an attempt to assess this possible explanation we re-studied one of our subjects at his typical bedtime. These preliminary data show the same changes in the chromophores that we obtained during the day.

Other differences in methods between the current and past studies which include, differences in scalp locations of the optodes, the current studies selection of state transitions that were clear and uniform, and differences in the NIRS apparatus, sampling rate, and different light wavelengths employed, may explain the discrepancies in findings. Only more work will settle the issue.

Although we only analyzed short segments of data we observed a pattern of small changes in oxy-Hb and deoxy-Hb, both before and after the transition to sleep. The pattern was not uniform; in some trials the two chromophores were reciprocally related and in other trials parallel changes occurred. Because we did not examine longer-term trends a direct comparison to the findings of previous work is not possible.

Falling asleep is gradual as reflected in a number of parameters, including decreased tonus of the skeletal musculature and responsively to sensory stimulation [28]. The current finding of a transient reduction of substantial magnitude in oxy-Hb coupled with a smaller reduction in deoxy-Hb that is bracketed by smaller, mixed changes, suggests that cortical hemodynamics are switched abruptly into a specific mode at sleep onset.

The validity of the current findings at sleep onset is supported by the opposite

results obtained when subjects are awakened from sleep. The increases in both oxy-Hb and deoxy-Hb are synchronized and time locked to the awakening period. Because we abruptly awakened subjects, the precise point of sleep offset is more distinct than sleep onset. This ease of identification may be reflected in the reduced variability in the time between Scored Sleep Offset to the Switch Point compared to Scored Sleep Onset to the Switch Point. While this difference is probably due to the sharp contrast between sleep and wakefulness at the abrupt awakening, it may also, in part, be due to the adaptive advantage of consistency of cerebral responsibility to an awakening.

Many studies employing NIRS in the evaluation of the cerebral hemodynamic response to mental activation have also shown oxy-Hb increases as we have found at sleep offset [50, 54]. While most studies have found that deoxy-Hb is decreased during activation [54] there has been one study using intrinsic optical signals and two studies using f-MRI in which activation produced an initial, short lived, increase in deoxy-Hb as we have found at sleep offset [36, 52, 55]. The parallel changes in oxy-Hb and deoxy-Hb that define the Switch Point and last for approximately 3 to 4 s, suggest that the vascular response takes in the order of seconds to make the switch in response to changes in neuronal demands associated with sleep and wakefulness. While the parallel and synchronized changes in oxy-Hb and deoxy-Hb at the transition between sleep and wakefulness were clearly seen, they were not invariably present. In a minority of trials only small reciprocal changes occurred. It is not clear if this represents a limitation of the NIRS technique or the variability of hemodynamics at the global central nervous system change in the sleep state transition period.

The modified Beer-Lambert algorithm used to establish the concentration of oxy-

Hb and deoxy-Hb requires the knowledge of the pathlength of the light through the tissue [54]. There are NIRS techniques, such as frequency domain and time-resolved methods, that assess pathlength and permit the derivation of absolute levels of the hemoglobin molecules [55, 56]. Because the reflectance mode used in this study does not permit the determination of pathlength, it is necessary to assume that this distance does not change during the measurement period. While pathlength is affected by changes in the chromophore concentrations themselves [54] this assumption of constant pathlength is reasonable in measurements taken within the individual at the same location [57]. The data thus obtained is semi-quantitative, trend data, with no absolute levels determined. Relative changes in concentration of the hemoglobin molecules within the same individual, at the same optode position are possible. Moving the optodes to a different location on the head in the same individual or to a different subject will necessarily void the assumption of constant light pathlength and obviate comparisons of absolute amplitudes of the chromophores. This limits the applicability of this reflectance mode method. The within subject design of the current work avoids the problem of individual differences.

In summary, a synchronized, parallel change in oxy-Hb and deoxy-Hb is a discrete event that occurs in the transition from both sleep to wakefulness and wakefulness to sleep. The major source of these changes measured in this study is the cerebral cortex at the frontal pole. This transient and abrupt change in cerebral hemodynamics resembles a switch process that resets the concentration of both chromophores to a new level; lower at sleep onset and higher at sleep offset. To the extent that these changes in the optical density of these hemoglobin molecules represent

changes in cerebral blood flow or volume they, reflect the different perfusion demands of these different states.

8.5. References

1. National Commission on Sleep Disorders Research. (1993). Wake up America: A national sleep alert: Vol. 1. Executive summary and executive report. Washington, DC: Author.
2. Rechtschaffen, A., and Kales, A. (1968). "A manual of standardized terminology, techniques, and scoring system fro sleep stage of human subjects" (National Institutes of Health Publication No. 204). Washington, DC: U.S. Government Printing Office.
3. Buchsbaum M S, Gillin J C, Wu J, et al. "regional cerebral glucose metabolic rate in human sleep assessed by positron emission tomography", Life Sciences, 45(15), 1349-1356, (1989).
4. Kamba M, Suto M, Ohta Y, et al., "Cerebral metabolism in sleep apnea: Evaluation by magnetic resonance spectroscopy", Am. J. Respir. Crit. Care Med. 156: 296-298, (1997).
5. Toga, A.W. and Mazziotta, J.C. (Eds.), Brain Mapping: The Methods, Academic Press, San Diego, 1996, 471 pp.
6. McCormick, P.W., Stewart, M., Goetting, M.G., Dujovny, M., Lewis, G., and Ausman, J.I., Noninvasive cerebral optical spectroscopy for monitoring cerebral oxygen delivery and hemodynamics, Critical Care Med., 19 (1) (1991) 89-97.
7. Braun, A.R., Balkin, T.J., Wesenten, N.J., Carson, R.E., Varga, M., Baldwin, P., Selbie, S., Belenky, G., and Herscovitch, P., Regional cerebral blood flow

throughout the sleep-wake cycle: An $H_2{}^{15}O$ PET study, Brain, 120 (1997) 1173-1197.

8. Buchsbaum, M.S., Gillin, J.C., Wu, J., Hazlett, E., Sicotte, N., Dupont, R.M., and Bunney, Jr., W.E., Regional cerebral glucose metabolic rate in human sleep assessed by positron emission tomography, Life Sciences, 45 (1989) 1349-1356.

9. Buchsbaum, M.S., Mendelson, W.B., Duncan, W.C., Coppola, R., Kelsoe, J., and Gillin, J.C., Topographic cortical mapping of EEG sleep stages during daytime naps in normal subjects, Sleep, 5 (3) (1982) 248-255.

10. Droste, D.W., Berger, W., Schuler, E., and Krauss, J.K., Middle cerebral artery blood flow velocity in healthy persons during wakefulness and sleep: A transcranial doppler study, Sleep, 16 (7) (1993) 603-609.

11. Heiss, W.D., Pawlik, G., Herholz, K., Wagner, R., and Wienhard, K., Regional cerebral glucose metabolism in man during wakefulness, sleep, and dreaming, Brain Res., 327 (1985) 362-366.

12. Hong, C.C., Gillin, J.C., Dow, B.M., Wu, J., and Buchsbaum, M.S., Localized and lateralized cerebral glucose metabolism associated with eye movement during REM sleep and wakefulness: A positron emission tomography (PET) study, Sleep, 18 (7) (1995). 570-580.

13. Madsen, P.L., Schmidt, J.F., Wildschiodtz, G., Friberg, L., Holm, S., Vorstrup, S., and Lassen, N.A., Cerebral oxygen O_2 metabolism and cerebral blood flow in humans during deep and rapid-eye-movement sleep, J. Appl. Physiol., 70 (6) (1991) 2597-2601.

14. Maquet, P., Positron emission tomography studies of sleep and sleep disorders, J. Neurol., 244 (Suppl. 1) (1997) S23-S28.

15. Maquet, P., Dive, D., Salmon, E., Sadzot, B., Franco, G., Poirrier, R., , von Frenckell, R., and Franck, G., Cerebral glucose utilization during sleep-wake cycle in man determined by positron emission. tomography and [18F]2-fluoro-2-deoxy-D-glucose method, Brain Res., 513 (1990) 136-143.

16. Meyer, J.S., Sakai, F., Karacan, I., Derman, S., and Yamamoto, M., Sleep apnea narcolepsy, and dreaming: Regional cerebral hemodynamics, Ann. Neurol., 7 (1980) 479-485.

17. Meyer, J.S., Ishikawa, Y., Hata, T., Karacan, I., Cerebral blood flow in normal and abnormal sleep and dreaming, Brain and Cognition, 6 (1987) 266-294.

18. Ogilvie R.D. and Harsh, J.R. (Eds.) Sleep Onset: Normal and Abnormal Processes, American Psychological Association, Washington DC, 1994, 397 pp.

19. Sakai, F., Meyer, J.S., Karacan, I., Derman, S., and Yamamoto, M., Normal human sleep: Regional cerebral Hemodyamics, Ann. Neurol., 7 (1980) 471-478.

20. Van der Zee, P, Cope, M, Arridge SR, et al Experimentally measured optical pathlengths for the adult head, calf and forearm and the head of the newborn infant as a function of interoptode spacing. In: Goldstick, TK, Cabe, MML, Maguire, DJ (eds) Oxygen Transport to Tissue XII, P. Plenum Press, New York, 1992.

21. Wright Jr., K.P., Badia, P., and Wauquier, A.., Topographical and temporal patterns of brain activity during the transition from wakefulness to sleep, Sleep 18 (10) (1995) 880-889.

22. Maquet, P. and Phillips, C., Functional brain imaging of human sleep, J. Sleep Res., 7 (Suppl. 1) (1998) 42-47.

23. Chance, B., Leigh, J.S., Miyake, H., Smith, D., Nioka, S., Greenfeld, R., Finander, M., Kaufmann, K., Levy, W., and Young, M., Comparison of time resolved and un-resolved measurements of deoxyhemoglobin in brain. Proc. Natl. Acad. Sci. 85: (1988) 4971-4975.

24. Merica, H. and Gaillard, J.M., The EEG of the sleep onset period in insomnia: A discriminant analysis, Physiology & Behavior, 52 (1992) 199-204.

25. Ogilvie, R.D., Simons, I.A., Kuderain, R.H., MacDonald, T., and Rustenburg, J., Behavioral, event-related potential, and EEG/FFT changes at sleep onset, Psychophysiology, 28 (1) (1991) 54-64

26. Hajak, G., Klingelhöfer, J., Schulz-Varszegi, M., Matzander, G., Sander, D., Conrad, B., and Rüther, E., Relationship between cerebral blood flow velocities and cerebral electrical activity in sleep, Sleep, 17 (1) (1994) 11-19.

27. Madsen, P.L., Schmidt, J.F., Holm, S., Vorstrup, S., Lassen, N.A., and Wildschiodtz, G., Cerebral oxygen metabolism and cerebral blood flow in man during light sleep (stage 2), Brain Res., 557 (1991) 217-220.

28. Rechtschaffen, A.., Sleep onset: Conceptual Issues. In: R.D. Ogilvie and J.R. Harsh. (Eds.) Sleep Onset: Normal and Abnormal Processes. American Psychological Association, Washington DC, 1994, pp. 3-17.

29. Jobsis, F.F., Noninvasive, infrared monitoring of cerebral and myocardial oxygen sufficiency and circulatory parameters, Science, 198 (4323) (1977) 1264-1267.

30. Delpy, D.T., Cope, M., van der Zee, P., Arridge, S., Wray, S., and Wyatt, J., Estimation of optical path length, Phys. Med. Biol., 33 (1988) 1433-1442.

31. Delpy, T., Cope, M.C., Cady, E.B., Wyatt, J.S., Hamilton, P.A., Hope, P.L., Wray, S., and Reynolds, E.O.R., Cerebral monitoring in newborn infants by magnetic resonance and near infrared spectroscopy, Scand. J. Clin. Lab. Invest., 47, Suppl 188, (1987) 9-17.

32. Ferrari, M., Wilson, D.A., Hanley, D.F., Hartmann, J.F., Rogers, M.C., and Traystman, R.J., Noninvasive determination of hemoglobin saturation in dogs by derivative near-infrared spectroscopy, Am. J. Physiol., 256 (5 part 2) (1989) H1493-H1499.

33. Kurth, C.D., Steven, J.M., Benaron, D., and Chance, B., Near-infrared monitoring of the cerebral circulation, J. Clin. Monit., 9 (1993) 163-170.

34. McCormick, P.W., Stewart, M., Goetting, M.G., and Balakrishnan, G., Regional cerebrovascular oxygen saturation measured by optical spectroscopy in humans, Stroke, 22 (1991) 596-602.

35. McCormick, P.W., Stewart, M., Ray, P., Lewis, G., Dujovny, M., and Ausman, J.I., Measurement of regional cerebrovascular haemoglobin oxygen saturation in cats using optical spectroscopy, Neurol. Res., 13 (1) (1991) 65-70.

36. Menon, R.S., Ogawa, S., Hu, X., Strupp, J.P., Anderson, P., and Ugurbil, K., BOLD based functional MRI at 4 tesla includes a capillary bed contribution: Echo-planar imaging correlates with previous optical imaging using intrinsic signals, Magn. Reson. Med. 33 (3) (1995) 453-459.

37. Punwani, S., Ordidge, R.J., Cooper, C.E., Amess, P., and Clemence, M., MRI measurements of cerebral deoxyhaemoglobin concentration [dHb]--correlation with near infrared spectroscopy (NIRS), NMR Biomed., 11 (6) (1998) 281-289.

38. Skov, L., Pryds, O., and Greisen, G., Estimating cerebral blood flow in newborn infants: Comparison of near infrared spectroscopy and 133Xe clearance, Pediatr. Res., 30 (6) (1991) 570-573.

39. Smielewski, P., Kirkpatrick, P., Minhas, P., Pickard, J.D., and Czosnyka, M., Can cerebrovasular reactivity be measured with near-infrared spectroscopy?, Stroke 26 (12) (1995) 2285-2292.

40. Tamura, M., Hazeki, O., Nioka, S., Chance, B., and Smith, D.S., The simultaneous measurements of tissue oxygen concentration and energy state by near-infrared and nuclear magnetic resonance spectroscopy, Exp. Med. Biol, 222 (1988) 359-363.

41. Yoxall, C.W., Weindling, A.M., Dawani, N.H., and Peart, I., Measurement of cerebral venous oxyhemoglobin saturation in children by near-infrared spectroscopy and partial jugular venous occlusion, Pediatr. Res., 38 (1995) 319-323.

42. Hayakawa, T, Terashima, M, Kayukawa, Y, Ohta, T, Okada, T. Changes in cerebral oxygenation and hemodynamics during obstructive sleep apneas. Chest, 109, 4, 1996, 916-921.

43. Zhang G, Spielman AJ, D'Ambrosio P, Nagato M, Serizawa S, Conroy D , Lombardo G, and Alfano RR. The cerebral hemodynamics of obstructive sleep apnea probed by Near-Infrared Spectroscopy (NIRS). Sleep Research, 1998.

44. Skov, L, Ryding, J, Pryds, O, and Greisen, G. Changes in cerebral oxygenation and cerebral blood volume during endotracheal suctioning in ventilated neonates. Acta Paediatr 81, 389-393, 1992.

45. Smith, DS, Levy, W, Maris, M, Chance, B. Reperfusion hyperoxia in brain after circulatory arrest in humans. Anesthesiology, 73, 12-19, 1990.

46. Hoshi, Y., Mizukami, S., and Tamura, M., Dynamic features of hemodynamic and metabolic changes in the human brain during all-night sleep as revealed by near-infrared spectroscopy, Brain Res., 652 (1994) 257-262.

47. Shiotsuka, S., Atsumi, Y., Ogata, S., Yamamoto, R., Igawa, M., Takahashi, K., Hirasawa, H., Koyama, K., Maki, A., Yamashita, Y., Koizumi, H., and Toru, M., Cerebral blood volume in the sleep measured by near-infrared spectroscopy, Psychiatry and Clinical Neurosciences, 52 (2) (1998) 172-173.

48. Hazan, J, Broughton, R. Qantitative topographic EEG mapping during drowsiness and sleep onset. In: Ogilvie R.D. and Harsh, J.R. (Eds.) Sleep Onset: Normal and Abnormal Processes, American Psychological Association, Washington DC, 1994, 219-235.

49. Jasper, H., Report of the committee on methods of clinical examination in electroencephalography, Electroencephalogr. Clin. Neurophysiol., 10 (1959) 370-375.

50. Obrig, H. and Villringer, A.., Near-infrared spectroscopy in functional activation studies. Can NIRS demonstrate cortical activation?. In: Villringer A.., and Dirnagl U., (Eds.), Optical Imaging of Brain Function and Metabolism II, Plenum Press, New York, 1997, pp. 113-127.

51. Villringer, A., and Dirnagl, U., Coupling of brain activity and cerebral blood flow: Basis of functional neuroimaging, Cerebrovascular and Brain Metabolism Reviews, 7 (1995) 240-276.

52. Ernst, T., and Henning, J., Observation of a fast response in functional MR, Magn. Reson. Med. 32 (1994) 146-149.

53. Cohen, J., and Cohen, C., Applied Multiple Regression/Correlation Analysis for the Behavioral Sciences, Lawrence Erlbaum, NY, 1975, 490 pp.

54. Villringer, A., Functional neuroimaging: Optical approaches, In: Villringer A., and Dirnagl U., (Eds.), Optical Imaging of Brain Function and Metabolism II, Plenum Press, New York, 1997, pp. 1-18.

55. Sevick, EM, Chance, B, Leigh, J, Nioka, S, Maris, M. Quantitation of time- and frequency-resolved optical spectra for the determination of tissue oxygenation. Analytical Biochemistry, 195, 330-351, 1991.

56. Mantulin, WW, Fishkin, JB, So, PTC, Gratton, E, Maier, JS. Quantitative diffusive wave spectroscopy in tissues. SPIE Proceedings, 1888, 420-427, 1993.

57. Germon, TJ, Evans, PD, Manara AR, Barnett, NJ, Wall, P, Nelson, RJ. Sensitivity of near infrared spectroscopy to cerebral and extra-cerebral oxygenation changes is determined by emitter-detector separation. J Clinical Monitoring and Computing 14, 353-360, 1998.

8.6. Tables

Table 8-1: Electrophysiological Characteristics of Sleep Stages

Stage of sleep	Predominant EEG Activity	EOG characteristics	EMG activity
1	Low voltage, mix frequency	Slow	Decreased from awake
2	Sleep spindles and K complexes	None	Decreased from awake
3	Sleep spindles and slow waves	None	Decreased from awake
4	Mostly slow waves	None	Decreased from awake
REM	Low voltage, mix frequency	Rapid	Nearly absent

EEG: electroencephalograph, EOG: electrooculographic, EMG: electromyography, REM: rapid eye movement [2].

Table 8-2 Data analytic procedure and strategy for the examination of sleep onset and sleep offset.

Sequence	Method	Aim
Step 1	Expert sleep scorer determines the time when EEG alpha disappears (appears).	Point of human Scored Sleep Onset (Offset).
Step 2	Computer FFT identification of the point at which spectral power of EEG alpha is maximally reduced (increased).	Point of computer FFT Sleep Onset (Offset).
Step 3	Test if there is a difference between the points of Scored and FFT Sleep Onset (Offset).	Convergent validity.
Step 4	Determines the maximal change in the concentration of oxy-Hb in the region of Scored Sleep Onset (Sleep Offset).	Confirms that the oxy-Hb response is a decrease at sleep onset (increase at sleep offset).
Step 5	Identifies the point of maximal decrease (increase) in the concentration of oxy-Hb in the region of Scored Sleep Onset (Sleep Offset).	Locates the region of the NIRS signal to be used to identify the coordinated changes in the hemoglobin parameters.
Step 6	Compares the magnitude and direction of the changes in the concentration of oxy-Hb, deoxy-Hb and t-Hb at the point of maximal decrease (increase) of oxy-Hb.	Assesses frontal cerebral hemodynamics associated with falling asleep (waking up).
Step 7	Determines the duration of the synchronized and parallel decrease (increase) in oxy-Hb and deoxy-Hb during the sleep onset (offset) period.	Measures the duration of the hemodynamic Switch Point.
Step 8	Assesses the time delay between the Scored Sleep Onset (Offset) and the synchronized and parallel changes in the chromophores at the Switch Point.	Describes the timing of changes in NIRS in relation to state change.
Step 9	Calculates the correlation between oxy-Hb and deoxy-Hb before, after, and at the Switch Point, in the sleep onset (offset) period.	Describes the relationship between oxy-Hb and deoxy-Hb before, after and at the Switch Point.

The sequence of analyses used for examining sleep onset and, in the parentheses, the analogous strategy for sleep offset. The Fast Fourier Transform (FFT) of alpha power, maximal change in oxy-Hb, maximal decrease (and increase) in oxy-Hb, and changes in deoxy-Hb and total hemoglobin (t-Hb) were determined by a computer analysis of the difference in the average values between two successive 5 s windows.

Table 8-3 Changes in alpha power (μV^2 units) and hemoglobin concentrations (arbitrary units) in the transition from wakefulness to sleep.

Parameter	mean	SD	t	p <
ΔFFT alpha power C_3-A_1A_2 (log scale)	-1.1423	0.4145	5.56	0.0005
ΔFFT alpha power O_1-F_Z (log scale)	-1.1498	0.4070	5.75	0.0005
Δoxy-Hb	-0.0386	0.0124	5.29	0.001
Δdeoxy-Hb	-0.0056	0.0126	2.00	0.063
Δt-Hb	-0.0441	0.0199	4.47	0.002

The segment of the transition period where there was a maximal reduction in oxy-Hb between two successive 5 s periods was used for analysis of hemoglobin changes. The data set was based on a total of 26 observations in 9 subjects. The mean of each subject's data was used for the statistical analysis. The symbol Δ stands for change, calculated as follows: Average parameter value in the second 5 s window minus the value in the first 5 s window. Negative values mean a reduction in the parameter from wakefulness to sleep.

Table 8-4 Changes in alpha power (μV^2 units) and hemoglobin concentrations (arbitrary units) in the transition from sleep to wakefulness.

Parameter	mean	SD	t	p <
ΔFFT alpha power C_3-A_1A_2 (log scale)	1.57	0.28	7.14	0.0001
ΔFFT alpha power O_1-F_Z (log scale)	1.57	0.40	5.93	0.0005
Δoxy-Hb	0.100	0.036	5.01	0.001
Δdeoxy-Hb	0.014	0.023	2.32	0.05
Δt-Hb	0.114	0.039	5.11	0.001

The segment of the transition period where there was a maximal increase in oxy-Hb between two successive 5 s periods was used for analysis. The data set was based on a total of 37 observations in 9 subjects. The mean of each subject's data was used for the statistical analysis. Definitions as in Table 8-3.

8.7. Figures

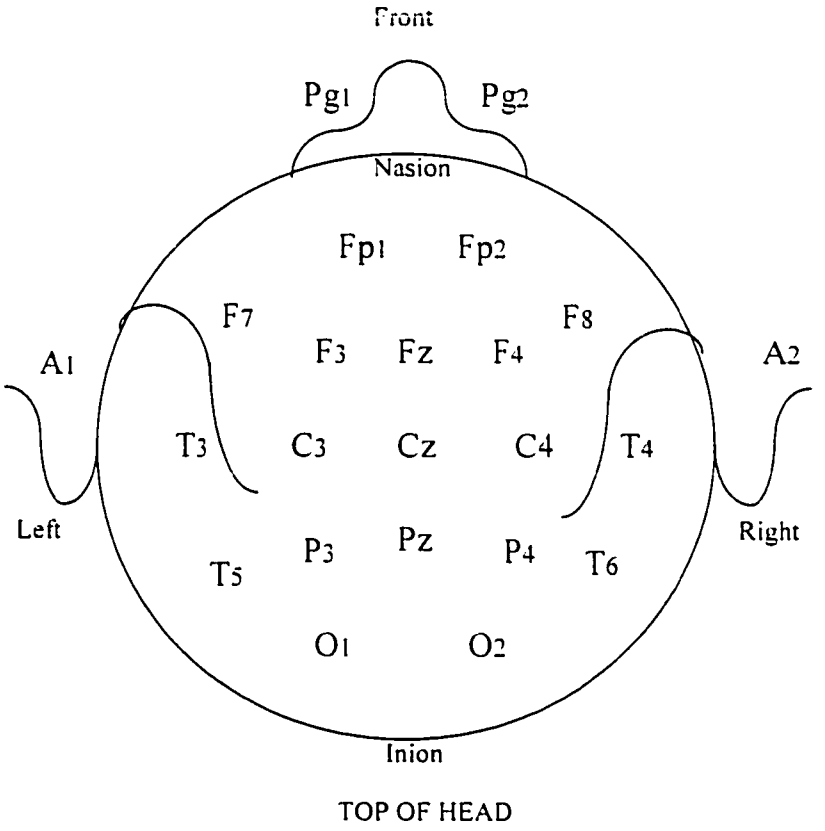

Figure 8-1 Standard International (12-20) Electrode Placement.

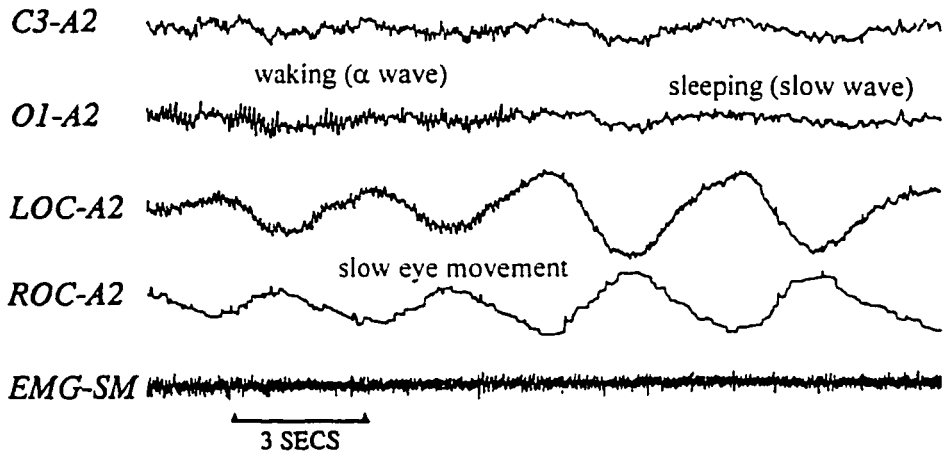

Figure 8-2 Typical EEG record of sleep on set transition with EEG α wave disappearance and slow eye movements.

The main part of the brain activity is recorded in O1-A2 channel. This section of EEG time trace is recorded the procedure of a subject from wake to sleep transition. Left part represents the subject in wake status, and right part shows the subject in sleep status.

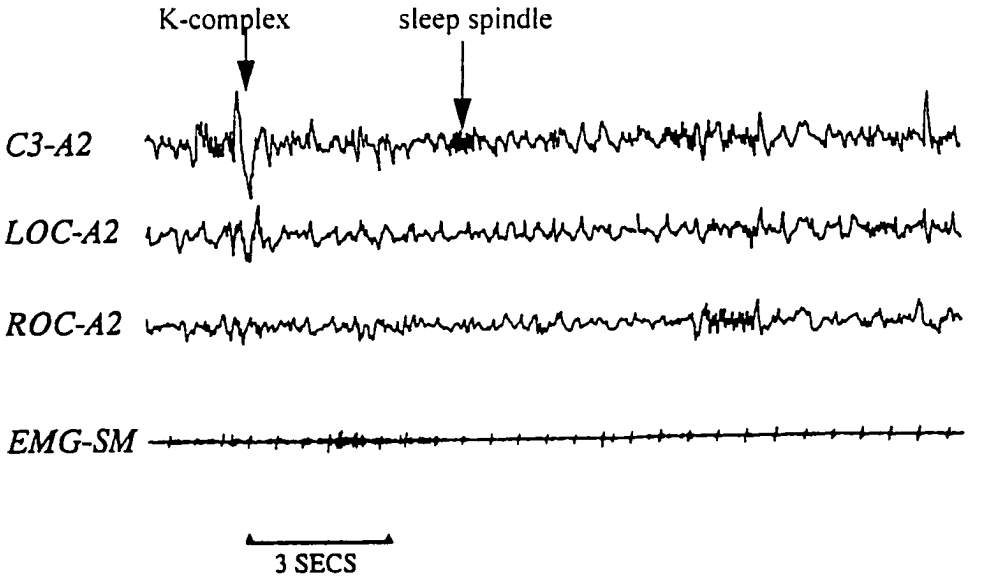

Figure 8-3 Typical EEG record trace of sleep stage 2 with K-complex activity and sleep spindle activity.

The main part of the brain activity is recorded in C3-A2 channel. This section of EEG time trace is the typical status stage 2 sleep. The finger print wave shapes, K-complex and sleep spindle, are appear in this record section.

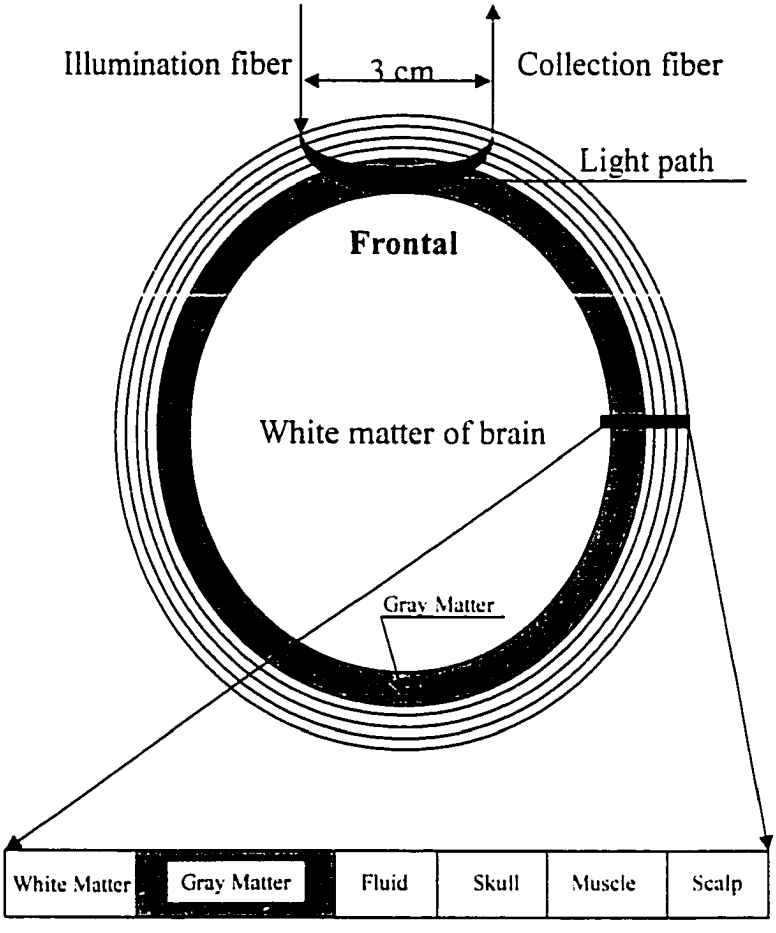

Figure 8-4 Schematic of the near infrared probes and light path

A schematic representation of the NIRS set-up used to monitor local intracerebral brain activity is depicted. The view is looking down on the top of the head. The theoretical light path through the head represents only the major portion of the light delivered that scatters back and is detected in the collection fiber.

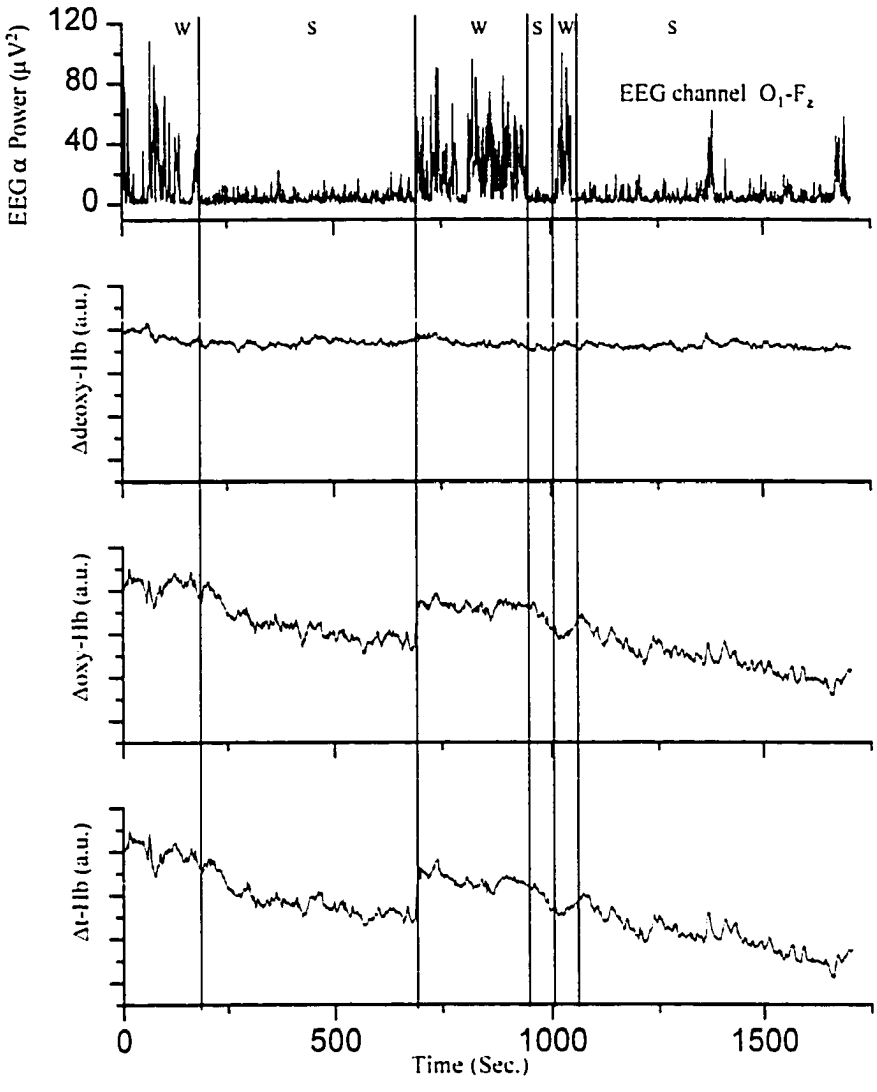

Figure 8-5 Long-term changes in EEG and NIRS between sleep and waking.

Illustration of the relative changes in hemoglobin concentration (oxygenated hemoglobin [oxy-Hb], deoxygenated hemoglobin [deoxy-Hb] and total hemoglobin [t-Hb]) calculated from the NIRS signal and changes in the Fourier Fast Transform (FFT) derived EEG alpha power as one subject goes through multiple transitions between waking and sleep. The vertical lines indicate the time of human Scored Sleep Onset and Offset. W indicates wakefulness, S indicates sleep and a.u. stands for arbitrary units.

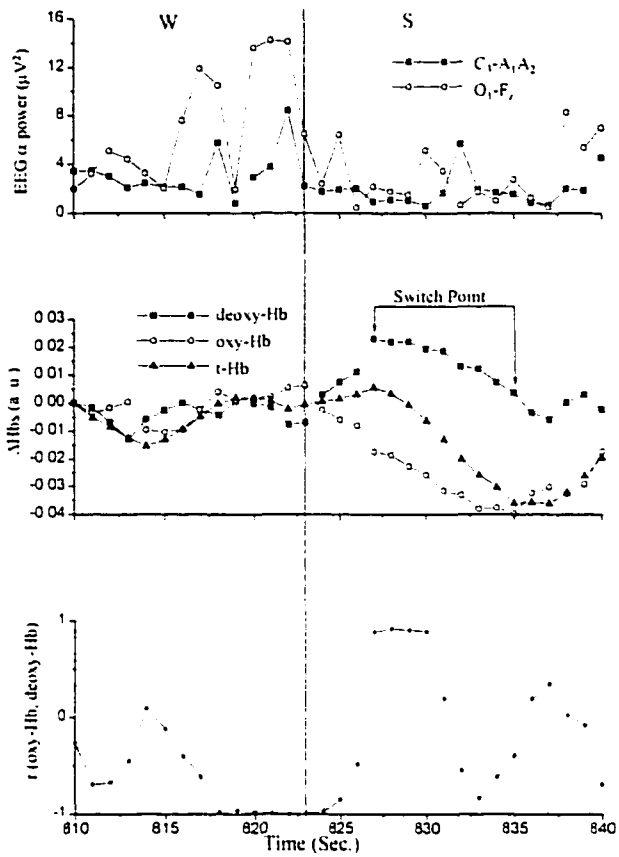

Figure 8-6 Cerebral hemodynamics at sleep onset.

Measurements are from one subject in the transition from wakefulness to sleep. An additional curve shows the cross correlation between oxy-Hb and deoxy-Hb for a 5 s window. The axis label ΔHbs refers to the relative changes in the three hemoglobin parameters. The vertical line, at the 823rd second, indicates the point of human Scored Sleep Onset. Arrows at the 827th and 835th seconds point to the beginning and ending (respectively) of the synchronized reduction in both oxy-Hb and deoxy-Hb called the Switch Point. Abbreviations list as in Figure 8-5.

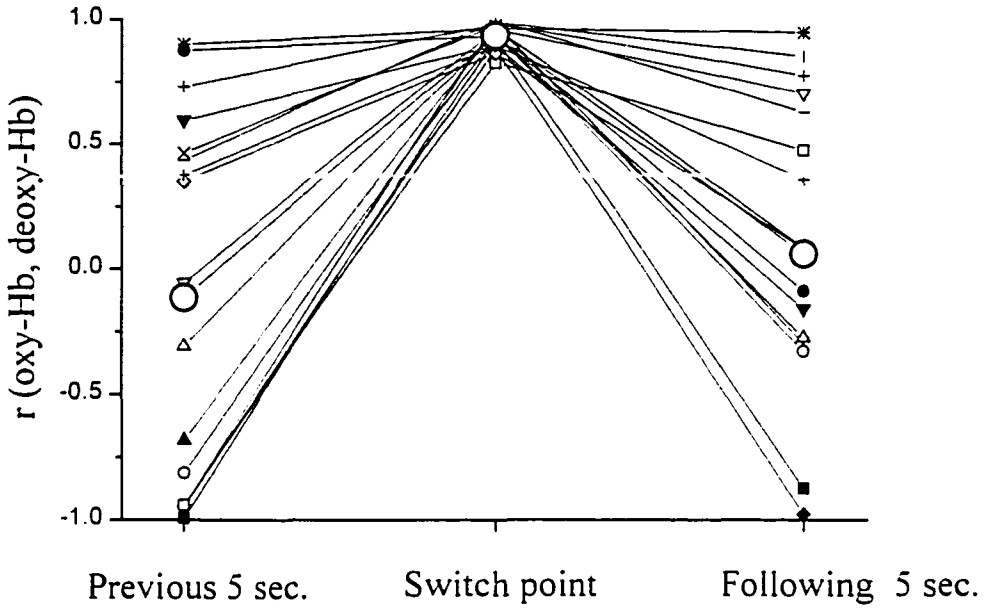

Figure 8-7 Correlation of oxy-Hb and deoxy-Hb around sleep onset

The middle set of values are the standardized correlation coefficients between oxy-Hb and deoxy-Hb at each sleep onset trial during the Switch Point. The first set of standardized correlations was obtained from the 5 seconds prior to the Switch Point and the third set from the 5 seconds after the Switch Point. The large open circles indicate the mean values (n = 18).

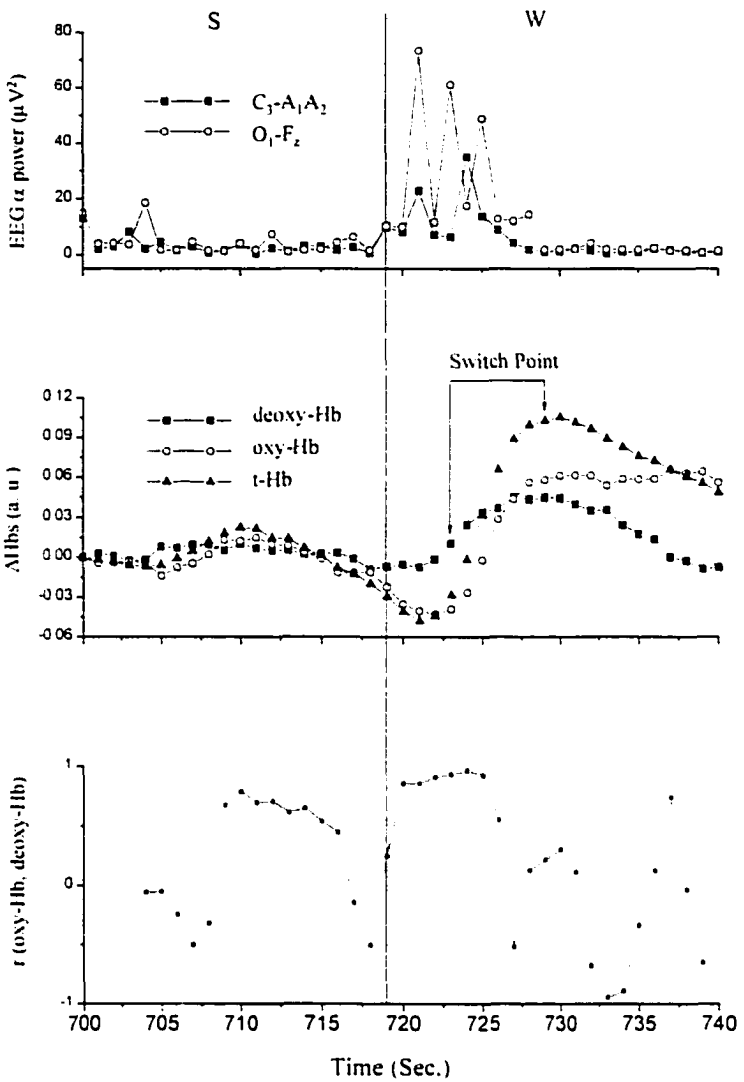

Figure 8-8 Cerebral hemodynamics at sleep offset

Measurements from one subject in the transition from sleep to wakefulness. Symbols are same as in Figure 8-6. The vertical line, at the 719th second, indicates the point of human Scored Sleep Offset. Arrows at the 723rd and 729th seconds point to the beginning and ending (respectively) of the synchronized increase in both oxy-Hb and deoxy-Hb called the Switch Point.

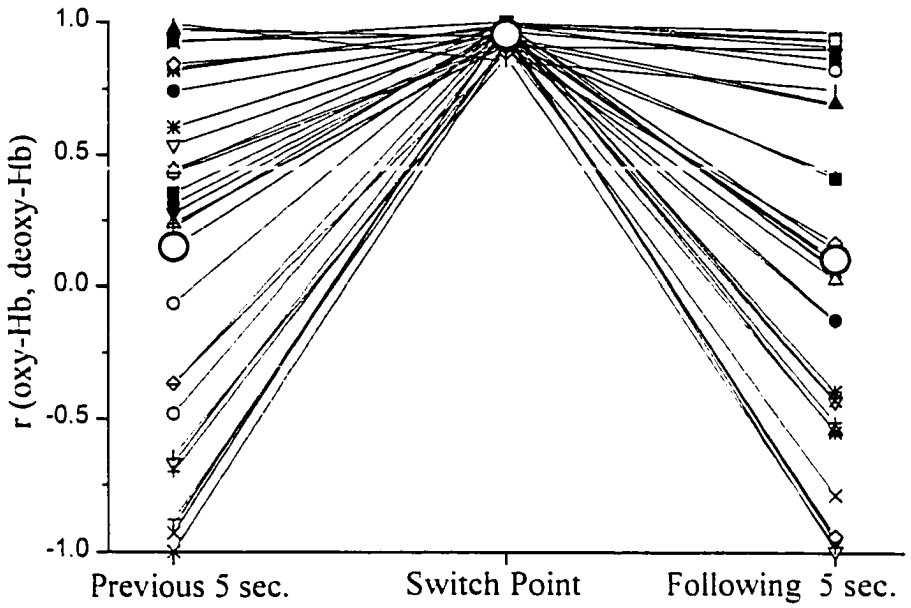

Figure 8-9 Correlation of oxy-Hb and deoxy-Hb around sleep offset

Definitions are same as in Figure 8-7. n = 32.

9. Cerebral hemodynamics of obstructive sleep apnea syndrome probed by CW NIRS method

9.1. Introduction

One of the most serious sleep disorder diseases is obstructive sleep apnea syndrome (OSAS) because it can leads to hypoxia and hypoxemia, and possibly death. Since the brain is very sensitive to hypoxia, recurrent decrease of the arterial oxygen saturation in sleep apnea could cause the patient not to get enough rest, and could induce brain injury [1]. OSAS has been associated with altered quality of life, daytime sleepiness, neuro-psychological dysfunction and cognitive deficits as well as cardiovascular disease, including systemic and pulmonary hypertension, arrhythmias and ischemic heart disease. Cerebro-vascular accidents, ranging from transient ischemic attacks to fatal strokes is closely associated to sleep apnea [2, 3].

Conventional polysomnography [4] detects sleep apnea in correlation to the various sleep stages. Polysomnography is a multi-channel record on paper for different signal channels. One signal, finger pulse oximetry, used to determine arterial oxygen saturation does not provide information on brain oxygenation, especially in subjects with preexisting anatomical and functional vascular pathology. Finger pulse oximetry, a peripheral measure of oxyhemoglobin saturation, is the standard measure of hemodynamics in the chemical assessment of obstructive sleep apnea.

This chapter describes the use of NIRS technique to OSAS patient in order to investigate the brain hemodynamic changes that accompany recurrent episodes of obstructive hypopnea during sleep with nasal continuous positive airway pressure (NCPAP) treatment. The NCPAP is accepted as a standard care for the treatment of obstructive sleep apnea-hypopnea syndrome.

9.2. *Material and method*

9.2.1. Subject

One patient was investigated. A 47 year old woman with witnessed loud snoring, apneas and a two year history of excessive sleepiness. Past medical history was significant for fibromyalgia, gastroesophageal reflux, arthritis, allergic rhinitis, urinary stress incontinence and intermittent high blood pressure. Medications at the time of the study included lansoprazole, naproxen and budesonide. The patient is 5' 1" tall and weighs 177 lbs. She had enlarged tonsils with nasal congestion on exam and a restrictive defect on pulmonary function testing. The study was approved by the City College of New York Institutional Review Board (see copy in appendix) and written documentation of informed consent was obtained from the subject.

9.2.2. Instrumentation

The NIRS device and EEG device setup for the sleep apnea subject investigations are described in Chapter 8.

For the daytime nap experiment, the arterial blood oxygenation (SaO_2) status was obtained from a finger of the subject by a finger pulse oximeter (Ohmeda Biox 3700 Pulse Oximeter, Ohmeda, a division of the BOC Group Inc. USA). Airflow was obtained

from the nose tidal air by an end tidal CO_2 monitor (Transportable End Tidal CO_2 Monitor, Model 602-11, Criticare Systems Inc. USA). The SaO_2 signal, end tidal CO_2 signal and the NIRS signals were simultaneously recorded by connecting to a polygraph recorder and a PC computer based digital recorder. During waking calibrations a number of breath holding maneuvers were conducted.

For the night experiment, an air mask was hooked up on the face of the subject. Nasal CPAP titration equipment (BiPAP airway management system, model 332092, Resperonics Inc. USA) was initiated as part of the treatment to improve the breathing of the subject during sleep apnea.

9.2.3. Procedure

The napping protocol was conducted from 2 to 5 p.m. Following preliminary calibrations and 3 minutes of waking recording with eyes alternatively opened and closed the room lights were turned off. Then the subject was requested to stop breathing by the order of an operator in order to produce a voluntary apnea to be compared with sleep apnea. After the three trails of the breathing holding test, the door of the sound attenuated room closed and the subject was told to go to sleep.

The night time sleep began around 11 p.m., which is the typical sleeping time of the subject. The additional air mask was hooked up on the subject face and connected to a CPAP treatment equipment to help the subject improving the breath quality during the night sleep. The beginning procedure is the same as the nap experiment. Following preliminary calibrations and 3 minutes of waking recording with eyes alternatively opened and closed, the room lights were turned off, the subject was requested to stop breathing by the order of an operator in order to produce a voluntary apnea that was

compared with sleep apnea. After the three trails of the breathing holding test, the door of the sound attenuated room closed and the subject was told to go to sleep. NCPAP pressure was set at 3 cm of H_2O at the start of the nocturnal polysomnogram. Shortly after falling asleep CPAP was increased to 6 cm of H_2O and this resolved the mixed obstructive apneas.

9.2.4. Data analysis method

The latencies from the start of apneas to changes in SaO_2, deoxy-Hb and oxy-Hb were compared to the latencies from the end of the apnea to the changes in these parameters. The latencies were calculated from the start and end of the apnea to the point when the hemodynamic change had just begun: 2% change for SaO_2, and a change of 10% of the mean peak to trough values for oxy-Hb and deoxy-Hb. These criteria for the start of the hemodynamic change were employed to discount minor fluctuations associated with normal physiological variations or instability of the devices.

In a separate analysis, the difference between the central and peripheral measures for the duration of the de-oxygenation and re-oxygenation phases associated with apnea were compared. The beginning of the de-oxygenation phase was defined as the start of the changes in the parameters from the start of the apnea, as defined above. The end of the de-oxygenation phase and the beginning of the re-oxygenation phase were defined as the minimum SaO_2 and oxy-Hb and deoxy-Hb values and the minimum deoxy-Hb value. Grouped data was analyzed by paired t-test.

9.3. Result

9.3.1. Daytime nap with sleep apnea

There were 177 breathing events during the 124.3 minutes of sleep in two naps (see Table 9-1 for descriptive summary). Virtually all-breathing events were obstructive hypopneas in that there was some minor airflow during part of the breathing events. The apnea plus hypopnea index was 85.4 events per hour of sleep. The patient remained supine during the entire recording and no REM sleep was recorded. Oxy-hemoglobin saturation measured by finger pulse oximetry was 92-95% during waking and on average fell to 68.8% in association with the apneas/hypopneas. The lowest SaO_2% value recorded was 47%.

We examined 27 sleep disordered breathing events in detail. The timing of the SaO_2 and NIRS responses were different, as one would expect from two different devices at different locations on the body. Overall the latency from the beginning and end of a breathing event to the SaO_2 and NIRS change was 30.2 sec and 11.1 sec respectively.

Figure 9-1 illustrates the analysis of one obstructive (effort not shown) sleep disordered breathing event of 32 sec duration. The upper panel represents the SaO_2 changes from fingertip. The blood with high oxygenation during normal breathing is seen in the peak part of the curve; and blood with low oxygenation induce by apnea is seen in the trough part of the curve. The second panel is the curve of deoxy-Hb change in the brain tissue during normal breath and apnea. The third panel shows the curve of oxy-Hb change in brain tissue during normal breathing and apnea. The bottom panel represents airflow from the subject's nose; the high amplitude part indicates the normal breath airflow and the flat part indicates no airflow during apnea by breathing stopped.

We have labeled this event an apnea although some diminished airflow occurs at times. There was a marked difference in the response time from the cessation and resumption of breathing. The NIRS measures showed a shorter delay to the response at the apnea termination compared to the delay at the beginning of the breathing event. For example, the oxy-Hb started 19 sec after the cessation of breathing while the rise in oxy-Hb started 9 sec after the resumption of breathing at the 41st second. In contrast, the time from the start of the apnea to the fall in SaO_2 was 26 sec and it was similar to the 31 sec latency to the rise in SaO_2, which occurred at the 63rd second.

9.3.2. Nighttime sleep with CPAP treatment

Figure 9-2 shows a three minutes obstructive hypopnea at a sub-optimal nasal CPAP pressure. The upper panel is the trace of respiratory effort, the high amplitude part indicates increased effort and the low amplitude part indicates reduced respiratory effort. The second panel is the trace curve of fingertip SaO_2, and the trough parts represent low blood oxygenation during the hypopnea. The third panel shows the oxy- and deoxy-Hb concentration in brain tissue. The solid line indicates deoxy-Hb change and dashed line represents the oxy-Hb change. The bottom panel shows the trace curve of end tidal CO_2 pressure from subject, the property of the curve is similar to the trace of respiratory effort. There is the same coordination between oxy-Hb, deoxy-Hb and SaO_2 but the process takes place very gradually.

Nasal CPAP pressure was set at 3 cm of H_2O at the start of the nocturnal polysomnogram. When the patient went into REM sleep, a sustained obstructive hypopnea of 180 sec was ensued (Figure 9-2). The SaO_2 fell from an initial value of 95% to 48% at the end of the breathing event. Decreased oxy-Hb and increased deoxy-Hb

changed in association with the SaO_2 decline of the hypopnea. Nasal CPAP pressure of 6 cm of H_2O (not shown) resolved the sleep disordered breathing.

9.3.3. Comparison of breathing events during wakefulness and sleep

The five minutes segment of data illustrated in Figure 9-3, consists of a sequence of four events; one breath hold maneuver during wakefulness, two obstructive hypopneic events during brief sleep episodes followed by a breath hold. The upper panel is the trace of respiratory effort, the high amplitude portion indicates increased effort and low amplitude portion and the flat portion represent decreased effort or no effort. The second panel is the trace curve of fingertip SaO_2, and the trough portion represent low blood oxygenation during the apnea. The third panel shows the oxy- and deoxy-Hb concentration in brain tissue. The solid line indicates deoxy-Hb change and dashed line represents the oxy-Hb change. The bottom panel shows the trace curve of end tidal CO_2 pressure and indicates relative airflow. The breath hold events are clearly displayed the voluntary breath holds on upper and bottom panels (see the labeled part in). The spontaneous breath stopping by apnea events are also shown in same panels. This sequence of events permits us to compare the NIRS response to the SaO_2% response during both wakefulness and sleep at close temporal proximity.

The breath hold maneuvers were initiated at approximately the middle of the expiratory phase of the breathing cycle. After the first breath hold, the subject was

allowed to rest undisturbed for just over two minutes. During this time two sleep episodes during which two obstructive hypopneic events occurred. In general, the four disordered breathing events were fairly comparable in duration, with fall in both SaO_2% and in oxy-Hb and with increased deoxy-Hb.

9.3.4. Comparison of peripheral and central hemodynamics

Grouped data for the 27 apneas analyzed showed a shorter delay to the cerebral response at the apnea termination compared to the delay at the beginning of the breathing event (Table 9-2). This shorter latency to the cerebral hemodynamic response was found for both oxy-Hb and deoxy-Hb. In contrast, there was no difference in the latency to the SaO_2 change after the apnea ended, compared to the latency from the start of the apnea.

As a result of the shorter delay to the NIRS response at the end compared to the start of the apnea, the duration of the de-oxygenation and re-oxygenation phases were different for finger pulse oximetry and NIRS; the duration of the decline of SaO_2 (mean = 25.3, [SD = 9.8] sec) was longer than both the duration of the deoxy-Hb increase (mean = 15.8, [SD = 4.8] sec, $t = 5.89$, $p < 0.0001$) and the oxy-Hb decrease (mean = 20.0, [SD = 4.7] sec, $t = 3.67$, $p < 0.002$). In contrast, during re-oxygenation, the duration of the rise of SaO_2 was shorter (mean = 10.0, [SD = 2.99] sec) than both the deoxy-Hb fall (mean = 22.2, [SD = 7.1] sec, $t = -8.18$, $p < 0.0001$) and oxy-Hb rise (mean = 19.0, [SD = 5.5] sec, $t = -6.61$, $p < 0.0001$).

9.4. Discussion

The current observations in a patient with severe OSA Syndrome illustrate the usefulness of the back scattering NIRS device, in describing cerebral hemodynamic

changes that complement the information obtained by finger pulse oximetry. As oxygen levels decline, apnea induced hypoxic exposure is of shorter duration in the brain compared to the periphery. There are a number of mechanisms associated with obstructive sleep apnea that may explain the short delay to the start of recovery in the brain. During apnea, cerebral blood flow velocity (CBFV) increases due to (a) an increase in the arterial blood pressure, as well as (b) an increase in CO_2 causing a dilation of cerebral vessels [5-10]. When breathing resumes, newly oxygenated blood would therefore be delivered to the brain at a rapid rate.

These mechanisms, that may explain the short delay to the start of re-oxygenation of a distal part of the brain's vasculature, do not continue for long during the post apneic period. Previous work has shown that the apnea induced increase in CBFV is short-lived and within seconds after breathing resumes CBFV declines abruptly [5, 9, 10]. These changes as well as the relatively larger portion of the mixed venous blood, compared to arterial blood, interrogated by NIRS, may explain the current findings of a longer duration of the re-oxygenation phase in the brain compared to the periphery.

During nasal CPAP titration, the failure to rapidly increase pressure during REM sleep, resulted in a long hypopnea and the lowest de-saturation seen with or without nasal CPAP. Assessment of cerebral oxy-Hb by NIRS showed a decline parallel with SaO_2. This episode illustrates that application of sub-optimal nasal CPAP may create unforeseen problems. This discovery is a cautionary tale and indicates that the brain is not spared during prolonged hypoxic events.

While these results are limited to observations in one patient with OSA Syndrome, data suggest that the dynamic changes in oxygenation produced by

obstructive sleep apnea are different in the peripheral and central compartments. Following apnea, the brain starts to re-oxygenation faster than the periphery. In addition to detecting these changes, optical monitoring of the brain has advantages that may help clarify cerebral based morbidity. If cerebral sites have different exposure to hypoxia, for example, this may help identify sites that are more vulnerable to damage in patients with OSA Syndrome. Furthermore, the rapid response of NIRS to changes in brain oxygenation represents a distinct clinical advantage over the slow response of finger pulse oximetry. In clinical situation, such as nasal CPAP titration, use of NIRS may allow more rapid correction of sleep-disordered breathing, and thus limit the brain's exposure to hypoxia.

In summary, while these results were limited to the observation in one patient, NIRS provided a measure of the changes in specific biochemical markers of oxy-Hb and deoxy-Hb. In addition, NIRS detected insufficient nasal CPAP pressure and the different response of the peripheral and central compartments to breathing events. The longer time delay of SaO_2 signal obtained by finger pulse oximetry than the response time of hemodynamic change obtained by NIRS device suggest that optical monitoring of the brain may have advantages that may help clarify the morbidity of OSA Syndrome.

These findings, using the new NIR optical neuron technique, show reciprocal changes in the concentration of oxy-hemoglobin and deoxy-hemoglobin in the frontal pole of the cerebrum during obstructive sleep hypopneas. There is a potential clinical significance of neuro-psychological deficits cerebral damage [1] and periodic intracerebral vascular stress [5] in obstructive sleep apnea. This potential clinical significance suggests that measures of cerebral hemodynamics should be regular

components of clinical monitoring. The NIRS technique, which is non-invasive, can be used over extended periods of time and has high temporal resolution. It may be a useful measure of central hemodynamics in the assessment of sleep disordered breathing.

9.5. References

1. Kamba M, Suto Y, Ohta Y et al., "Cerebral metabolism in sleep apnea: Evaluation by magnetic resonance spectroscopy", Am J Respir Crit Care Med, 1997, 156, 296-298.
2. Redline S, and Strohl K. P., "Recognition ans consequences of obstructive sleep apnea syndrome", Clin. Chest. Med. 19(1), 1-19 (1998).
3. Marrone O, Bonsignore M. R., Insalaco G., and Bonsignore G., "What is the evidence that obstructive sleep apnea is an important illness?", Monadi Arch. Chest Dis. 53(6), 630-639 (1998).
4. Douglas N. J. and Thomas J. M. A., "Clinical value of polysomnography", Lancet 339(8789), 347-350 (1992).
5. Klingelhofer J, Hajak G, Sander D, et al., "Assessment of intracranial hemodynamics in sleep apnea syndrome", Stroke, 1992, 23(10) 1427-1433.
6. Shephard J.W. (1989) "Cardiorespiratory changes in obstructive sleep apnea." In M.H. Kryger, T. Roth and W.C. Dement, editors. Principles and Practice of Sleep Medicine, 2nd ed. Saunders, Philadelphia, 657-666.
7. Hayakawa T., Terashima M., Kayukawa Y.,Ohta T., and Okada T., (1996) "Changes in cerebral oxygenation and hemodynamics during obstructive apneas," Chest, 109(4): 916-921.
8. Spielman A.J., Zhang G., Yang C.M., D'Ambrosio P., Serizawa S., Nagata M., von Gizycki H, and Alfano R.R., "Intercerebral hemodynamics probed by near

infrared spectroscopy in the transition between wakefulness and sleep," Brain Research (in press).

9. Markwalder T-M., Grolimund P., Seiler R.W., Roth F., and Aaslid R., (1984) "Dependency of blood flow velocity in the middle cerebral artery in end-tidal carbon dioxide partial pressue," J. Cereb. Blood Flow Metabbol., 4:368-372.

10. Baltors E.M., and Franklin K.A., (1994) "Impairment of cerebral perfusion during obstructive sleep apneas," Am. J. Respir. Crit. Care Med., 150: 1587-1591.

9.6. Tables

Table 9-1 Statistical summary of the SaO_2% changes during sleep.

There were 177 apnea cycles in 7460 sec. The average SaO_2 was 78.8 (±10.2) %.

Variable	Mean	SD	Max	Min
$Sa0_2$% High	88.6	5.7	98	74
SaO_2% Low	66.2	8.1	87	47
SaO_2% Difference (High – Low)	22.4	7.3	46	7
Duration of apnea/hypopnea cycle, sec	41.1	9.7	70	22

Table 9-2 The speed of the hemodynamic response from the start and the end of sleep apnea.

Latency from the start of apnea. Hemodynamic change mean [SD] sec		Latency from the end of apnea. Hemodynamic change mean [SD] sec		t level	Significance p <
SaO_2 fall	29.2 [8.9]	SaO_2	31.2 [3.4]	-1.18	NS
Deoxy-Hb rise	15.6 [4.4]	Deoxy-Hb fall	7.7 [3.7]	6.70	0.0001
Oxy-Hb fall	12.4 [3.4]	Oxy-Hb rise	8.7 [2.4]	4.39	0.0005

9.7. Figures

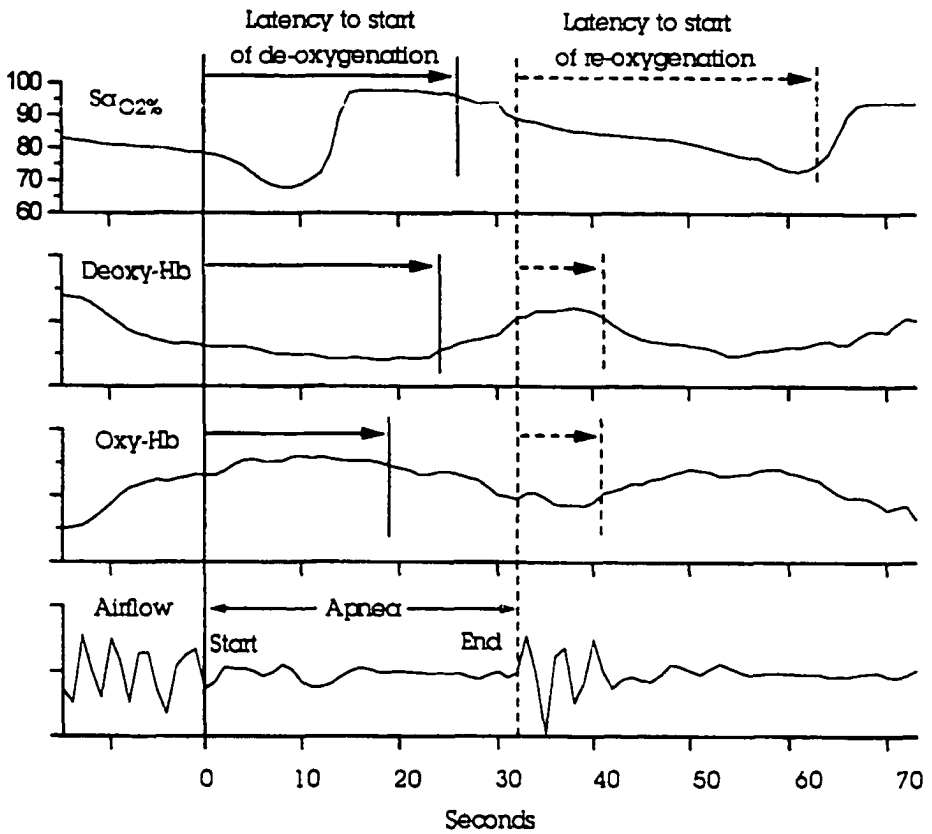

Figure 9-1 Latency to the hemodynamic response in the peripheral (SaO_2) and the cerebral (deoxygenated hemoglobin [deoxy-Hb] and oxygenated hemoglobin [oxy-Hb]) components.

Latencies are represented by arrows from the start (solid lines) and end (dashed lines) of one obstructive (respiratory effort not shown) sleep apnea event to the beginning of the de-oxygenation and re-oxygenation respectively. Values for deoxy-Hb, oxy-Hb and airflow are in arbitrary units.

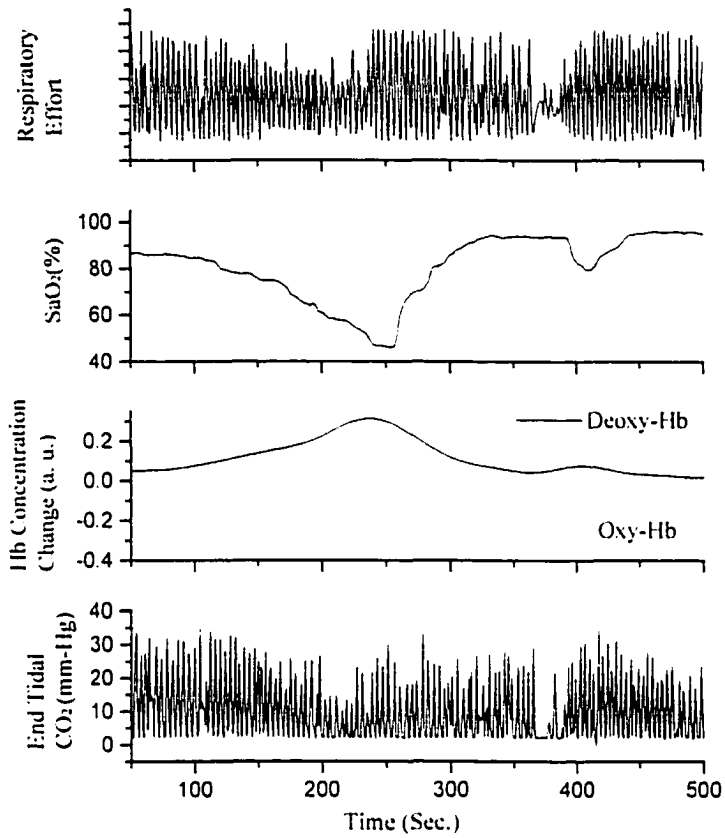

Figure 9-2 Insufficient nasal continuous positive airway pressure during REM sleep (not shown) results in a long hypopnea.

The extended decline in peripheral oxy-hemoglobin saturation (SaO_2) pressure in parallel with central decreases in oxy-Hb and increases in deoxy-Hb concentrations, measured from the intact skull. a.u., arbitrary units.

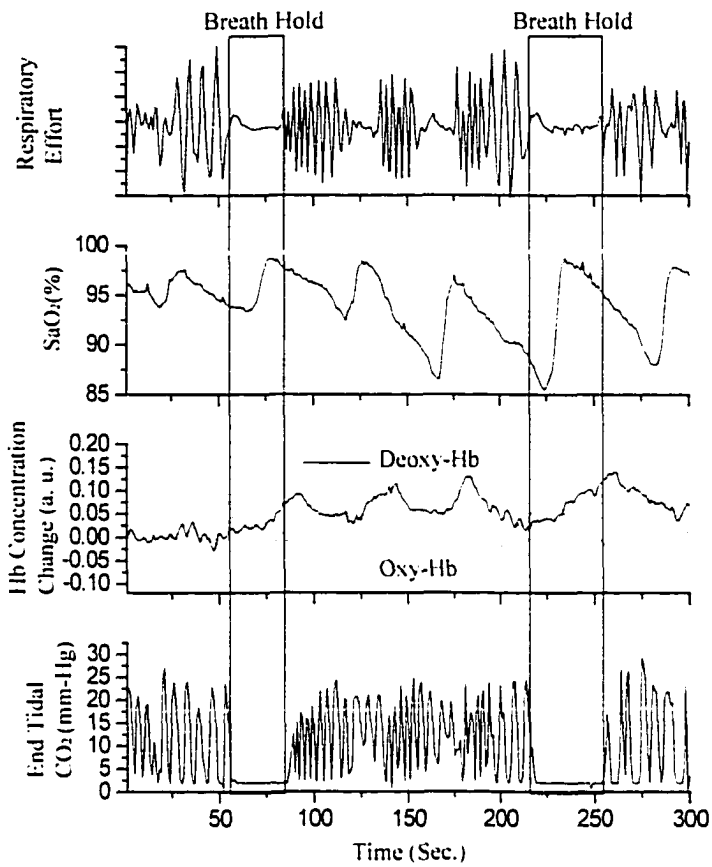

Figure 9-3 Comparison between breath holding and nature sleep apnea.

The artificial apnea records are labeled "Breath Hold" showing in the flat parts in the top panel of respiratory effect. The spontaneous apnea records are shown in the flat parts in top panel without labeling.

10. Summary of current research work

This chapter summarizes the discovers of current research work, including far-red to NIR spectral wing emission from biomedical samples under light excitation. Then it compares FD and CW method to measure hemodynamics of brain tissue and uses the CW method to investigate brain blood dynamics of sleep procedure in healthy and in sleep disordered human subjects.

10.1. Summary of the research work of far-red and NIR emission spectral wing

The application of far-red and NIR emission spectral wing from biomedical tissue sample has been demonstrated. The emission in this spectral region is relatively very weak compared with the Raman scattering signal. The far-red and NIR emission has generally been considered as the background noise in the Raman spectra profile. This research work demonstrates that the wing emission has some meaningful information. Even if the mechanism of the wing is not known, the spectral parameters can give us some useful information. The intensity can be used to classify some kind of tissues. Especially it can be used to differentiate the cancer part from normal human breast tissues. The research work of the emission from thermal damaged tissue samples shows that the emission intensity in this spectral region is proportional to the extent of the thermal damage of the tissue sample.

A simplified physical model has been used to explain the phenomena of the far-red emission from biomedical samples under laser excitation. Curve fitting results show

that the thermal damaged tissue has higher quantum efficiency than the non-treated tissue, and tumor tissue has higher quantum efficiency than the normal tissue.

10.2. Summary of research work of hemodynamic monitoring of brain tissue with NIRS method

The instrumentation research work describes the correlation between the signals obtained simultaneously with CW and FD method instruments in a newborn piglet brain perfusion-oxygenation model. The results demonstrate the CW method is able to detect and monitor both small and large changes in brain hemodynamics and oxygenation. This result indicates that the CW type NIRS device can be used to investigate brain blood perfusion and oxygenation in similar precession with FD type device.

The research work of using NIRS method to monitor blood perfusion and oxygenation in brain tissue for human subject sleep and wake transition with traditional EEG method, shows us that the brain tissue metabolism has a switch point at the front pole of the head. These metabolism switches are generally about few second delayed from the transition point between sleep and wake artificially determined. This is due to the EEG method monitoring of the neuron electrical process and the NIRS method monitoring of the blood mechanical processing. Using NIRS method and EEG method to monitor the brain activity, give us more information on the brain tissue. Generally, the EEG signal sends out fast global information of the brain activity. The skull bone is as a shell to block out the local electrical signal transferred to the surface of the head. Therefore the EEG signal looks similar from the electrode, located at different places of the head. The NIRS signal locally reflects the brain tissue blood perfusion and oxygenation. Therefore it may have potential to get more information about the brain

activity.

From the preliminary observation on one sleep apnea patient, the NIRS provide a useful information on the changes in specific biomedical markers of oxy-Hb and deoxy-Hb during apnea. These are associated with recurrent apnea, insufficient nasal CPAP pressure and the different response of the peripheral and central compartment to breathing events. The difference of the signal from finger pulse oxymeter and NIRS device suggest that optical monitoring of the brain may have advantage to help clarify the morbidity of OSA syndrome.

11. Future direction

The future research orientation will be described in this chapter, which includes theoretical analysis of far-red emission from biomedical samples, and the brain activity investigation using NIRS technology with conventional methods.

11.1. Further theoretical analysis of far-red emission from biomedical samples

This thesis research work demonstrates that the spectral wing of far-red emission could bring some useful information from biomedical samples, beyond the discovery of noise [1, 2, 3]. The simple physical model could roughly explain the origins of the spectral wing, coming from the laser excited tissue sample and its properties. We have to set up better theoretical models or modify existing the simple physical model of the mechanism of the far-red and NIR emission spectral wing. Model generated from the data of different tissue sample type and status will lead to a better understanding of the reason of the emission phenomena and will direct future research work on their applications. One of the key points of the future research is to find the relationship between the quantum efficiency and the shape of the spectral wing emission, with the type and conditions of the tissue. The wavelength dependent time profile of the emission may get more parameters of the emission and help us to find the mechanism from biomedical samples.

11.2. The brain activity investigation using NIRS technology

Different psychology activities could be stimulating the metabolism rate in different brain locations. Some sophisticated instrument are used to investigate the metabolism change by mapping different brain locations, such as optical method [4], fMRI [5], PET [6], and conventional EEG [7]. The multi-channel NIRS measurement is necessary for further investigation of brain function. The first step is building of the additional NIRS device to investigate the brain activity at different head locations simultaneously. More information can be obtained than just one detector to compare the neuron activity in different brain locations. One of the advantages of using NIRS method compared to the EEG method to monitor the brain activity, is that, through NIRS, the local changes of the brain tissue status can be obtained. A design of two NIRS devices is shown in Figure 11-1. The detecting location can be determined by the practical experiment purpose.

In current study, we use two NIR wavelengths setup to do brain research as it is shown in part B of Figure 11-1, which assumes every change comes from the hemoglobin concentration change. Using three wavelengths (such as 780, 805, and 830 nm) setup to monitor the metabolism change in tissue will yield three biochemical components concentrations, which include oxy- and deoxy- hemoglobin and cytochrome aa_3 oxidize in tissue.

The setup needs three modulated NIR laser light sources with three lock-in amplifiers for coherent electrical signal demodulation to separate the optical signal from different wavelength with one PMT detector.

11.3. References

1. Zhang G., Demos S. G., and Alfano R. R., "Far-red and NIR spectral wing emission from tissue samples under 532 nm and 632 nm photo-excitation", Lasers in Life Sciences., Vol. 9, pp 1-16, 1999.
2. Zhang G., Tang J., Ho P. P. and Alfano R. R., "Probing thermal damage and monitoring the treatment temperature of tissues using the near-infrared emission wing", Lasers in Life Sciences., Vol. 10, pp 1-15, 2000.
3. Hanlon EB, Itzkan I, Dasari RR, Feld MS, Ferrante RJ, McKee AC, Lathi D, Kowall NW, "Near-infrared fluorescence spectroscopy detects Alzheimer's disease in vitro", Photochem. Photobiol. 1999 Aug;70(2):236-42
4. Malonek D., and Grinvald A., "interaction between electrical activity and cortical microcirculation revealed by imaging spectroscopy: implications for functional brain mapping," (1996) Science **272** 551-554
5. Menon, R.S., Ogawa, S., Hu, X., Strupp, J.P., Anderson, P., and Ugurbil, K., BOLD based functional MRI at 4 tesla includes a capillary bed contribution: Echo-planar imaging correlates with previous optical imaging using intrinsic signals, Magn. Reson. Med. 33 (3) (1995) 453-459.
6. Buchsbaum M S, Gillin J C, Wu J, et al, "regional cerebral glucose metabolic rate in human sleep assessed by positron emission tomography", Life Sciences, 45(15), 1349-1356, (1989).

7. Buchsbaum, M.S., Mendelson, W.B., Duncan, W.C., Coppola, R., Kelsoe, J., and Gillin, J.C., Topographic cortical mapping of EEG sleep stages during daytime naps in normal subjects, Sleep, 5 (3) (1982) 248-255.

11.4. Figures

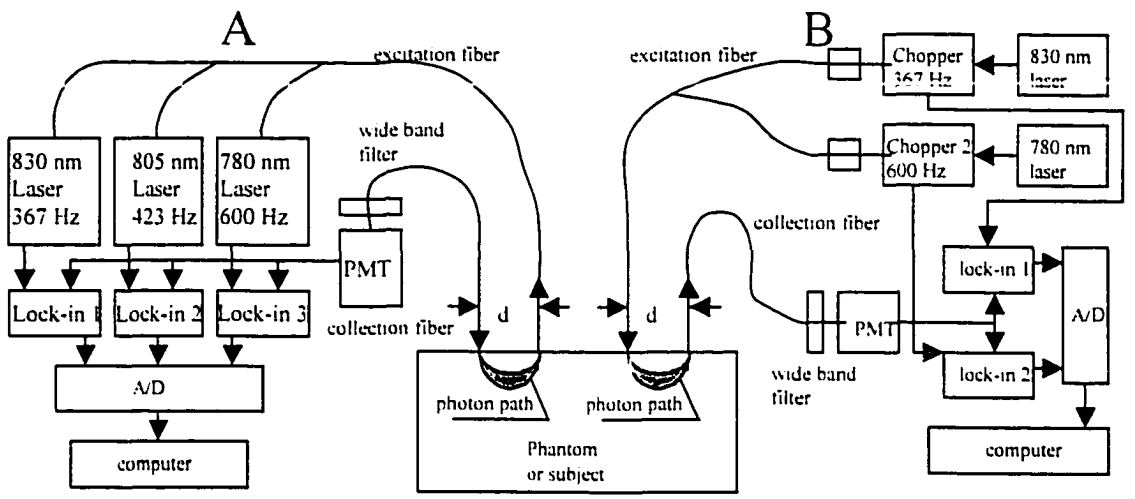

Figure 11-1 Block diagram of CW NIRS measurement system setup with two independent devices.

Part A is the new system to be built with three wavelengths, and part B is the system in current use with two wavelengths.

12. Appendix

12.1. IRB permission of normal sleep subject experiment with NIRS device at sleep lab of CCNY.

☐OMB No 0925-0418
Approved for use through 01/31/2001

Protection of Human Subjects
Assurance Identification/Certification/Declaration
(Common Federal Rule)

Policy: Research activities involving human subjects may not be conducted or supported by the Departments and Agencies adopting the Common Rule (56FR28003, June 18, 1991) unless the activities are exempt from or approved in accordance with the common rule. See section 101(b) the common rule for exemptions. Institutions submitting applications or proposals for support must submit certification or appropriate Institutional Review Board (IRB) review and approval to the Department or Agency in accordance with the common rule. Institutions with an assurance of compliance that covers the research to be conducted on file with the Department, Agency, or the Department of Health and Human Services (HHS) should submit certification of IRB review and approval with each application or proposal unless otherwise advised by the Department or Agency. Institutions which do not have such an assurance must submit an assurance and certification of IRB review and approval within 30 days of a written request from the Department or Agency.

1 Request Type	2. Type of Mechanism	3 Name of Federal Department or Agency and, if known, Application or Proposal Identification No.
XORIGINAL ☐FOLLOWUP ☐EXEMPTION	☐GRANT ☐ CONTRACT ☐ FELLOWSHIP ☐COOPERATIVE AGREEMENT ☐OTHER:	
4 Title of Application or Activity Regional Changes in Cerebral Oxygen Saturation During the Wake to Sleep Transition: Comparison of Near-Infrared Spectroscopic measures with Electroencephalographic and Subjective Measures Title on Consent form: Study of Low Power Near-Infrared Laser Light Response of the Brain at the Onset of Sleep		5. Name of Principal Investigator, Program Director, Fellow, or Other Professor A. Spielman

6 Assurance Status of this Project *(Respond to one of the following)*

☒ This Assurance, on file with Department of Health and Human Services, covers this activity:
Assurance identification no M-1111-XM IRB identification no 4XM

☐ This Assurance, on file with *(agency/dept)*_____, covers this activity
Assurance identification no._____ IRB identification no _____*(if applicable)*

☐ No assurance has been filed for this project. This institution declares that it will provide an Assurance and Certification of IRB review and approval upon request.

☐ Exemption Status: Human subjects are involved, but this activity qualifies for exemption under Section 101(b), paragraph_____

7 Certification of IRB Review (Respond to one of the following IF you have an Assurance on file)

X This activity has been reviewed and approved by the IRB in accordance with the common rule and any other governing regulations or subparts on *(date)*_9/18/97__ by: ☒Full IRB Review or ☐ Expedited Review

☐This activity contains multiple projects, some of which have not been reviewed. The IRB has granted approval on condition that all projects covered by the common rule will be reviewed and approved before they are initiated and that appropriate further certification will be submitted

8. Comments

9. The official signing below certifies that the information provided above is correct and that, as required, future reviews will be performed and certification will be provided		10. Name and Address of Institution The City College of The City University of New York Convent Avenue @ 138th Street New York, NY 10031
11. Phone No. *(with area code)* (212) 650-5418	12. Fax No. *(with area code)* (212) 650-7906	
13. Name of Official Regina Masterson		14. Title Director, Office of Research Administration
15. Signature Regina Masterson		16. Date 9/18/97

Authorized for Local Reproduction OPTIONAL FORM 310 (Rev. 1-98) Sponsored by HHS/NIH

Public reporting burden for this collection of information is estimated to average less than an hour per response. An agency may not conduct or sponsor, and a person is not required to respond to, a collection of information unless it displays a currently valid OMB control number. Send comments regarding this burden estimate or any other aspect of this collection of information, including suggestions for reducing this burden to: NIH, Project Clearance Office, 6701 Rockledge Drive, MSC 7730, Bethesda, Md. 20892-7730, ATTN: PRA 0925-0418. *Do not return the completed form to this address.*

12.2. IRB permission of sleep apnea subject experiment with NIRS device at sleep lab of CCNY

☐OMB No. 0925-0418
Approved for use through 01/31/2001

Protection of Human Subjects
Assurance Identification/Certification/Declaration
(Common Federal Rule)

Policy: Research activities involving human subjects may not be conducted or supported by the Departments and Agencies adopting the Common Rule (56FR28003, June 18, 1991) unless the activities are exempt from or approved in accordance with the common rule. See section 101(b) the common rule for exemptions. Institutions submitting applications or proposals for support must submit certification or appropriate Institutional Review Board (IRB) review and approval to the Department or Agency in accordance with the common rule. Institutions with an assurance of compliance that covers the research to be conducted on file with the Department, Agency, or the Department of Health and Human Services (HHS) should submit certification of IRB review and approval with each application or proposal unless otherwise advised by the Department or Agency. Institutions which do not have such an assurance must submit an assurance and certification of IRB review and approval within 30 days of a written request from the Department or Agency.

1. Request Type	2. Type of Mechanism	3. Name of Federal Department or Agency and, if known, Application or Proposal Identification No.
XORIGINAL ☐FOLLOWUP ☐EXEMPTION	☐GRANT ☐ CONTRACT ☐ FELLOWSHIP ☐COOPERATIVE AGREEMENT ☐OTHER:	

4. Title of Application or Activity	5. Name of Principal Investigator, Program Director, Fellow, or Other
Near Infrared Spectroscopy in Patients with Obstructive Sleep Apnea Syndrome	Professors A. Spielman and R. R. Alfano

6. Assurance Status of this Project *(Respond to one of the following)*

☒ This Assurance, on file with Department of Health and Human Services, covers this activity
Assurance identification no. M-1111-XM IRB identification no. 4XM

☐ This Assurance, on file with *(agency/dept)*_____, covers this activity
Assurance identification no._____ IRB identification no._____ *(if applicable)*

☐ No assurance has been filed for this project. This institution declares that it will provide an Assurance and Certification of IRB review and approval upon request.

☐ Exemption Status: Human subjects are involved, but this activity qualifies for exemption under Section 101(b), paragraph_____

7. Certification of IRB Review (Respond to one of the following IF you have an Assurance on file)

X This activity has been reviewed and approved by the IRB in accordance with the common rule and any other governing regulations or subparts on *(date)* 4/13/00 by: X Full IRB Review or ☐ Expedited Review

☐ This activity contains multiple projects, some of which have not been reviewed. The IRB has granted approval on condition that all projects covered by the common rule will be reviewed and approved before they are initiated and that appropriate further certification will be submitted.

8. Comments

9. The official signing below certifies that the information provided above is correct and that, as required, future reviews will be performed and certification will be provided.		10. Name and Address of Institution
		The City College of The City University of New York Convent Avenue @ 138th Street New York, NY 10031
11. Phone No. *(with area code)* (212) 650-5418	12. Fax No. *(with area code)* (212) 650-7906	
13. Name of Official Regina Masterson		14. Title Director, Office of Research Administration
15. Signature Regina Masterson		16. Date 4/13/00

Authorized for local Reproduction | OPTIONAL FORM 310 (Rev. 1-98) | Sponsored by HHS/NIH

Public reporting burden for this collection of information is estimated to average less than an hour per response. An agency may not conduct or sponsor, and a person is not required to respond to, a collection of information unless it displays a currently valid OMB control number. Send comments regarding this burden estimate or any other aspect of this collection of information, including suggestions for reducing this burden to: NIH, Project Clearance Office, 6701 Rockledge Drive, MSC 7730, Bethesda, Md. 20892-7730, ATTN: PRA 0925-0418. *Do not return the completed form to this address.*

12.3. Bibliography

1. Alfano R. R., Liu C. H., Sha W. L., Zhu H. R., Akins D. L., Cleary J., Prudente R., E Cellmer., "Human Breast Tissues Studied by IR Fourier Transform Raman Spectroscopy", Laser Life Sci. 4, 23-28 (1991).
2. Alfano R. R., Tang G. C., Pradham A., Lam W., Choy D. S. J., Opher E., "Fluorescence Spectra from Normal Human Breast and Lung Tissues," IEEE Journal of Quantum Electronics 23, 1806-1811 (1987).
3. Alfano R. R., Tata D. B., Cordero J., Tomashefsky P., Longo R. W., Alfano M. A., "Laser Induced Fluorescence Spectroscopy from Native Cancerous and Normal Tissue," IEEE Journal of Quantum Electronics 20, 1507-1511 (1984).
4. Alfano R.R, Demos SG, and G. SK, "Advances in optical imaging of biomedical media". Ann N Y Acad Sci, 1997. 820: p. 248-70.
5. Alfano RR, Demos SG, Galland P, Gayen SK, Guo Y, Ho PP, Liang X, Liu F, Wang L, Wang QZ, Wang WB, "Time-resolved and nonlinear optical imaging for medical applications". Ann N Y Acad Sci, 1998. 838: p. 14-28.
6. Badeau, A. F., C. E. Lee, J. R. Morris, S. Thompson, E. G. Malk and A. J. Welch. (1986) Temperature response during microvascular anastomosis using milliwatt CO2 laser. Lasers Surg. Med. 6,179.
7. Bailey, A. J., T. J. Sims, N. C. Avery and C. A. Miles. (1993) Chemistry of collagen cross-links: glucose-mediated covalent cross-linking of type-IV collagen in lens capsules. Biochem. J. 296, 489-496.

8. Balfors E.M., and Franklin K.A., (1994) "Impairment of cerebral perfusion during obstructive sleep apneas," Am. J. Respir. Crit. Care Med., 150: 1587-1591.

9. Baraga J J, Feld M S, and Rava R P, "In situ histochemistry of human artery using near infrared Fourier transform Raman spectroscopy", Proc. Natl. Acad. Sci. USA 89, 3473-3477 (1992).

10. Baraga J. J., Taroni P., Park Y. D., An K., Maestri A., Tong L. L., Rava R. P., Kittrell C., Dasari R. R., Feld M. S., "Ultraviolet Laser-Induced Fluorescence of Human Aorta", Spectrochimica Acta 45A, 95-99 (1989).

11. Baraga, J. J., Feld, M. S. and Rava, R. P. "Rapid near-infrared Raman spectroscopy of human tissue with a spectrograph and CCD detector," Appl. Spectrosc. 46(2), 187-190 (1992).

12. Benaron DA, Benitz WE, Ariagno RL, "Noninvasive methods for estimating in vivo oxygenation". Clinical Pediatrics, 1992. 31: p. 258-273.

13. Benaron DA, Cheong WF, and S. DK., "Tissue Optics". Science, 1997. 276: p. 2002-2003.

14. Benaron DA, Cheong WF, and Stevenson DK, "Tomographic time-of-flight optical imaging device" Adv Exp Med Biol, 1994. 361: p. 609-617.

15. Bown, S.G. (1983) Phototherapy of tumors. World J. Surg. 7, 700-709.

16. Braun, A.R., Balkin, T.J., Wesenten, N.J., Carson, R.E., Varga, M., Baldwin, P., Selbie, S., Belenky, G., and Herscovitch, P., Regional cerebral blood flow throughout the sleep-wake cycle: An H215O PET study, Brain, 120 (1997) 1173-1197.

17. Brazy JE, "Cerebral oxygen monitoring with near infrared spectroscopy: Clinical application to neonates". J Clin Monit, 1991. 7: p. 325-334.

18. Brun NC, Moen A, Borch K, Saugstad OD, Greisen G 1997 Near-infrared monitoring of cerebral tissue oxygen saturation and blood volume in newborn piglets. Am J Physiol.. 273(2 Pt 2): p. H682-6.

19. Buchsbaum M S, Gillin J C, Wu J, et al, "regional cerebral glucose metabolic rate in human sleep assessed by positron emission tomography", Life Sciences, 45(15), 1349-1356, (1989).

20. Buchsbaum, M.S., Gillin, J.C., Wu, J., Hazlett, E., Sicotte, N., Dupont, R.M., and Bunney, Jr., W.E., Regional cerebral glucose metabolic rate in human sleep assessed by positron emission tomography, Life Sciences, 45 (1989) 1349-1356.

21. Buchsbaum, M.S., Mendelson, W.B., Duncan, W.C., Coppola, R., Kelsoe, J., and Gillin, J.C., Topographic cortical mapping of EEG sleep stages during daytime naps in normal subjects, Sleep, 5 (3) (1982) 248-255.

22. Caspani B., P. R. Cecconi, R. Bottelli, P. Della Vigna, G. Ideo and G. Gozzi. (1997) The interstitial photocoagulation with laser light of liver tumors. Radiol. Med. (Torino) 94, 346-354.

23. Chance B, "Near-infrared images using continuous, phase-modulated, and pulsed light with quantitation of blood and blood oxygenation". Ann N Y Acad Sci, 24. 1998. 838: p. 29-45.

24. Chance B, Cope M, Gratton E, Ramanujam N, Tromberg B 1998b Phase measurement of light absorption and scatter in human tissue. Rev Sci Instrum,. 69(10): p. 3457-3481.

25. Chance B, Luo Q, Nioka S, Alsop DC, Detre JA 1997 Optical investigations of physiology: a study of intrinsic and extrinsic biomedical contrast. Philos Trans R Soc Lond B Biol Sci,. 352: p. 707-716.

26. Chance, B., Leigh, J.S., Miyake, H., Smith, D., Nioka, S., Greenfeld, R., Finander, M., Kaufmann, K., Levy, W., and Young, M., Comparison of time resolved and un-resolved measurements of deoxyhemoglobin in brain. Proc. Natl. Acad. Sci. 85: (1988) 4971-4975.

27. Clarke R. H., Hanlon E. B., Isner J. M., Brody H., "Laser Raman Spectroscopy of Calcified Atherosclerotic Lesions in Cardiovascular Tissue", Appl. Opt. 26, 3175-3177 (1987).

28. Cohen, J., and Cohen, C., Applied Multiple Regression/Correlation Analysis for the Behavioral Sciences, Lawrence Erlbaum, NY, 1975, 490 pp.

29. Cope M and Delpy DT, 1988 System for long-term measurement of cerebral blood flow and tissue oxygenation on newborn infants by infra-red transillumination. Med Biol Eng Comput,. 26: p. 289-294.

30. Cope M, VanDerZee P, Essenpreis M, Arridge SR, and Delpy DT, "Data analysis methods for near infrared spectroscopy of tissue: problems in determining the relative cytochrome aa3 concentration", in Time-resolved spectroscopy and imaging of tissues, Ed. By Chance B., Proc. SPIE Vol. 1431, p 251-262 (1991).

31. Cothren R. M., Richards-Kortum R., . Sivak M. V, Fitzmaurice Jr., M., Rava R. P., Boyce G. A., Doxtader M., Blackman R., Ivanc T. B., Hayes G. B., Feld M. S., Petras R. E., "Gastrointestinal Tissue Diagnosis by Laser-Induced Fluorescence Spectroscopy at Endoscopy", Gastrointestinal Endoscopy 36, 105-111 (1997).

32. Cruz J and Miner ME, 1986 Modulating cerebral oxygen delivery and extraction in acute traumatic coma, in Neurotrauma, W. KA, Editor., Butterworth: Boston. p. 55-72.

33. Delpy D., "Optical spectroscopy for diagnosis," Phys. World, 1994, Aug. 34-39.

34. Delpy DT, Cope M, van der Zee P, Arridge S, Wray S, Wyatt J, "Estimation of optical pathlength through tissue from direct time of flight measurement" Phys Med Biol, 1988. 33: p. 1433-1442.

35. Delpy DT, Cope M., 1997 Quantification in tissue near-infrared spectroscopy. Philos Trans R Soc Lond B Biol Sci,. 352: p. 649-659.

36. Delpy, D.T., Cope, M., van der Zee, P., Arridge, S., Wray, S., and Wyatt, J., Estimation of optical path length. Phys. Med. Biol., 33 (1988) 1433-1442.

37. Delpy, T., Cope, M.C., Cady, E.B., Wyatt, J.S., Hamilton, P.A., Hope, P.L., Wray, S., and Reynolds, E.O.R., Cerebral monitoring in newborn infants by magnetic resonance and near infrared spectroscopy. Scand. J. Clin. Lab. Invest., 47, Suppl 188, (1987) 9-17.

38. Dinerman, J. L., R. D. Berger, and H. Calkins. (1996) Temperature monitoring during radiofrequency ablation. J. Cardiovasc. Electrophysiol. 7,163-173.

39. Douglas N. J. and Thomas J. M. A., "Clinical value of polysomnography", Lancet 339(8789), 347-350 (1992).

40. Droste, D.W., Berger, W., Schuler, E., and Krauss, J.K., Middle cerebral artery blood flow velocity in healthy persons during wakefulness and sleep: A transcranial doppler study, Sleep, 16 (7) (1993) 603-609.

41. Ernst, T., and Henning, J., Observation of a fast response in functional MR, Magn. Reson. Med. 32 (1994) 146-149.

42. Essenpreis, M., C. E. Elwell, M. Cope, P. van der Zee, S. R. Arridge, and D. T. Delpy, (1993) "Spectral dependence of temporal point spread function in human tissues," Appl. Opt. Vol. 32, No. 4, p 418-25.

43. Fantini S, Franceschini M. A., Fishkin J. B., Barbieri B., and Gratton E., "Quantitative determination of the absorption of chromophores in strongly scattered media: a light-emitting-diode based technique", Appl. Opt. 33, 5204-5213.

44. Fantini S, Franceschini MA, and G. E, Semi-Infinite-Geometry Boundary Problem for Light Migration in Highly Scattering Media: a Frequency-Domain Study in the Diffusion Approximation. J Opt Soc Am, 1994. B 11: p. 2128-2138.

45. Fantini S, Franceschini-Fantini M A, Maier J S, Walker S A, Barbieri B, and Gratton E, "Frequency-domain multichannel optical detector for noninvasive tissue spectroscopy and oximetry", Opt. Engr. 34(1), 32-42 (1995)

46. Fantini S, Hueber D, Franceschini MA, Gratton E, Rosenfeld W, Stubblefield PG, Maulik D, Stankovic MR, 1999 "Non-invasive optical monitoring of the newborn piglet brain using continuous wave and frequency domain spectroscopy." Phys Med Biol,. 44: p. 1543-1563.

47. Feld, M.S., Manoharan, R., Salenius, J., Orenstein-Carndona, J., Romer, T.J., Brennan, J.F., Dasari, R.R., and Wang, Y., "Detection and characterization of human tissue lesion with near infrared Raman spectroscopy," in: Advances in

fluorescence Sensing technology, Vol. II, J.R. Lokowicz, ed. Proc. SPIE 2388, 99-104 (1995).

48. Feng S, and Zeng F, "perturgation theory of photon migration in the presence of a single defect", OSA Proc. On Advances in Optical Imaging and Photon Migration, 1994, Vol. 21, pp 217-228.

49. Feng S, Zeng F, and Chance B, "Monte Carlo simulation of photon mifration phat distribution in multiple scattering media", Proc. of Photon Migration and Imaging in Random Media and tissues, 1993, SPIE 1888, pp 78-89.

50. Ferrari M, Wilson DA, Hanley DF, et al., 1989 Determination of cerebral venous hemoglobin saturation by derivative near infrared spectroscopy. Adv Exp Med Biol., 248: p. 47-53.

51. Ferrari M.,De Blasi RA, Fantini S, Franceschini MA, Barbieri B, Quaresima V, Gratton E 1995 Cerebral and muscle oxygen saturation measurement by a frequency-domain near-infrared spectroscopic technique. Proc. SPIE 2389, 868-874.

52. Ferrari, M., Wilson, D.A., Hanley, D.F., Hartmann, J.F., Rogers, M.C., and Traystman, R.J., Noninvasive determination of hemoglobin saturation in dogs by derivative near-infrared spectroscopy, Am. J. Physiol., 256 (5 part 2) (1989) H1493-H1499.

53. Fishkin J. B., and Gratton E., "Propagation of photon-density waves in strongly scattering media containing an absorbing semi-infinite plane bounded by a straight edge', J. Opt. Soc. Am. A, vol.10, No. 1, 1993, 127-140.

54. Franceschini MA, Fantini S, Paunescu LA, Maier JS, Gratton E, "Influence of a Superficial Layer in the Quantitative Spectroscopic Study of Strongly Scattering Media". Appl. Opt., 37(31) p. 7447-7458 (1998)

55. Frank C J, McCreery R L, and Redd D C B, "Raman spectroscopy of nomal and diseased human breast tissues", Anal. Chem. 67(5), 777-783, (1995).

56. Frank C J, Redd D C B, Gansler T S, and McGreery R L, "Characterization of human breast biopsy specimens with near-IR Raman spectroscopy", Anal. Chem., 66(3), 319-326 (1994).

57. Germon, TJ, Evans, PD, Manara AR, Barnett, NJ, Wall, P, Nelson, RJ. Sensitivity of near infrared spectroscopy to cerebral and extra-cerebral oxygenation changes is determined by emitter-detector separation. J Clinical Monitoring and Computing 14, 353-360, 1998.

58. Glantz, S. A. Primer of Biostatistics, 3rd ed., McGraw-Hill, Inc. (1992)

59. Glassman, W. S., Steinberg, M. and Alfano, R. R. "Time resolved and steady state fluorescence spectroscopy from normal and malignant cultured human breast cell lines", Lasers in Life Sci. 6(2), 91-98 (1994).

60. Goddard-Finegold J, Louis PT, Rodriguez DL, David Y, Contant CF, Rolfe P 1998 Correlation of near infrared spectroscopy cerebral blood flow estimations and microsphere quantitations in newborn piglets. Biol Neonate,. 74(5): p. 376-84.

61. Gratton E, Fantini S, Franceschini MA, Gratton G, Fabiani M, "Measurements of scattering and absorption changes in muscle and brain". Philos Trans R Soc Lond B Biol Sci, 1997. 352: p. 727-735.

62. Grubhofer G, Tonninger W, Keznickl P, Skyllouriotis P, Ehrlich M, Hiesmayr M, Lassnigg A 1999 A comparison of the monitors INVOS 3100 and NIRO 500 in detecting changes in cerebral oxygenation. Acta Anaesthesiol Scand,. 43(4): p. 470-5.

63. Haines, D. E. and D. D. Watson. (1989) Tissue heating during radiofrequency catheter ablation: a thermodynamic model and observations in isolated perfused and super-perfused canine right ventricular free wall. PACE 12, 962-976.

64. Haines, D. E., D. D. Watson and A. F. Verow. (1990) Electrode radius predicts lesion radius during radiofrequency energy heating. Circ. Pes. 67, 124-129.

65. Hajak, G., Klingelh"fer, J., Schulz-Varszegi, M., Matzander, G., Sander, D., Conrad, B., and R□ther, E., Relationship between cerebral blood flow velocities and cerebral electrical activity in sleep, Sleep, 17 (1) (1994) 11-19.

66. Haller R. G., "Oxygen utilization and delivery in metabolic myopathis", Annals of Neurology, 1994, 36(6): 811-813.

67. Hanlon EB, Itzkan I, Dasari RR, Feld MS, Ferrante RJ, McKee AC, Lathi D, Kowall NW, "Near-infrared fluorescence spectroscopy detects Alzheimer's disease in vitro", Photochem. Photobiol. 1999 Aug;70(2):236-42

68. Hayakawa T., Terashima M., Kayukawa Y.,Ohta T., and Okada T., (1996) "Changes in cerebral oxygenation and hemodynamics during obstructive apneas," Chest, 109(4): 916-921.

69. Hazan, J, Broughton, R. Qantitative topographic EEG mapping during drowsiness and sleep onset. In: Ogilvie R.D. and Harsh, J.R. (Eds.) Sleep Onset:

Normal and Abnormal Processes, American Psychological Association, Washington DC, 1994, 219-235.

70. Heiss, W.D., Pawlik, G.,, Herholz, K., Wagner, R., and Wienhard, K., Regional cerebral glucose metabolism in man during wakefulness, sleep, and dreaming, Brain Res., 327 (1985) 362-366.

71. Hildebrand, Francis B. "Advanced Calculus for Applications", 2nd Edition, pp 6-31, Prentice-Hall, Inc., 1976.

72. Hintz SR, Cheong WF, van Houten JP, Stevenson DK, Benaron DA 1999 Bedside imaging of intracranial hemorrhage in the neonate using light: comparison with ultrasound, computed tomography, and magnetic resonance imaging. Pediatr Res,. 45(1): p. 54-59.

73. Hirtz DG, 1993 Report of the National Institute of Neurological Disorders and Stroke workshop on near infrared spectroscopy. Pediatrics,. 91: p. 414-417.

74. Hong, C.C., Gillin, J.C., Dow, B.M., Wu, J., and Buchsbaum, M.S., Localized and lateralized cerebral glucose metabolism associated with eye movement during REM sleep and wakefulness: A positron emission tomography (PET) study, Sleep, 18 (7) (1995). 570-580.

75. Hoshi, Y., Mizukami, S., and Tamura, M., Dynamic features of hemodynamic and metabolic changes in the human brain during all-night sleep as revealed by near-infrared spectroscopy, Brain Res., 652 (1994) 257-262.

76. Ingrams D. R., J. K. Dhingra, K. Roy, D. F. Perrault, I. D. Bottrill, S. Kabani, E. E. Rebeiz, M. M. Pankratov, S. M. Shapshay, R. Manoharan, I. Itzkan, M. S.

Feld, Autofluorescence Characterization of Oral Mucosa, Head & Neck 19, 27-32 (1997).

77. Jacques S.L., "Optical techniques for tissue science and engineering", SPIE Proceeding of Biomedical Optics 99, 3863, 2-7

78. Jasper, H., Report of the committee on methods of clinical examination in electroencephalography, Electroencephalogr. Clin. Neurophysiol., 10 (1959) 370-375.

79. Jobsis FF, "Noninvasive infrared monitoring of cerebral and myocardial sufficiency and circulatory parameters". Science, 1977. 198: p. 1264-1267.

80. John Travis. "Outside Influences: A cancer cell's physical environment controls its growth." Science News (1997); Aug. 30 152:138-9

81. Kamba M, Suto M, Ohta Y, et al., "Cerebral metabolism in sleep apnea: Evaluation by magnetic resonance spectroscopy", Am. J. Respir. Crit. Care Med. 156: 296-298, (1997).

82. Keller S., Schrader B., Hoffmann A., Schrader W., Metz K., Rehlaender A., Pahnke J., Ruwe M., Budach W., "Application of Near-Infrared-Fourier Transform Raman Spectroscopy in Medical Research", J. Raman Spectrosc. 25, 663-671 (1994).

83. Klingelhofer J, Hajak G, Sander D, et al., "Assessment of intracranial hemodynamics in sleep apnea syndrome", Stroke, 1992, 23(10) 1427-1433.

84. Kozikowski S. D., Wolfram L. J., Alfano R. R., "Fluorescence Spectroscopy of Eumelanins", IEEE Journal of Quantum Electronics 20, 1379-1382 (1984).

85. Kurth CD, Steven JM, Benaron D, Chance B, "Near-infrared monitoring of cerebral circulation." J Clin Monit, 1993. 9: p. 163-170.

86. Laser Institute of America, American National Standards for Use of Lasers, ANSI. Z136.1, 1993, Table 6, p 42, Table 7, p 43, Table 8, p44.

87. Liu C. H., Tang G. C., Pradhan A., Sha W. L., Alfano R. R., "Effects of Self-Absorption by Hemoglobins on the Fluorescence Spectra from Normal and Cancerous Tissues," Lasers in Life Sciences 3, 167-176 (1990).

88. Liu C. H., Das B. B., Sha Glassman W. L., Tang G. C., Yoo K. M., Zhu H. R., Akins D. L., Lubicz S. S., Cleary J., Prudente R., Celmer E., Caron A., Alfano R. R., "Raman, Fluorescence, and Time-Resolved Light Scattering as Optical Diagnostic Techniques to Separate Diseased and Normal Biomedical Media," J. Photochem. Photobiol. B: Biol., 16, 187-209 (1992).

89 Liu C. H., Sha Glassman W. L., Zhu H. R., Akins D. L., Deckelbaum L. I., Stetz M. L., O'Brien K., Scott J., Alfano R. R., "Near-IR Fourier Transform Raman Spectroscopy of Normal and Atherosclerotic Human Aorta", Laser Life Sci. 4, 257-264 (1992)

90. Madsen, P.L., Schmidt, J.F., Holm, S., Vorstrup, S., Lassen, N.A., and Wildschiodtz, G., Cerebral oxygen metabolism and cerebral blood flow in man during light sleep (stage 2), Brain Res., 557 (1991) 217-220.

91. Madsen, P.L., Schmidt, J.F., Wildschiodtz, G., Friberg, L., Holm, S., Vorstrup, S., and Lassen, N.A., Cerebral oxygen O_2 metabolism and cerebral blood flow in humans during deep and rapid-eye-movement sleep, J. Appl. Physiol., 70 (6) (1991) 2597-2601.

92. Mahadevan A., Mitchel M. F., Silva E., Thomsen S., Richards-Kortum R., "Study of the Fluorescence Properties of Normal and Neoplastic Human Cervical Tissue", Lasers in Surgery and Medicine 13, 647-655 (1993).

93. Mahadevan, A., Ramanujam, N., Mitchell, M. F., Malpica, A., Thomsen, S. and Kortum, R. R. "Optical techniques for the diagnosis of cervical precancers: Comparison of Raman and fluorescence spectroscopies," in Advances in Fluorescence Sensing Technology II, J. R. Lakowicz, ed., Proc. SPIE 2388, 110-120 (1995).

94. Maier JS, Gratton E, "frequency-domain methods in optical tomography: detection of localized absorbers and a backscattering reconstruction scheme", Proc. of Photon Migration and Imaging in Random Media and tissues, 1993, SPIE 1888, pp 440-449.

95. Maitinot, V. J., S. R. Mordon, V. A. Mitchell, P. N. Pellerin, and J.M. Brunetaud. (1994) Determination of efficient parameters for argon laser-assisted anastomoses in rats: macroscopic, thermal, and histological evaluation. Lasers Surg. Med. 15, 168-175.

96. Malonek D., and Grinvald A., "interaction between electrical activity and cortical microcirculation revealed by imaging spectroscopy: implications for functional brain mapping," (1996) Science 272 551-554

97. Mantulin, WW, Fishkin, JB, So, PTC, Gratton, E, Maier, JS. Quantitative diffusive wave spectroscopy in tissues. SPIE Proceedings, 1888, 420-427, 1993.

98. Maquet, P. and Phillips, C., Functional brain imaging of human sleep, J. Sleep Res., 7 (Suppl. 1) (1998) 42-47.

99. Maquet, P., Dive, D., Salmon, E., Sadzot, B., Franco, G., Poirrier, R., , von Frenckell, R., and Franck, G., Cerebral glucose utilization during sleep-wake cycle in man determined by positron emission. tomography and [18F]2-fluoro-2-deoxy-D-glucose method, Brain Res., 513 (1990) 136-143.

100. Maquet, P., Positron emission tomography studies of sleep and sleep disorders, J. Neurol., 244 (Suppl. 1) (1997) S23-S28.

101. Markwalder T-M., Grolimund P., Seiler R.W., Roth F., and Aaslid R., (1984) "Dependency of blood flow velocity in the middle cerebral artery in end-tidal carbon dioxide partial pressue," J. Cereb. Blood Flow Metabbol., 4:368-372.

102. Marrone O, Bonsignore M. R., Insalaco G., and Bonsignore G., "What is the evidence that obstructive sleep apnea is an important illness?", Monadi. Arch. Chest Dis. 53(6), 630-639 (1998).

103. McCormick, P.W., Stewart, M., Goetting, M.G., and Balakrishnan, G., Regional cerebrovascular oxygen saturation measured by optical spectroscopy in humans, Stroke, 22 (1991) 596-602.

104. McCormick, P.W., Stewart, M., Goetting, M.G., Dujovny, M., Lewis, G., and Ausman, J.I., Noninvasive cerebral optical spectroscopy for monitoring cerebral oxygen delivery and hemodynamics, Critical Care Med., 19 (1) (1991) 89-97.

105. McCormick, P.W., Stewart, M., Ray, P., Lewis, G., Dujovny, M., and Ausman, J.I., Measurement of regional cerebrovascular haemoglobin oxygen saturation in cats using optical spectroscopy, Neurol. Res., 13 (1) (1991) 65-70.

106. McCully K. K., Kakihira H., Vanderborne K., et al., "Noninvasive measurement of activity-induced changes in muscle metabolism", J. Biomed., 1991, 24: 153-156.

107. Meech S. R., Stubbs C. D., Phillips D., "The Application of Fluorescence Decay Measurements in Studies of Biological Systems", IEEE Journal of Quantum Electronics 20, 1343-1352 (1984).

108. Meek JH, Tyszczuk L, Elwell CE, Wyatt JS 1998 Cerebral blood flow increases over the first three days of life in extremely preterm neonates. Arch Dis Child Fetal Neonatal Ed., 78(1): p. F33-F37.

109. Menon, R.S., Ogawa, S., Hu, X., Strupp, J.P., Anderson, P., and Ugurbil, K., BOLD based functional MRI at 4 tesla includes a capillary bed contribution: Echo-planar imaging correlates with previous optical imaging using intrinsic signals, Magn. Reson. Med. 33 (3) (1995) 453-459.

110. Merica, H. and Gaillard, J.M., The EEG of the sleep onset period in insomnia: A discriminant analysis, Physiology & Behavior, 52 (1992) 199-204.

111. Meyer, J.S., Ishikawa, Y., Hata, T., Karacan, I., Cerebral blood flow in normal and abnormal sleep and dreaming, Brain and Cognition, 6 (1987) 266-294.

112. Meyer, J.S., Sakai, F., Karacan, I., Derman, S., and Yamamoto, M., Sleep apnea narcolepsy, and dreaming: Regional cerebral hemodynamics, Ann. Neurol., 7 (1980) 479-485.

113. National Commission on Sleep Disorders Research. (1993). Wake up America: A national sleep alert: Vol. 1. Executive summary and executive report. Washington, DC: Author.

114. Nelson KB and Ellenberg JH, 1986 Antecedents of cerebral palsy: Multivariate analysis of risk. N Engl J Med,. 315: p. 81.

115. Obrig, H. and Villringer, A.., Near-infrared spectroscopy in functional activation studies. Can NIRS demonstrate cortical activation?. In: Villringer A.., and Dirnagl U., (Eds.), Optical Imaging of Brain Function and Metabolism II, Plenum Press, New York, 1997, pp. 113-127.

116. Ogilvie R.D. and Harsh, J.R. (Eds.) Sleep Onset: Normal and Abnormal Processes, American Psychological Association, Washington DC, 1994, 397 pp.

117. Ogilvie, R.D., Simons, I.A., Kuderain, R.H., MacDonald, T., and Rustenburg, J., Behavioral, event-related potential, and EEG/FFT changes at sleep onset, Psychophysiology, 28 (1) (1991) 54-64

118. Patterson M. S., Chance B., and Wilson B. C., "Time resolved reflectance and transmittance for the noninvasive measurement of tissue optical properties", Appl. Opt. 28, 2331-2336. (1989)

119. Perelman LT, Wu J, Itzkan I, Wang Y, Dasari R and Feld MS, "Photon paths in turbid media: theory and experimental observation", OSA Proc. On Advances in Optical Imaging and Photon Migration, 1994, Vol. 21, pp 153-155.

120. Perlman JM, K.K., Volpe JJ., 1984 "The effect of eliminating fluctuating cerebral blood flow velocity in preterm infants with respiratory distress syndrome on the incidence and severity of intraventricular hemorrhage". Ann Neurol,. 16: p. 380.

121. Pollard V, Prough DS, DeMelo AE, Deyo DJ, Uchida T, Stoddart HF 1996a "Validation in volunteers of a near-infrared spectroscope for monitoring brain oxygenation in vivo. Anesth Analg," 82: p. 269-77.

122. Pollard V, Prough DS, DeMelo AE, Deyo DJ, Uchida T, Widman R 1996b "The influence of carbon dioxide and body position on near-infrared spectroscopic assessment of cerebral hemoglobin oxygen saturation". Anesth Analg,. 82: p. 278-287.

123. Post, M. J., A. N. de Graaf-Bos, G. Posthuma, P. G. de Groot, J. J. Sixma, and C. Borst. (1996) Interventional thermal injury of the arterial wall: unfolding of von Willebrand factor and its increased binding to collagen after 55øC heating. Thrombosis and Haemostasis 75, 515-519.

124. Pradhan, A., Das, B. B., Yoo, K. M., Cleary, J., Prudente, R., Celmer, E. and Alfano, R. R. "Time-resolved UV photoexcited fluorescence kinetics from malignant and non-malignant human breast tissues". Lasers in Life Sci. 4(4), 225-234 (1992)

125. Profio A. E., "Laser Excited Fluorescence of Hematoporphyrin Derivative for Diagnosis of Cancer", IEEE Journal of Quantum Electronics 20, 1502-1505 (1984).

126. Prudhomme, M., J. Tang, S. Rouy, G. Delacretaz, R. P. Salathe and G. Godlewski. (1996) Interstitial diode laser hyperthermia in the treatment of subcutaneous tumor. Lasers Surg. Med. 19, 445-450.

127. Pryds O, Greisen G, Skov LL, Friis-Hansen B 1990 Carbon dioxide-related changes in cerebral volume and cerebral blood flow in mechanically ventilated preterm neonates: comparison of near infrared spectrophotometry and 133Xenon clearance. Pediatr Res,. 27: p. 445-9.

128. Punwani, S., Ordidge, R.J., Cooper, C.E., Amess, P., and Clemence, M., MRI measurements of cerebral deoxyhaemoglobin concentration [dHb]--correlation with near infrared spectroscopy (NIRS), NMR Biomed., 11 (6) (1998) 281-289.

129. Rechtschaffen, A., and Kales, A. (1968). "A manual of standardized terminology, techniques, and scoring system fro sleep stage of human subjects" (National Institutes of Health Publication No. 204). Washington, DC: U.S. Government Printing Office.

130. Rechtschaffen, A., Sleep onset: Conceptual Issues. In: R.D. Ogilvie and J.R. Harsh. (Eds.) Sleep Onset: Normal and Abnormal Processes. American Psychological Association, Washington DC, 1994, pp. 3-17.

131. Redline S. and Strohl K. P., "Recognition ans consequences of obstructive sleep apnea syndrome", Clin. Chest. Med. 19(1), 1-19 (1998).

132. Robertson, G. S., M. Thomas, J. Jamieson, P. S. Veitch and A. R. Dennison. (1996) Palliation of oesophageal carcinoma using the argon beam coagulator. Br. J. Surg. 83, 1769-1771.

133. Sakai, F., Meyer, J.S., Karacan, I., Derman, S., and Yamamoto, M., Normal human sleep: Regional cerebral Hemodyamics, Ann. Neurol., 7 (1980) 471-478.

134. Schmitt J.M., Knuttel A., and Knutson J.R., "Interference of diffusive light waves," J. Opt. Soc. Am. A Vol. 9(10), 1832-1843.

135. Schober, R., M. Bettage, M. Sabel, F. Ulrich and S. Hessel. (1993) Fine structure of zonal change in experimental Nd:YGY laser-induced interstitial hyperthermia. Lasers Surg. Med. 13, 234-241.

136. Severinghaus J. W., Kelleher J. F., "Recent developments in pulse oximetry", Anesthesiology, 1992, 76(6): 1018-1037

137. Sevick, EM, Chance, B, Leigh, J, Nioka, S, Maris, M. Quantitation of time- and frequency-resolved optical spectra for the determination of tissue oxygenation. Analytical Biochemistry, 195, 330-351, 1991.

138. Sha Glassman W. L., Liu C. H., Tang G. C., Lubicz S., Alfano R. R., "Ultraviolet Excited Fluorescence Spectra from Non-Malignant and Malignant Tissues of the Gynecological Tract". Lasers in the Life Sciences 5, 4958 (1992).

139. Shephard J.W. (1989) "Cardiorespiratory changes in obstructive sleep apnea." In M.H. Kryger, T. Roth and W.C. Dement, editors. Principles and Practice of Sleep Medicine, 2nd ed. Saunders, Philadelphia, 657-666.

140. Shina T., Tanabe L., Nakase Y., et al, "Development of a portable tissue oximeter using near infrared spectroscopy", med. & Biol. Eng. & Compt., 1995, July: 622-626

141. Shiotsuka, S., Atsumi, Y., Ogata, S., Yamamoto, R., Igawa, M., Takahashi, K., Hirasawa, H., Koyama, K., Maki, A., Yamashita, Y., Koizumi, H., and Toru, M., Cerebral blood volume in the sleep measured by near-infrared spectroscopy, Psychiatry and Clinical Neurosciences, 52 (2) (1998) 172-173.

142. Skov L, Pryds O, Greisen G 1991 Estimating cerebral blood flow in newborn infants: Comparison of near infrared spectroscopy and 133Xenon clearance. Pediatr Res,. 30: p. 570-573.

143. Skov, L, Ryding, J, Pryds, O, and Greisen, G. Changes in cerebral oxygenation and cerebral blood volume during endotracheal suctioning in ventilated neonates. Acta Paediatr 81, 389-393, 1992.

144. Smielewski, P., Kirkpatrick, P., Minhas, P., Pickard, J.D., and Czosnyka, M., Can cerebrovasular reactivity be measured with near-infrared spectroscopy?, Stroke 26 (12) (1995) 2285-2292.

145. Smith, DS, Levy, W, Maris, M, Chance, B. Reperfusion hyperoxia in brain after circulatory arrest in humans. Anesthesiology, 73, 12-19, 1990.

146. Smith, Kendric C. "The science of photobiology", 2nd edition, Plenum press, 1989.

147. Spielman A.J., Zhang G., Yang C.M., D'Ambrosio P., Serizawa S., Nagata M., von Gizycki H. and Alfano R.R., "Intercerebral hemodynamics probed by near infrared spectroscopy in the transition between wakefulness and sleep," Brain Research (in press).

148. Stankovic MR, Fujii A, Maulik D, Boas D, Kirby D, "Optical monitoring of cerebral hemodynamics and oxygenation in the neonatal piglet." J Maternal Fetal Invest, 1998. 8(2): p. 71-78.

149. Stankovic MR, Fujii A, Maulik D, Kirby D, Stubblefield PG 1998b Optical brain monitoring of the cerebrovascular effects induced by the acute cocaine exposure in neonatal pigs. J Maternal Fetal Invest,. 8(3): p. 108-112.

150. Stankovic MR, Maulik D, Boas DA, Stubblefield PG, 1998a Emerging Technologies: Fetal Optical Monitoring, in Asphyxia and Fetal Brain Damage, M. D, Editor., John Wiley & Sons, Inc.: New York. p. 345-364.

151. Stankovic MR, Maulik D, Rosenfeld W, Stubblefield PG, Kofinas AD, Drexler S, Nair R, Franceschini MA, Hueber D, Gratton E, Fantini S, 1999 Real-time optical imaging of experimental brain ischemia and hemorrhage in neonatal piglets. J Perinatol,. 27(4): p. 1-8.

152. Stankovic MR, Maulik D, Rosenfeld W, Stubblefield PG, Kofinas AD, Gratton E, Franceschini MA, Fantini S, Hueber D, (2000) ""The role of frequency domain optical spectroscopy in the detection of neonatal brain hemorrhage - a newborn piglet study"". J Maternal Fetal Medicine (In Press).

153. Sterenborg H. J. C. M., Thomsen S., Jacques S. L., "In Vivo Autofluorescence, of an Unpigmented Melanoma in Mice. Correlation of Spectroscopic Properties to Microscopic Structure", Melanoma Research 5, 1-6 (1995).

154. Tamura, M., Hazeki, O., Nioka, S., Chance, B., and Smith, D.S., The simultaneous measurements of tissue oxygen concentration and energy state by near-infrared and nuclear magnetic resonance spectroscopy, Exp. Med. Biol. 222 (1988) 359-363.

155. Tang G. C., Pradhan A., Sha W., Chen J., Liu C. H., Wahl S. J., Alfano R. R., "Pulsed and CW Laser Fluorescence Spectra from Cancerous, Normal, and Chemically Treated Normal Human Breast and Lung Tissues", Applied Optics 28, 2337-2342 (1993).

156. Thomsen, S., J. A. Pearce, and W. Cheong. (1989) Changes in birefringence as markers of thermal damage in tissues. IEEE Trans. Biomed. Engin. 36, 1174-1179.

157. Toga, A.W. and Mazziotta, J.C. (Eds.), Brain Mapping: The Methods, Academic Press, San Diego, 1996, 471 pp.

158. Torres, J. H., T. A. Springer, A. J. Welch and J.A. Pearce. (1990) Limitations of a thermal camera in measuring surface temperature of laser-irradiated tissue. Lasers Surg. Med. 10, 510-523.

159. Tsuji M, duPlessis A, Taylor G, Crocker R, Volpe JJ, "Near infrared spectroscopy detects cerebral ischemia during hypotension." Pediatr Res. 1998. 44(4): p. 591-595.

160. Tsuji M, Naruse H, Volpe J, Holtzman D 1995 Reduction in cytochrome aa3 measured by near-infrared spectroscopy predicts cerebral energy loss in hypoxic piglets. Pediatr Res,. 37: p. 253-259.

161. van Assendelft, O.W., "Spectrophotometry of haemoglobin derivatives", Cherls C. Thomas, Assen, The Netherlands, 1970, pp.53-57.

162. Van der Zee, P, Cope, M, Arridge SR, et al Experimentally measured optical pathlengths for the adult head, calf and forearm and the head of the newborn infant as a function of interoptode spacing. In: Goldstick, TK, Cabe, MML, Maguire, DJ (eds) Oxygen Transport to Tissue XII, P. Plenum Press, New York, 1992.

163. Van Houten JP, Benaron DA, Spilman S, Stevenson DK 1996 Imaging brain injury using time resolved near infrared light scanning. Pediatr Res,. 39(3): p. 470-476.

164. Villringer, A., and Dirnagl, U., Coupling of brain activity and cerebral blood flow: Basis of functional neuroimaging, Cerebrovascular and Brain Metabolism Reviews, 7 (1995) 240-276.

165. Villringer, A., Functional neuroimaging: Optical approaches, In: Villringer A., and Dirnagl U., (Eds.), Optical Imaging of Brain Function and Metabolism II, Plenum Press, New York, 1997, pp. 1-18.

166. Volpe JJ, 1989 Intraventricular hemorrhage and brain injury in the premature infant. Neuropathology and pathogenesis. Clin Perinatol,. 16: p. 361-386.

167. Volpe JJ, 1997 Brain injury in the premature infant - from pathogenesis to prevention. Brain & Development,. 19: p. 519-534.

168. Wagnieres G. A., Linuma S., Schomacker K. T., Deutsch T. F., Hasan T., "In Vivo Tissue Characterization Using Environmentally Sensitive Fluorochromes", In: Fluorescence Microscopy and Fluorescent Probes, Ed. J. Slavik, Plenum Press, New York, NY, 1996.

169. Wahr JA, Tremper KK, Samra S, Delpy DT, "Near-infrared spectroscopy: Theory and applications". J Cardiothoracic and Vascular Anesthesia, 1996. 3: p. 406-418.

170. Walsh, J. T. Jr., T. J. Flotte, R. R. Anderson and T. F. Deutsch. (1988) Pulsed CO2 laser tissue ablation: effect of tissue type and pulse duration on thermal damage. Laser Surg. Med. 8, 108-118.

171. Wolbarsht M.L., Walsh A.W., and George G., ""Melanin, a unique biological absorber"", Appl. Opt., 20(13), (1981) 2184-2186.

172. Wray S, Cope M, Delpy DT, Wyatt JS and Reynolds E O, "Characterization of the near infrared absorption spectra of cytochrome aa3 and hemoglobin for the

non-invasive monitoring of cerebral oxygenation" Bioch. Biophy Acta, 933 (1988) 184-192.

173. Wright Jr., K.P., Badia, P., and Wauquier, A.., Topographical and temporal patterns of brain activity during the transition from wakefulness to sleep, Sleep 18 (10) (1995) 880-889.

174. Wyatt JS, 1997 Cerebral oxygenation and haemodynamics in the foetus and newborn infant. Philos Trans R Soc Lond B Biol Sci.. 352: p. 697-700.

175. Wyatt JS, Edwards AD, Cope M, Delpy DT, McCormick DC, Potter A, Reynolds EO 1991 Response of cerebral blood volume to changes in arterial carbon dioxide tension in preterm and term infants. Pediatr Res.. 29: p. 553-557.

176. Yang Y., Celmer E. J., Zurawska-Szczepaniak M., Alfano R. R., "Excitation Spectrum of Malignant and Benign Breast Tissues: A Potential Optical Biopsy Approach," Lasers in the Life Science 7, 249-265 (1997).

177. Yang Y., Tang G. C., Bessler M., Alfano R. R., "Fluorescence Spectroscopy as a Photonic Pathology Method for Detecting Colon Cancer," Lasers in Life Sciences 6, 259-276 (1995).

178. Yang Y.L., Celmer E. J., Koutcher J.A., and Alfano R.R., "DNA and protein changes in tissue probed by Kubelka Munk spectral function", Optical Biopsy III, (2000), pp 150-153. SPIE Proc. 3917

179. Yang Y.L., Celmer E. J., Koutcher J.A., Ho P.P., and Alfano R.R., "DNA and protein change in human breast tissues by diffuse reflectance spectrum", in Optical sensing, imaging, and manipulation for biological and biomedical applications, SPIE Proc. 4082, pp 71-74, (2000).

180. Yoxall, C.W., Weindling, A.M., Dawani, N.H., and Peart, I., Measurement of cerebral venous oxyhemoglobin saturation in children by near-infrared spectroscopy and partial jugular venous occlusion, Pediatr. Res., 38 (1995) 319-323.

181. Zhang G, Spielman AJ, D'Ambrosio P, Nagato M, Serizawa S, Conroy D, Lombardo G, and Alfano RR. The cerebral hemodynamics of obstructive sleep apnea probed by Near-Infrared Spectroscopy (NIRS). Sleep Research, 1998.

182. Zhang G., Demos S. G., and Alfano R. R., "Far-red and NIR spectral wing emission from tissue samples under 532 nm and 632 nm photo-excitation", Lasers in Life Sciences., Vol. 9, pp 1-16, 1999.

183. Zhang, G., S. G. Demos, and R. R. Alfano. (1998), "Far-red and NIR emission from tissues," SPIE Proceeding of Optical Biopsy II 3250, 72-77.

184. Zhang, G., Tang, J., Ho, P. P., and Alfano, R. R. (2000) "Probing thermal damage and monitoring the treatment temperature of tissues using the near-infrared emission wing", Lasers in Life Sci. 10(1), 95-109.